UCRL-11857

University of California

Ernest O. Lawrence Radiation Laboratory

SURFACE IONIZATION OF CESIUM AND THERMIONIC EMISSION FROM PLANAR SINGLE CRYSTALS OF TUNGSTEN

Berkeley, California

DISCLAIMER

UCRL-11857

UNIVERSITY OF CALIFORNIA

Lawrence Radiation Laboratory
Berkeley, California

AEC Contract No. W-7405-eng-48

SURFACE IONIZATION OF CESIUM AND THERMIONIC EMISSION FROM PLANAR SINGLE CRYSTALS OF TUNGSTEN

Daniel René Koenig

(Ph.D. Thesis)

June 1966

SURFACE IONIZATION OF CESIUM AND THERMIONIC EMISSION FROM PLANAR SINGLE CRYSTALS OF TUNGSTEN

Daniel Rene Koenig

Inorganic Materials Research Division, Lawrence Radiation Laboratory, and Department of Nuclear Engineering, College of Engineering, University of California, Berkeley, California

ABSTRACT

June 1966

The thermal emission of electrons, and cesium atoms and ions from two large (≈ 1.5 cm^2), flat, monocrystalline, tungsten surfaces oriented in the [100] and [110] crystallographic directions was investigated.

All experimental results were obtained by measuring the current-voltage-time characteristics of two diodes, each having one of the tungsten single crystals for the cathode (emitter). A guard ring in the plane of the collector insured accuracy of the current measurements.

The work function ϕ_o of each crystal surface, determined from measurements of the field-free thermionic emission in vacuum in the temperature range 1400 to 2200°K was:

ϕ_o (100) = 4.65 ± 0.02 eV, and ϕ_o (110) = 5.33 ± 0.04 eV.

The desorption energies ϕ_{io} and ϕ^*_{ao} of cesium ions and atoms, respectively, evaporating from the (essentially) bare crystal surfaces, determined from measurements of the evaporation rates of these particles in the temperature range 1000 to 1500°K, were:

ϕ_{io} (100) = 2.05 ± 0.05 eV, and ϕ^*_{ao} (100) = 2.77 ± 0.05 eV,

ϕ_{io} (110) = 2.06 eV, and ϕ^*_{ao} (110) = 3.28 eV.

The change in the work function of each crystal surface due to

adsorption of cesium was evaluated from measurements of both the field-free electron and cesium-ion emissions in the surface-temperature range 850 to 1450°K and the cesium-reservoir temperature range 0 to 100°C. Excellent agreement was found between these two independent determinations.

Much of the data obtained from the (110) crystal exposed to cesium could not be confidently related to the vacuum data because the crystal surface was believed to have become contaminated.

As part of this study, the flux of cesium vapor in equilibrium with its condensed phase was measured in the temperature range 0 to 120°C.

TABLE OF CONTENTS

I. INTRODUCTION

Since the original work of Langmuir and Kingdon, the adsorption of alkali atoms on metal surfaces was known to decrease their work function.[56] New theories to describe this effect have been introduced in conjunction with the recent development of the thermionic energy-conversion field.[24,31,35,76,16] Although these theories have been applied with considerable success to polycrystalline surfaces, they are strictly valid only for surfaces with uniform work functions. Studies of thermionic emission and surface ionization of alkali vapors from single crystals which have been done since the thirties have shown that the work function of a polycrystalline surface is not uniform.

The first experiments were done on single-crystal wires operating in vacuum or in an alkali vapor; by azimuthal scan around the wire, the work function of refractory metal surfaces was demonstrated to depend on their crystallographic orientation.[45,68,82,81] Additional evidence for the dependence of the work function on the crystallographic orientation came from field-emission, thermionic-emission, and surface-ionization experiments on hemispherical and point crystals.[61,9,98,8,66,96] Most of these studies can be considered only qualitative, because of the uncertainties in the actual area of current emission. More recently, better quantitative results were obtained from flat single-crystal ribbons or etched wires.[13,80,42,87,77] It was not until quite recently, as this work was in progress, that large (1 cm^2) monocrystalline electrodes were incorporated in cesium-plasma diodes for the study of thermionic energy conversion.[73,12,52,69,70]

The object of this dissertation was to study experimentally the change in the work function of planar monocrystalline-tungsten surfaces

exposed to a cesium vapor, and to systematically measure the physical properties needed to describe this phonomenon. According to the theoretical work of Carabateas,[15] and Rasor and Warner,[76] the work function depression $\Delta\phi$ of a metal surface that is at temperature T_E and is exposed to a cesium vapor in thermodynamic equilibrium with its liquid or solid phase at temperature T_{Cs} should be a unique function of the ratio T_E/T_{Cs} involving the bare work function ϕ_o of the metal, the heats of evaporation ϕ_{io} and ϕ_{ao} of cesium ions and atoms for the bare metal surface, the change in the enthalpy h of cesium going to the vapor phase, and the first ionization potential V_i of cesium. All of these quantities but the last were measured in this investigation.

These measurements were done by observing the current-voltage-time characteristics of cesium-plasma diodes having planar monocrystalline-tungsten emitters oriented in the [110] and [100] crystallographic directions. Chronologically the (110) crystal was studied first, but the results obtained for both crystals were analyzed together and the development of this paper will follow the chronological order in which the various surface properties were measured.

The diodes were first operated in vacuum and the bare work functions were evaluated from field-free electron emission data. Then cesium was introduced into the diodes, and the desorption energies of cesium ions and atoms were determined from measurements of the evaporation rates of very dilute films of cesium adsorbed on the crystal surfaces. The detailed analysis of these experimental results led to the suggestion of a technique for studying the sputtering of alkali metal surfaces under bombardment by ions of their own vapor. Finally, the current-voltage characteristics of the diode operating in cesium vapor were measured. From the cesium-ion

current data, the vapor flux of cesium and the threshold temperatures for 100% ionization on the crystal surfaces were measured as a function of the cesium-reservoir temperature. The effective work functions of the cesiated (having adsorbed cesium) emitters were evaluated from field-free cesium-ion emission-data by means of the Saha-Langmuir equation, and from field-free electron-emission data by means of the Richardson equation. All of our results were compared wherever possible with theoretical predictions and also with earlier experimental data for single-crystal and polycrystalline tungsten. The results obtained from the (100) crystal were quite consistent and were sufficiently complete to make such a comparison. However, most of the data obtained from the (110) crystal exposed to cesium could not be confidently related to the vacuum data because the crystal surface was believed to have become contaminated.

An attempt was made to evaluate the work-function uniformity of the crystal surfaces from the over-all results of this study. This effort resulted in part in the development of a simple and sensitive way of measuring the bare work-function distribution on electrode surfaces.

A list of the symbols used in this report is contained in the nomenclature. The appendices, which contain a detailed description of the diode and associated equipment, include also circuit diagrams, an experimental and theoretical analysis of the radial temperature distribution of the emitter, the detailed presentation of various arguments introduced in the main body of the thesis, and tabulations of most of the data obtained in the experiments.

II. DESCRIPTION OF DIODE

A general description of the diode is given here, but the reader may refer to Appendices A through K for more details.

All experimental results were obtained by measuring the current-voltage-time characteristics of a diode that had a planar emitter and collector, and was capable of operating in vacuum or in a cesium vapor. The diode was contained within the cylindrical metal-and-ceramic body shown in Figs. II.1 through II.3.

The emitter (E) was a flat monocrystalline disk of tungsten 0.524 in. in diameter and 0.18 in. thick, oriented with either the [110] or [100] crystallographic directions normal to the surface. The crystal, molybdenum brazed at 2700°C to a tantalum support (J), was heated in the diode by electron bombardment from a spirally wound tungsten filament (F). The emitter temperature was measured by sighting an optical pyrometer through one of two sapphire windows (D) (calibrated for light absorption) onto a small hole, 0.1 in. deep and 0.015 in. in diameter, drilled into the side of the tungsten disk. The emitter and the bottom of the collector assembly were surrounded by a molybdenum heat shield (H). A separate thermal mock-up, incorporating the actual emitter assembly of the diode, was constructed to determine the radial temperature distribution on the surface of the emitter. Up to 1950°C the emitter temperature was uniform within the precision of the pyrometer (±2°C).

The collector assembly was mounted on a bellows (B) and consisted of a copper rod collector (C) electrically insulated from a surrounding, concentric, copper cylinder (G) which served as a guard ring. The diameter of the face of the collector was 0.370 in. and the width of the annular gap between collector and guard ring was 0.004 in. The effective area of

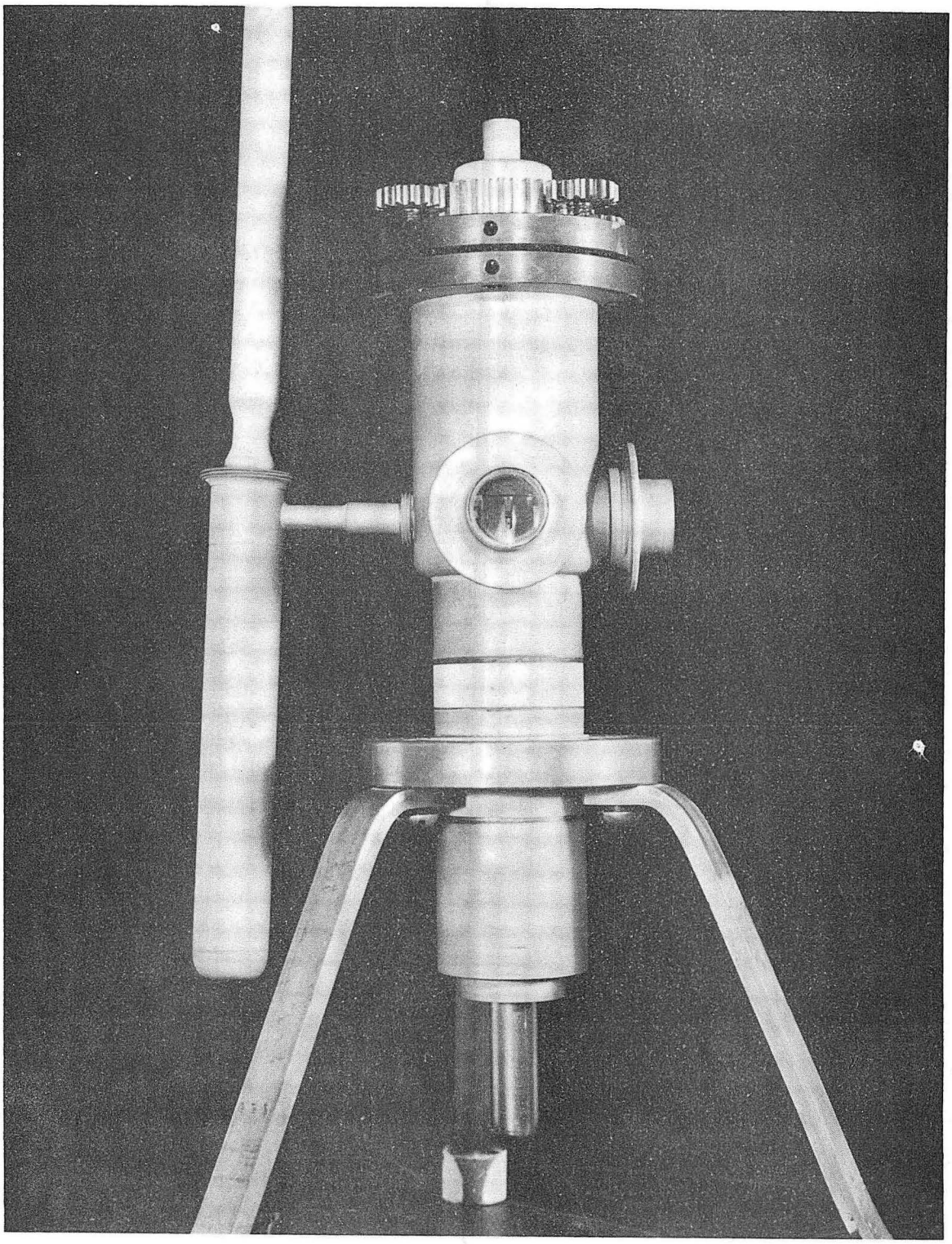

ZN-5591

Fig. II. 1

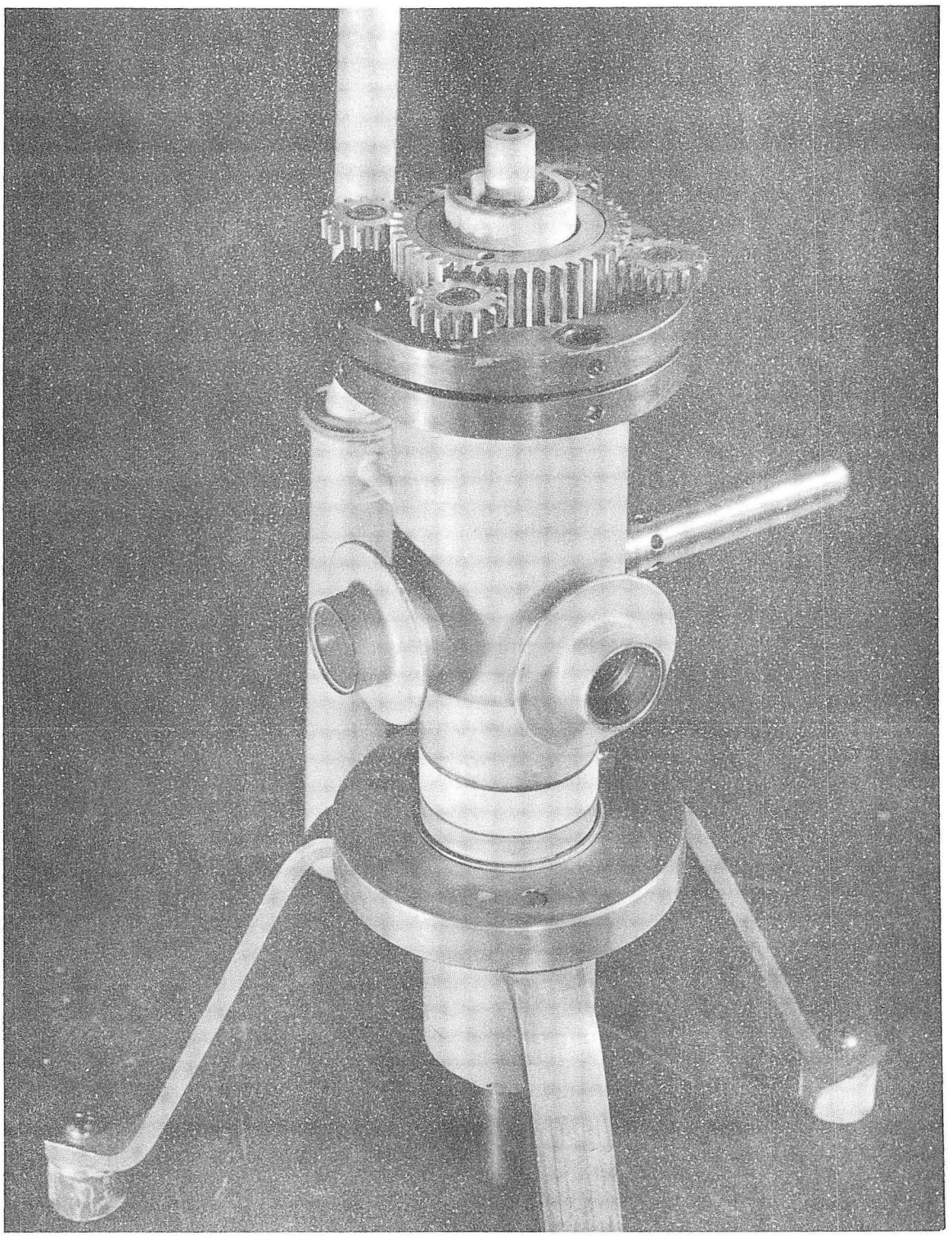

ZN-5592

Fig. II.2

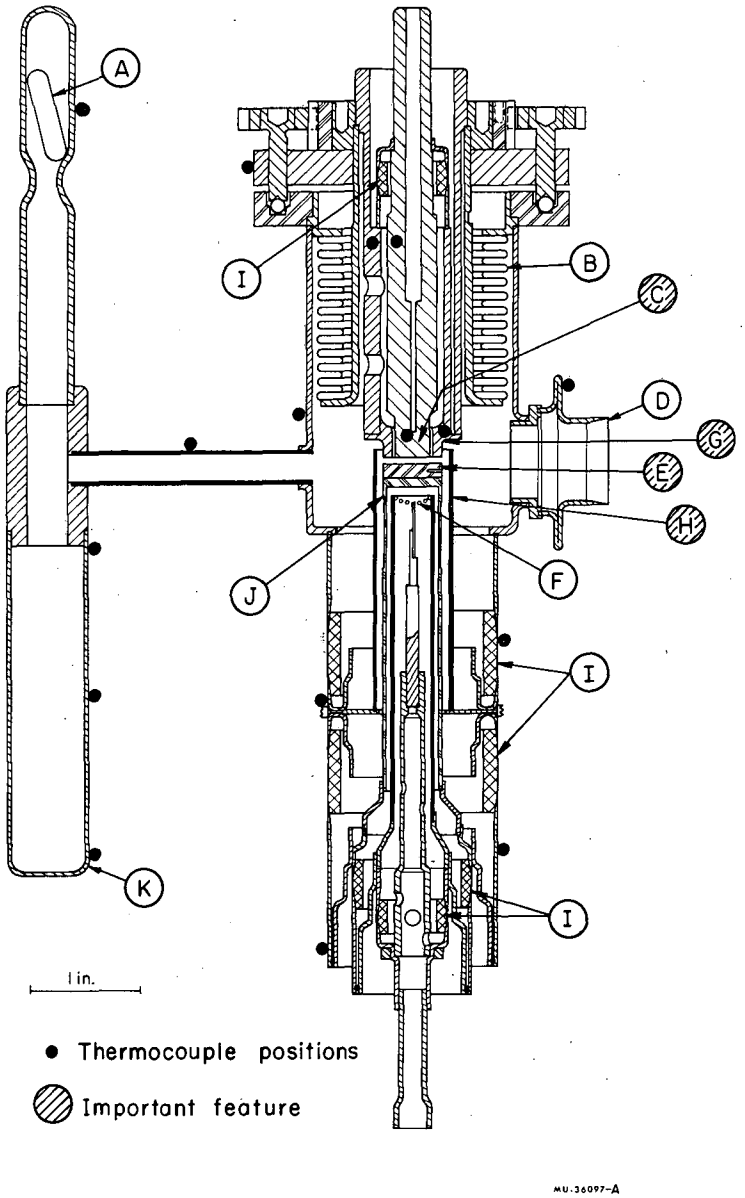
A
I
B
C
D
G
E
H
J
F
I
K
I
1 in.
Thermocouple positions
Important feature
MU-36097-A

Fig. II.3

the collector was taken to be the area of its face plus half the gap area and was 0.71 cm^2 (approximately half of the emitter area). The temperatures of the faces of the collector and guard ring were individually monitored by means of thermocouples. The difference in these temperatures was maintained at all times at less than 10°C by external heating or cooling.

Spacing and parallelism between the emitter and the collector assembly were continuously adjustable and were observed by sighting through the windows with a cathetometer having a precision of about 0.1 mil. Data were normally taken at a spacing of 0.010 to 0.015 in.

The top of the side appendage to the diode contained a Pyrex-glass ampoule (A) of vacuum-distilled cesium (Fig. II.3). After the vacuum data were obtained, the capsule was crushed and the cesium transferred by evaporation and subsequent condensation to the bottom of the appendage (K). This part of the appendage was held tightly in a copper jacket whose temperature was maintained by a combination of heating and cooling, at a desired value in order that the flux of cesium vapor in the diode body could be adjusted. Heating wires, wrapped around the diode body, including the top of the appendage, maintained its temperature at all points well above that of the cesium condensed in the reservoir.

The diode was outgassed for a period ranging from 30 to 60 hours, with the emitter operating at 1750°C and the body at about 600°C during much of this period, until the static pressure in the diode under these conditions dropped to between 10^{-8} and 10^{-7} torr. When cold, the diode was sealed off at a pressure of about 2×10^{-9} torr.

The single-crystal disks were cut from a bulk crystal (Linde Company), with a spark cutter used to minimize surface deformations, and were lapped, electropolished, and x-rayed for orientation. Figures II.4 and II.5 show

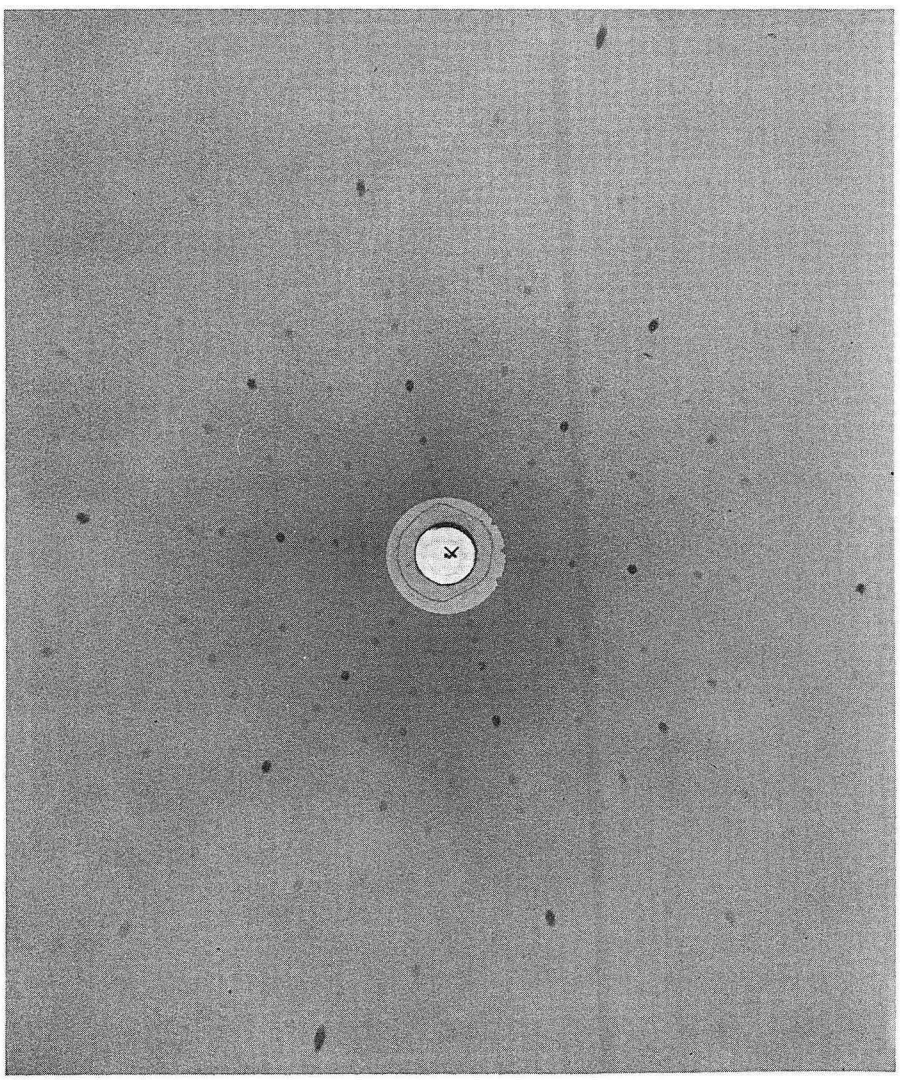

ZN-5117

Fig. II.4

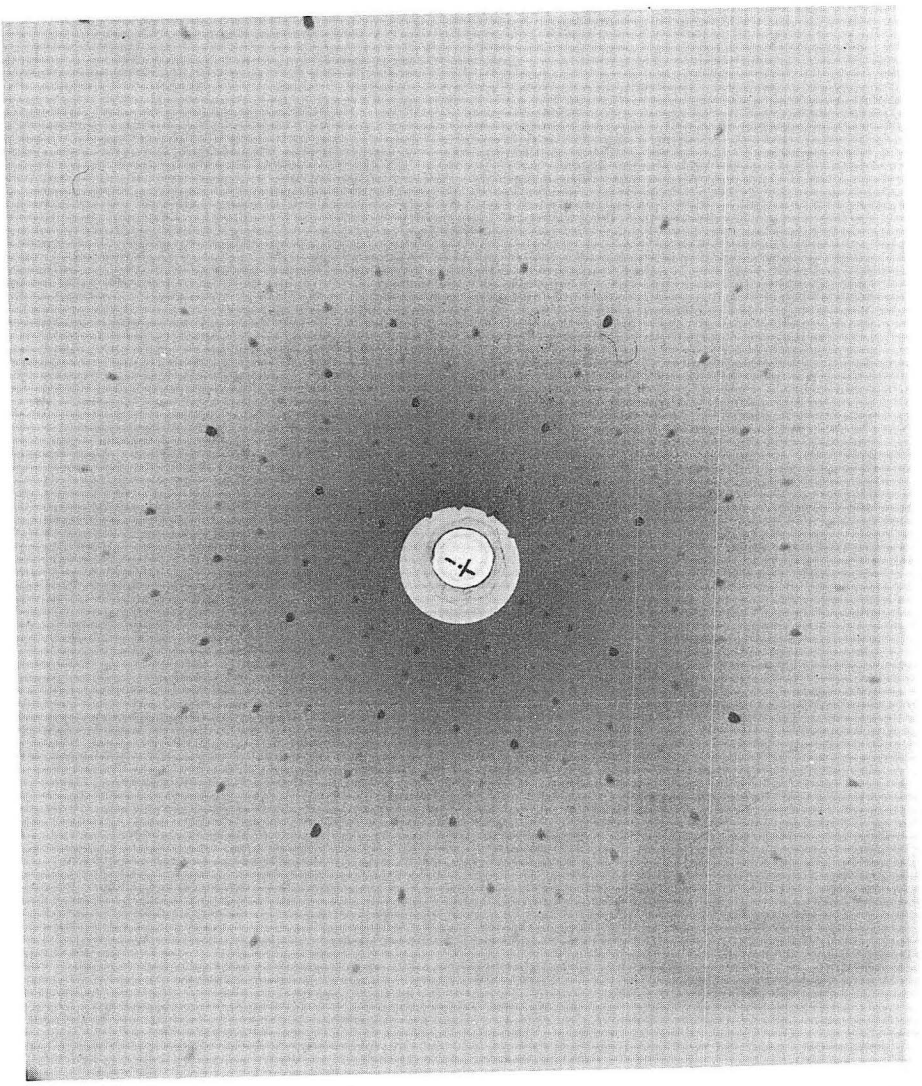

ZN-5116

Fig. II.5

the Laue patterns of the (110) and (100) emitters respectively, taken normal to the emitter surfaces just prior to their insertion in the diodes. In both cases the surface normals lie within 1° of the desired lattice orientation. This does not necessarily mean that either the (110) or (100) planes were ever exposed to the surface. Laue patterns taken at different points on the surface sometimes gave close-grouped double-spot patterns as shown in Fig. II.6. This pattern indicates that the crystals actually consisted of many small crystals all oriented within a fraction of a degree of each other.

After the crystals were brazed to their tantalum support, they were again electropolished and subsequently heated in vacuum to 2000°C to insure a clean surface prior to their installation in the diode.

During operation the diode, suspended from a flange, was either exposed to air as shown in Fig. II.7 or inserted in an environmental chamber that could be evacuated or filled with oxygen-free helium or argon.

The general operating characteristics of the diode were as follows:

Emitter temperature	1900°C maximum
Collector temperature	500°C maximum
Body temperature	500°C maximum
Interelectrode spacing	0 to 0.25 in. (continuous)
Electron-gun filament power	8 V at 11 amperes
Electron-gun bombarding power	500 V at 250 mA to heat emitter to 1900°C.

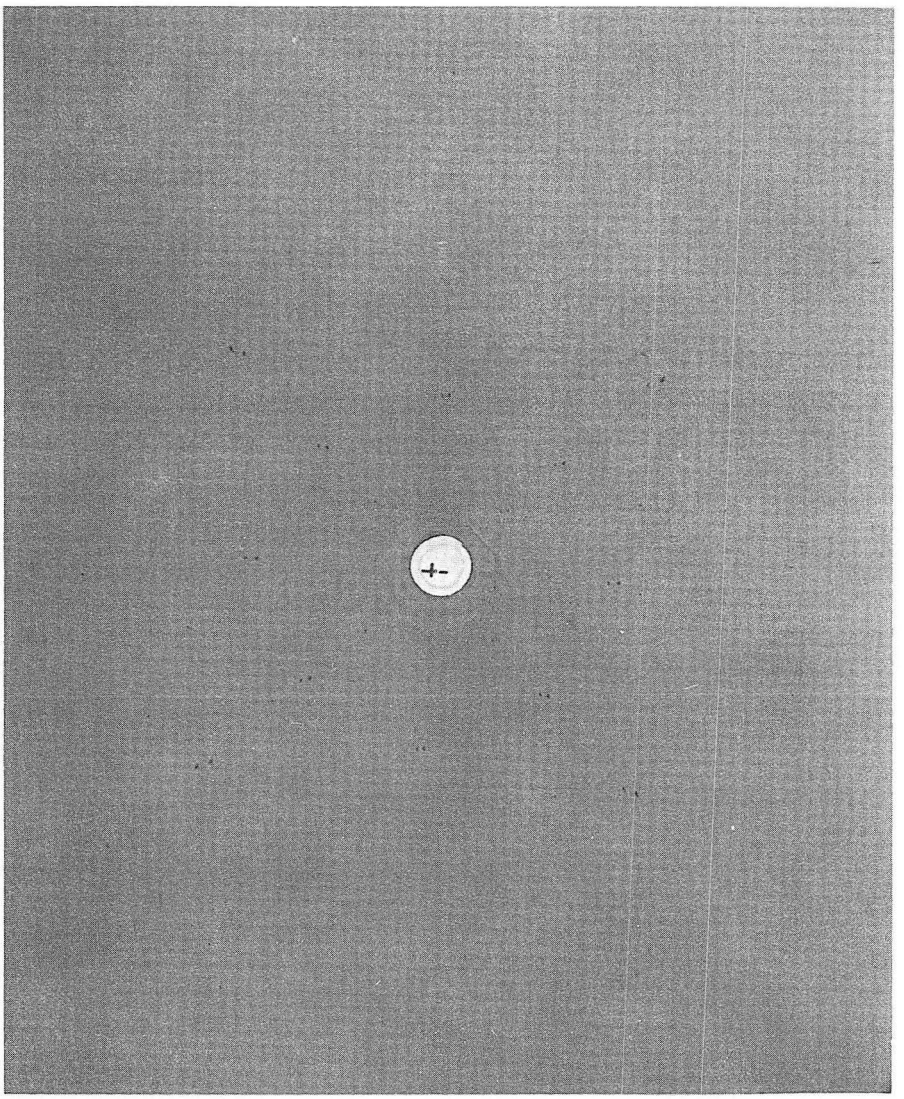

ZN-5115

Fig. II.6

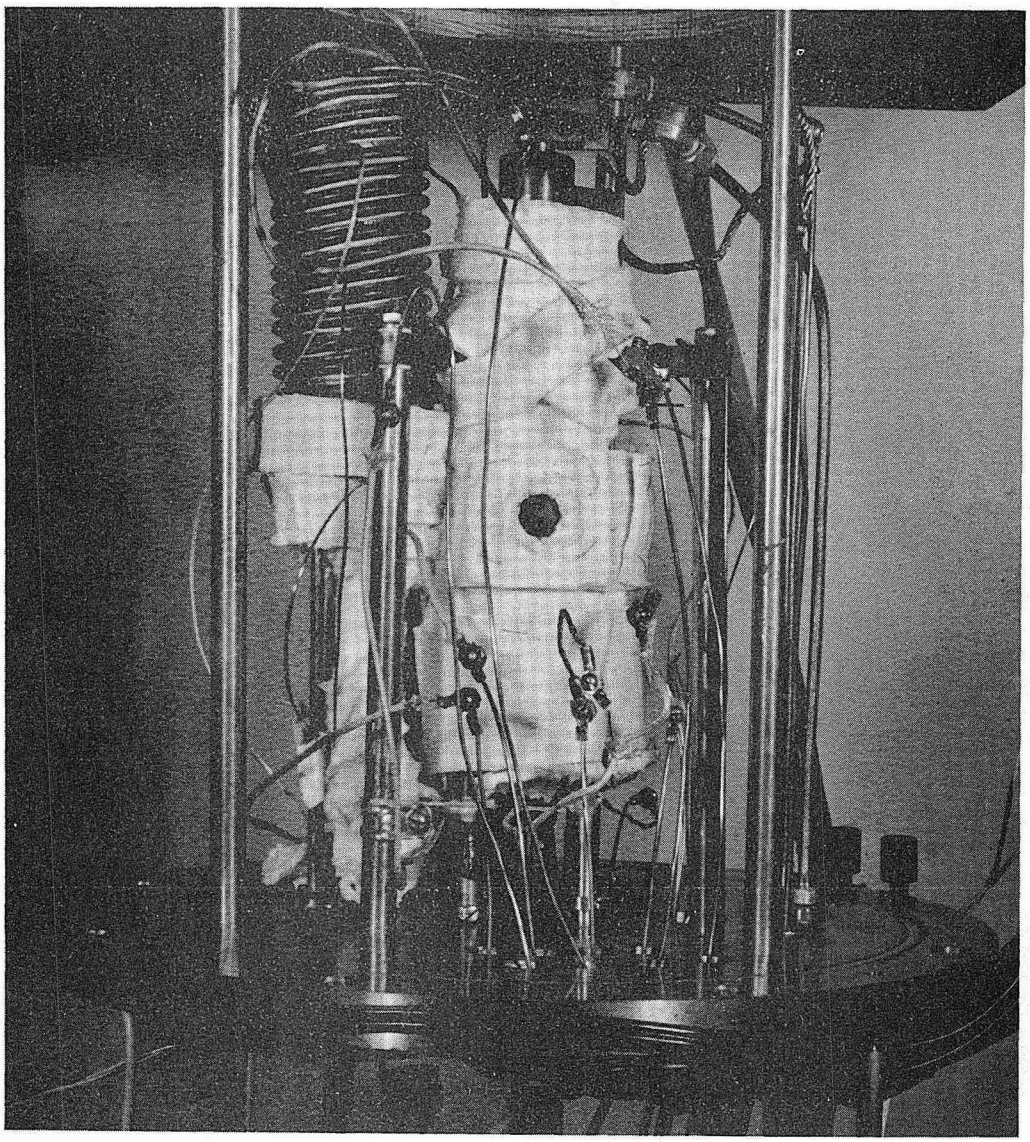

ZN-5597

Fig. II.7

III. BARE WORK FUNCTION OF (110) AND (100) TUNGSTEN CRYSTALS

A. Theory of Thermionic Emission

The process of thermionic emission from metals involves the relative positions of three electronic energy levels, namely, according to the Sommerfeld model, the bottom of the conduction band, the Fermi level, and free space. The bottom of the conduction band E_c is defined as the lowest energy that a free electron can have in the metal. Let W be the height of the potential energy barrier at the surface of the metal. Or, in other words, W is the energy difference between E_c and the energy level of an electron at rest in field-free space. The Fermi level E_f is defined as the energy state in the metal having a 50% probability of occupancy. The work function ϕ associated with a metal and its interface with free space is defined as the change in energy that an electron experiences in going from the Fermi level in the metal to a position at rest in field-free space, an infinite distance from the surface; this energy difference is

$$\phi = W - E_f. \qquad \text{(III.1)}$$

In the case of crystalline solids, W and E_f are functions of the crystallographic orientation; so in order to define the work function, one must specify the crystallographic orientation of the surface through which the electron passes. In addition, the work function is influenced strongly by the presence of adsorbed layers of foreign atoms on the surface, so the extent of surface contamination must be described also. The theoretical evaluation of the work function of metals and its dependence on crystallographic orientation has been the object of several investigations;[97,6,83] the results of these studies have been contradictory and not very successful. Part of the problem of this evaluation lies in the

determination of the spatial variation of the Fermi level near the surface, and in the scarcity of reliable experimental data on single crystals.

The maximum (saturation) electron-current-density J_{so} that can be emitted in field-free space from a metal surface at temperature T_E and characterized by a work function ϕ is given by the Richardson-Dushman equation

$$J_{so} = A t\, T_E^2 \exp\left(-\frac{\phi}{kT_E}\right), \qquad \text{(III.2)}$$

where

$$A = 4\pi\, emk^2/h^3 = 120 \text{ ampere/cm}^2\text{-}^\circ\text{K}^2 \qquad \text{(III.3)}$$

t is the quantum mechanical transmission coefficient of the escaping electrons (usually assumed to be unity), k and h are the Boltzmann and Planck constants, and m and e are the electron's mass and charge. The derivation of this equation can be found in most text books on solid-state physics and in several review articles.[90,8,39,27,71] The same applies for most of the following remarks. Equation (III.2) is the result of summing all the free electrons that are in a metal characterized by a square-well potential of height W, and whose (the electron's) component of kinetic energy normal to the surface is greater than W, as determined from Fermi-Dirac statistics. This equation is strictly applicable only to surfaces having a uniform work function, although it is also commonly used to describe the emission from polycrystalline surfaces. In the numerical evaluation of A in Eq. (III.3), the effective mass of the electrons in the metal is assumed to be identical to the rest mass in free space. According to this model, A is a universal constant.

The work function ϕ represents the barrier that an average electron has to overcome to escape through the surface. Equation (III.2) can be applied to the case in which this barrier is increased by the application of a retarding potential V_d (< 0) for electrons at the emitting surface. The electron current-density J that can pass over this additional potential will be

$$J = A t\, T_E^2 \exp\left(-\frac{\phi - eV_d}{kT_E}\right) = J_{so} \exp\left(\frac{eV_d}{kT_E}\right). \qquad \text{(III.4)}$$

We can deduce from Eq. (III.4) the ideal, not space-charge limited, current-voltage characteristics of a vacuum thermionic diode having a hot emitter with a uniform work function ϕ, and a cold (nonemitting) collector with uniform work function ϕ_c. This is shown in Fig. III.1(a). The motive diagrams in Fig. III.1(b) are schematic representations of the changes in the potential energy of an electron as it leaves its starting position at the emitter's Fermi level and arrives at the collector Fermi level.

Each motive diagram has been drawn for the corresponding region of the I-V curve in Fig. III.1(a), for the case $\phi \geq \phi_c$. It is evident that the diode produces power in the regions (1) and (3), because the potential energy of an electron at the collector's Fermi level is higher than at its starting position in the emitter. The applied voltage V_o at the knee of the I-V curve is equal to the difference per electron in collector and emitter work functions, commonly called the contact potential, i.e.,

$$V_o = \frac{1}{e}(\phi_c - \phi). \qquad \text{(III.5)}$$

From the measurement of V_o, the work function of one of the electrodes can be determined if that of the other electrode is known. Also, if the work function of one of the electrodes can be maintained constant

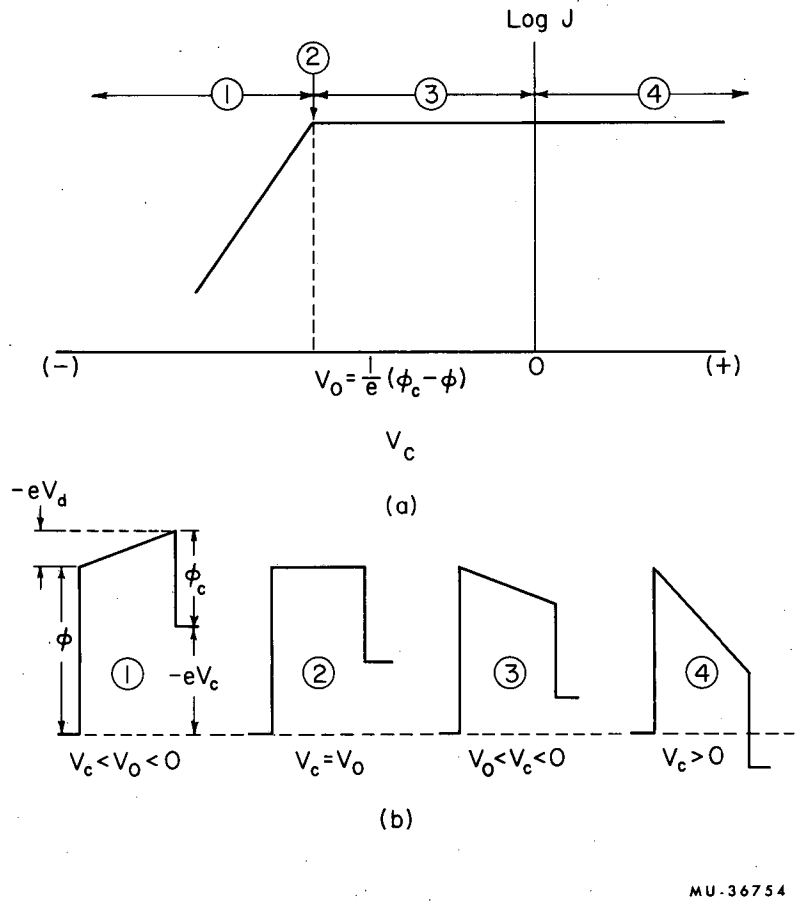
Log J
2
1
3
4
(−)
$V_0=\frac{1}{e}(\phi_c-\phi)$
0
(+)
V_c
(a)
$-eV_d$
ϕ_c
ϕ
1
$-eV_c$
2
3
4
$V_c<V_0<0$
$V_c=V_0$
$V_0<V_c<0$
$V_c>0$
(b)
MU-36754

Fig. III. 1

during a series of experiments, changes in V_o provide a direct measurement of the changes in the work function of the other electrode.

The application of an electric field $\mathcal{E}$ attractive for electrons at the emitter surface lowers the work function of the emitter according to the Schottky effect, as follows,

$$\phi(\mathcal{E}) = \phi(0) - e\sqrt{e\mathcal{E}} \, . \qquad \text{(III.6)}$$

This effect is a consequence of the algebraic addition of the image-charge potential of the electron as it leaves the metal surface and the potential due to the applied field. The saturation electron current-density J_s in the presence of the attractive field becomes

$$J_s = J_{so} \exp\left(+ \frac{0.438\sqrt{\mathcal{E}}}{T_E} \right) , \qquad \text{(III.7)}$$

where $\mathcal{E}$ is in volt/m and T_E is in °K. This equation is valid for fields under 10^8 V/m. At stronger fields, electrons are capable of tunnelling through the potential barrier at the surface and the saturation current is no longer given by Eq. (III.7). In practice, J_{so} is obtained by plotting the ℓn of the current J_s, observed in a diode, versus the square root of the interelctrode potential $(V_c - V_o)^{1/2}$ and extrapolating the best straight line through the data to zero potential. Very careful measurements of the Schottky effect have demonstrated that deviations from a straight-line relationship exist and can be attributed to changes in the quantum-mechanical-transmission coefficient t at the surface, and to surface nonuniformities.[46,47,23] From these observations, it is possible to deduce information leading to the determination of the actual shape of the work-function barrier.

The work function of the emitter in a thermionic diode is determined as follows: I-V characteristics of the diode are measured at different emitter temperatures. The value of $J_{so}(T_E)$ is obtained from the Schottky plots. A plot of $\ell n\, J_{so}(T_E)/T_E^2$ versus $1/T_E$ (hereafter referred to as a Richardson plot) is made, and a straight line is fitted to the data. If the emitter work function is uniform and independent of temperature, then the slope and intercept of the line are from Eq. (III.2) $-\phi/k$ and $\ell n\, A$ (assuming $t \approx 1$) respectively. Obviously a straight line would fit the data even if ϕ is a linear function of T_E. That is, if

$$\phi(T_E) = \phi_r + \eta T_E , \qquad \text{(III.8)}$$

the slope of the line is $-\phi_r/k$ and the intercept is $\ell n\, A' = \ell n\, A - \eta/k$.

Shelton demonstrated that A can be determined independently, from the retarding region of the I-V curves, if the collector work function ϕ_c is uniform and can be maintained constant while T_E is varied.[80] He determined A by making a Richardson plot of the currents obtained at a constant value of the applied voltage to the collector V_c, where $eV_c < (\phi_c - \phi)$. From Fig. III.1(b)(1) and Eq. (III.4) we see that the current collected for a retarding interelectrode potential $V_d = \frac{1}{e}(\phi - \phi_c) + V_c$ is

$$J(V_c, T_E) = AT_E^2 \exp\left(\frac{eV_c - \phi_c}{kT_E}\right). \qquad \text{(III.9)}$$

Note that this current is independent of the emitter work function ϕ.

The slope and intercept of the Richardson plot of this equation are $(eV_c - \phi_c)/k$ and $\ell n\, A$. These are the true, temperature-independent, thermionic constants, provided that $\phi_c \neq f(T_E)$.

Since V_c is known, ϕ_c can be calculated from the slope and $\phi(T_E)$ can be determined by direct substitution of A into Eq. (III.3). A self-consistent check on the evaluation of $\phi_c - \phi(T_E)$ is obtained from the observed contact potential $V_o(T_E)$. From Eq. (III.9) we see that for a constant value of T_E the slope of a $\ell nJ(V_c,T_E)$ versus V_c curve in the retarding region should be e/kT_E. The success of the above method for determining A depends on this experimental observation. Deviations from the true e/kT_E slope are caused by many factors such as space charge, non-uniform work function of either electrode, and geometric effects (such as the lack of proper guard rings). All of these factors tend to make the slope shallower, or the calculated electron temperature T_e (determined from the slope) greater than the true emitter temperature T_E.

The non-uniformity of the work function of the electrodes can be evaluated quantitatively from the variations in the slope of the retarding I-V curve, as discussed in Sec. VII.

In summary, let us briefly recapitulate step by step the way to obtain the true Richardson constant A, and the true emitter and collector work functions ϕ and ϕ_c (assuming they are uniform). (a) A set of I-V curves for different T_E is obtained, while ϕ_c remains constant (if possible). (b) The saturation currents $J_{so}(T_E)$ are obtained from the extrapolation of Schottky plots $\ell n\, J_s$ versus $(V_c - V_o)^{1/2}$, to zero potential. (c) The currents $J(V_c,T_E)$ at constant applied voltage V_c in the retarding potential region are obtained from the I-V curves. (d) A Richardson plot of $\ell n\, J(V_c,T_E)/T_E^2$ versus $1/T_E$ yields the true A and $(eV_c - \phi_c)$, and therefore ϕ_c also. (e) $\phi(T_E)$ is obtained by inserting this A and $J_{so}(T_E)$ into the Richardson equation (III.3). (f) The value of $\phi_c - \phi(T_E)$ is compared with

the contact potential $V_o(T_E)$. (g) If $\phi(T_E) = \phi_r + \eta T_E$, the Richardson plot of the saturation currents, $\ell n\, J_{so}(T_E)/T_E^2$ versus $1/T_E$ gives ϕ_r and $A' = A \exp\left(-\frac{\eta}{k}\right)$. Obviously if $\eta \approx 0$, the true values of ϕ and A are obtained in this way also.

The main parameters of a vacuum or collisionless plasma diode are the collector and emitter work functions and the emitter temperature. For visual clarification we have included Fig. III.2, which demonstrates the effects of individual variations of ϕ, ϕ_c, and T_E on the ideal log J versus V_c curves.

In conclusion, note that the above remarks apply only if the electrode work functions are uniform. Usually they are not, and therefore in general the observed A and ϕ will both be temperature depentent; furthermore, the observed ϕ will be some average value of the emitter work function and will also be affected by the non-uniformity in the collector work function. Hence, in this case, the observed ϕ and A may not be more than parameters to fit the data and thus may not have the implied physical significance. These considerations have been extensively discussed in the literature.[8,39,27,71,85,19,26]

B. Experimental Procedure

The current-voltage characteristics of both the (110) and (100) diodes were measured point by point, by means of the circuits shown in Figs. III.3(a) and (b), respectively. The voltage on the guard ring was maintained at all times within a fraction of a mV of the collector voltage. For the (110) diode this was done by manually adjusting at each data point the voltage divider in series with the guard ring. This maneuver was performed automatically in the (100) diode circuit (Fig. III.3(b)) by replacing the

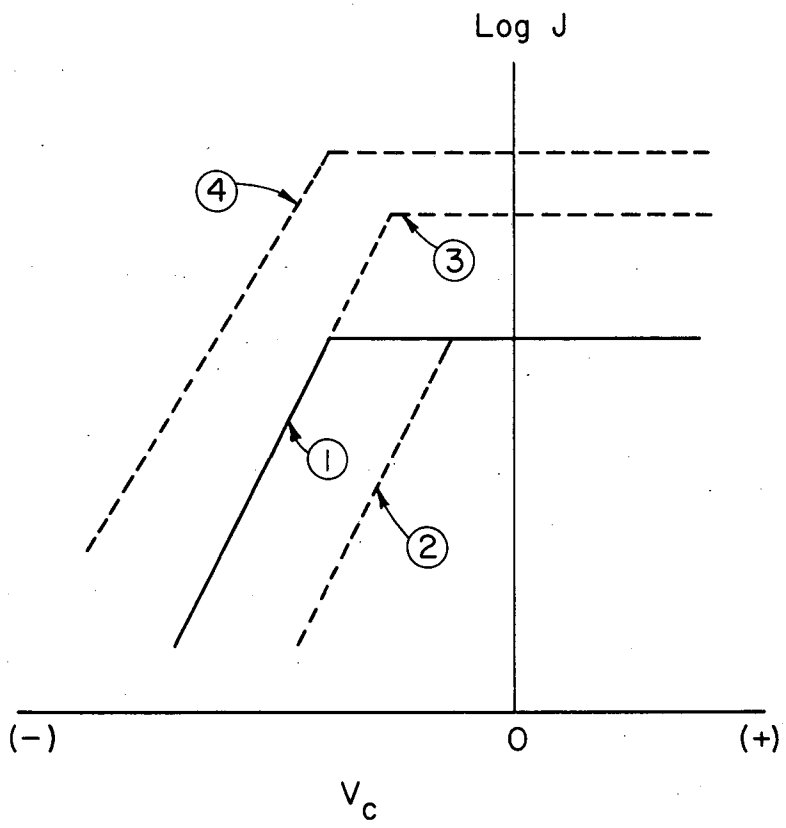

Fig. III.2

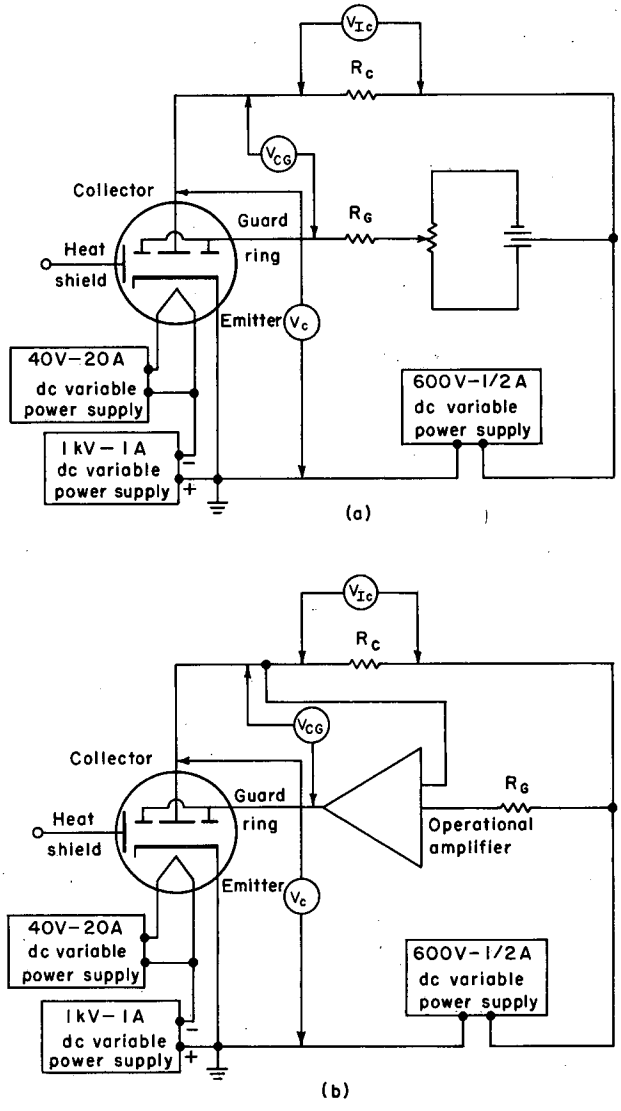
V_{Ic}
R_c
V_{CG}
Collector
Guard
ring
R_G
Heat
shield
Emitter
V_c
40V–20A
dc variable
power supply
1kV–1A
dc variable
power supply
600V–1/2A
dc variable
power supply
(a)
V_{Ic}
R_c
V_{CG}
Collector
Guard
ring
R_G
Operational
amplifier
Heat
shield
Emitter
V_c
40V–20A
dc variable
power supply
1kV–1A
dc variable
power supply
600V–1/2A
dc variable
power supply
(b)
MU-36756

Fig. III.3

voltage divider with an operational amplifier having an input impedance of about 200 MΩ. The performance characteristics and circuit diagram of the amplifier, which was built for this circuit, are described in Appendix L. The heat shield, which was electrically isolated, was normally kept free to assume its own potential. Shorting it to either the grounded emitter or the guard ring had no measurable effect on the collector current, thereby demonstrating the effectiveness of the guard ring. The necessity of using a properly designed guard ring in these experiments is clearly demonstrated in Fig. III.4, which shows typical collector and guard-ring current-voltage curves that were obtained by using the heat shield as a guard, operating at the same applied voltage as that of both collector and guard ring. The current in the top curve should have been about twice that in the bottom if the heat shield had been an effective guard, because the area of the faces of both collector and guard ring were each essentially equal to half the emitter area. But in fact the saturation current collected by the guard-ring and the collector was about 25 times that reaching the collector only. Some additional remarks on the guard-ring effectiveness are presented in Appendix M. The collector-to-guard-ring voltage difference was monitored with a digital voltmeter having floating inputs, a 2-MΩ input impedance, and a sensitivity of 0.1 mV. The collector current was very insensitive to this voltage difference except when cesium was introduced to the diode; then the resistance of the ceramic insulators in the diode decreased considerably due to surface adsorption of cesium, and appreciable current leakage could occur between collector and guard ring. Because the collector and guard rings were made out of the same material, polycrystalline copper, it was presumed that the average contact potential between either of these electrodes and the emitter had

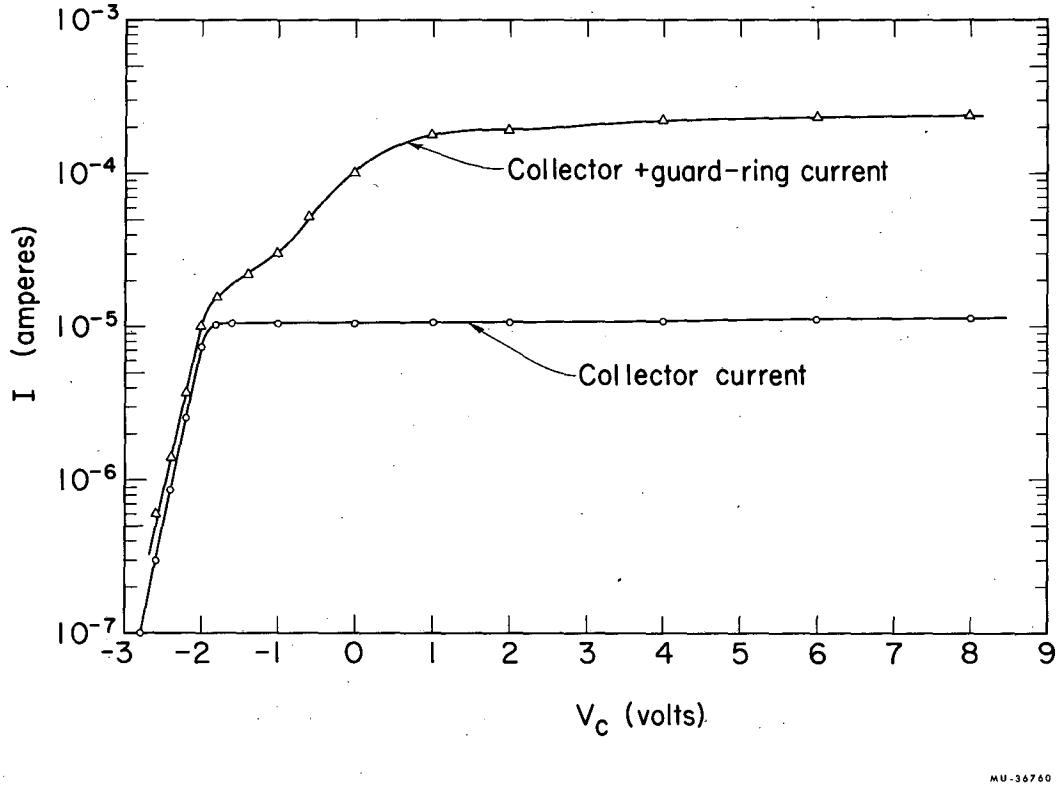
10^{-3}
10^{-4}
10^{-5}
10^{-6}
10^{-7}
I (amperes)
Collector +guard-ring current
Collector current
-3
-2
-1
0
1
2
3
4
5
6
7
8
9
V_C (volts)
MU-36760

Fig. III.4

the same value. From all experimental evidence it appears that this was a reasonable assumption.

The applied voltage V_c across the diode was measured with an electrometer having a 10^{14}-Ω input impedance, and a linearity of 0.1%. The current passing through the collector was determined by measuring the voltage drop across the calibrated resistor R_c, which could be varied in steps of 10 from 0.1 to 10^6 Ω. The calibration of the resistors was better than 0.5%. The voltage across R_c was measured with a digital voltmeter having floating inputs, a 10^4-MΩ input impedance, and an accuracy of ± 1 digit (± 1MV on the 0 to 9.999V scale). The value of R_c was selected so as to maintain the current signal between 50 and 500 mV, whenever possible, so that the accuracy of the current measurement was better than 2%. Necessary precautions were taken to exclude voltage drops through lead wires and contact resistances from the voltage measurements made across the various components of the diode circuit.

The power supply in the diode circuit was voltage regulated to ± 20 mV. The power supply of the filament was voltage regulated to ± 4 mV. It could also be made current regulated; however, since the stability of the emitter temperature seemed to be independent of the mode of operation, the power supply was operated by regulating the voltage, in order to protect the filament from accidental burn-out. The bombarding power supply for the electron gun was not regulated for load changes. It was usually quite stable so that the emitter temperature could be maintained constant within the precision of the optical pyrometer (± 2°C). However, the output of the supply would occasionally drift, resulting in a ±5°C change in emitter temperature.

A complete set of vacuum current-voltage characteristics for the diodes was obtained in the following manner. The emitter temperature was increased slowly until a measurable electron current ($\approx 10^{-9}$ amperes) flowed to the collector. About half an hour was allowed for the diode to reach thermal equilibrium. During this time the temperature of the emitter was monitored with the optical pyrometer as a check on the temperature stability. Then, as fast as possible, an I-V curve was measured point by point in the minimum range of -20 to +20V on the collector, usually up to + 100V and sometimes up to + 300V. This took about 5 minutes. The initial current reading was always repeated as a check on temperature drift, and the temperature was also measured again. If an appreciable (more than 5°C) change in emitter temperature had occurred, the I-V curve was remeasured. The emitter temperature was then increased to a new value and the above procedure was repeated. In this way, the emitter temperature was raised to a maximum value. Then the emitter was cooled in the same manner. The incremental change in emitter temperature varied from 20 to 100°C. Taking such a set of data took from 12 to 18 hours. No attempt was made to maintain a constant interelectrode spacing during these experiments because that was not necessary, but the spacing was adjusted periodically to keep it in the range of 10 to 15 mils. Because the diodes at this stage had not yet been wrapped with heating wires, except for the top of the collector stem, the temperatures of the collector and guard ring could not be held constant. They increased as the emitter temperature increased, in the range of 50 to 200°C, depending on the minimum and maximum emitter temperatures. It was possible though, to maintain at all times, the difference in the surface temperature of the collector and that of the guard ring below 10°C.

Besides the I-V curve, the following data were generally recorded at each emitter temperature: The time, the temperatures of the collector and guard ring, the interelectrode spacing, and the filament and bombardment currents and voltages.

C. Discussion of Results for (110) Crystal

Five sets of vacuum current-voltage curves were obtained for the (110) diode. In addition a sixth set of data was obtained after the cesium capsule had been broken and the cesium transferred to the bottom of the reservoir which was kept immersed in liquid nitrogen. Each set of data normally consisted of I-V curves taken as the emitter temperature was raised to a maximum value, plus another series of I-V curves as the emitter was again cooled. The only exception was the fourth set of data, which was aborted soon after the emitter temperature had been decreased from its maximum value because the electron-gun filament broke.

For illustration we include here the log I-V curves in the retarding potential region of set No. 4 (emitter temperature increasing) in Fig. III.5 and similar curves for set No. 5 in Fig. III.6 (temperature increasing) and Fig. III.7 (temperature decreasing). Figure III.5 is representative of the data of sets 1 to 4. The saturation-current lines (horizontal) in these figures are the extrapolation to zero interelectrode potential of the corresponding Schottky plots.

Several features of these I-V curves will now be discussed in turn. They are the deviations of the data points from the lines drawn in the retarding potential region, the slope of these lines, the sharpness of the transition (the knee) between the saturation and retarding potential regions, and the shift in the position of the contact potential which occurs at a certain temperature.

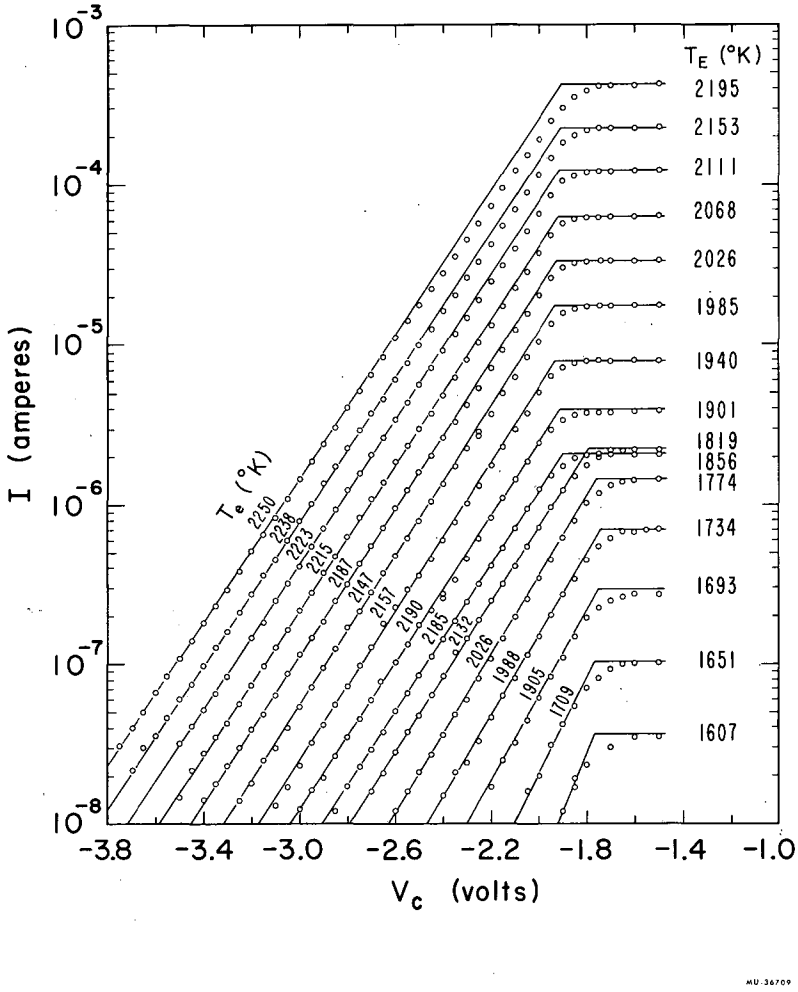
10^{-3}
10^{-4}
10^{-5}
10^{-6}
10^{-7}
10^{-8}
I (amperes)
-3.8
-3.4
-3.0
-2.6
-2.2
-1.8
-1.4
-1.0
V_c (volts)
T_E (°K)
2195
2153
2111
2068
2026
1985
1940
1901
1819
1856
1774
1734
1693
1651
1607
T_e (°K)
2250
2238
2223
2215
2187
2147
2157
2190
2185
2132
2026
1988
1905
1709
MU-36709

Fig. III. 5

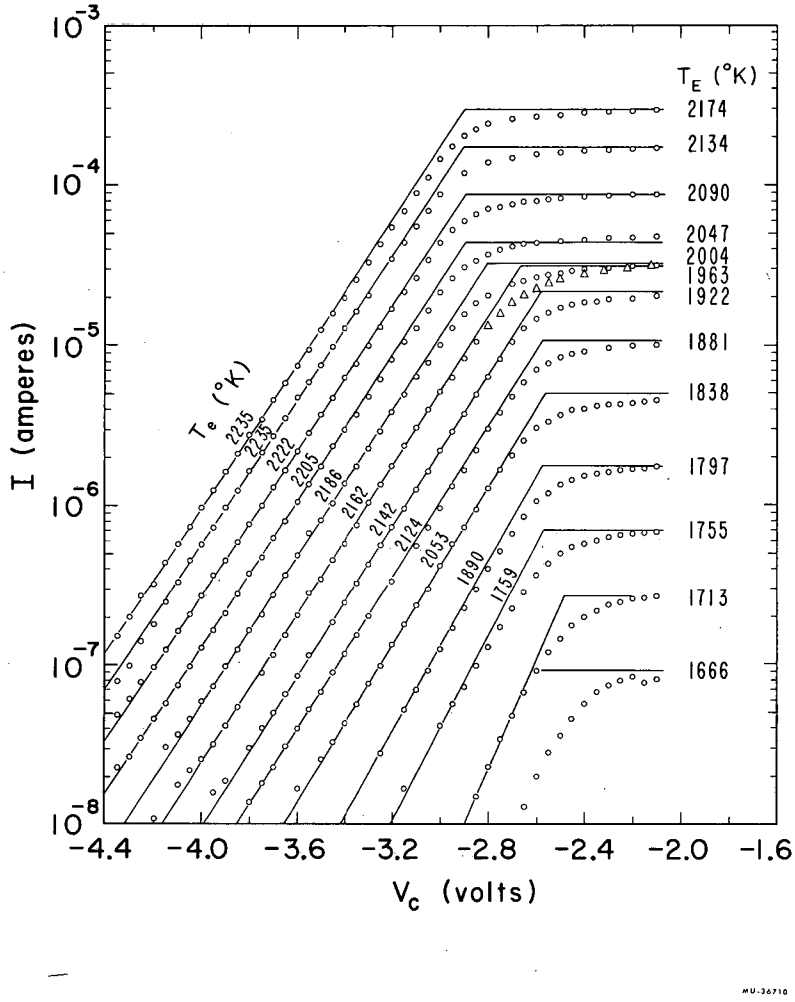
10^{-3}
10^{-4}
10^{-5}
10^{-6}
10^{-7}
10^{-8}
I (amperes)
-4.4
-4.0
-3.6
-3.2
-2.8
-2.4
-2.0
-1.6
V_c (volts)
T_E (°K)
2174
2134
2090
2047
2004
1963
1922
1881
1838
1797
1755
1713
1666
T_e (°K)
2235
2230
2222
2205
2186
2182
2142
2124
2053
1890
1759
MU-36710

Fig. III.6

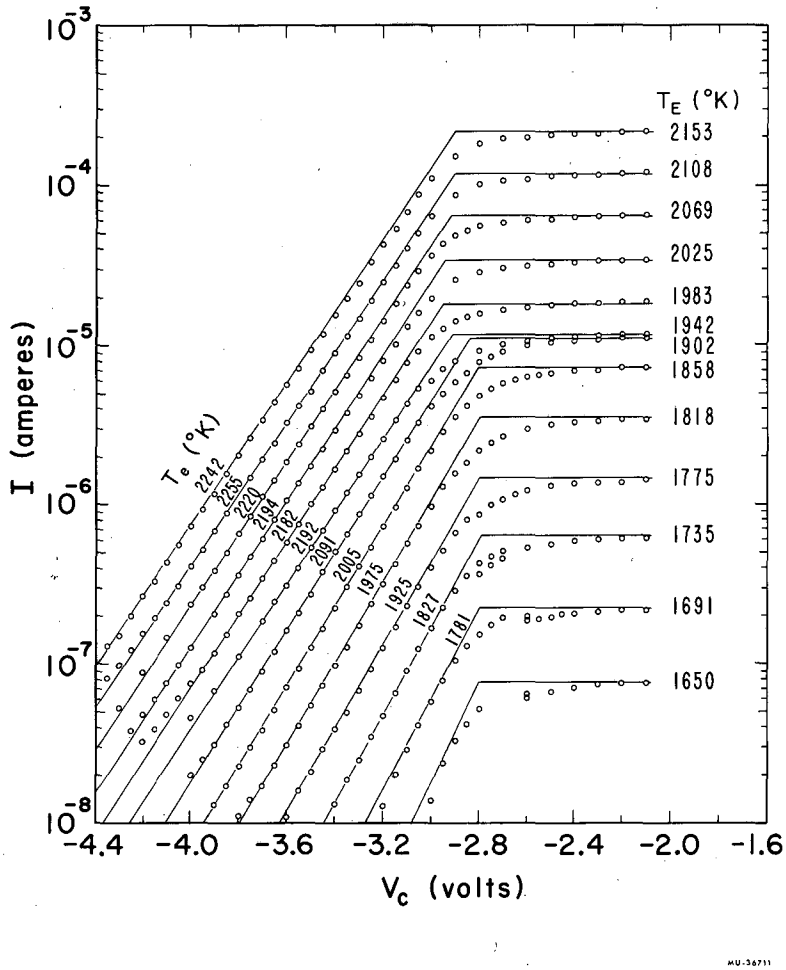
10^{-3}
10^{-4}
10^{-5}
10^{-6}
10^{-7}
10^{-8}
I (amperes)
T_E (°K)
2153
2108
2069
2025
1983
1942
1902
1858
1818
1775
1735
1691
1650
T_e (°K)
2242
2235
2220
2194
2182
2192
2091
2005
1975
1925
1827
1781
-4.4
-4.0
-3.6
-3.2
-2.8
-2.4
-2.0
-1.6
V_c (volts)
MU-36711

Fig. III.7

The first three items are descriptive of the nonuniformity of one or both electrode surfaces. Some of these factors were mentioned in Sec. III.A and are discussed further in Sec. VII. Space-charge limitations can be ruled out because the currents and the interelectrode spacing (about 0.010 in.) were too small. The deviations of the data in the retarding potential region indicate that the work function of the emitter, the collector, or both were not uniform. This observation was expected since the collector was made of polycrystalline copper. In general, a truly exponential decrease in current with voltage will not occur in a diode having patchy electrodes until all portions of the emitter surface are operating in the retarding potential region (Fig. III.1(b)(1)); this condition can be obtained by applying a sufficiently high retarding voltage on the collector, because physically the work function distributions on patchy surfaces have finite lower and upper bounds. For this reason we have usually drawn the sloping lines in Figs. III.5 through III.7 through the low-current data points, far from the knee of each curve. Unfortunately the experimental uncertainty of the data was greatest in the region of low currents, partly because our current resolution was 10^{-9} ampere and partly because the I-V curves had to be corrected for reverse currents. In sets 1 through 4, the reverse current was due to a low-level dc noise of about 10^{-8} ampere. In set 5 the reverse current increased with emitter temperature from 10^{-8} to 10^{-6} ampere. This increase was due either to cesium-ion emission from the emitter and/or to photoelectron emission from the collector whose work function had decreased 1 volt below its value in the preceding data sets. The changes in the current-voltage characteristics of the diode after the fourth data set are the result of having to replace the electron gun, as will be discussed later in this section.

The temperatures T_e listed by each sloping line are the electron temperatures calculated from the slope of the lines. The observed pyrometric temperatures T_E are listed next to the corresponding saturation-current line. The electron temperatures exceed the measured temperatures by 50 to 300°K. We believe that this temperature difference is greater than any reasonable systematic error in the absolute value of the temperature measurements or in the measurements of currents and voltage. Therefore it must be due to the nonuniformity of the collector work function and perhaps that of the emitter also. Hence, as discussed in Sec. III.A, we were not able to obtain very meaningful results from a Richardson plot of the currents at constant voltage in the retarding potential region. This means that we can rely only on the saturation currents to calculate the emitter work function and the Richardson constant A.

It is evident from the I-V curves of Figs. III.5 through III.7 that there is an abrupt shift in the position of the contact potential as a certain emitter temperature is reached, and that this shift is not accompanied by the expected change in the saturation current. The dependence of the saturation current on temperature is further illustrated in Fig. III.8, which is a Schottky plot, log I versus $(V_c - V_o)^{1/2}$, for set No. 5, with temperature increasing. This figure shows that the saturation current did not change as the emitter temperature was increased from 1963 to 2004°K. The behavior of both the saturation current and the contact potential indicate that the emitter work function increases as the temperature is increased through the "transition" region. This effect is demonstrated again in Fig. III.9, which shows the Richardson plots of the field-free, saturation-current densities, log J_{so}/T_E^2 versus $1/T_E$, for all sets of data. The bottom line in Fig. III.9 is a Richardson plot of the current

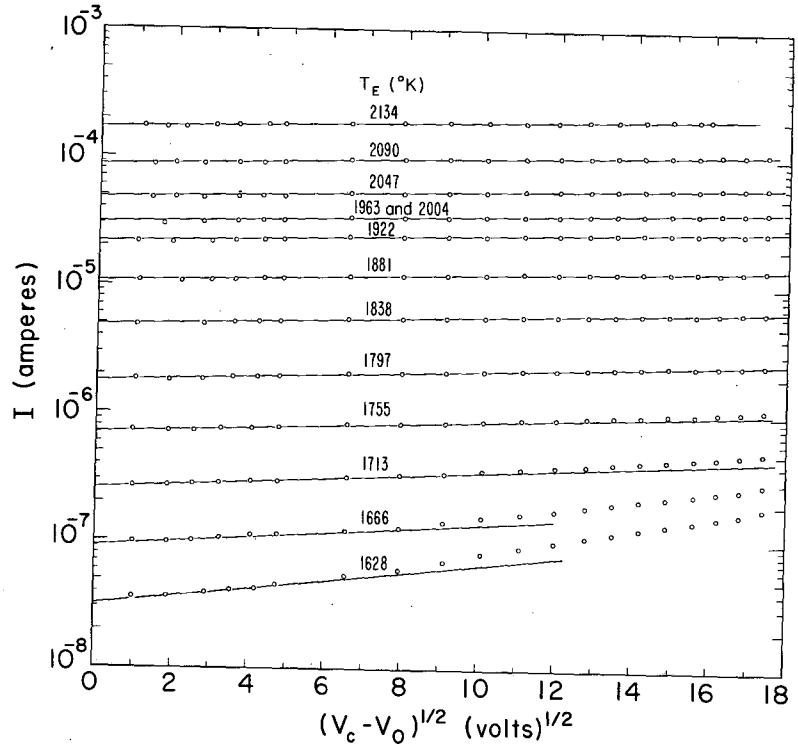
10^{-3}
10^{-4}
10^{-5}
10^{-6}
10^{-7}
10^{-8}
I (amperes)
T_E (°K)
2134
2090
2047
1963 and 2004
1922
1881
1838
1797
1755
1713
1666
1628
0
2
4
6
8
10
12
14
16
18
$(V_c - V_0)^{1/2}$ (volts)$^{1/2}$

Fig. III. 8

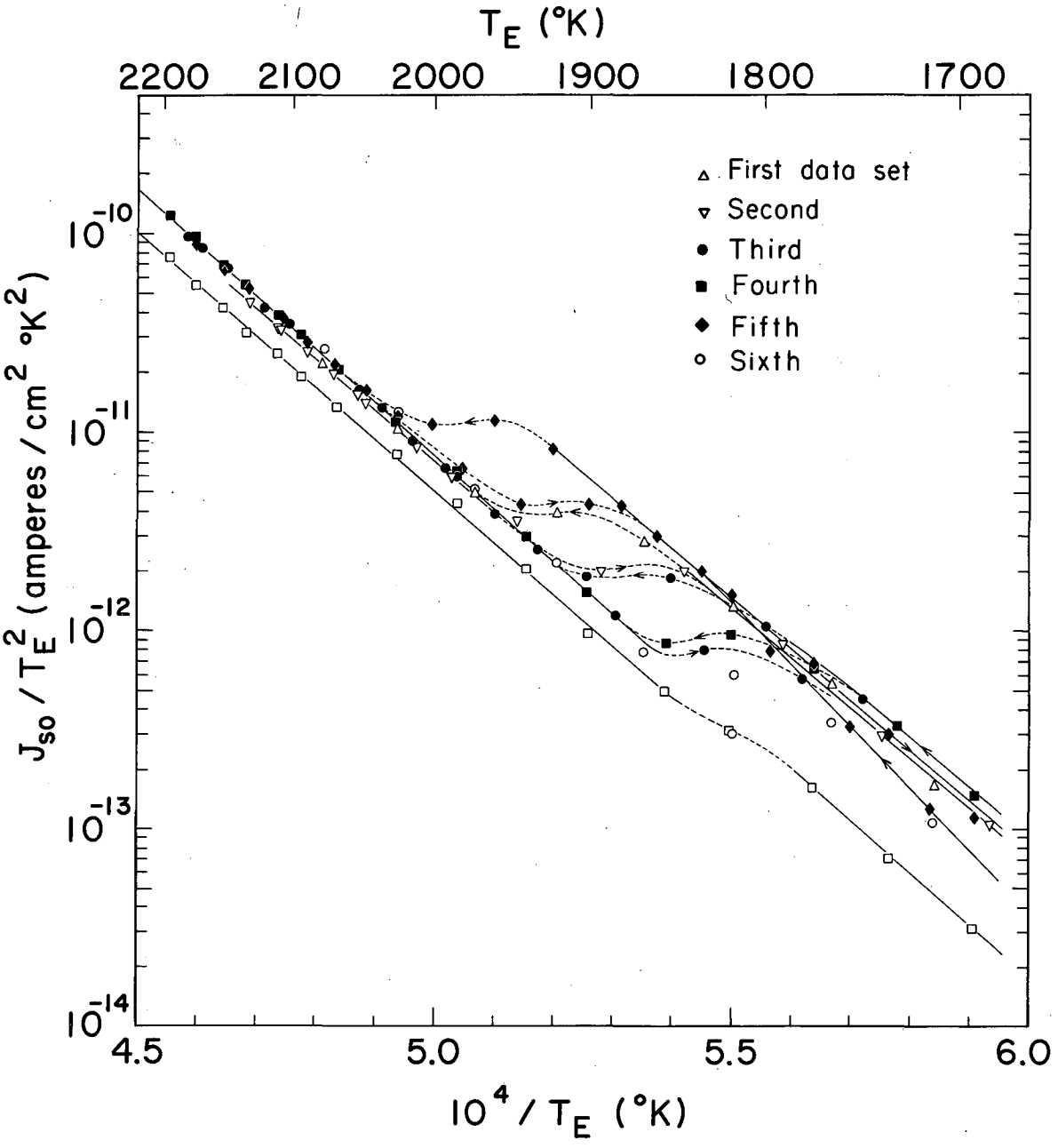
T_E (°K)
2200
2100
2000
1900
1800
1700
First data set
Second
Third
Fourth
Fifth
Sixth
10^{-10}
10^{-11}
10^{-12}
10^{-13}
10^{-14}
J_{so} / T_E^2 (amperes / cm^2 °K^2)
4.5
5.0
5.5
6.0
$10^4 / T_E$ (°K)
MU-36740-A

Fig. III.9

densities of set No. 4 (Fig. III.5) in the retarding potential region, obtained for a constant collector voltage of -2.0V. As described in Sec. III.A, this latter plot is indicative of the collector work function. But in view of the discrepancy in the calculated versus measured temperatures discussed above, we cannot attach much confidence to the quantitative analysis of such a plot; it was included only to illustrate that the change in collector work function through the transition region was considerably less than that of the emitter.

It was observed that the transition temperature decreased from about 1900 to 1800°K with each succeeding set of data through the fourth (Fig. III.9). We believe that this phenomenon is due to the desorption of some gaseous impurity from the emitter surface at some critical temperature, that depends in part on the residual gas pressure in the diode; and that gradually the residual gas was removed by gettering or by readsorption on a cold part of the diode, thereby lowering the temperature at which the concentration of the gaseous impurity on the emitter surface becomes negligible. The adsorbed impurity here was not oxygen, as it is well known that its desorption would have lowered the emitter work function, contraty to our observation. Perhaps it was nitrogen, which could have been gettered by the tantalum cup supporting the crystal emitter.

With the fifth data set, the transition temperature increased again to nearly 2000°K. As mentioned earlier, the filament broke after the fourth set and nearly a month elapsed until it could be replaced. It was replaced without opening the diode chamber containing the electrodes; but the electron-gun chamber, confined by the tantalum cup, had to be opened to the atmosphere, of course, and then re-evacuated. This evacuation was done without benefit of another high-temperature bake out, and the diode chamber undoubtedly became recontaminated again, possibly by diffusion of air through

the thin wall of the tantalum cup. The large decrease to 1800°K in the transition temperature of the sixth data set, as shown in Fig. III.9, indicates that cesium, which was introduced into the diode between sets 5 and 6, may have been effective in the removal of this contaminant.

A comparison of the log I-V curves of sets 4 and 5 shown in Figs. III.5 through III.7 shows that the collector work function decreased by one volt after the diode was reprocessed. The fact that the curvature of the knees in Figs. III.6 and III.7 is much broader than that of knees in Fig. III.5 indicates that the spread in the work-function distribution of the collector was greater in set 5 than in the earlier sets. We believe that these effects are due to changes in the collector rather than in the emitter, because had they occurred in the emitter we would have observed a significant difference between the Richardson plots of sets 4 and 5 above and their respective transition temperatures. The effective work function of the collector in set 5 was about 2.4 eV, as we will see later. Such a low work function can be explained only if an appreciable fraction of a monoatomic layer of cesium (which has a work function of 1.8 eV) was adsorbed on the collector. This possibility was substantiated by the observation of a small but significant reverse current through the diode when the applied voltage on the collector was large ($\gg|V_o|$) and negative. It is not known how cesium could have been introduced to the diode between sets 4 and 5 even in this minute amount, because presumably the cesium capsule had not yet been broken. Perhaps it had cracked slightly in handling. A small concentration of cesium in the diode would have large effects on the work function of the cold (less than 200°C) collector but would not affect the emitter in the temperature range in which it was operating; this is another reason why we feel that the differences in the I-V characteristics of sets

4 and 5 were primarily caused by changes occurring in the collector.

The field-free saturation-current densities J_{so} needed for the Richardson plot shown in Fig. III.9 were evaluated from the intercept at zero interelectrode potential of Schottky plots similar to those shown in Fig. III.8. The simple Schottky theory fits the data very well except for currents below 10^{-6} ampere, where monotonic deviations begin to appear at high voltages. The deviations cannot be completely accounted for by assuming a small leakage current proportional to the applied voltage, and remain unexplained. The bare work function ϕ_o (the subscript o denotes a clean surface, free of cesium) of the (110) crystal emitter and the Richardson constant A were determined from the slope and intercept of Richardson plots for each data set. These quantities were computer evaluated, by the method of least squares, using only the data measured above the transition temperature of each particular set. The results are tabulated in Table III.I, which includes in addition the results of Richardson plots for currents at three constant voltages in the retarding potential region. These latter results were also obtained by the method of least squares for the data measured above the transition temperatures. Sets 1 and 2 were analyzed together because they agreed very closely with each other. They fitted a line corresponding to a work function $\phi_o = 5.08 \pm 0.08$ eV and an A value of 45 ± 20 ampere/cm^2-°K^2. This line is shown as the second highest line in Fig. III.9. Sets 3, 4, and 5 also agreed well with each other and we believe the combined analysis of these three sets best represents the properties of the (110) crystal. They fitted a line corresponding to

$$\phi_o = 5.33 \pm 0.04 \text{ eV and } A = 207 \pm 50 \text{ ampere/cm}^2\text{-°K}^2 .$$

This line is the highest line in Fig. III.9.

Table III.I Results of the measurements of thermionic emission in vacuum for the (110) diode above the emitter's transition temperatures. All the values listed have been obtained by the method of least squares. The errors are equal to twice the standard deviation of the means.

Data Set	1 and 2 (March 2,4)	3 (March 11)	4 (March 18)	5 (April 11)	3,4, and 5
No. of data points	12	13	11	6	32
ϕ_o(eV)	5.08±0.08	5.33±0.06	5.35±0.04	5.22±0.14	5.33±0.04
A (amperes/cm^2°K^2)	45±20	200±68	229±58	114±87	207±50
V_c (volt)	-2.0	-2.0	-2.0	-3.0	
ϕ_c-eV_c(eV)	5.20	5.31	5.19	5.01	
A (amperes/cm^2°K^2)	58	113	59	20	
V_c (volt)	-2.2	-2.2	-2.2	-3.2	
ϕ_c-eV_c (eV)	5.30	5.42	5.23	5.00	
A (amperes/cm^2°K^2)	37	76	27	6.8	
V_c (volt)	-2.4	-2.4	-2.4	-3.4	
ϕ_c-eV_c (eV)	5.41	5.52	5.27	5.05	
A (amperes/cm^2°K^2)	24.	48	12	3.1	

The errors listed for these quantities are equal to twice the standard deviation of the mean. We estimate that the error quoted for ϕ_o is reasonable because the evaluation of ϕ_o is practically independent of a systematic error in the measurement of T_E arising from uncertainties in the effective emissitivity of the emitter hohlraum and the absorptivity of the windows; it is also independent of a systematic current-measurement error that is directly proportional to the value of the current. These two systematic errors are the only ones that we could reasonably expect from our instruments. On the other hand, the evaluation of A is very sensitive to these two types of errors. Because our voltmeters and current-measuring resistors were well calibrated, we estimate that any error in A resulting from a systematic error in the current measurement is small compared with the value listed. We cannot say the same of the temperature measurement and it is quite possible that the above value of A is high (compared to the theoretical value of 120) because of a constant error in $1/T_E$ resulting from an emissivity or absorptivity uncertainty. If anything, we expect that the true emitter temperature was larger than the observed temperature because we assumed that the emissivity of the emitter "black-body" hole was unity and because the sapphire windows incorporated in the diode may not have been as clean as the one which we calibrated (Fig. J.1 of Appendix J). A constant error in $1/T_E$ of about $8.6 \times 10^{-5}/°K$, corresponding to an error in T_E of 34°K at 200°K, would reduce A from 207 to its theoretical value of 120 amperes/cm^2-$°K^2$. Although we do not believe that our uncertainty in the absolute temperature was that high, such an error is not out of the realm of possibility.

The discrepancy between the results of the first two and the last three sets is not consistent with the observed contact potentials for these sets. The average contact potentials above the transition temperature in sets 1 to 4 were identical within 0.02V. This means that the emitter work function was essentially the same for all four sets, assuming of course that the collector work function remained constant. The possibility that the absorptivity of the diode window increased after set 2 can be ruled out because (a) such an effect would displace the Richardson line but would not noticeably change its slope, and because (b) an accurate record of the power input to the emitter did not reveal any discrepancy in the temperature measurement.

The cause for the change in the slope of the Richardson plot may be due to a time and temperature dependence in the work function and/or the effective area for electron emission, caused probably by the gradual desorption of a teancious surface contaminant. If we assume that the correct A value is 207, we find by substituting this value in the Richardson equation (Eq. (III.2)) and calculating the work function from the measured current at each temperature that the work function in sets 1 and 2 varied from 5.35 eV at 2132°K to 5.34 eV at 1988°K. This work-function difference is within the precision with which the contact potential could be determined. If, on the other hand, we assume that sets 1 and 2 are correct and that A = 45, then a similar calculation applied to set 4 gives ϕ_o = 5.04 eV at T_E = 2195°K and ϕ_o = 5.08 at T_E = 1941°K. The change in contact potential for this temperature interval was about 0.02 - 0.03 eV in the corresponding direction, as seen in Fig. III.5. From these calculations we obviously cannot tell with absolute certainty which of the data sets are correct, especially since we have no way of determining in-

dependently that the collector work function stayed absolutely constant during each set. It should be evident from the results presented in Table III.I that, as discussed earlier, we cannot rely on the Richardson plots of the currents in the retarding potential region to calculate either A or ϕ_c. For each data set these plots should have given the same value of A irrespective of the value of the constant voltage V_c at which the currents were measured, and the value of $(\phi_c - eV_c)/e$ should have varied by exactly the same amount as the change in the voltage.

We did not calculate a work function for the data of set 6, which were obtained at very low cesium pressure; but the electron emission above the transition temperature was essentially the same as that of the previous 3 sets, indicating that the emitter work function was also similar. However, the contact potential above the transition temperature in set 6 was 3.9V, as shown in Fig. VII.2 of Sec. VII. Therefore, if the emitter work function was 5.08 eV, that of the collector was less than 1.2eV. Such a work function is lower than any reported in the literature for cesium adsorbed on clean metals or on metals contaminated with adsorbed gases, such as oxygen, hydrogen, or fluorine. The minimum work function observed for these surfaces is 1.3 to 1.4 eV.[1,64,53,20,78] This is below the value of our collector work function when the latter is calculated on the basis of an emitter work function equal to 5.33 eV.

We have greater confidence in the values of ϕ_o = 5.33 eV and A = 207 amperes/cm^2 ^{o}K^2 than in those obtained in the first two sets because of the evidence presented in the preceding paragraph, because the diode seemed to decontaminate itself with each succeeding data set, and because the measurements of sets 3 to 5 extended to higher temperatures where we can be more sure of a clean surface. Sytaya et al. in studying the evaporation

of oxygen adsorbed on (110) and (100) tungsten crystals found that the threshold temperature for desorption from the (110) crystal is about 2000°K.[87] So we expect that our high-temperature measurements were characteristic of a surface free of oxygen.

The emitter work function below the transition temperature was evaluated by substituting the value of the observed currents and of A = 207 amperes/$cm^2 °K^2$ into Eq. (III.2) and solving for ϕ. The same procedure was used to calculate the collector work function from the currents in the retarding potential region [Eq. (III.9)]. The results obtained for set 4 are given in Table III.II. The comparison between the observed contact potential V_o and $\phi_c - \phi$ in the last two columns is a measure of the consistency of these calculated results.

D. Discussion of Results for (100) Crystal

Three sets of vacuum current-voltage curves were obtained for the (100) diode, plus a fourth set of data after cesium was introduced into the diode, but with the cesium reservoir immersed in liquid nitrogen. The current-voltage curves for the third set are shown in Figs. III.10 and III.11 and the Schottky plots corresponding to the data of Fig. III.11 are shown in Fig. III.12. These figures are typical examples of all the vacuum data obtained for the (100) diode. The temperatures T_e listed alongside each sloping line in Figs. III.10 and III.11 were calculated from the slope of the line, whereas the temperature T_E listed next to each saturation current line was the measured emitter temperature. The value of the contact potential, initially -1.8V, changed gradually whenever the collector temperature exceeded about 120°C in each set of vacuum data, to a final value (Fig. III.11) of -0.56V. This effect was not accompanied by a corresponding change in saturation current and was therefore due to a gradual increase in collector work function.

Table III.II Emitter and collector work function in eV of (110) diode, calculated for set 4 from the Richardson equation with A = 207 amperes/cm^2°K^2.

T_E(°K)	ϕ_o	ϕ_c	$\phi_o - \phi_c$	$-eV_o$
2195	5.33	3.42	1.91	1.91
2153	5.33	3.41	1.92	1.91
2111	5.33	3.41	1.92	1.92
2068	5.33	3.41	1.92	1.92
2026	5.33	3.40	1.93	1.93
1985	5.33	3.39	1.94	1.94
1940	5.33	3.39	1.94	1.93
1901	5.33	3.41	1.92	1.91
1856	5.30	3.38	1.91	1.90
1819	5.17	3.35	1.82	1.80
1774	5.11	3.32	1.79	1.76
1734	5.10	3.33	1.77	1.74
1693	5.09	3.31	1.78	1.75
1651	5.11	3.38	1.73	1.76
1607	5.11	3.39	1.72	1.77

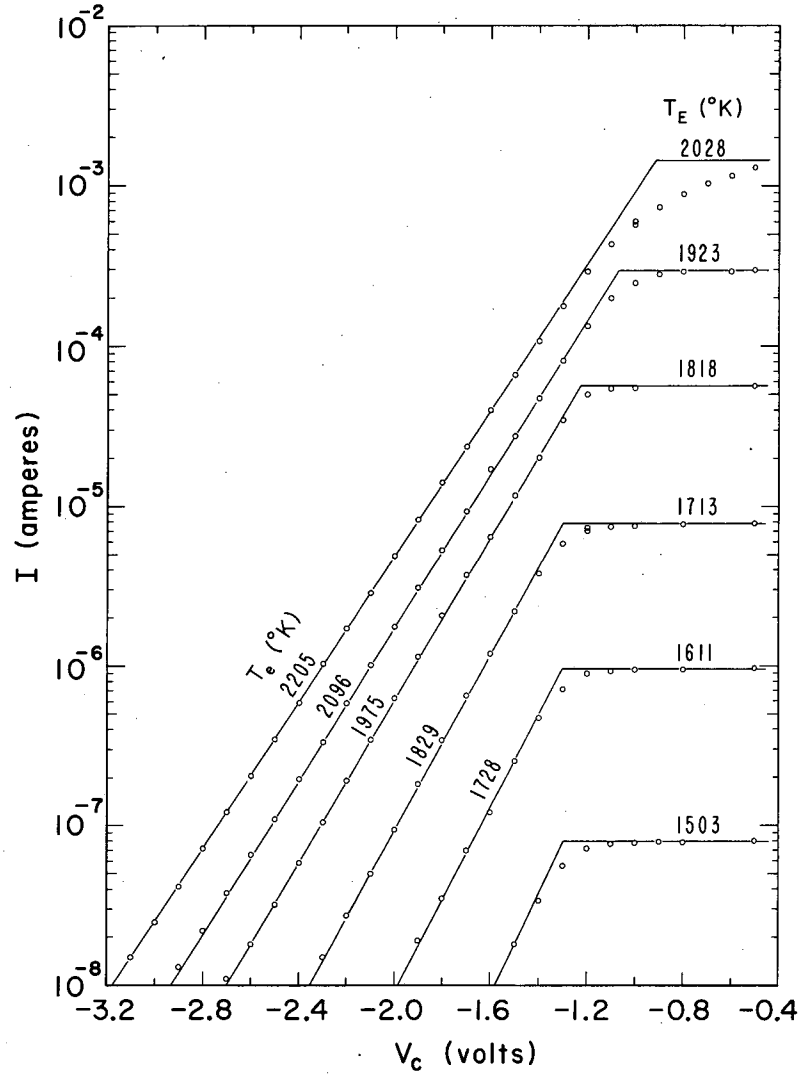
10^{-2}
10^{-3}
10^{-4}
10^{-5}
10^{-6}
10^{-7}
10^{-8}
I (amperes)
T_E (°K)
2028
1923
1818
1713
1611
1503
T_e (°K)
2205
2096
1975
1829
1728
-3.2
-2.8
-2.4
-2.0
-1.6
-1.2
-0.8
-0.4
V_c (volts)
MU-36713

Fig. III. 10

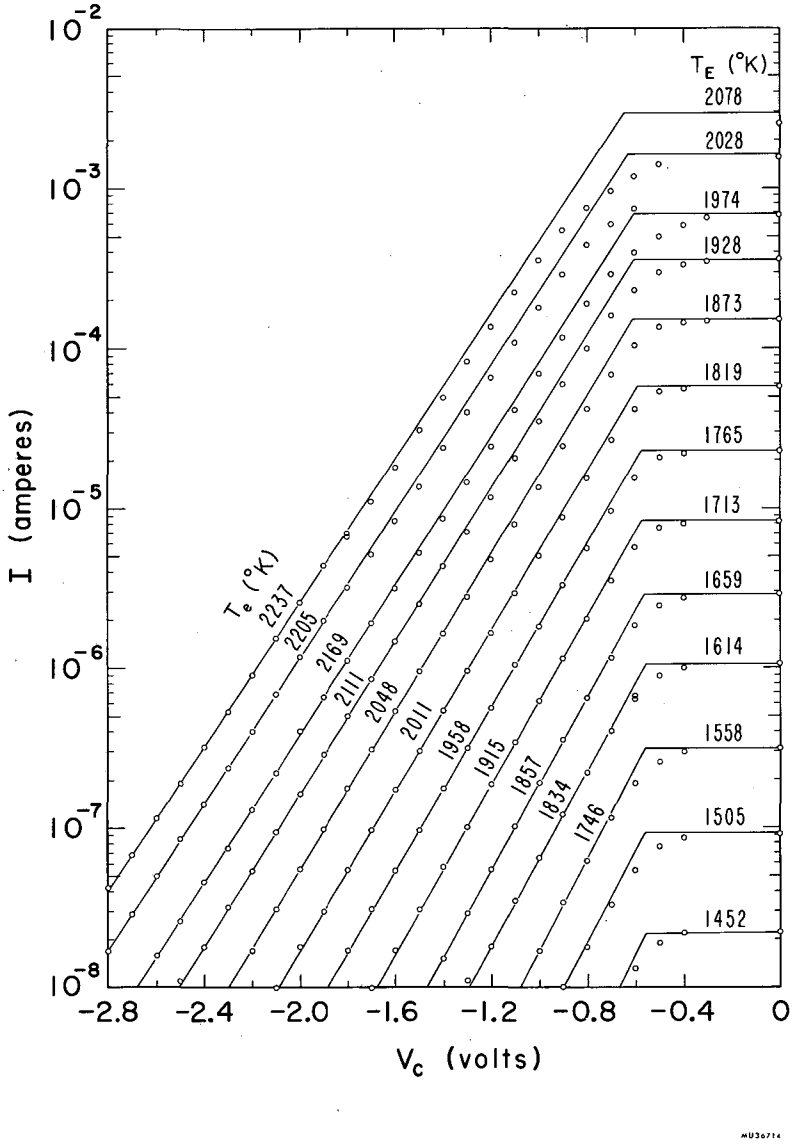
10^{-2}
10^{-3}
10^{-4}
10^{-5}
10^{-6}
10^{-7}
10^{-8}
I (amperes)
T_E (°K)
2078
2028
1974
1928
1873
1819
1765
1713
1659
1614
1558
1505
1452
T_e (°K)
2237
2205
2169
2111
2048
2011
1958
1915
1857
1834
1746
-2.8
-2.4
-2.0
-1.6
-1.2
-0.8
-0.4
0
V_c (volts)
MU36714

Fig. III. 11

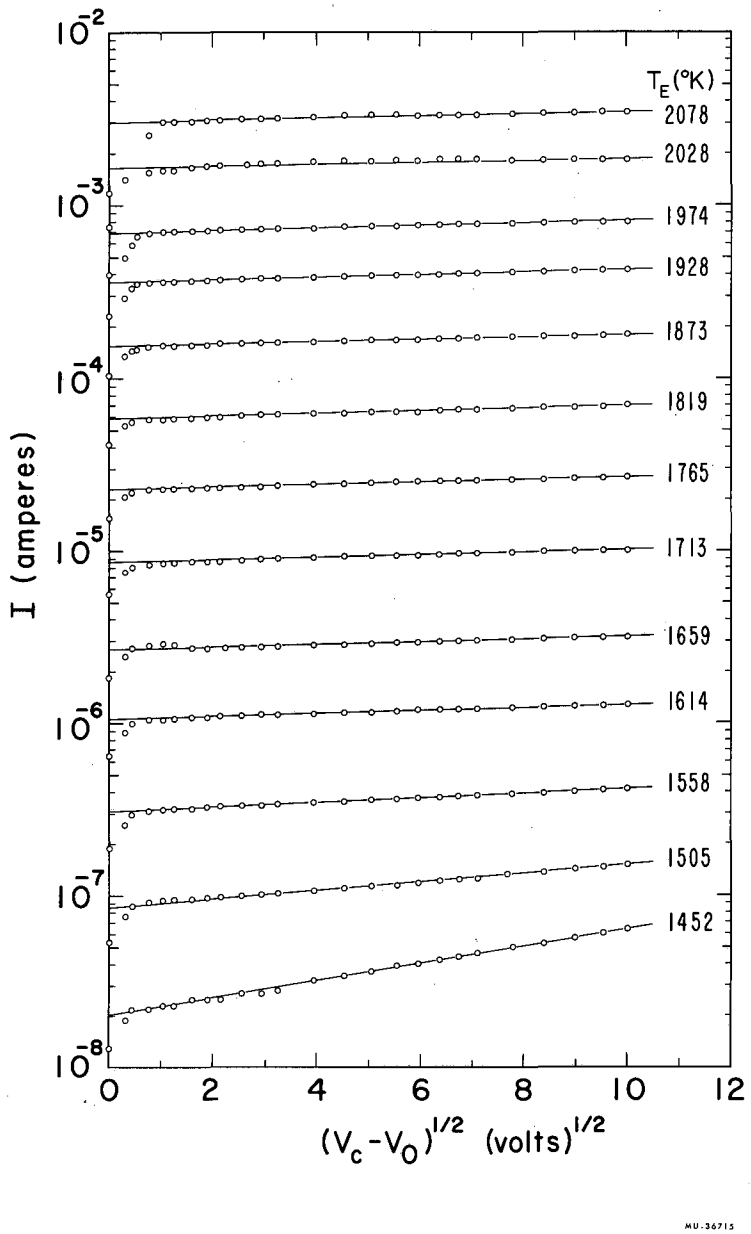
T_E(°K)
2078
2028
1974
1928
1873
1819
1765
1713
1659
1614
1558
1505
1452
I (amperes)
10^{-2}
10^{-3}
10^{-4}
10^{-5}
10^{-6}
10^{-7}
10^{-8}
0
2
4
6
8
10
12
$(V_c - V_0)^{1/2}$ (volts)$^{1/2}$
MU-36715

Fig. III. 12

The initial and final values of the collector work function, determined from the emitter work function and the contact potential, were 2.9 and 4.1 eV. Such a change was probably due to the desorption from the collector of some electropositive impurity, possibly cesium, having a low heat of evaporation. However, if there was any cesium vapor in the diode, it was at such a low concentration as to be unmeasurable ($2 < \times 10^{-9}$ ampere/cm^2).

The variation and nonuniformity of the collector work function prevented us from determining A and ϕ_c from the retarding potential region of the I-V curves. As with the (110) data, the field-free saturation currents were obtained from the intercept of the Schottky plots at zero interelectrode potential. These currents were then used in making the Richardson plots shown in Fig. III.13.

For each data set, the slopes and intercepts of the best lines through the data were again computer evaluated by the method of least squares. It was found for all three vacuum sets that within a given set the Richardson plot obtained as the emitter temperature was increased to its maximum value did not match that obtained as the emitter was cooled. So these two subsets of data were analyzed separately. All the data of the fourth set (cesium in the reservoir at -196°C) were very consistent and were consequently fitted to one line.

The results of the computations are shown in Table III.III. Except for that of the fourth set, each line in Fig. III.13 was drawn through the data obtained in each set for decreasing emitter temperatures only. The most striking feature of the data is that the slopes of the Richardson plots for all the decreasing temperature data and including the fourth set are the same and are equal to 4.65 ± 0.02eV. Apparently the emitter work function was constant throughout the experiments, whereas the value of A gradually

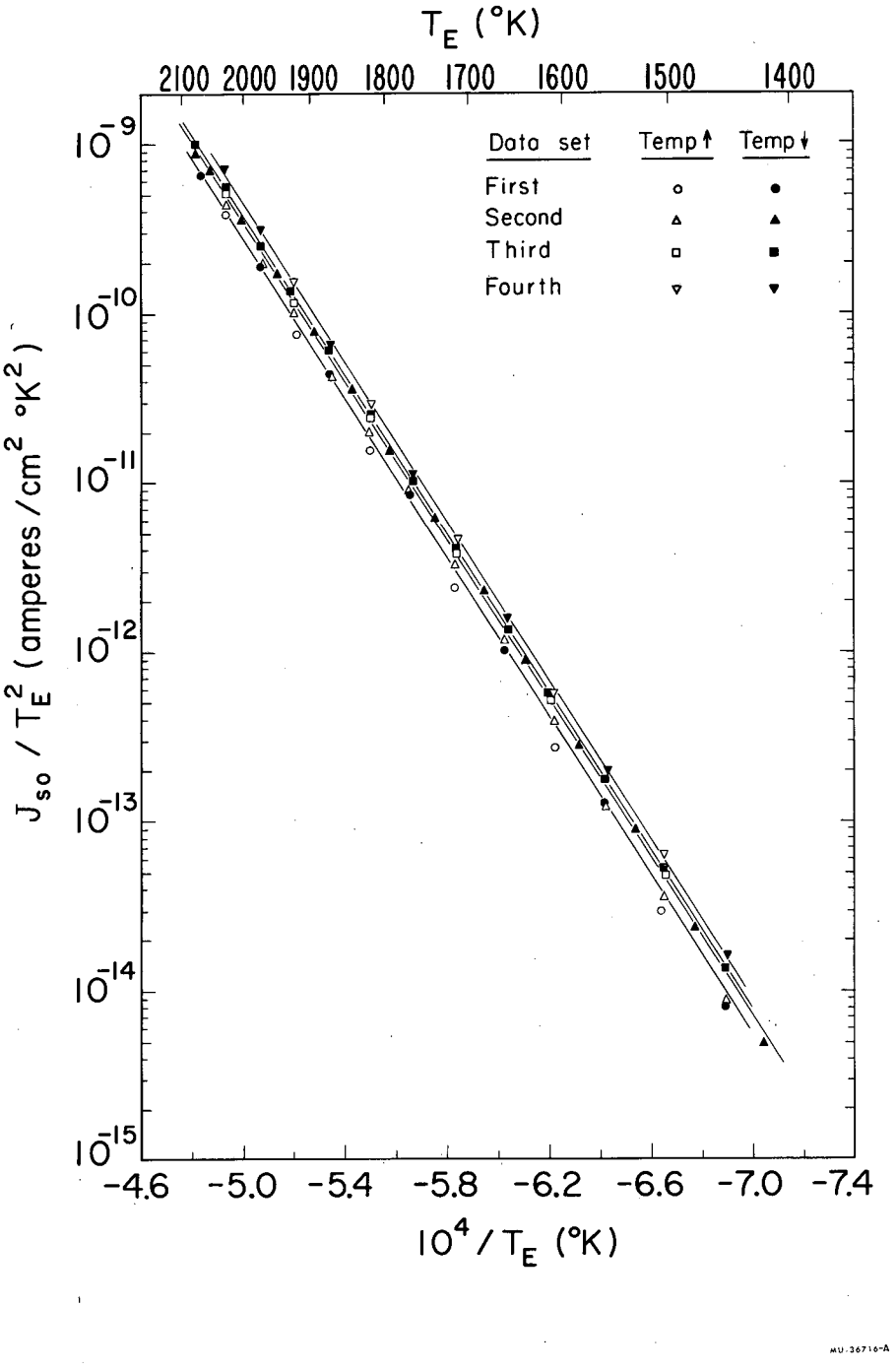
T_E (°K)
2100 2000 1900 1800 1700 1600 1500 1400
Data set
Temp ↑
Temp ↓
First
Second
Third
Fourth
J_{so} / T_E^2 (amperes / cm^2 °K^2)
10^{-9}
10^{-10}
10^{-11}
10^{-12}
10^{-13}
10^{-14}
10^{-15}
-4.6 -5.0 -5.4 -5.8 -6.2 -6.6 -7.0 -7.4
$10^4 / T_E$ (°K)
MU-36716-A

Fig. III. 13

Table III.III Slope and intercept of the Richardson plots for the (100) crystal. All values listed were obtained by the method of least squares. The errors are equal to twice the standard deviation of the means.

Set	ϕ_o (eV)	A (ampere/cm^2°K^2)	Number of data points
1 (Feb. 4), T_E increasing	4.78±0.04	273±40	7
1 (Feb. 4); T_E decreasing	4.65±0.05	147±46	6
2 (Feb. 7), T_E increasing	4.71±0.04	220±52	12
2 (Feb. 7), T_E decreasing	4.63±0.03	162±32	13
3 (Feb. 16), T_E increasing	4.64±0.02	169±26	6
3 (Feb. 16), T_E decreasing	4.65±0.02	192±23	13
4 (March 5), all data points	4.66±0.05	238±75	11

increased. Information concerning the time or temperature behavior of the emitter work function could not be obtained from the observed contact potential, becuase the collector work function was changing widely during these experiments.

The results of Table III.III can best be eludicated by considering the detailed chronological behavior of the four data sets. For clarification, a chronological schematic plot, grossly exaggerating the differences in the data of Fig. III.13, is shown in Fig. III.14. The first two sets of data were obtained by heating the emitter to a maximum temperature and cooling it again as fast as the time necessary to reach thermal equilibrium and record the data would permit. From the results of these two data sets, the effective area of electron emission appeared to increase with time whenever the emitter was operating near the top of its temperature range. This apparent effect was most pronounced with the first set and less so with the second even though the time spent at high temperatures was about the same in each case. The increasing temperature data of the third set closely matched the decreasing temperature data of the second set, and it seemed that a stable emitter condition had finally been reached. We decided, nevertheless, to hold the emitter temperature at 2020°K for several hours and monitor the change in saturation current with time. A plot of this, shown in Fig. III.15, shows the saturation current at 2025°K versus the total accumulated time at or above 2025°K, including the first two data sets. When it appeared that a steady current value had been obtained, the emitter's temperature was raised to 2078°K long enough to take data and then lowered gradually, with many measurements taken on the way down. The value of the work function obtained from this data is identical within the experimental error to that obtained from the temperature-increasing data of the same set.

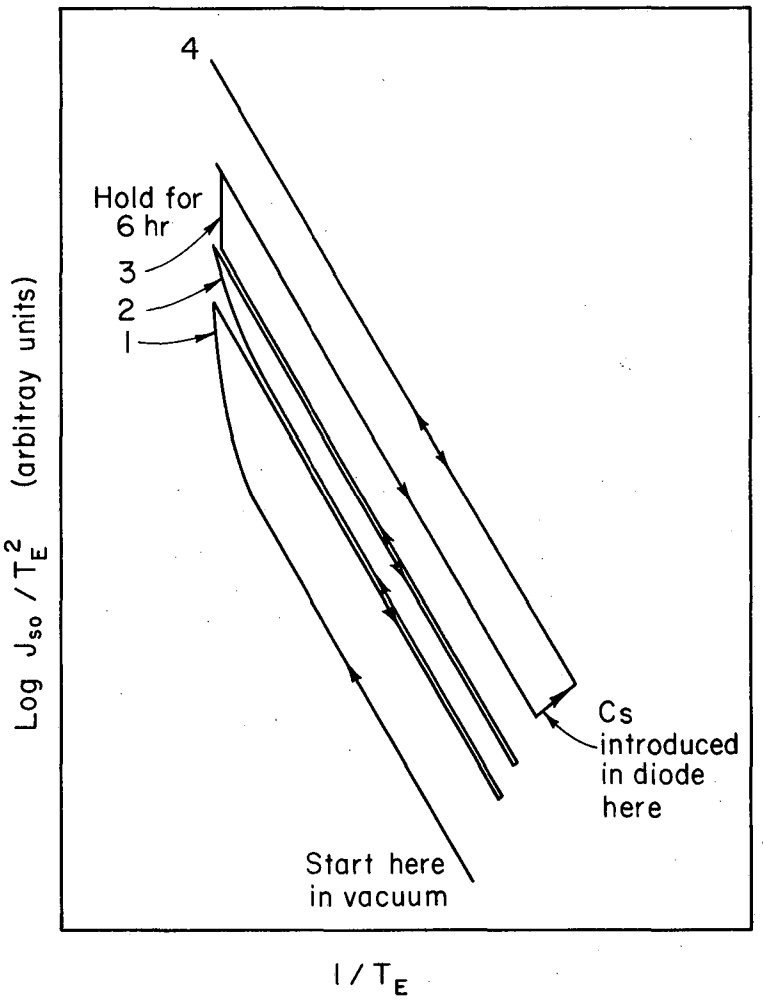

MU-36752

Fig. III. 14

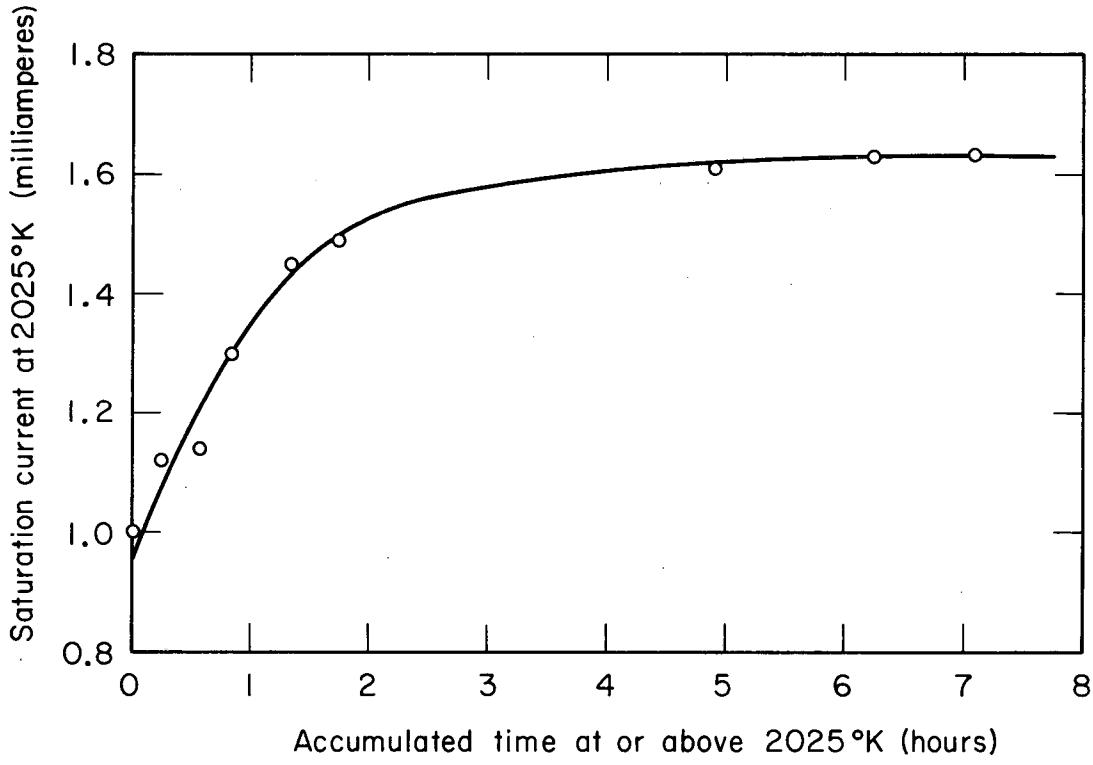
Saturation current at 2025°K (milliamperes)
1.8
1.6
1.4
1.2
1.0
0.8
0
1
2
3
4
5
6
7
8
Accumulated time at or above 2025°K (hours)
MU-36753

Fig. III. 15

Hence, the parallel shift in the Richardson curve within this third set can be explained only by an increase in the effective area of emission. From Fig. III.15 it was thought that a final effective emitter area had been achieved. Between the third and fourth sets, the cesium capsule was broken and the cesium transferred by evaporation and recondensation to the bottom of the cesium reservoir. All parts of the diode were exposed to a high cesium flux during the transfer and the emitter temperature was at no time above 1500°K. The results of the fourth data set, portrayed in Fig. III.14, indicate that this exposure to a cesium atmosphere apparently had an additional effect in increasing the effective emission area of the emitter, totally independent of the emitter temperature, at least above 1500°K.

The input-power curves versus emitter temperature of the first and fourth sets agreed within the experimental error. Therefore the increase in the emitter area was not the apparent result of an increase in the absorptivity of the sapphire window through which the emitter temperature was measured.

In light of the evidence presented above, it appears that the work function of the crystal surface remained constant but that the effective area of electron emission increased with time at high temperatures. This effect could be due to the evaporation from the emitter surface of adsorbed electronegative atoms such as oxygen. It has been known since the early experiments of Langmuir that the adsorption of oxygen on tungsten and other metals can greatly increase their work function, with the result that the thermionic emission from a metal surface with adsorbed oxygen can be negligible compared with the emission from the clean surface. Any desorption of oxygen will then appear as an increase in emitting area. Further substantiation that oxygen was responsible for our observations comes

from the work of Sytaya et al., who, as mentioned in Sec. III.C., studied the adsorption of oxygen on (100) and (110) tungsten crystals.[87] They found that the threshold temperature for oxygen adsorption on the (100) crystal is about 2100°K. The fact that our emitter temperature maximum (2078°K) was very near but slightly below this value might explain the slow time dependence of the desorption that we observed.

Cesium, of course, getters oxygen and appears to have been instrumental in removing adsorbed oxygen (if it was oxygen) from our (100) crystal surface.

We conclude from this experiment that the bare work function and Richardson constant for our (100) crystal were (assuming no temperature dependence in the work function)

$$\phi_o = 4.65 \pm 0.02\text{eV}, \text{ and } A = 238 \pm 80 \text{ amperes/cm}^2\text{°K}^2.$$

The errors listed and the somewhat high final value of A are subject to the same remarks that were made for the result of the (110) crystal in Sec. III.C.

E. Comparison with the Literature

The work functions of various crystallographic planes of tungsten have been measured many times in the past. However, as mentioned in Sec. I, few studies have been performed on flat crystals, with known emitting areas and with the use of appropriate guard rings. In Table III.IV we have listed in reverse chronological order only those results obtained within the last 15 years. References to older works can be found in some of the papers listed in the table.

Table III.IV Work functions (in eV) of the (110) and (100) crystallographic planes of tungsten.

Investigator	$\phi_o(110)$	$\phi_o(100)$	Method
Koenig (this study)	5.33	4.65	Thermionic emission from planar crystals
Reynolds[77] (1963)	5.41		Surface ionization of Sr and Ca from planar crystals
Sytaya el al.[87](1961)	5.30	4.66	Thermionic emission from planar crystals. Substantiated by surface ionization of Na
Young and Müller[99](1961)	≈6.0		Field-emission with probe
Hughes et al.[42] (1958)	5.25		Surface ionization of Na and thermionic emission from etched single crystal wires
Shuppe et al.[81] (1956)	>5.1		Surface ionization of Na and thermionic emission from single crystal wires
Hutson[43] (1955)	5.1	4.44	Thermionic emission from single crystal wires
Müller[66] (1954)	5.7-6.0		Field emission with probe
Smith[82] (1953)	4.72	4.52	Thermionic emission from single crystal wires
Dyke et al.[28] (1953)	5.0-5.5		Field emission by photometric measurement
Wilkinson[98] (1953)	4.68	4.56	Field emission by photometric measurement
Brown et al.[13] (1949)		4.59	Thermionic emission from planar crystal

Of particular pertinence to this study are the results of Reynolds, who kindly furnished us with our own crystals and who measured the work function of several (110) crystals cut from the same bulk crystal as was ours.[77] He used the method of surface ionization which, if the surface under study is not quite uniform, will tend to give an upper limit to the work function of the surface, whereas the method of thermionic emission will favor the lower limit. The results of Reynolds and our experiments have placed rather narrow limits then on the (110) tungsten work function.

Our results agree closely with those of the next two most recent thermionic emission studies of Sytaya et al.[87] and Hughes et al.[42] As mentioned earlier, Sytaya et al.also studied the evaporation of adsorbed oxygen from (110) and (100) tungsten crystal and found that the threshold for evaporation was 2000°K and 2100°K, respectively. Since most of our good (110) data were obtained between 2000 and 2200°K, we can deduce that our results are for surfaces free of adsorbed oxygen. Our data for the (100) crystal suggest that the threshold temperature for oxygen evaporation may be as low as 2025°K, although this cannot be affirmed conclusively since we had no way of measuring directly the nature of the gases adsorbed on our emitters in the low-temperature range.

The results of the field-emission experiments listed in Table III.IV have a considerable spread and generally disagree with those obtained from thermionic emission or surface ionization. The difficulty with the field-emission method lies in the determinations of the electric field at the emitting surface and the evaluation of the emitting area. The former is usually assumed to be uniform and the latter is assumed to be constant, independent of the applied field.

F. Summary

The work functions of the (110) and (100) crystal planes of tungsten were determined from measurements of thermionic emission in vacuum, in the temperature range 1400 to 2200°K. The results, obtained from the slope and intercept of Richardson plots ($\log J_{so}/T_E^2$ versus $1/T_E$), are as follows:

$$\phi_o(110) = 5.33 \pm 0.04\text{eV}, \; A = 207 \pm 50 \text{ ampere/cm}^2{}^\circ\text{K}^2$$

$$\phi_o(100) = 4.65 \pm 0.02\text{eV}, \; A = 238 \pm 75 \text{ ampere/cm}^2{}^\circ\text{K}^2.$$

The values of the work function for both crystals agree quite well with the most recent values published in the literature. The somewhat high value of A in each case may be due to an uncertainty in the measurement of the absolute emitter temperature. We were unable to determine A independently of the work function, for either crystal, from the emission in the retarding-potential region as described by Shelton,[80] because of the nonuniformity and instability of the collector work function. For the same reasons, the temperature dependence of the bare work functions of the emitters could not be determined from changes in the contact potential.

IV. HEAT OF EVAPORATION OF CESIUM ATOMS AND IONS ON (100) AND (110) CRYSTALS

The surface ionization of atoms and molecules impinging on a hot metal surface has been extensively described in several good review articles,[101,27,49] and therefore we will present here only the aspects of the theory essential to the analysis of our experimental observations. We will describe theoretically and experimentally the method that we used to determine the desorption energies of cesium ions and atoms evaporating from the essentially bare crystal emitters. We will conclude this section with a discussion of our experimental results, including a comparison with existing data for tungsten.

A. Theory of Surface Ionization

Two parameters that quantitatively characterize the phenomenon of surface ionization are the degree of ionization (α)

$$\alpha = n_i/n_a \qquad \text{(IV-1)}$$

and the ionization coefficient (β)

$$\beta = n_i/n_o \qquad \text{(IV-2)}$$

where n_o is the atomic flux (atoms per cm^2 per second) incident on the surface, and n_i and n_a are the ion (positive in the case of cesium) and neutral-atom fluxes, respectively, evaporating from the surface. At steady state,

$$n_o = n_i + n_a, \qquad \text{(IV-3)}$$

and therefore Eqs. (IV-1) and (IV-2) combine to give

$$\beta = \frac{\alpha}{1+\alpha} \qquad \text{(IV-4)}$$

$$\alpha = \frac{\beta}{1 - \beta} \quad . \qquad \text{(IV-5)}$$

The degree of ionization is evaluated from the temperature T_E and electron work function ϕ of the metal surface, and from the ionization energy V_i of a free incident atom by the Saha-Langmuir equation[56,57]

$$\alpha = \frac{g_i}{g_a} \exp\left[(\phi - V_i)/kT_E\right] . \qquad \text{(IV-6)}$$

Here g_i/g_a, the ratio of statistical weights of the ionic and atomic states, is equal to 1/2 for the alkali atoms because of the double spin state of the valence electron in the atom.

Equation (IV-6) was derived in 1924 by Langmuir and Kingdon by solving for the concentrations of ideal electronic, ionic, and atomic gases in thermodynamic equilibrium with a metal enclosure at temperature T_E. They used a statistical expression involving the ionization energy for the equilibrium constant, and from kinetic theory related the electron gas concentration to the flux of electrons emitted thermionically from the surface of the enclosure. They assumed that the metal surface was homogeneous and that there was no electric field.

Zandberg has derived a rather formidable expression for α which takes into account the nonuniformity (patchiness) of the ionizing surface, the effects of an electric field and reflection coefficients, and more complex functions for the statistical weights.[101] However, since our experiments were performed on single crystals and with small applied electric fields, we will assume that Eq. (IV-6) adequately describes our system.

We now introduce the desorption energies of ions and atoms by deriving Eq. (IV-6) from the following approach.[27,48] The term α may

be regarded as the product of two relative probabilities: The ratio of the probabilities W_i and W_a that the evaporating particle be in the ionic or atomic state outside a critical distance beyond which charge exchange is no longer possible; and the ratio of the probabilities per unit time P_i' and P_a' that the ion or atom has sufficient energy to evaporate from the surface.

$$\alpha = \left(W_i/W_a\right)\left(P_i'/P_a'\right) \qquad \text{(IV-7)}$$

It is generally agreed that the potential-energy diagram for adsorption (or desorption) of cesium atoms and ions on tungsten is similar to that represented in Fig. IV.1. The term E is the energy required to neutralize the adsorbed ion on the surface; hence the charge-transfer probability is given from statistical mechanics by

$$\left(W_i/W_a\right) = \frac{g_i}{g_a} \exp\left(E/kT_E\right) . \qquad \text{(IV-8)}$$

Similarly it can be shown that the probability per unit time that the kinetic energy of an adsorbed atom or ion will exceed the evaporation energy, ϕ_a or ϕ_i in Fig. IV.1, is

$$P_a' = \omega_a \exp\left(-\phi_a/kT_E\right) \qquad \text{(IV-9)}$$

$$P_i' = \omega_i \exp\left(-\phi_i/kT_E\right) \qquad \text{(IV-10)}$$

or

$$\left(\frac{P_i'}{P_a'}\right) = \frac{\omega_i}{\omega_a} \exp\left(\frac{\phi_a - \phi_i}{kT_E}\right) \qquad \text{(IV-11)}$$

where $\omega_{i,a}$ are the frequencies of vibration (normal to the surface) of the adsorbed ion or atom. However, charge exchange between an adsorbed cesium particle and the metal surface occurs many times within one period of oscillation, so that one cannot make the distinction

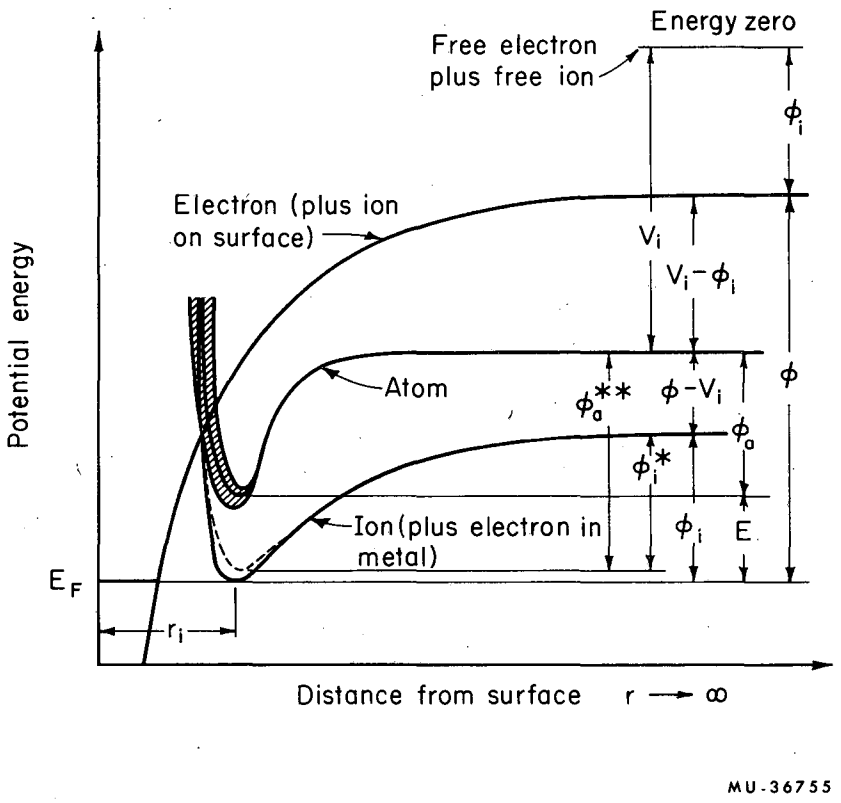
Energy zero
Free electron
plus free ion
ϕ_i
Electron (plus ion
on surface)
V_i
$V_i - \phi_i$
Atom
ϕ_a^{**}
$\phi - V_i$
ϕ
ϕ_a
ϕ_i^*
Ion (plus electron in
metal)
ϕ_i
E
E_F
r_i
Potential energy
Distance from surface $r \longrightarrow \infty$
MU-36755

Fig. IV.1

between ω_i and ω_a. Therefore, assuming $\omega_i = \omega_a = \omega$, we obtain from Eqs. (IV-7),(IV-8), and (IV-11),

$$\alpha = \frac{g_i}{g_a} \exp\left(\frac{\phi_a + E - \phi_i}{kT_E}\right) . \qquad \text{(IV-12)}$$

Comparing Eqs. (IV-12) and (IV-6) we obtain the relation

$$\phi_a + E - \phi_i = \phi - V_i . \qquad \text{(IV-13)}$$

Equation (IV-13) can be deduced from Figs. IV.1 and also from Fig. IV.2 which describes perhaps more visually the path of a single particle through a hypothetical closed cycle. Starting with an ion adsorbed on the surface, we see that energy E is required to neutralize it on the surface and energy ϕ_a is then needed to evaporate the atom to free space. The ionization energy V_i must be added to convert the free atom into a free ion and a free electron. The adsorption energy ϕ_i is recovered when the free ion condenses on the surface, and the electron work-function energy ϕ is also recovered when the free electron returns to the metal, thus completing the cycle. The net energy change in traversal of this closed cycle must be zero; therefore

$$E + \phi_a + V_i - \phi_i - \phi = 0, \qquad \text{(IV-14)}$$

which is the result obtained in Eq. (IV-13).

So far we have made no statement concerning the concentration of adsorbed particles on the surface. Equations (IV-1) to (IV-14) are quite general and apply for a clean surface as well as for a surface with adsorbed particles. For a clean surface Eq. (IV-14) becomes

$$E_o + \phi_{ao} + V_i - \phi_{io} - \phi_o = 0, \qquad \text{(IV-15)}$$

where the subscript o denotes the properties of a clean (bare) surface.

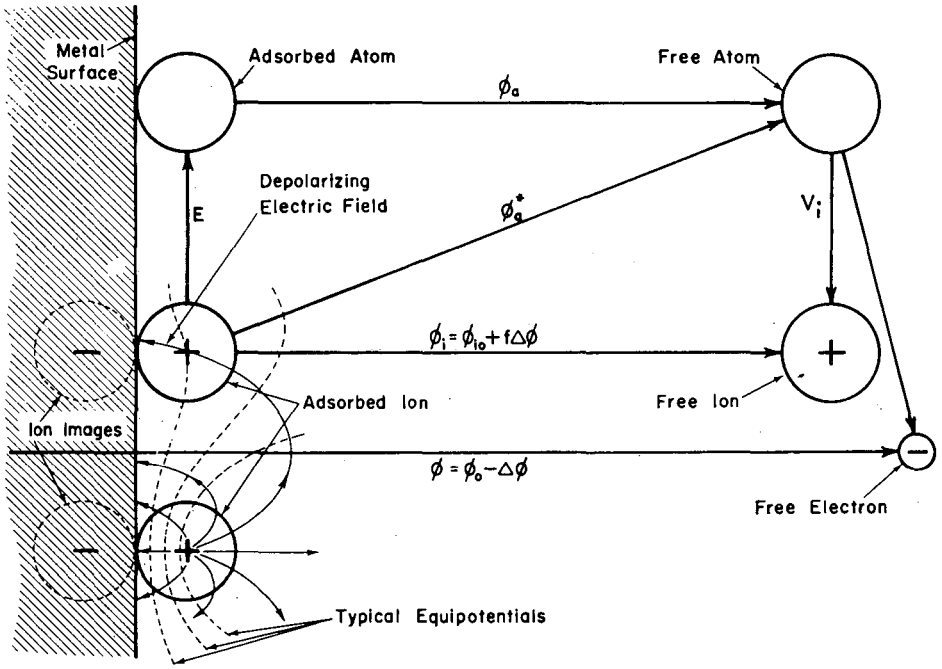

MU-36994

Fig. IV.2

From Fig. IV.1 and IV.2 we see that

$$\phi_a^* = \phi_a + E, \qquad \text{(IV-16)}$$

is the energy required to convert an adsorbed ion into a free atom. From Eqs. (IV-16) and (IV-13) we thus obtain

$$\phi_a^* - \phi_i = \phi - V_i \quad . \qquad \text{(IV-17)}$$

For the case of $E > 0$ (as shown in Fig. IV.1), the energy ϕ_a^* governs the atom evaporation rate and would be the observed atom's heat of evaporation; whereas ϕ_i would be the observed ion's desorption energy. In other words, the observed probability per unit time that an adsorbed particle evaporates as an atom P_a is

$$P_a = \left(W_a/W_i\right) P_a' \, g_i = \omega g_a \exp\left(-\phi_a^*/kT_E\right) \qquad \text{(IV-18)}$$

and similarly for ions

$$P_i = P_i' = \omega g_i \exp\left(-\phi_i/kT_E\right) \quad . \qquad \text{(IV-19)}$$

The degree of ionization for this case is, according to these definitions,

$$\alpha = P_i/P_a \quad . \qquad \text{(IV-20)}$$

We believe, though, for this case ($E > 0$), that the observed desorption energies would more accurately be ϕ_a^{**} and ϕ_i^* as shown in Fig. IV.1. We cannot say that an adsorbed particle is an atom or an ion because of the continuous charge exchange that takes place with the metal, even as the particle is in the act of evaporating from the surface.[34,91] Therefore, because we have chosen to plot in Fig. IV.1 potential energy rather than just potential, the potential-energy diagram for the ion should be

$$\phi_i^{**}(r) = \frac{\bar{q}(r)}{e} \, \phi_i(r), \qquad \text{(IV-21)}$$

where $\bar{q}(r)$ is the time-average charge of the ion at position r. So,

to the extent that the wave function of the electron extends into the adsorbed ion, and this will depend on the magnitude of E of course, the observed heat of evaporation ϕ_i^{**} for ions will be $\leq \phi_i$. Note, though, that Eq. (IV-17) is unchanged, i.e.,

$$\phi_a^{**} - \phi_i^{*} = \phi - V_i \quad . \tag{IV-22}$$

This point was mentioned in passing and from here on we will define the desorption energies according to Eq. (IV-17).

For cesium on tungsten it is well established that $E_o \gg kT > 0$,[76] so that the observed cesium-atom desorption energy for the clean surface is in fact ϕ_{ao}^{*}, where

$$\phi_{ao}^{*} = \phi_{ao} + E_o \quad . \tag{IV-23}$$

We conclude from this discussion that the observed probability per unit time P_{ao} that an adsorbed cesium particle evaporates from the bare tungsten surface as an atom is [from Eqs. (IV-18 and IV-19)]

$$P_{ao} = Q_{ao} \exp\left(- \phi_{ao}^{*}/kT_E\right) \tag{IV-24}$$

and similarly for ions,

$$P_{io} = Q_{io} \exp\left(- \phi_{io}/kT_E\right) \tag{IV-25}$$

where

$$Q_{io} = \omega_o g_i, \text{ and } Q_{ao} = \omega_o g_a \quad . \tag{IV-26}$$

We have differentiated ω_o from ω because the vibration frequency may be a weak function of coverage.[88,94,59]

The quantities ϕ_{io}, ϕ_{ao}^{*}, Q_{io} and Q_{ao} can be determined experimentally from measurements of P_{io} and P_{ao} versus the temperature T_E. The desired quantities are evaluated (assuming they are independent of T_E) from the slope and intercept of Arrhenius plots of P_{io} and P_{ao}.

We conclude this theoretical presentation by noting that in general the evaporation rates of adsorbed atoms and ions n_a and n_i are not found simply by multiplying the surface concentration N (particles/cm^2) of adsorbed particles by the evaporation probabilities per unit time P_a and P_i [Eqs. (IV-18 and IV-19)], because such a procedure does not take into account the interaction or lateral forces between the adsorbed particles. When these effects are considered one finds that, according to our notation

$$n_a = \sigma K^*(\theta) P_a \quad ; \quad n_i = \sigma K^*(\theta) P_i \ , \qquad \text{(IV-27)}$$

where σ is the surface concentration of a complete monolayer of adsorbed particles, and $\theta = N/\sigma$ is the fractional surface coverage ($\theta = 1$, when $N = \sigma$). The function $K^*(\theta)$ depends on the equation of state of the adsorbed particles and can be calculated from statistical thermodynamics.[57,94,59,16] It is a function of θ alone and does not depend on the properties of either the substrate or the adsorbate. Obviously the same function $K^*(\theta)$ applies to both n_i and n_a because their ratio must equal $\alpha = P_i/P_a$. It should be intuitively evident that for $\theta \ll 1$, $K^*(\theta) \to \theta$, because at low surface coverage the adsorbed particles are too far apart to interact with each other; and the evaporation rates are indeed given by the simple product mentioned above. For convenience in analyzing some of our data, let us define the function $K'(\theta) = K^*(\theta)/\theta$ and substitute it in Eq. (IV-27). The atom evaporation rate n_a (and similarly for n_i) becomes

$$n_a = \sigma\, \theta\, K'(\theta) P_a = \sigma\, \theta\, P_a^*(\theta) = N\, P_a^*(\theta) \qquad \text{(IV-28)}$$

where

$$P_a^*(\theta) = K'(\theta)\, \omega g_a \exp[-\phi_a^*(\theta)/kT_E] \ . \qquad \text{(IV-29)}$$

Various theoretical estimates of $K^*(\theta)$ are presented in Sec. VI [see Table VI.I, where $K(\theta) = \ell n\ K^*(\theta)$]. For illustration here, Eq. (IV-30) shows a typical formulation, derived and experimentally verified by Langmuir and Taylor[57,88]

$$K^*(\theta) = \theta K'(\theta) = \frac{\theta}{1-\theta} \exp\left(\frac{\theta}{1-\theta}\right) \quad . \qquad \text{(IV-30)}$$

This equation shows that $K'(\theta) \to 1$ and $K^*(\theta) \to \theta$ as $\theta \to 0$. Consequently $P_a^*(\theta) \to P_{ao}$ also, as $\theta \to 0$.

B. Determination of Desorption Energies for Cesium Ions and Atoms

Our technique to measure ϕ_{io} and ϕ^*_{ao} was an adaptation of a method first used by Moon and Oliphant for studying the adsorption of potassium on tungsten,[65] and subsequently developed by Evans to study potassium, rubidium, and cesium on tungsten.[29,30] The principal difference between our method and that of Moon and Oliphant is that their source of alkali atoms was a collimated ionic and/or atomic beam, whereas our source was the random flux of the cesium vapor in our diode. We selected this method because (a) it allowed us to measure the heats of evaporation without modifying the diode, and (b) it did not involve rapidly flashing the emitter temperature, a procedure which could have disturbed the emitter surface. Some of the inherent advantages and disadvantages of the method will be discussed at the end of this subsection.

Suppose that a steady beam (or in our case a random flux) of cesium atoms n_o (atom/cm^2 sec) is incident on a metal surface at temperature T_E; a concentration N (particles/cm^2) of adsorbed particles will be established on the surface in such a way that the evaporation rate of cesium is equal to the incident flux. As mentioned at the end of Sec. IV.A, for small surface concentrations (less than 1% of an adsorbed monolayer) the evaporation probabilities of ions and atoms are independent of N, and are therefore equal to those (P_{io} and P_{ao}) characteristic of a clean surface.

If a small electric field, retarding for ions, is applied at the surface so as to prevent the evaporation of ions, the surface concentration of adsorbed cesium will assume a definite value N_o so that

$$n_o = N_o P_{ao} \quad . \qquad \text{(IV-31)}$$

If then, at time zero, the applied electric field is suddenly made attractive for ions, their evaporation results in a change in surface concentration given by

$$\frac{dN}{dt} = n_o - PN \qquad \text{(IV-32)}$$

where

$$P = P_{io} + P_{ao} \; . \qquad \text{(IV-33)}$$

With Eq. (IV-31) used as an initial condition, the solution of Eq. (IV-32) is

$$N(t) = \frac{n_o}{P}\left[1 + \frac{P_{io}}{P_{ao}} \exp(-Pt)\right]. \qquad \text{(IV-34)}$$

The observed cesium-ion current density is (assuming the absence of any secondary electron emission from the collecting electrode)

$$J_{Cs}(t) = e\, P_{io}\, N(t) = J_{Cs}(\infty) + [J_{Cs}(0) - J_{Cs}(\infty)] \exp(-Pt). \qquad \text{(IV-35)}$$

The initial and final current densities are

$$J_{Cs}(0) = e\, P_{io}\, N_o = e\, \frac{P_{io}}{P_{ao}}\, n_o \qquad \text{(IV-36)}$$

$$J_{Cs}(\infty) = e\, P_{io}\, N_\infty = e\, \frac{P_{io} n_o}{P} \; , \qquad \text{(IV-37)}$$

where N_∞ is the final surface concentration and e is the electron charge. Combining Eqs. (IV-36), (IV-37),(IV-20), and (IV-4), we obtain the coefficient of ionization (and hence also the degree of ionization)

$$\beta = \frac{J_{Cs}(0) - J_{Cs}(\infty)}{J_{Cs}(0)} \; . \qquad \text{(IV-38)}$$

Equation (IV-35) is displayed in Fig. IV.3. The integral of the shaded area is equal to the difference between the initial and final surface concentration. Equations (IV-35) to (IV-37) demonstrate that P_{ao}, P_{io}, n_o, N_o, and N_∞ can be determined from the observed ion current

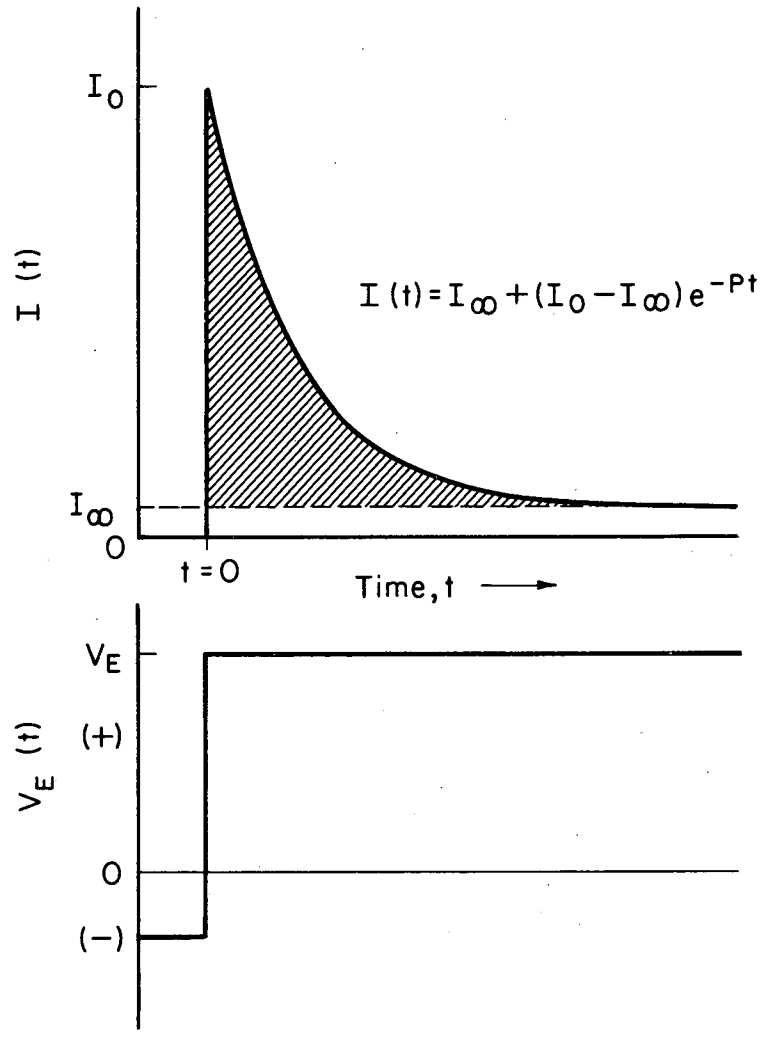
I_0
$I(t)$
$I(t) = I_\infty + (I_0 - I_\infty)e^{-Pt}$
I_∞
0
t = 0
Time, t
V_E
(+)
$V_E(t)$
0
(−)
MU-36607

Fig. IV.3

and its time dependence. However it should be obvious from the ratio $J_{Cs}(0)/J_{Cs}(\infty)$ that an appreciable current pulse will not be observed unless $P_{io} \geq P_{ao}$. Therefore this method is useful only when $\phi^*_{ao} \geq \phi_{io}$ or $\phi_o \geq V_i$. This condition is satisfied by the emitter materials of interest to thermionic energy conversion.

In this experiment ϕ_o is greater than V_i, so $P_{io} \approx P$. Therefore, P_{io} is obtained from the slope of the exponential decay of the current. The incident flux n_o is obtained from Eq. (IV-37), i.e.,

$$n_o \approx J_{Cs}(\infty)/e, \qquad \text{(IV-39)}$$

and P_{ao} is obtained from Eq. (IV-36).

By repeating this experiment for different surface temperatures, we obtain P_{ao} and P_{io} as a function of temperature. As mentioned near the end of subsection A above, a plot of $\ell n\ P_{io}$ versus $1/kT_E$ yields a straight line of slope $-\phi_{io}$ and intercept $\ell n\ Q_{io}$, and similarly for P_{ao}. The accuracy of P_{ao} (and therefore ϕ^*_{ao} and Q_{ao}) as measured by this method is contingent upon the precise determination of n_o. The measurement of n_o is influenced by possible secondary electron emission and ion reflection at the collector, and several other factors, as will be discussed in Sec. IV.D and in Sec. V. The determination of ϕ_{io} is independent of n_o, but is influenced by the applied electric field, according to the Schottky effect on the ion potential barrier. This problem can be circumvented either by applying very small electric fields or by plotting the calculated ϕ_{io} versus the square root of the field and extrapolating to zero field (Schottky plot).

C. Experimental Procedure

Cesium encapsulated in a Pyrex ampoule was introduced into the diode by pinching the side appendage containing the capsule, which caused the capsule to break and release the cesium.

The cesium was condensed into the reservoir by heating the whole diode body, including the side appendage, to a temperature above 200°C for several hours while the bottom inch of the reservoir was immersed in liquid nitrogen.

Then, as mentioned in Sec. III, a complete set of I-V curves was obtained for T_{Cs} = -196°C (liquid nitrogen) and compared with the vacuum data to ascertain that the introduction of cesium did not in other ways contaminate the diode. Following this confirmation the diode was connected to the circuit (Fig. IV.4) that was used to reverse the bias across the electrodes. The dc power supply, voltage regulated to ±4mV, had a recovery time of less than 50 μsec for a no-load to full-load step change. The load change before and after closing the switch S was around 5% and did not cause any problems. The current reaching the collector was obtained by measuring the voltage across the 1% carbon resistor R_c. The value of R_c was 10^3 or $10^4\Omega$ and was normally selected so that the current signal (C_1-C_2) did not exceed a few hundred millivolts. The variable carbon resistor R_g was selected so that the amplitude of the signal (G_1-G_2) matched that of (C_1-C_2). We observed that the collector signal was practically insensitive to the value of R_g. The collector current signal (C_2-C_1) was displayed on an oscilloscope and recorded with a Polaroid camera. The oscilloscope trace was triggered by the change in the polarity of the voltage at E_1. The switch S (actually a mercury relay) had a closing time of about 50 nanoseconds. With the emitter cold,

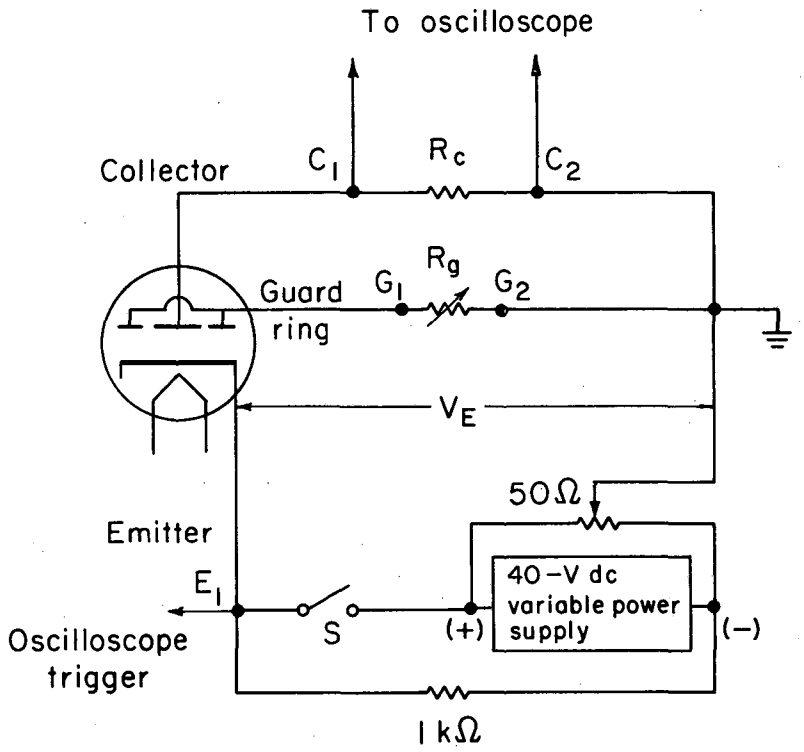
To oscilloscope
Collector
C_1
R_c
C_2
R_g
Guard ring
G_1
G_2
V_E
50Ω
Emitter
E_1
S
(+)
40-V dc variable power supply
(−)
Oscilloscope trigger
1 kΩ
MU-36608

Fig. IV.4

and hence the diode not conducting, the voltage at E_1 could be switched from -10V to +20V in less than 0.5 μsec. However, this produced a small collector current pulse with an amplitude of about 1 μA per volt change across the diode and with a time constant of about 3 μsec. This meant, practically, that the smallest residence time for adsorbed cesium that we could measure was on the order of a microsecond.

The experiments were performed in the following way: The cesium reservoir was immersed in liquid nitrogen (or in an ice bath) and the emitter was heated to the desired temperature (1000 to 1500°K) by thermal radiation from the electron gun filament. A waiting period of about half an hour allowed the diode to reach thermal equilibrium. Then an I-V curve was measured point by point to determine the flux of cesium vapor incident on the emitter. In this case the collector current and the voltage across the electrodes were measured with the voltmeters described in Sec. III. The emitter voltage was then made a few volts negative for several seconds by maintaining the switch S in the open position. The ratio of negative-to-positive emitter-voltage swing could be varied by adjusting the setting of the voltage divider across the power supply, while the magnitude of the voltage swing was determined by the supply voltage. When the switch was closed the emitter voltage became positive and the subsequent cesium-ion current trace was recorded on the oscilloscope. Because the shape of the current trace was dependent on the magnitude of the positive emitter voltage, several traces were recorded on each photograph corresponding to varying applied positive voltage. When enough data had been obtained, an I-V curve was again measured to confirm that the cesium flux had remained steady during the experiment.

The emitter temperature was changed to a new value and the whole procedure repeated. The cesium flux was determined at each emitter temperature because, although it should have been a function of the reservoir temperature only, it was found to be dependent on the temperature of the diode body and the emitter.

D. Results

The data shown in Fig. IV.5 were observed during what was supposed to be a preliminary experiment; unfortunately they represent all that were obtained for the (110) crystal. The five traces in each photograph were obtained by varying the emitter voltage swing. In all cases the applied voltage, retarding for ions, was equal to the attractive voltage. The applied voltage varied from 18 volts for the tallest trace to 7.5 volts for the shallowest. In the case of the (100) crystal we maintained the retarding voltage constant at 5V and just varied the attractive voltage.

After noting the disparity between Figs. IV.5 and IV.3, we realized that the ion currents in Fig. IV.5 were simply limited by their own space charge until such time as the emitter current supply dropped below the current specified by the Child-Langmuir three-halves power law[55]

$$J_{max} = K \frac{V_d^{3/2}}{d^2} \qquad \text{(IV-40)}$$

$$K = \frac{\sqrt{2}}{9\pi} \left(\frac{e}{m}\right)^{1/2} \qquad \text{(IV-41)}$$

$$= 2.33 \times 10^{-6} \text{ (ampere)(volt)}^{2/3} \text{ for electrons} \qquad \text{(IV-42)}$$

where J_{max} is the maximum current density in ampere/cm^2, which can be drawn with a potential difference V_d in volts between plane parallel electrodes d centimeters apart. Substituting the mass of a cesium ion in Eq. (IV-41) gives the result

$$J_{Cs\ max} = 4.65 \times 10^{-9} \frac{V_d^{3/2}}{d^2} \text{ ampere/cm}^2 \qquad \text{(IV-43)}$$

The current plateaus in Fig. IV.5 do indeed fit this equation.

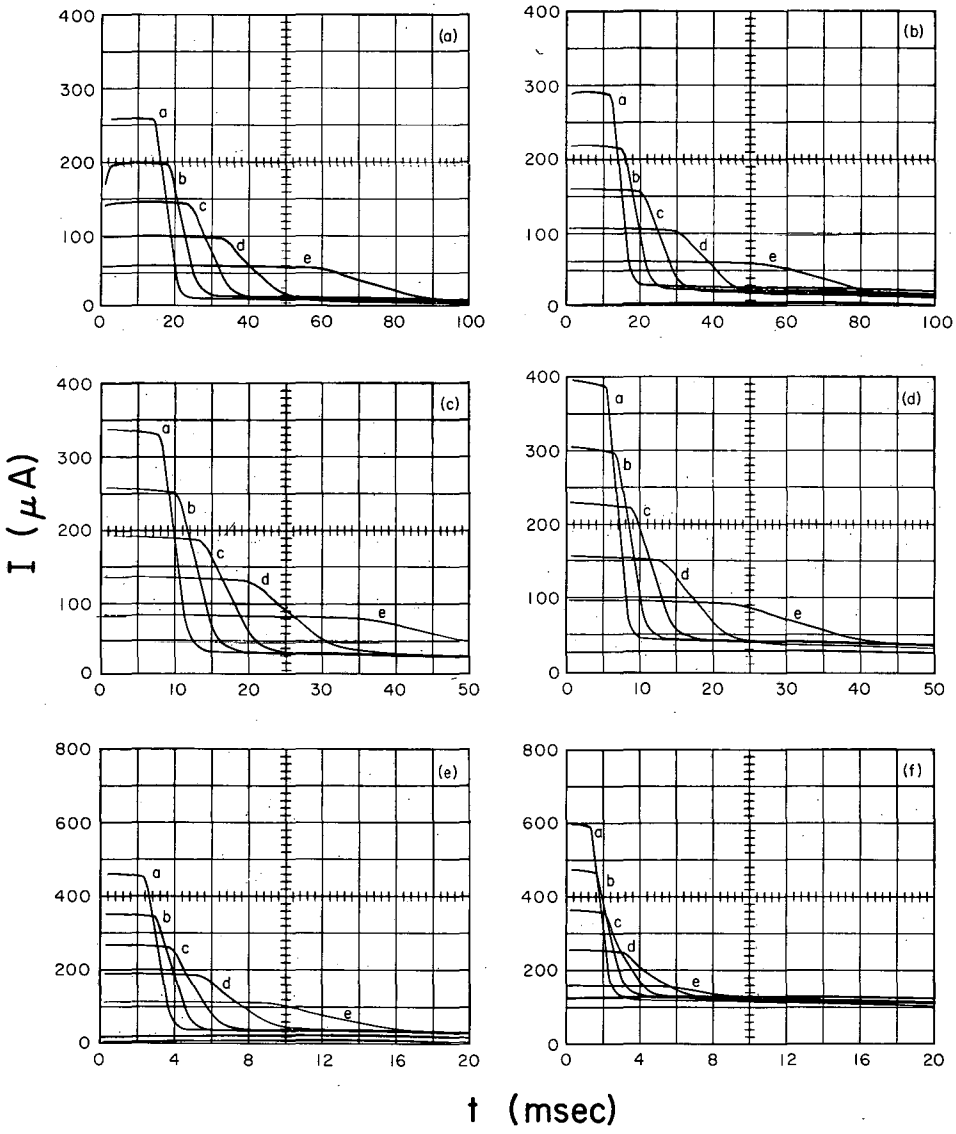

ZN-5123

Fig. IV.5

Further evidence of the space-charge hypothesis was not available until we obtained the (100) crystal data. Although we took over a hundred oscilloscope pictures, we include here only a representative sample, shown in Figs. IV.6 through IV.8. The data in Figs. IV.6 and IV.7 all have a common emitter temperature. In Fig. IV.6(a) the cesium flux n_o incident on the emitter is small enough that for the operating conditions the ion current predicted by Eqs. (IV-35) and (IV-36) is not space-charge-limited, and we observe the expected result (Fig. IV.3). In Figs. IV.6 (b), (c) and IV.7, photographed consecutively, n_o has been increased by about 2 orders of magnitude. The initial current in Fig. IV.6(b) has become space-charge-limited, according to Eq. (IV-43). Beyond the knee of the curve the surface concentration N(t) has decreased to the point that the current is limited no longer by space charge but by the surface evaporation of ions, and we should observe an exponential decrease in current. We notice, however, that the current first decreases through a transition region before assuming an exponential time dependence. Figure IV.6(c) showing the exponential part of Fig. IV.6(b) was obtained by delaying the oscilloscope trigger by about 300 μsec. The extent and slope of the transition region seemed to depend on the applied voltage and on the surface concentration as evidenced in Figs. IV.7(a) and (b) which simply show the effects of decreasing the attractive voltage. For low voltages the transition region completely masks the exponential time dependence. These effects are not understood and remain unexplained; we do not know if they are the result of experimental uncertainties or if they in fact represent the behavior of the evaporation process. The traces in Figs. IV.8(a) and (b) which were taken under different conditions than those of Figs. IV.6 and IV.7, are identical to each other

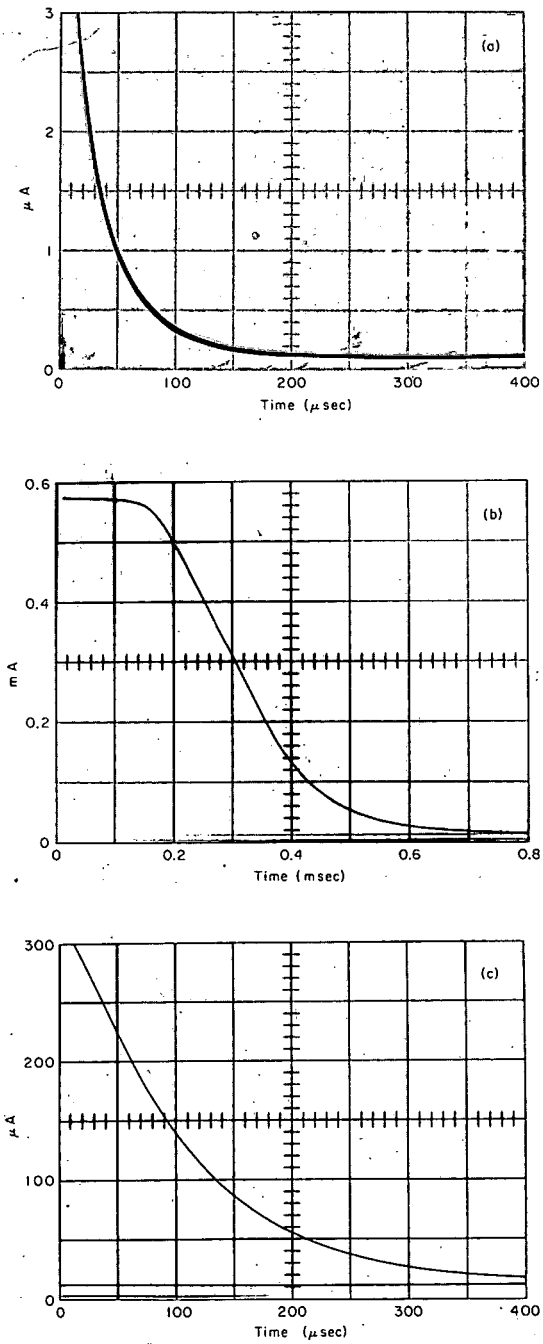

ZN-5146

Fig. IV.6

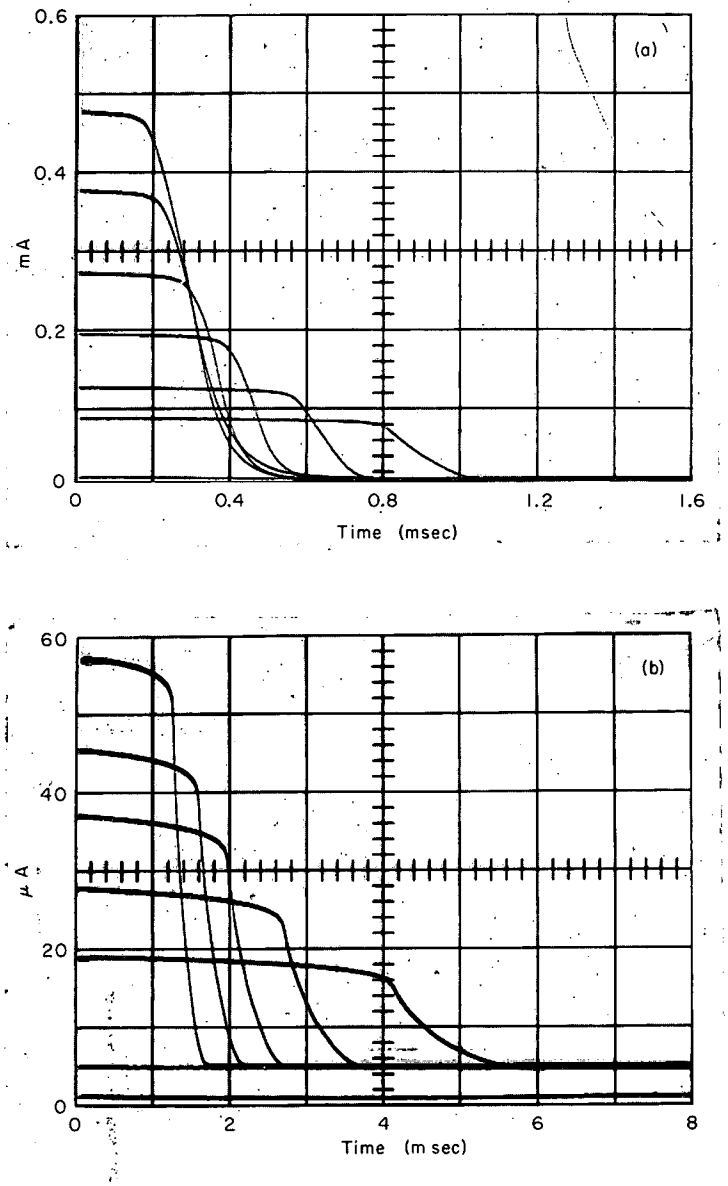
0.6
0.4
0.2
0
mA
(a)
0
0.4
0.8
1.2
1.6
Time (msec)
60
40
20
0
μA
(b)
0
2
4
6
8
Time (m sec)
ZN-5145

Fig. IV.7

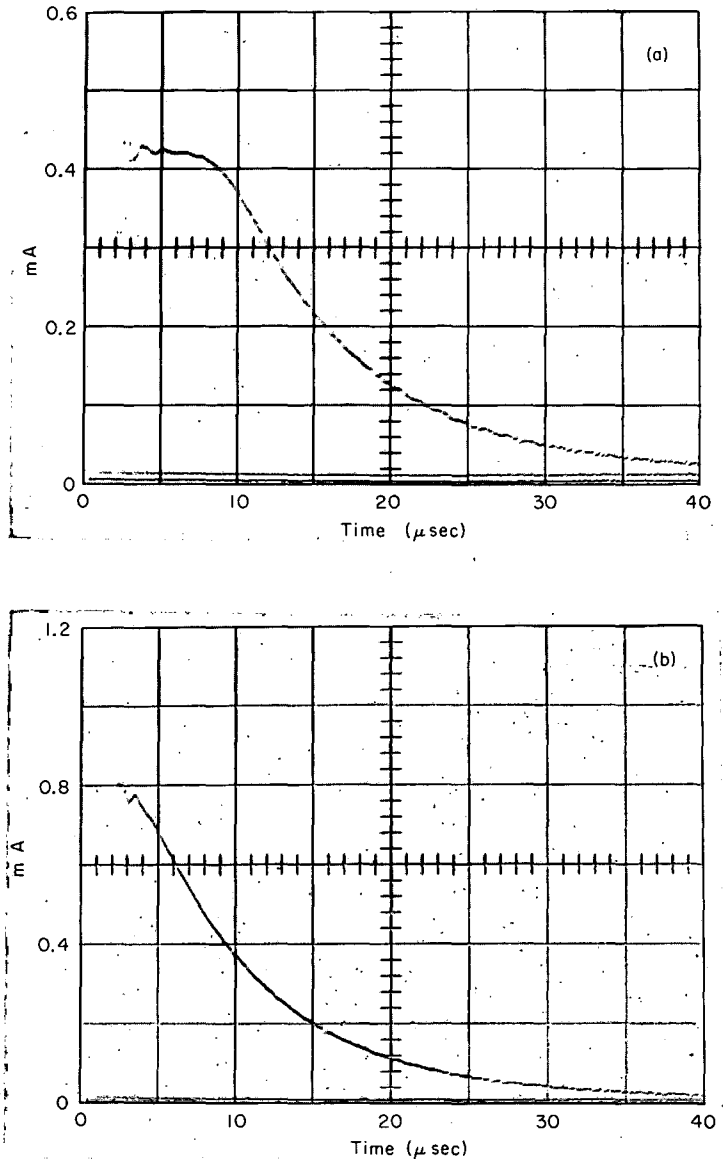
0.6
0.4
0.2
0
mA
(a)
0
10
20
30
40
Time (μsec)
1.2
0.8
0.4
0
mA
(b)
0
10
20
30
40
Time (μsec)
ZN-5147

Fig. IV.8

in all respects except for the interelectrode spacing. The ratio of the current plateaus is equal within 4% to the inverse ratio of the square of the spacings; this observation is an additional verification that the initial ion currents were space-charge limited according to Eq. (IV-43).

For the (100) crystal, one set of data was obtained with the cesium reservoir immersed in liquid nitrogen, and in ice water for another set. Figures IV.9 and IV.10 show some of the (apparent) ion-current-voltage curves that were measured during the two experiments. The vapor pressure of cesium at -196°C (temperature of liquid nitrogen) is so low that we could not hope to establish thermodynamic equilibrium between the cesium reservoir and the cesium vapor in the diode body. We expected therefore that the flux of cesium vapor incident on the emitter would be governed by the desorption rate of cesium from the body surfaces; and because the temperature of the diode body was affected by that of the emitter, we also expected to see an increase in the cesium flux with increasing emitter temperature. However, a comparison of the results for P_{ao} obtained at a cesium-reservoir temperature of -196°C with those determined at 0°C (for which we obtained reliable cesium-vapor flux measurements), indicates that the actual cesium current in Fig. IV.9 was in the range 10^{-8} to 10^{-7} ampere; and that the apparent increase with temperature was due to photoelectron emission from the collector. This deduction was consistent with order-of-magnitude calculations of the photoelectron contribution; it was also substantiated by consideration of the ionization coefficient β given by Eq. (IV-38). The factor $(1-\beta)$ determined experimentally should equal that from the Saha-Langmuir equation using the bare work function and operating temperature of the surface.

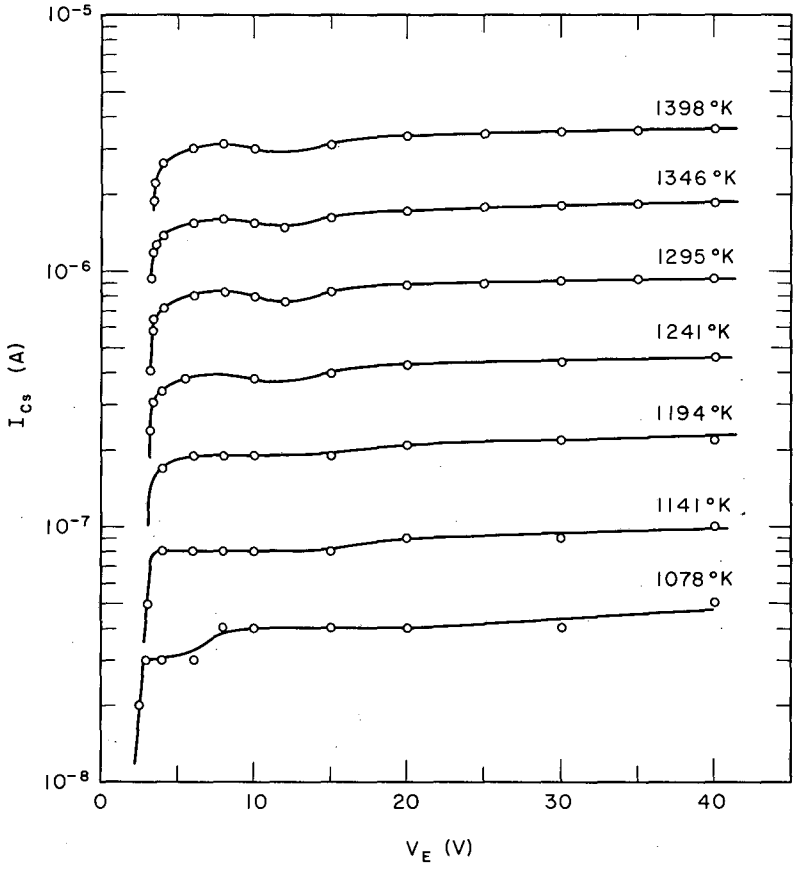
10^{-5}
10^{-6}
10^{-7}
10^{-8}
I_{Cs} (A)
1398°K
1346°K
1295°K
1241°K
1194°K
1141°K
1078°K
0
10
20
30
40
V_E (V)
MU-36616

Fig. IV.9

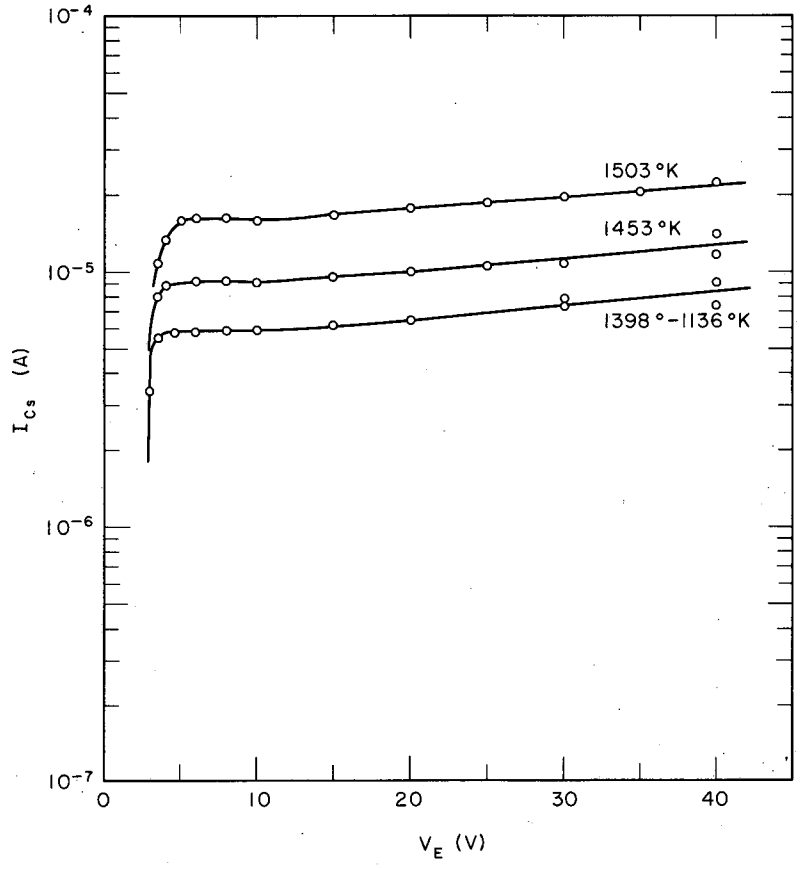
10^{-4}
10^{-5}
10^{-6}
10^{-7}
I_{Cs} (A)
1503 °K
1453 °K
1398 °-1136 °K
0
10
20
30
40
V_E (V)
MU-36615

Fig. IV.10

At high temperatures, we obtained experimental values of $(1 - \beta)$ on the order of 50% versus < 1% predicted, indicating that the apparent $J_{Cs}(\infty)$ was too high to be all cesium. Consequently we were not able to determine ϕ^*_{ao} for this set of data; but we did evaluate ϕ_{io} since the measurement of P_{io} is not influenced by any secondary electron emission.

The observed ion current in the experiment with the cesium reservoir at 0°C (Fig. IV.10) was constant in the emitter temperature range 1100 to 1400°K, and then increased with increasing emitter temperature. The best fit in the determination of ϕ^*_{ao} was obtained in this case by assuming that n_o was in fact equal to the observed positive current density, evaluated at the plateau lying between 5V and 10V. The increase in saturation ion currents with applied voltage evident in Fig. IV.10 will be discussed later in this subsection.

The space-charge limitation required a modification of the analysis derived in Sec. IV.B to determine the initial surface concentration N_o. To a first approximation N_o is equal to the area under the current trace. However, if the elapsed time to the knee of the curve is long, an appreciable fraction of the adsorbed cesium can evaporate as atoms and never be detected. The rate of change of surface concentration given by Eq. (IV-32) can be generalized as follows:

$$\frac{dN}{dt} = n_o - \frac{1}{e} J_{Cs}(t) - P_{ao} N(t). \qquad \text{(IV-44)}$$

We now approximate the shape of the oscilloscope traces in Fig. IV.7 as follows: Let

$$J_{Cs}(t) = J_{Cs}(0), \; 0 < t < t_o, \qquad \text{(IV-45)}$$

where $J_{Cs}(0)$ is the average value of the current plateau and t_o is the elapsed time at the knee of the curve. And let

$$J_{Cs}(t) = J_{Cs}(\infty) + [J_{Cs}(0)-J_{Cs}(\infty)] \exp[-P(t-t_o)],\ t_o < t < \infty. \quad \text{(IV-46)}$$

A second-order approximation to the solution of Eqs. (IV-44) through (IV-46), derived in Appendix N, is

$$N_o = \frac{n_o}{P_{ao}} = \frac{J_{Cs}(\infty)}{eP_{io}} + \frac{1}{e}\int_0^\infty [J_{Cs}(t)-J_{Cs}(\infty)]\,dt + \frac{t_o}{2e}[J_{Cs}(0)-J_{Cs}(\infty)][P_{ao}t_o + \frac{1}{3}(P_{ao}t_o)^2]. \quad \text{(IV-47)}$$

The first term on the right side of the equation represents the final, equilibrium, surface concentration after the field reversal and is practically negligible. The integral is the net number of ions removed from the surface. The last term represents the net number of atoms that evaporate from the surface during time t_o; it was normally only a few percent of the integral and at most 15%, hence, P_{ao} could be evaluated in one or two iterations. A final term representing the net removal of atoms after time t_o was negligible and was therefore omitted. The integral was evaluated by means of a planimeter on enlarged photographs of the oscilloscope traces. This procedure was more accurate than the analytic evaluation of the integral obtained from our model [Eqs. (IV-45) and (IV-46)].

The analysis of all the data obtained for both the (110) and (100) crystals has been summarized in Tables O.I through O.IV of Appendix O. Let us consider the results of the (100) crystal first. Figure IV.11 is a plot of P_{ao} versus applied emitter voltage V_E. We can find no explanation for the variation of P_{ao} with applied voltage, unless this effect is due to emission of secondary electrons or cesium-atoms from the collector by ion impact. The probability P_{ao} is inversely proportional to the

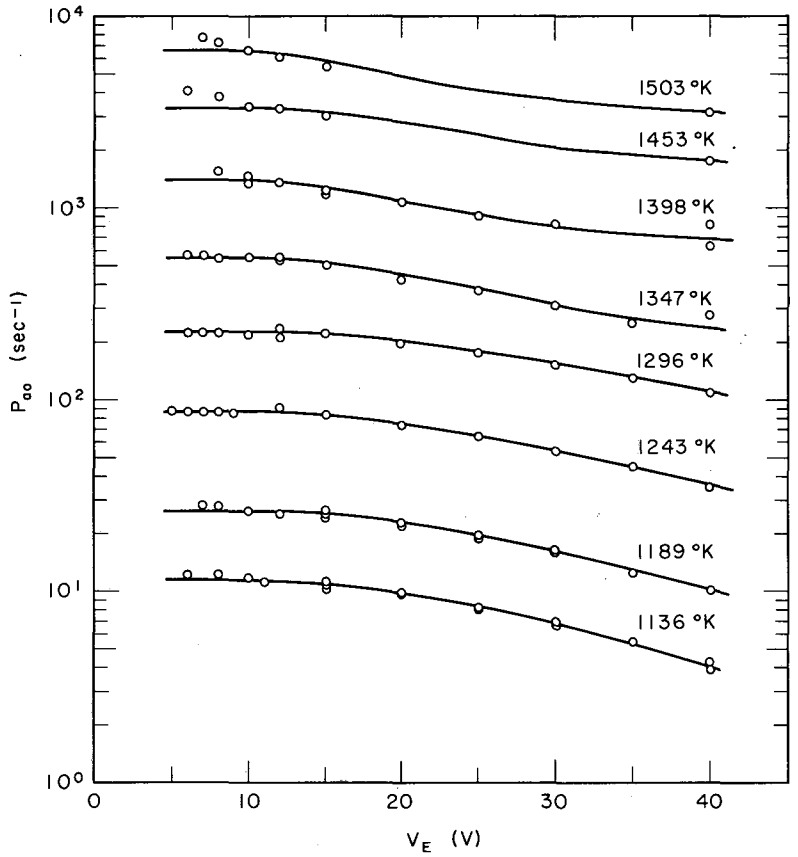
10^4
10^3
10^2
10^1
10^0
P_{ao} (sec^{-1})
1503 °K
1453 °K
1398 °K
1347 °K
1296 °K
1243 °K
1189 °K
1136 °K
0
10
20
30
40
V_E (V)
MU-36614

Fig. IV.11

initial surface concentration N_o, which we measure essentially by integrating the ion current. Therefore, if electrons are emitted from the collector in numbers proportional to the ion current, they will contribute positively to the time integral of the measured current pulse; and we will obtain an erroneously high value of N_o and consequently a low value of P_{ao}, as determined by the ratio n_o/N_o, where n_o was assumed to be characterized by the value of the saturation ion-current between 5 and 10V (Fig. IV.10). Should the secondary electron emission increase with ion energy, we would then have a reasonable explanation for the voltage dependence shown in Figs. IV.10 and IV.11. We have to date found very little reliable work in the open literature with which to verify this postulate. Hagstrom, in studying secondary electron emission from metals by low-energy ion impact, has found that such a phenomenon (called Auger, or potential, ejection of electrons) is possible only if the work function of the metal is less than half of the ionization potential of the ion.[91,37,38] This condition was satisfied in our experiment since our collector surface was essentially cesium, $\phi_c \approx 1.9$ eV, and the ionization potential of cesium is 3.9 V. However, Hagstrom found the secondary-electron yield rather small, 25% for helium on tungsten and 4% for xenon on tungsten, and also independent of ion energy in the range 0 to 1 keV. Bosch and Kuskevics found that the secondary ejection of electrons from tungsten by high-energy (1 to 21 keV) cesium ions increases with surface coverage of cesium.[10] Arifov and Aiukhanov studied the secondary ion and electron emission from tantalum, tungsten, and molybdenum targets under bombardment by alkali ions, including cesium ions, in the energy range 150 to 1000 eV.[2] They observed the secondary electron yield on clean surfaces to be very small (< 1%), as predicted by Hagstrom, but

that the yield could increase to 30 to 40% for surfaces contaminated by alkali atoms. Although this evidence does not positively verify the possibility of secondary electron emission by ion bombardment in our experiment, it certainly does not rule it out.

Another possible and perhaps more plausible explanation of our result is that the ions from the emitter sputter cesium atoms off the collector surface and that these atoms then contribute to the flux of cesium incident on the emitter. Airfov, in the experiment mentioned above and in others,[3,4] studied the scattering of alkali ions from metal surfaces. He found, for example, that the yield of scattered cesium ion on nickel reaches a maximum of 90% at 40 eV and then decreases rather sharply. He measured indirectly the neutralization coefficient K_o (defined as the number of incident ions neutralized per incident ion on target) for 560-eV cesium ion incident on a tungsten target contaminated with adsorbed cesium atoms, and found it to be $\approx$ 80%. Unfortunately, he did not determine whether the neutralized cesium ions condensed on the surface, were ejected from it, or both. However, he later measured the energy distribution of the ejected cesium atoms and found it to be essentially the same as that of the scattered ions.[5] This would indicate that if not all, at least some of the neutralized ions are ejected.

Veksler, in studying the scattering of cesium and rubidium ions from a molybdenum surface in the energy range 10 to 250 eV, found that where adsorbed layers are present on the target surface, the sputtered adsorbed atoms are the main component of secondary-ion emission.[92] He observed that the secondary-ion-emission yield increased with the energy of the incident ion and reached a saturation value of about 50% at around 80 eV, indicating that for higher energies the incident ions begin to penetrate into the target. He did not measure the yield of secondary atom emission on clean

or cesiated surfaces but perhaps we could expect similar results. Bradley studied sputtering of sodium and potassium surfaces by inert gas ions in the energy range 0 to 1800 eV.[11] Although he was able to measure only relative yields of sputtered atoms (number of sputtered atoms reaching detector per positive ion incident on target), he estimates that the absolute yield could be as large as 30% for xenon on potassium at about 100 eV.

Here again we have found in the literature only sketchy evidence, much of it self contradictory, that our proposed sputtering phenomenon is possible. We must now find additional confirmation from our own results.

We have presented two possible schemes that could explain the variation of P_{ao} with applied voltage; let us now consider what effect they might have on the variation of P_{io}. The Auger ejection of electrons should not influence our determination of P_{io} at all. The observed currents will simply increase by a constant of proportionality. On the other hand, sputtering of cesium atoms from the collector will reduce both P_{ao} and P_{io}, because the rate of change of surface concentration becomes

$$\frac{dN}{dt} = n_o - PN + \gamma P_{io} N = n_o - (P - \gamma P_{io})N \approx n_o - P_{io}(1-\gamma)N, \quad \text{(IV-48)}$$

where γ is the number of sputtered atoms per ion incident on the collector (because of the geometry of our experiment we have essentially a 100% collection efficiency of sputtered atoms to the emitter). We see that the observed ion-evaporation rate is $P_{io}(1-\gamma) < P_{io}$. It should be obvious from Eq. (IV-48) and the analysis of Sec. IV.B that the observed P_{ao} also will be reduced by $(1-\gamma)$. Figure IV-12 shows the dependence of P_{io} on applied voltage. The decrease of P_{io} with increasing applied field definitely supports the sputtering theory, especially when in the absence

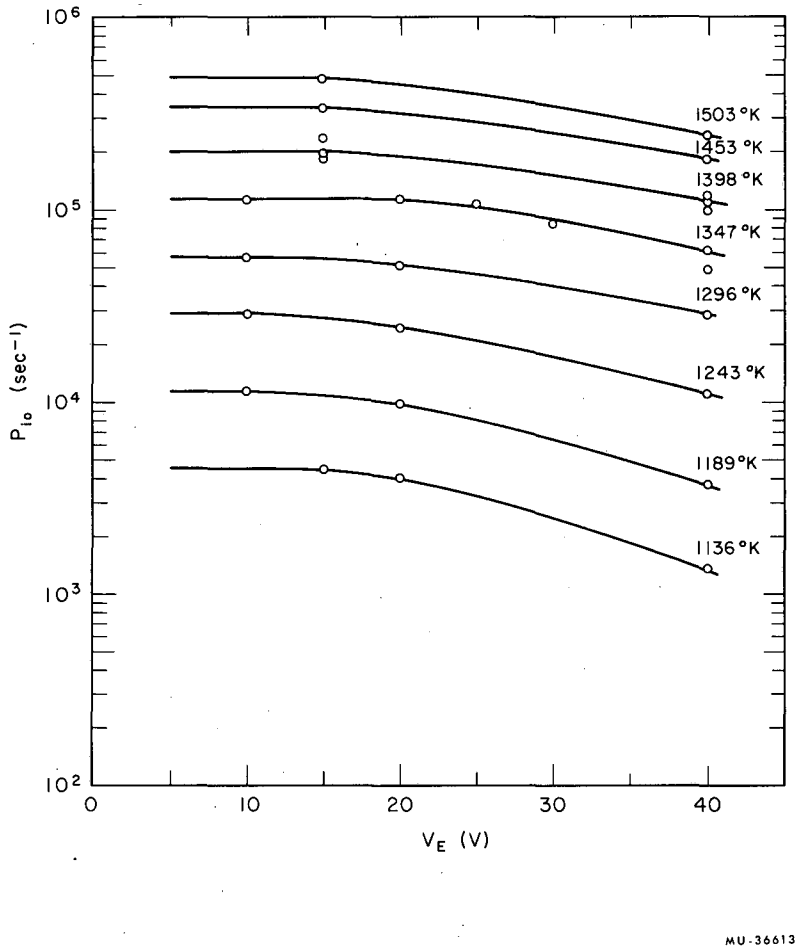
10^6
10^5
10^4
10^3
10^2
P_{io} (sec^{-1})
0
10
20
30
40
V_E (V)
1503 °K
1453 °K
1398 °K
1347 °K
1296 °K
1243 °K
1189°K
1136 °K
MU-36613

Fig. IV.12

of any sputtering P_{io} should have increased a little, if anything, with applied field, due to the Schottky effect at the emitter surface.

In Figs. IV.13 and IV.14 we have plotted log P_{io} vs $1/T_E$ for the experiments with the cesium reservoir at -196 and 0°C, respectively. Figure IV.13 is a plot of the maximum values of P_{io}, obtained for an applied voltage of 10 to 15V. The top line in Fig. IV.14 was plotted from data obtained at 15 to 20V, because although we obtained scope traces for lower voltages these traces did not exhibit an exponential decay rate; the bottom line in Fig. IV.14 is a plot of log P_{io} (40V). The deviation of the high-temperature data points is due to experimental uncertainties associated with the test-circuit time constant which was on the order of a few μsec. Figure IV.15 shows a plot of log P_{ao} vs $1/T_E$. The top line was plotted from the values of the curves in Fig. IV.11 evaluated at 10V; the deviation of the low-temperature datum point reflects the effect of cesium surface coverage, which was beginning to become appreciable (≈ 1%). The bottom line is a plot of log P_{ao}(40V). The range of surface coverage of cesium within which the ion heat-of-evaporation data points were measured was 5×10^{8} to 7×10^{11} atoms/cm^2. The latter concentration corresponds to about 0.2% of a monolayer. The range of surface coverage within which the atom heat of evaporation was evaluated was 2×10^{10} to 4.5×10^{12} atoms/cm^2, or a maximum of about 1% of a monolayer. From the slope and intercept of the top lines of Figs. IV.13 to IV.15, we obtain the following results for the (100) crystal:

cesium reservoir at -196°C experiment

$$\phi_{io} = 2.07\pm0.06 \text{ eV}$$

$$Q_{io} = 6.6\pm4.0\times10^{12} \text{ sec}^{-1},$$

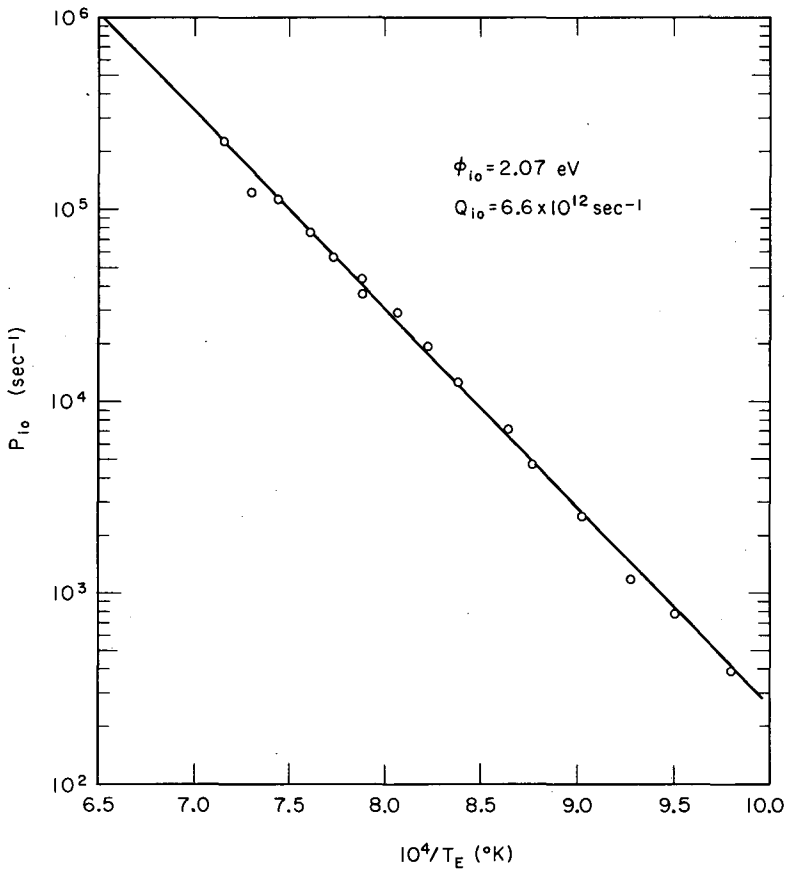
10^6
10^5
10^4
10^3
10^2
P_{io} (sec^{-1})
ϕ_{io} = 2.07 eV
Q_{io} = 6.6 x 10^{12} sec^{-1}
6.5
7.0
7.5
8.0
8.5
9.0
9.5
10.0
$10^4/T_E$ (°K)
MU-36618

Fig. IV. 13

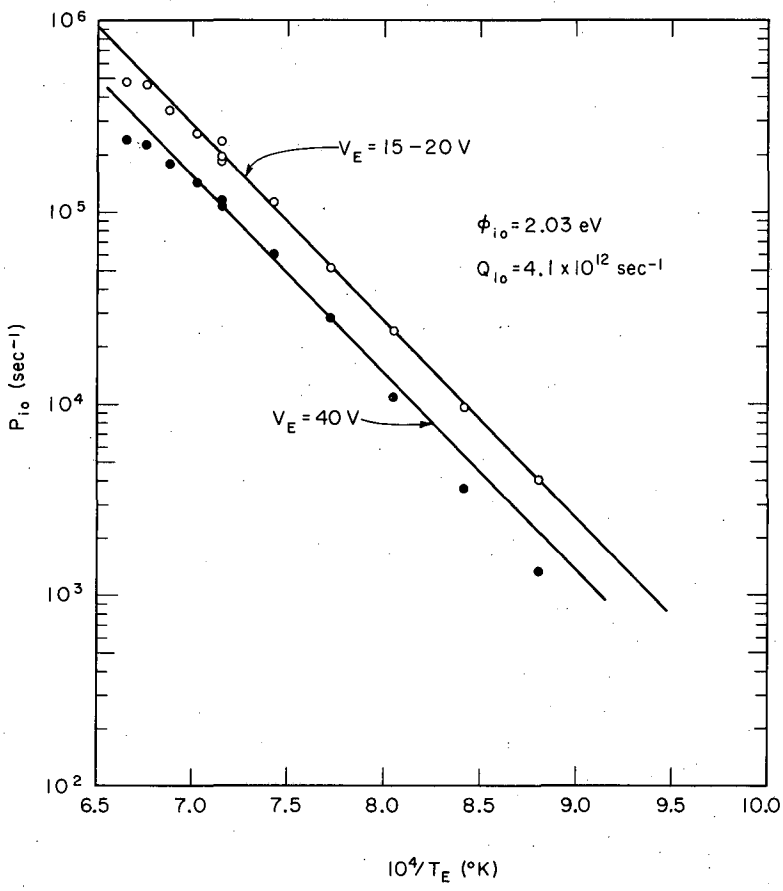
10^6
10^5
10^4
10^3
10^2
P_{io} (sec^{-1})
V_E = 15 – 20 V
ϕ_{io} = 2.03 eV
Q_{io} = 4.1 x 10^{12} sec^{-1}
V_E = 40 V
6.5
7.0
7.5
8.0
8.5
9.0
9.5
10.0
$10^4/T_E$ (°K)
MU-36619

Fig. IV. 14

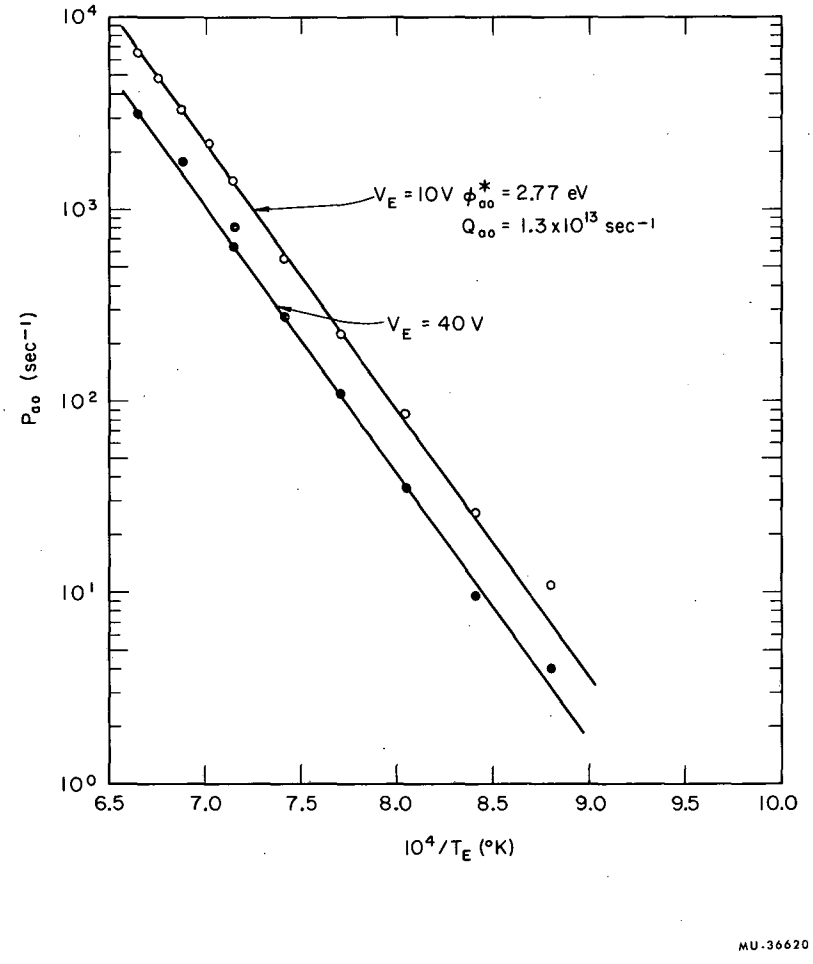
10^4
10^3
10^2
10^1
10^0
P_{ao} (sec^{-1})
V_E = 10V ϕ^*_{ao} = 2.77 eV
Q_{ao} = 1.3x10^{13} sec^{-1}
V_E = 40 V
6.5
7.0
7.5
8.0
8.5
9.0
9.5
10.0
$10^4/T_E$ (°K)
MU-36620

Fig. IV.15

cesium reservoir at 0°C experiment

$$\phi_{io} = 2.03 \pm 0.07 \text{ eV}$$

$$Q_{io} = 4.1 \pm 3.0 \times 10^{12} \text{sec}^{-1}, \text{ and}$$

$$\phi^{*}_{ao} = 2.77 \pm 0.05 \text{ eV}$$

$$Q_{ao} = 1.3 \pm 0.8 \times 10^{13} \text{sec}^{-1} .$$

The value of Q_{io} in the cesium reservoir at 0°C experiment is a little low because it comes from a plot of P_{io} (15 to 20V), which is already slightly influenced by the effect of the applied voltage. We believe then that the higher value of Q_{io} (in the experiment with the cesium reservoir at -196°C) is more accurate; whereas the average of the values of ϕ_{io} for the two experiments probably best represents the cesium-ion desorption energy for the (100) crystal. In other words,

$$\phi_{io} = 2.05 \pm 0.05 \text{ eV} \; ; \quad Q_{io} = 6.6 \pm 4.0 \times 10^{12} \text{ sec}^{-1}$$

represent our best estimate of the cesium-ion desorption properties for the (100) crystal.

The values for ϕ_{io} and Q_{io} in the cesium reservoir at -196°C experiment were determined by the method of least squares and the errors listed for these quantities are equal to twice the standard deviation of the mean. The other values listed above and their associated errors were estimated graphically. We estimate that the errors listed are larger than any reasonable random or systematic instrumental errors. The time base of the oscilloscope was calibrated within 2% on every time scale and this calibration was photographically recorded so that the data could be (and were) corrected for systematic errors within this 2%. The vertical deflection (current) of the oscilloscope was calibrated within 3%. An error in the time base calibration is essentially the only instrumental

error that affects the determination of P_{io}; whereas the determination of P_{ao} is affected in addition by instrumental errors in the measurement of current; although it is not affected by a systematic current-measurement error that is directly proportional to the value of the current. The determination of ϕ_{io} and ϕ_{ao} from the slope of Arrhenius plots of P_{io} and P_{ao} are independent of a systematic error in the absolute temperature resulting from uncertainties in emissivity or window absorptivity, because such an error is a constant error in $1/T_E$ and therefore does not affect the slope of the Arrhenius plots. The determinations of Q_{io} and Q_{ao}, on the other hand, are very sensitive to errors in absolute temperature, and it is conceivably possible that our values for Q_{io} and Q_{ao} contain such an error, which, judging from the somewhat high values for the Richardson constants A that we obtained in Sec. III, might make our calculated values for Q_{ao} and Q_{io} correspondingly high also (assuming that a slight temperature error did exist and was in fact responsible for the high values of the Richardson constants).

According to the sputtering argument we would expect the yield γ at constant voltage to be a function of the collector surface properties only, and hence the plots of log P_{ao} (40V) and log P_{io} (40V) versus $1/T_E$ should be straight lines parallel to those obtained at 10V. Such parallel lines have been fitted to the 40-V data in Figs. IV.14 and IV.15. The agreement is very good for P_{ao}(40V) but not quite as good for P_{io} (40V), where a line of slightly steeper slope would give a better fit.

The yield γ of sputtered atoms is given by the relation

$$\gamma(V) = 1 - \frac{P_{io}(V)}{P_{io}} \leq 1 - \frac{P_{ao}(V)}{P_{ao}} \quad . \qquad \text{(IV-49)}$$

The inequality arises because secondary electron emission from the collecto

would contribute to the apparent decrease in $P_{ao}(V)$.

Figure IV.16 is a plot of the sputtered-atom yield versus the interelectrode potential [obtained by subtracting the contact potential ($\approx$ 3V) from the applied voltage]. The plot was calculated from the data of Figs. IV.11 and IV.12 by averaging the ratios $P_{io}(V)/P_{io}(10V)$ and $P_{ao}(V)/P_{ao}(10V)$ over all temperatures and substituting this average in Eq. (IV-49). The agreement between the ion- and atom-evaporation data is remarkable; it indicates that the contribution of secondary electron emission was fairly small; otherwise the variation of P_{ao} with applied voltage would have been much greater than that of P_{io}.

We end our discussion of sputtering with the remark that evidently this heat-of-evaporation experiment can be extended to a study of the sputtering of alkali metal surfaces, or surfaces with adsorbed alkali atoms, under bombardment by ions of their own vapor. The possible emission of secondary electron could be avoided either by applying the proper magnetic field or by inserting a grid between the electrodes.

The difference between the heats of evaporation of atoms and ions should, according to Eq. (IV-17), equal the difference between the bare work function of the surface and the ionization potential of the vapor. From our results of the (100) crystal we obtain

$$\phi^{*}_{ao} - \phi_{io} = 2.77 - 2.05 = 0.72 \text{ eV};$$

this is to be compared with the bare work function obtained in Sec. III and the ionization potential of cesium,[21]

$$\phi_{o} - V_{i} = 4.65 - 3.89 = 0.76 \text{ eV}.$$

The agreement is within our experimental error. In addition we obtained

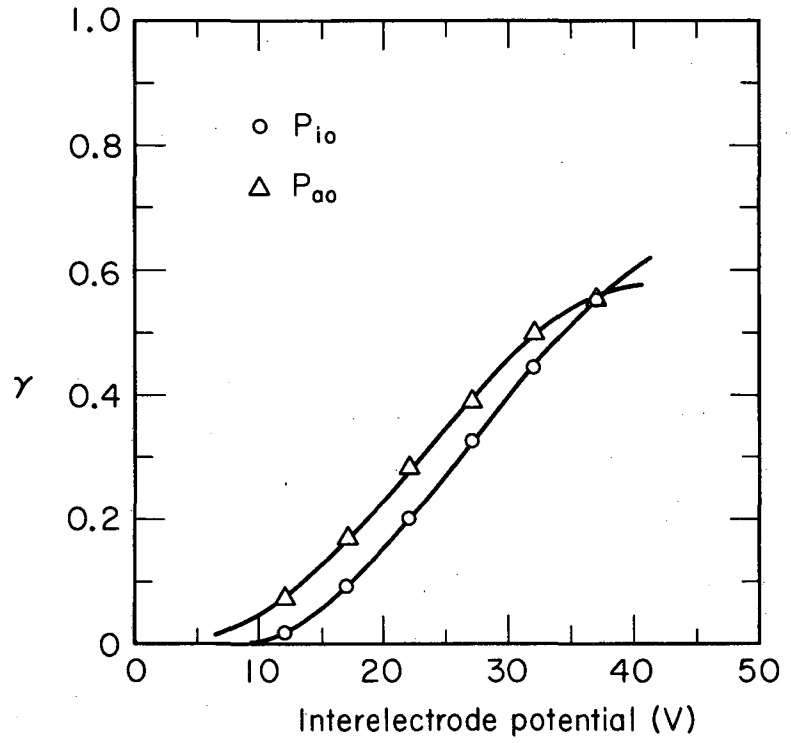

MU-36604

Fig. IV.16

$$\frac{Q_{io}}{Q_{ao}} = \frac{6.6\times10^{12}}{1.3\times10^{13}} = \frac{1}{2},$$

in agreement (fortuitous in view of the large experimental uncertainty in this ratio) with the theoretical value of 1/2.

Our results for the (110) crystal (Table O.I in Appendix O) are unfortunately not as good, primarily because the surface coverage of cesium was large enough to influence the evaporation rates that we measured. Although the cesium reservoir was immersed in liquid nitrogen, the observed flux of cesium vapor incident on the emitter was larger than that observed in the (100) diode operating with the cesium reservoir at 0°C. We observed also that the cesium flux was strongly influenced by the temperature of the diode body. We are quite sure therefore that our determination of the cesium flux n_o incident on the emitter was not measurably affected by photoelectric emission of electrons from the collector. The high value of the flux of cesium vapor in the (110) diode as compared to that in the (100) diode operating under similar condition was due to the fact that the inside diameter of the tube connecting the cesium reservoir to the diode was 1/8 in. in the (110) diode versus 1/2 in. in the (100) diode. Therefore the condition of non thermodynamic equilibrium between the reservoir (at -196°C) and the diode body was much worse in the(110) than in the (100) diode.

The atom heat-of-evaporation data were obtained at a surface coverage that varied between 5×10^{12} and 3×10^{13} atoms/cm^2. These concentrations correspond to a range of about 1 to 10% of a monolayer. The ion heat-of-evaporation data were evaluated at surface concentrations about one twentieth of these. In either case the coverage was sufficient to influence our determination of P_{io} and P_{ao}. The applied voltage dependence

of P_i and P_a were qualitatively similar to that of the (100) crystal experiments, that is, both decreased with increasing voltage. The scatter in the evaluation of P_{io} was too great to make this data meaningful. The atom evaporation rate is shown in Fig. IV.17, a plot of log P_{ao} versus $1/T_E$. The line is a least-squares fit of the 18-V data, with a slope and intercept corresponding to

$$\phi_{ao} = 2.14 \pm 0.2 \text{ eV}$$
$$Q_{ao} = 2 \times 10^9 \text{ sec}^{-1}$$

where the error is equal to two standard deviations of the mean. Both of these values are too low to be representative of the crystal surface and serve to indicate that the data points in Fig. IV.17 are not values of P_{ao} but rather of $P_a^*(\theta)$ as defined in Eqs. (IV-28) and (IV-29). So the correct way to analyze these data is to solve Eq. (IV-29) for $\phi_a^*(\theta)$ at each observed value of T_E and θ and extrapolate the variation of $\phi_a^*(\theta)$ versus θ to $\theta = 0$,

$$\phi_a^*(\theta) = kT_E \left[\ell n \, K'(\theta) \, Q_{ao} - \ell_n \, P_a^*(\theta) \right], \qquad \text{(IV-50)}$$

where we have assumed $\omega = \omega_o$ ($Q_{ao} = \omega_o \, g_a = 2\omega_o$). Table IV.I shows the result of such a calculation for the 12.5V data points which were intermediate between the 18 and 7.5 data points. Theta was calculated by dividing our measured surface concentrations by the value 4.8×10^{14} atom/cm^2 which is the concentration of a monolayer of cesium on polycrystalline tungsten measured by Taylor and Langmuir [using instead the theoretical value for (110) tungsten of 3.5×10^{14} atom/cm^2 does not appreciably affect the end result]. The value of $\ell n \, K'(\theta)$ in the range of θ shown is negligibly small and was omitted. The value of Q_{ao} was assumed to be that determined for the (100) crystal, that is

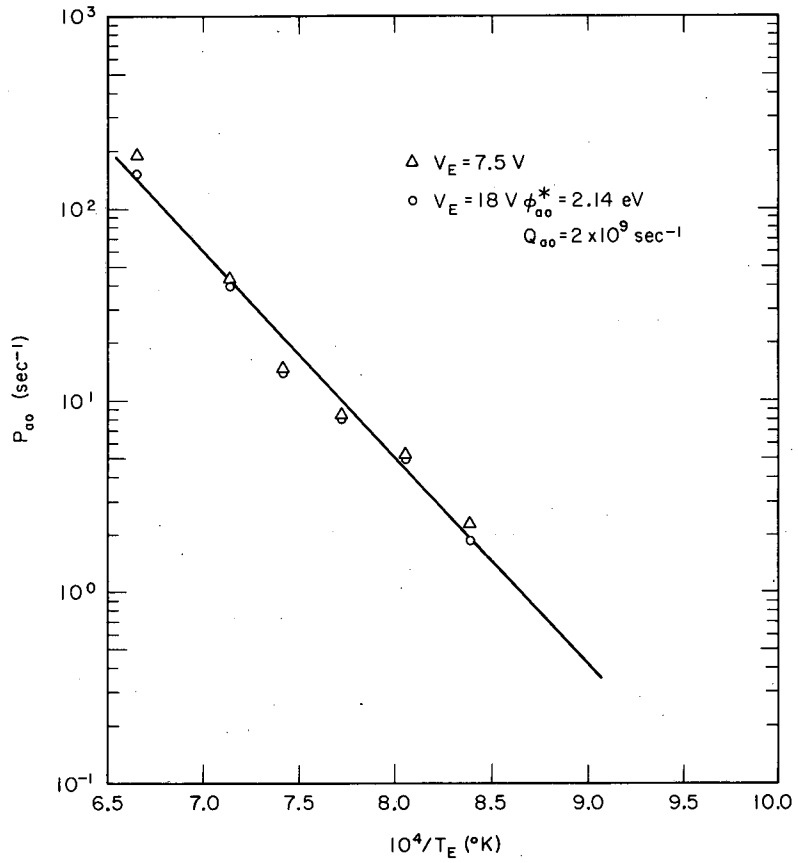
10^3
10^2
10^1
10^0
10^{-1}
P_{oo} (sec^{-1})
△ V_E = 7.5 V
○ V_E = 18 V ϕ^*_{oo} = 2.14 eV
$Q_{oo} = 2 \times 10^9$ sec^{-1}
6.5
7.0
7.5
8.0
8.5
9.0
9.5
10.0
$10^4/T_E$ (°K)
MU-36617

Fig. IV.17

$Q_{ao}(110) = Q_{ao}(100) = 1.3\times10^{13}\,sec^{-1}$. This assumption will be justified below.

Table IV.I. Atom desorption energy $\phi_a^*(\theta)$ versus surface coverage θ for the (110) crystal, V_E = 12.5V.

Fig. IV.5 no.	T_E (°K)	θ (%)	$P_a^*(\theta)$ (sec^{-1})	$\phi_a^*(\theta)$ (eV)
(a)	1193	7.0	2.06	3.04
(b)	1242	7.0	5.07	3.06
(c)	1295	5.3	8.33	3.14
(d)	1348	4.3	14.7	3.19
(e)	1399	2.4	42.3	3.19
(f)	1503	1.7	173	3.25

The extrapolation of $\phi_a^*(\theta)$ to $\theta = 0$ yields the value

$$\phi_{ao}^*(110) = 3.28\pm0.03 \text{ eV}$$

where the error is a graphical estimation of the scatter in the data.

We justify the assumption that $Q_{ao}(110) = Q_{ao}(100)$ on the basis of the theoretical work of Levine and Gyftopoulos.[59,35] According to their analysis the vibrational frequency of a cesium atom adsorbed on a tungsten surface is given by

$$\omega_o = (1/2\ \pi\ R \cos\beta)[\phi_{ao}^*\ (m_f + 4m_m)/2m_f m_m]^{1/2}\ , \qquad \text{(IV-51)}$$

where m_f and m_m are the masses of cesium and tungsten atoms, R is the interaction distance between the adsorbed cesium and tungsten surface (sum of the covalent radii of cesium and tungsten) and

$\cos \beta = (1 - 1/2\ \sigma_m R^2)^{1/2}$, where σ_m is the surface density of tungsten atoms. According to Eq. (IV-51) then

$$\frac{\omega_o\ (110)}{\omega_o\ (100)} = [\cos \beta\ (100)/\cos \beta\ (110)][\phi^*_{ao}(110)/\phi^*_{ao}(100)]^{\frac{1}{2}} \quad \text{(IV-52)}$$

They estimate that $\cos \beta\ (110) = 0.86$, $\cos \beta\ (100) = 0.79$. Substituting these values and our results for the atom desorption energies, we obtain

$$\frac{\omega_o(110)}{\omega_o(100)} = (0.79/0.86)(3.28/2.79)^{1/2} = 1.0\ ,$$

in agreement with our assumption.

We can estimate $\phi_{io}(110)$ from our value for the (110) crystal work function, obtained in Sec. III. At 1600°K (100°K above the maximum temperature in this experiment) the crystal surface was slightly contaminated and had a work function $\phi_o = 5.11$ eV (Table III.II), so

$$\phi_{io} = \phi^*_{ao} + V_i - \phi_o = 3.28+3.89 - 5.11 = 2.06 \text{ eV}\ .$$

This result is essentially identical with the measured ion desorption energy for our (100) crystal and for polycrystalline tungsten obtained by several investigators.[88,79] It appears therefore that the cesium-ion desorption energy is independent of the crystallographic orientation and exact state of cleanliness of tungsten surfaces. On this basis it may be reasonable to conclude that the atom-desorption energy for our (110) crystal, when clean ($\phi_o = 5.33$ eV), is

$$\phi^*_{ao}[\text{clean } (110)] = 3.28 + (5.33 - 5.11) = 3.50 \text{ eV}\ .$$

We conclude this discussion of our experimental results by remarking that, based on our experience, the method for measuring cesium desorption energies used in our investigation can probably be applied to the study

of the variation of cesium (or other alkali metals) - atom desorption energy with surface coverage. The range of surface coverage in such a study would be limited by the condition $P_i(\theta) \geq P_a(\theta)$.

E. Comparison with the Literature

The desorption of cesium from a hot tungsten surface was first studied in the twenties by Langmuir et al.[56,88] and by Becker.[7] In their experiments, a tungsten filament was exposed to a controlled cesium vapor. The concentration of cesium on the filament surface was measured by flashing the filament to a high temperature, thus driving off all the absorbed cesium as a detectable pulse of ions, or by measuring the time needed to readsorb cesium, after flashing, to a pre-existing surface concentration.

Then came the work of Evans,[29,30] who studied the desorption of cesium on tungsten by the technique of Moon and Oliphant[65] as described in Sec. IV.B.

More recent studies have been performed with pulsed or modulated beams of cesium ions or molecules.[54,79,72]

There have been a few qualitative studies on hemispherical or filament single crystals of tungsten.[45,61,86] Since we have not found in the literature any quantitative experiments on the desorption rates of cesium from tungsten single crystals, we can only compare our results for polycrystalline tungsten with those of others. Table IV.II shows a comparison between our results and those of some of the investigations mentioned above. Our studies covered a wider and higher temperature range than most of the studies shown here. The considerable spread in the data is probably a result of the varying surface conditions at which the experiments were done, as demonstrated by Scheer and Fine.[79] However, the properties of the contaminated surface listed in their study were evaluated from the slope and intercept of an Arrhenius plot of the evaporation probability (as were most of the results listed in Table IV.II).

Table IV.II. Heat of evaporation of cesium ions and atoms on tungsten.

Investigator	ϕ_{io}(eV)	Q_{io}(sec^{-1})	ϕ^*_{ao}(eV)	Q_{ao}(sec^{-1})	Method
Langmuir et al.[88](1923-33)	2.04		2.79	2.3×10^{12}	Flashing filament in Cs vapor (≈ 300° to 1200°K)
Evans[29](1933)	1.81	1.2×10^{10}			Steady ionic and molecular beam, reversing electric field (930° to 1025°K)
Knauer[54](1948)	3.60	2.2×10^{16}			Pulsed molecular beam (1300° to 1520°K)
Scheer and Fine[79](1962)					
Clean surface	2.04	1.0×10^{12}			Pulsed molecular beam (1070° to 1200°K)
Contaminated surface	1.55	1.7×10^{10}			(950° to 1130°K)
Swanson et al.[86](1964)			3.0		Field emission, using Langmuir data to calculate θ from $\phi(\theta)$ (725° to 975°K)
Perel et al.[72](1965)	~1.5	$\approx10^{8}$			ac Modulated molecular beam (925° to 1275°K)
This study, (100)W	2.05	6.6×10^{12}	2.77	1.3×10^{13}	Reversing electric field in Cs vapor (1020° to 1500°K)
(110)W[a]	2.06		3.28	1.3×10^{13}	

a. The (110) crystal surface was slightly contaminated and had a work function of 5.1 eV instead of the clean surface value of 5.33 eV.

Such a procedure can only yield valid results if the surface properties are temperature independent, a condition which is generally not met for contaminated surfaces. A more realistic way of analyzing such data is to assume a constant value for the oscillation frequency Q_i (equal to the value Q_{io} for the clean surface for example, since the frequency is a relatively insensitive function of the surface condition) and evaluate the desorption energy ϕ_i as a function of temperature. Applying this methodology to the contaminated data of Scheer and Fine, one finds that the ion desorption energy decreased with temperature from 1.95 to 1.85 eV over the temperature range of their measurement. This interpretation of their data indicates that the effect of contamination is much less than one is led to believe from their tabulated results.

Perel et al.[72] admit in their paper that they took no special precautions to ensure cleanliness of their surface and neither did we, except to heat the emitter above 1900°K before each set of data was taken. Knauer's results are unreasonably high;[54] he admits that they are not reliable because of large uncertainties in the measurement of the target temperature. In addition, it seems probable from his paper that his vacuum conditions were questionable and that the surface concentration of cesium on the target was large enough to affect his results over part of the temperature range.

Levine and Gyftopoulos have made an extensive theoretical study of the adsorption physics of metal surfaces covered by metallic particles.[58,59,60,35] As part of this work they have evaluated the desorption energies of alkali atoms for bare and partially covered metal surfaces, including tungsten. Their calculations, which are presented in considerable detail in Sec. VI, are based on the assumptions that the adsorbed particles consist of single

species (as opposed to atoms and ions) held onto the surface by bonds that are partially ionic and partially covalent. They expressed their results for the atom desorption energy in terms of the bare work functions and heats of sublimation (properties presumed to be independently known) of the substrate and adsorbate. Based on their analysis for the system cesium on tungsten, we obtain the following atom desorption energies at zero coverage:

ϕ_o(eV) :	4.65	5.11	5.33
ϕ^*_{ao}(eV):	2.90	3.21	3.37

These results agree within about 0.1eV with our measured desorption energies. They have also theoretically calculated the oscillation frequency $Q_{io} = \omega_o$(Eq. IV.51) and have obtained the value 1.1×10^{12} sec^{-1}, which, as shown at the end of Sec. IV.D, is essentially independent of crystallographic orientation. This value is in agreement with the measured values of Langmuir, and Scheer and Fine, which are all lower than our result. However, it must be emphasized that the experimental uncertainty in ω_o is quite large.

As mentioned at the end of Sec. IV.D, it appears from our results for the (100) and (110) crystals, together with those of the two most extensive studies of Langmuir et al. and Scheer and Fine for polycrystalline tungsten, that ϕ_{io} is essentially independent of the crystallographic orientation of the tungsten surface. The sum total of these results adds considerable credibility to the often-mentioned postulate that the cesium-ion desorption energy is equal to its image charge potential $e^2/4r_i$, where r_i is the radius of the adsorbed ion. According to this theory, r_i for tungsten is 1.80Å which is to be compared with the value 1.7Å for the radius of a free cesium ion.

F. Summary

In this section we have briefly outlined the theory of surface ionization. We have described a method for determining independently the desorption energies of cesium atoms and ions evaporating from a clean emitter surface; this method is ideally suited for the study of emitter materials of interest to thermionic energy conversion. Furthermore, we have demonstrated that the technique can be applied to the study of sputtering of alkali metal surfaces by alkali ions. We have measured the heats of evaporation of cesium atoms and ions for the bare (100) and (1$\bar{1}$0) crystal emitters in the temperature range 1000 to 1500°K. These results are summarized and compared with previous data for polycrystalline tungsten in Table IV.II of Sec. IV.E.

V. SURFACE IONIZATION OF CESIUM

The saturation, cesium-ion current density J_{Cs} produced at the surface of the emitter operating at temperature T_E in a cesium-vapor flux n_o is obtained by modifying the form of the Saha-Langmuir equation as follows,

$$J_{Cs} = en_o\left[1 + 2 \exp \frac{V_i - \phi}{k T_E}\right]^{-1} \qquad (V\text{-}1)$$

where $V_i = 3.89$eV is the first ionization potential of cesium (Ref. 21) and ϕ is the effective work function of the emitter surface. This relation can be used to determine ϕ from the observed ion current if n_o is known. The discussion of the manner in which adsorbed cesium reduces the work function of metal surfaces is deferred until Sec. VI. In this section (V) we describe how, from Eq. (V-1), the ion current-voltage characteristics of both (100) and (110) diodes operating in a cesium vapor were analyzed to determine n_o and $\phi(T_E)$ as a function of the cesium-reservoir temperature T_{Cs}. This T_{Cs} is a convenient parameter to use because at thermodynamic equilibrium it uniquely determines n_o; hence once the functional relationship between them is known, ϕ can be determined from measurements of T_E, T_{Cs} and J_{Cs}.

A. Vapor Flux of Cesium

From Eq. (V-1) it is evident that

$$J_{Cs} = en_o, \quad \text{if } (\phi - V_i) >> kT_E. \qquad (V\text{-}2)$$

This, the condition for essentially 100% surface ionization, is achieved experimentally by heating the emitter to a sufficiently high temperature that the surface coverage of cesium is small enough that the emitter work function is greater than V_i.

The cesium-reservoir temperature was varied over the range 0 to 120°C. The premature failure of both diodes prevented us from extending out measurements to higher cesium temperatures. The complete electron and ion current-voltage curves were obtained point by point with the same test circuit as was used for the vacuum operation, described in Sec. III.B. The electron-emission data obtained from these current-voltage curves are described in Sec. VI. In most cases the data were obtained by maintaining the emitter at a constant temperature and varying the cesium temperature through all or part of its range. Following each temperature change, the current-voltage characteristics were not recorded until the saturation electron or ion currents had stabilized to a constant value, indicating the attainment of thermal equilibrium. The temperature of the cesium reservoir was automatically controlled to 1/4°C. The temperature of the diode body was maintained at least 20°C above the cesium-reservoir temperature. The ceramic insulators were kept at somewhat higher temperatures to reduce the adsorption of cesium on their surfaces. The interelectrode spacing was maintained between 0.010 and 0.020 in.

A typical set of cesium-ion current versus collector voltage V_c (relative to the emitter voltage) curves obtained at a constant emitter temperature, high enough to satisfy the condition of 100% surface ionization, is shown in Fig. V-I. At low voltages the curves are space-charge limited and follow the 3/2 power law of Child-Langmuir [Eq. (IV-43) of Sec. IV.D]. In fact, the interelectrode spacing can be determined within about a 10% error, from the position of the curves. The saturation current was taken to be that at the top of the hump near the knee of the curves, because it was reproducible. The decrease in the value of the saturation currents as the applied voltage is increased remains unexplained; so also does the odd shape of the 17°C curve. Similar curves were observed in

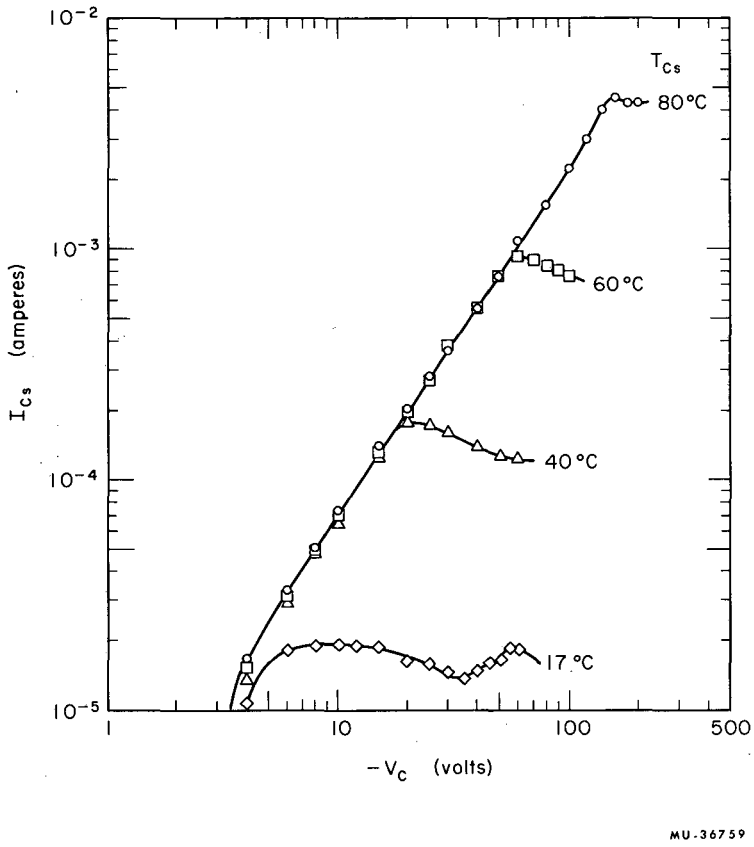
10^{-2}
10^{-3}
10^{-4}
10^{-5}
I_{cs} (amperes)
T_{cs}
80°C
60°C
40°C
17°C
1
10
100
500
$-V_c$ (volts)
MU-36759

Fig. V.1

practically every case. In general the curve in the saturation region obtained for increasing voltage did not match that for decreasing voltage, except for the value of the current at the knee. We also found that following each incremental step increase in applied voltage (beyond that of the knee), the ion currents underwent damped oscillations whose initial amplitudes gradually increased, until eventually a voltage was reached at which the oscillations seemed to diverge. The periods of oscillation were on the order of seconds. The oscillations were not investigated beyond the observations just mentioned and their origin is not understood. It does seem, however, from the long period of the oscillations, and the fact that the condition of collisionless plasma in the interelectrode space was always maintained, that these oscillations were the result of a surface effect on one or both electrodes; and that they were perhaps related to the possibility of sputtering adsorbed cesium from the collector as was evidenced in the cesium desorption energy experiments (Sec. IV.D).

Several data sets such as the one shown in Fig. V.1 were obtained for different emitter temperatures. The saturation currents for constant cesium temperatures were averaged and plotted versus $1/T_{Cs}$ as shown in Fig. V.2 to yield the desired relation between n_o and T_{Cs}. The data were plotted versus $1/T_{Cs}$ because they obey the Clausius-Clapeyron equation for a gas with a constant enthalpy change from the liquid to the vapor phase. The lower, dashed line in Fig. V.2 is the data of Taylor and Langmuir who measured the vapor pressure of cesium in the range -35 to 73°C (Ref. 89). Their data is characterized by an equation of the form $en_o = C \exp(-h/kT_{Cs})$, where $h = 0.75$eV and $C = 1.3\times10^{27}$ ions/cm^{2}sec $= 2.1\times10^{8}$ampere/cm^2.

Recently Carney extended the measurements of Taylor and Langmuir to 100°C and found that his results agreed with the extrapolation of their data.[17] The vapor-flux data of our (110) diode were reproducible only

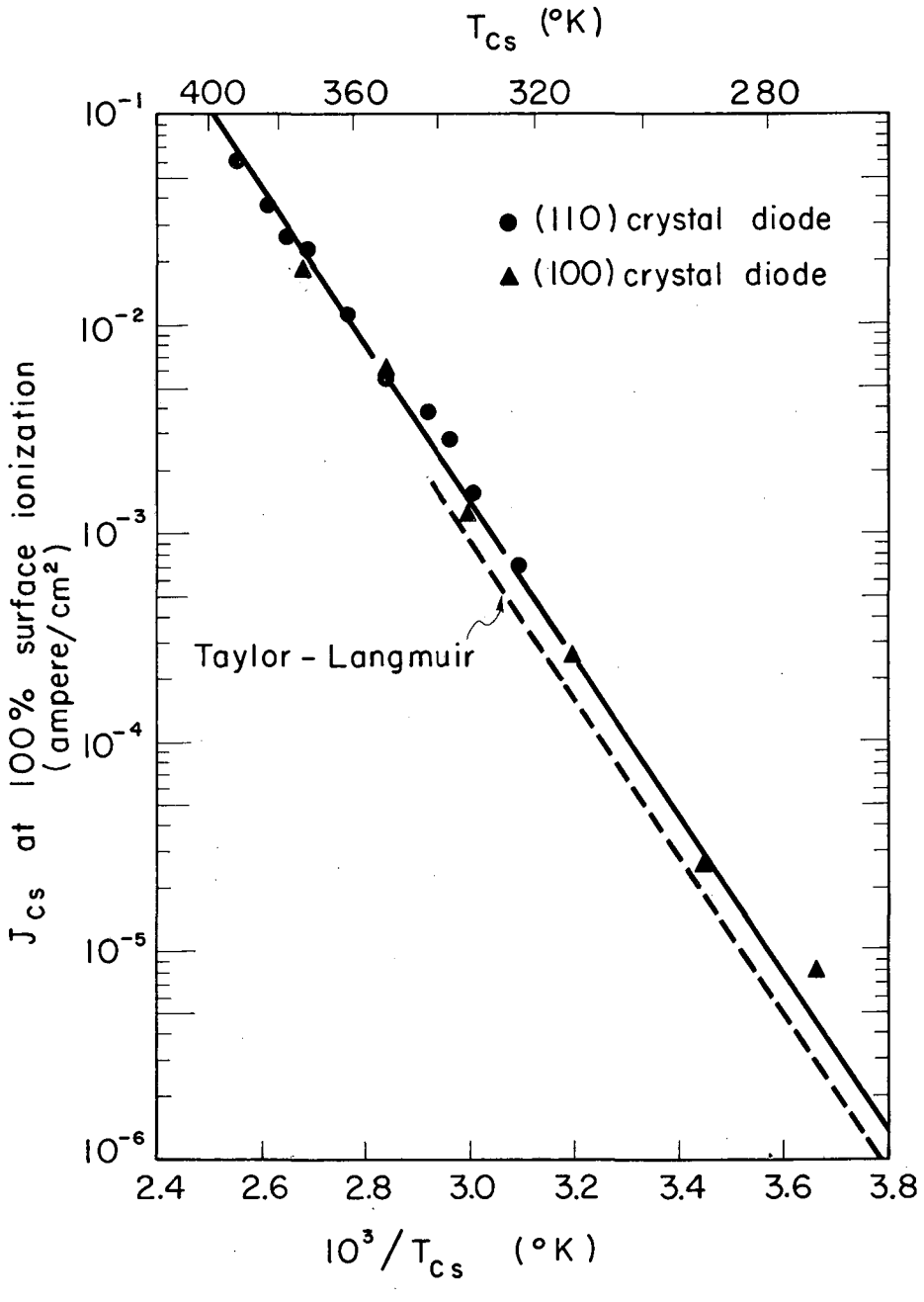
T_{Cs} (°K)
400
360
320
280
10^{-1}
10^{-2}
10^{-3}
10^{-4}
10^{-5}
10^{-6}
● (110) crystal diode
▲ (100) crystal diode
Taylor - Langmuir
J_{Cs} at 100% surface ionization (ampere/cm²)
2.4
2.6
2.8
3.0
3.2
3.4
3.6
3.8
$10^3/T_{Cs}$ (°K)
MU-36761

Fig. V.2

above 50°C. Below that temperature we could not obtain in a reasonable period of time, a condition of thermodynamic equilibrium between the cesium in the reservoir and the vapor in the diode because the diameter of the tube connecting the two was too small. This diameter was enlarged by a factor of 4 in the (100) diode, as described in Appendix B.

The saturation current densities measured in our diodes are a factor of about 1.5 greater than those to Taylor and Langmuir. This discrepancy cannot be due to the following causes: an error in calculating current density, an error of 6 to 8°C in the measurement of the reservoir temperature, other alkali metal impurities in the cesium, or secondary electron emission from the collector proportional to the ion current. The accuracy in the measurement of current was better than 2% and the collector area was known to 5%. The thermocouples used to measure the reservoir temperature were calibrated before and after the experiments and gave the correct temperature to better than 1/2°C. In the case of the (100) diode, a thermocouple was inserted into a copper block brazed to the bottom of the cesium reservoir as described in Appendix B. The copper block made contact only with the reservoir and not with the temperature-controlling jacket surrounding the reservoir; hence the block temperature was truly the same as that of the liquid cesium immediately above it. We also ascertained that the bottom of the reservoir was colder than any point above it. The impurity analysis of the cesium used in these experiments, furnished by the supplier (Appendix E) shows that the content of potassium, rubidium, and sodium was about 44 ppm. Since the vapor pressure of each of these three elements is lower than that of cesium, their partial pressure in the diode was negligible. We cannot rule out the possibility of secondary electron emission from the collector, due to ion impact.

However, the range of applied voltage and the value of the collector work function (essentially equal to that of cesium) in our measurements were similar to those in the experiments of Taylor and Langmuir. Hence, possible secondary electron emission at the collector would have affected their results in the same way as ours, and therefore cannot account for the difference in saturation currents evident in Fig. V.2.

It is likely that our higher saturation currents result from the geometry of our closely spaced planar electrodes, as compared with the cylindrical collector and wire emitter used by Taylor and Langmuir, and by Carney. We can think of two phenomena which could explain the discrespancy in Fig. V.2 or the basis of geometrical differences.

a. In the absence of an interelectrode electric field, thermodynamic equilibrium with the cesium vapor outside the interelectrode space is established by cesium leaving the emitter and collector isotropically, at equal rates in planar geometry, but almost entirely (depending on the ratio of collector to emitter radii) from the collector in the wire emitter-cylindrical collector geometry. The electric field, applied to obtain saturation ion currents, collimates the ions toward the collector, and removes the emitter as a source of cesium to establish equilibrium with the cesium vapor outside the interelectrode space. Therefore, the surface concentration of adsorbed cesium on the collector must increase until the evaporation rate of cesium from the collector alone increases sufficiently to maintain this equilibrium. This effect must necessarily increase the neutral flux incident upon the emitter and thereby increase the observed saturation ion current. Such an increase in ion current should be observable if sufficient time is allowed for equilibrium to be reestablished after applying the negative collector potential.

b. The possible sputtering of neutral cesium from the collector by ion bombardment (discussed in Sec. IV.D) would provide an additional contribution to the neutral flux incident on the emitter and would increase the observed saturation current. This increase would be observed if the data are taken after applying the negative collector potential in a time before the cesium in the interelectrode space has reached equilibrium with the outside vapor, by depleting the surface concentration of adsorbed cesium on the collector.

In both of these effects, the increase in the neutral cesium flux incident on the emitter following the application of the electric field (attractive for ions) is significant to the extent that the ion current from the emitter is a significant fraction of the total flux of cesium incident on the collector. Hence, in the geometry of the Taylor-Langmuir experiments, these effects are essentially negligible and their observed saturation cesium-ion currents at 100% surface ionization should represent the neutral flux of cesium n_o, characteristic of the cesium-reservoir temperature (the diode body in their experiment).

These effects are negligible in our geometry also, whenever the coefficient of surface ionization β is small; because in this case the emitted ions are a small fraction of the cesium atoms emitted from the emitter and incident on the collector. Therefore, for relatively low surface ionization, the flux of cesium incident on the emitter should be that characterized by the cesium reservoir temperature; hence the vapor flux data of Taylor and Langmuir has been used, in our determination of the cesiated work function ϕ from Eq. (V.1), as the basis for relating our measured ion currents to the coefficient of surface ionization.

The ratio 1.5 of our measured saturation ion currents at 100% surface ionization to those of Taylor and Langmuir (Fig. V.2) is qualitatively commensurate with estimates of either of the two effects described above, assuming an isotropic angular distribution for the cesium evaporating from the electrodes for a, and a sputtering yield of about 0.5 for b. However, because of difficulties in estimating the time needed to achieve thermodynamic equilibrium for each case, compounded by the lack of recorded data on the time needed to measure the current-voltage curves, we cannot determine whether one or the other or both of these possible phenomena were responsible for our observations. Further experimentation on the effects of applied voltage, interelectrode spacing, and time on the observed currents in the planar electrodes geometry is needed to calrify these hypotheses.

B. Work Function of (100) and (110) Crystals Exposed to Cesium Vapor; Evaluated from Ion Emission

Ion currents were measured at emitter temperatures low enough that, owing to the depression of the emitter work function resulting from the adsorption of cesium, the ionization coefficient $\beta = J_{Cs}/en_o$ was much less than 1. A typical set of data obtained at constant emitter temperature is shown in Fig. V.3; these curves were completely stable and free of the peculiarities of the I_{Cs} - V_c curves described in Sec. V.A. Note that in contrast to the ion currents in Fig. V.1, measured at a condition of 100% surface ionization, the saturation currents here decrease with increasing T_{Cs}. This effect arises because cesium adsorption which increases with T_{Cs} reduces the work function ϕ of the emitter; and from Eq. (V-1) we see that the increase in n_o with T_{Cs} is more than offset by an increase in the exponent, whose value is now positive.

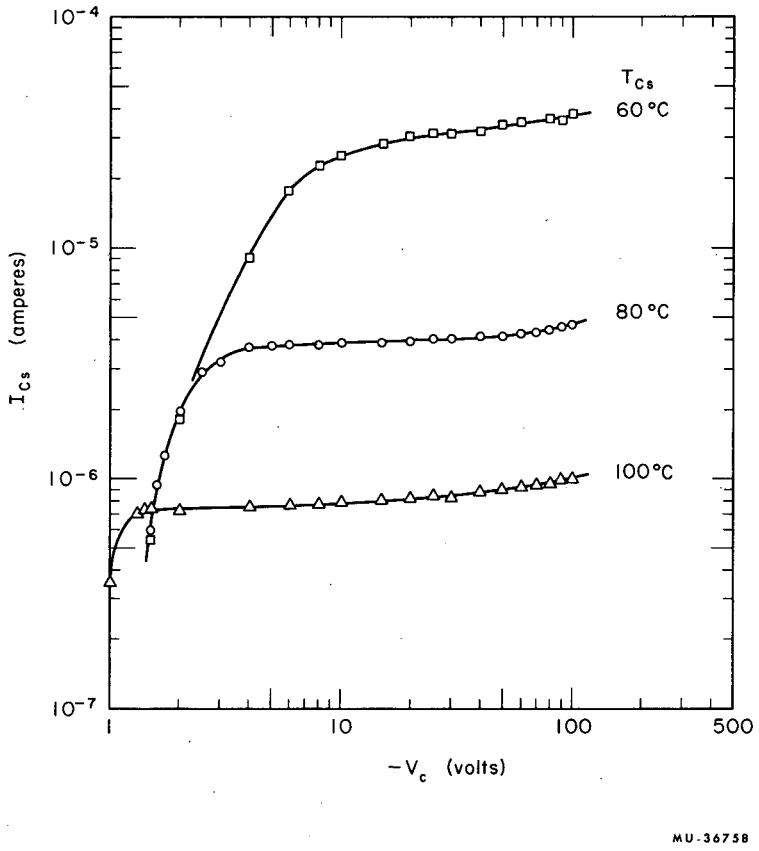
10^{-4}
10^{-5}
10^{-6}
10^{-7}
I_{Cs} (amperes)
T_{Cs}
60 °C
80 °C
100 °C
1
10
100
500
$-V_c$ (volts)
MU-36758

Fig. V.3

The surface concentration of adsorbed cesium when $\beta \ll 1$ is established essentially by the equilibrium between the incident flux and the atom evaporation rate. The latter is very insensitive to the magnitude or polarity of the applied field at the emitter surface, and consequently the surface coverage is also unaffected by electric fields. Therefore the increase in the saturation current with voltage (in Fig. V.3) is due to the Schottky effect on the ions; hence, Schottky plots, log I_{Cs} versus $(V_o - V_c)^{1/2}$, exemplified in Fig. V.4, were made to evaluate the saturation currents at zero field. These saturation currents, together with those obtained at a 100% surface ionization, have been plotted versus $1/T_E$ in Figs. V.5 and V.6 for the (100) and (110) diode respectively. The family of curves are lines of constant T_{Cs}. The current densities were plotted versus $1/T_E$ because the data below the saturation-current lines could be fitted by parallel straight lines. Figures V.5 and V.6 display all the ion-current data that we obtained for both diodes.

The shaded portion of the curves indicates the transition between the condition of 100% surface ionization and the condition of small surface ionization. This transition region occurs at a rather poorly resolved emitter temperature called the threshold temperature for 100% surface ionization. The transition region is discussed in Sec. V.C.

The work functions of the (100) and (110) emitter surfaces with adsorbed cesium were determined, by means of Eq. (V-1), from the experimentally observed ion-current densities at low fractional surface ionization. The Taylor-Langmuir values for ion-current densities at 100% surface ionization were used to represent the incident atomic flux n_o. The results have been tabulated in Tables P.I and P.II of Appendix P. The change in emitter work function $\Delta\phi$, defined as the difference between the bare work

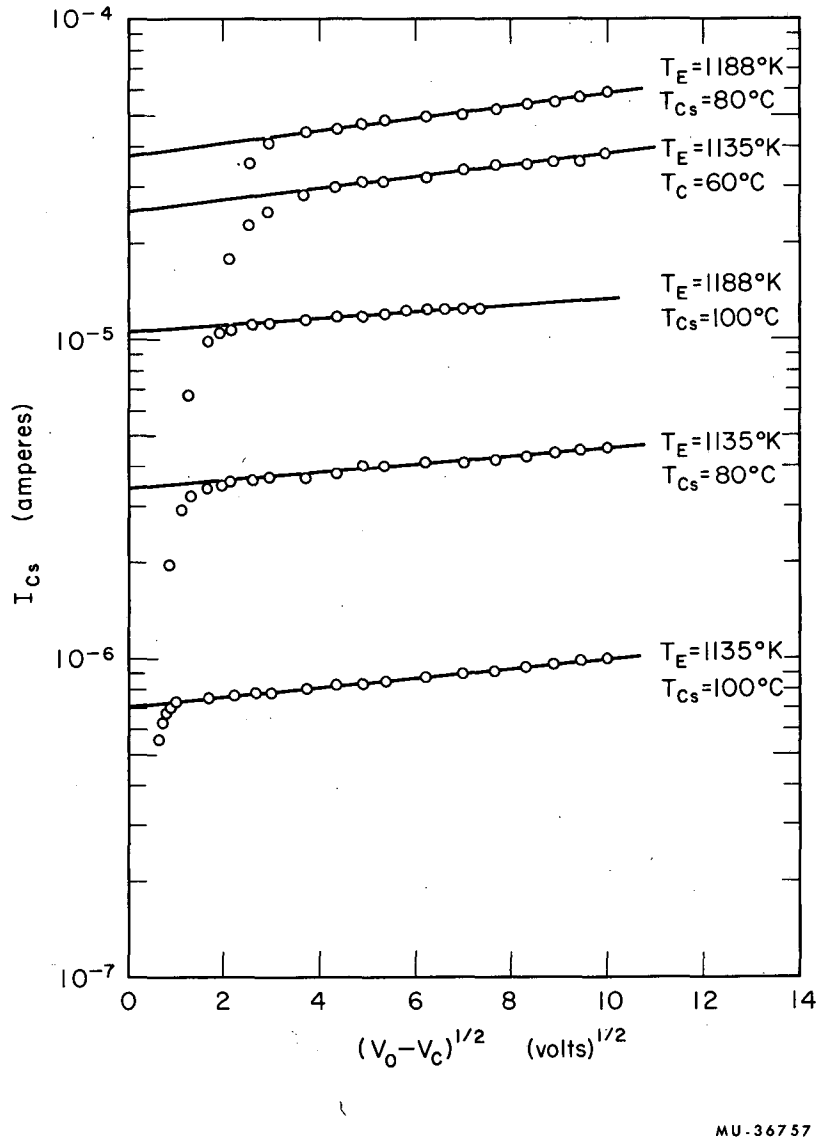
10^{-4}
10^{-5}
10^{-6}
10^{-7}
I_{Cs} (amperes)
T_E=1188°K
T_{Cs}=80°C
T_E=1135°K
T_C=60°C
T_E=1188°K
T_{Cs}=100°C
T_E=1135°K
T_{Cs}=80°C
T_E=1135°K
T_{Cs}=100°C
0
2
4
6
8
10
12
14
$(V_0-V_C)^{1/2}$ (volts)$^{1/2}$
MU-36757

Fig. V.4

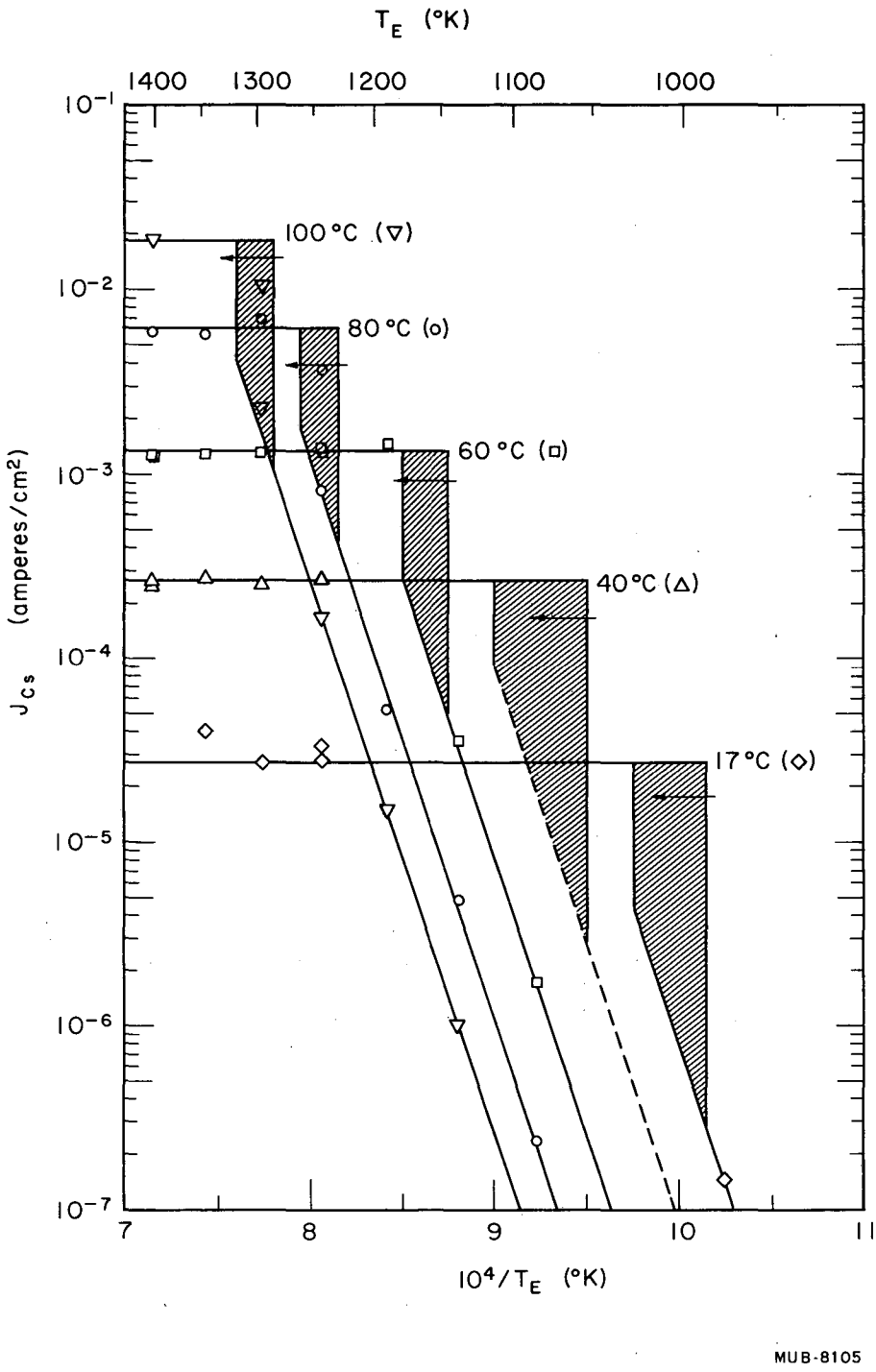
T_E (°K)
1400
1300
1200
1100
1000
10^{-1}
10^{-2}
10^{-3}
10^{-4}
10^{-5}
10^{-6}
10^{-7}
J_{cs} (amperes/cm^2)
100 °C (▽)
80 °C (○)
60 °C (□)
40 °C (△)
17 °C (◇)
7
8
9
10
11
$10^4/T_E$ (°K)
MUB-8105

Fig. V.5

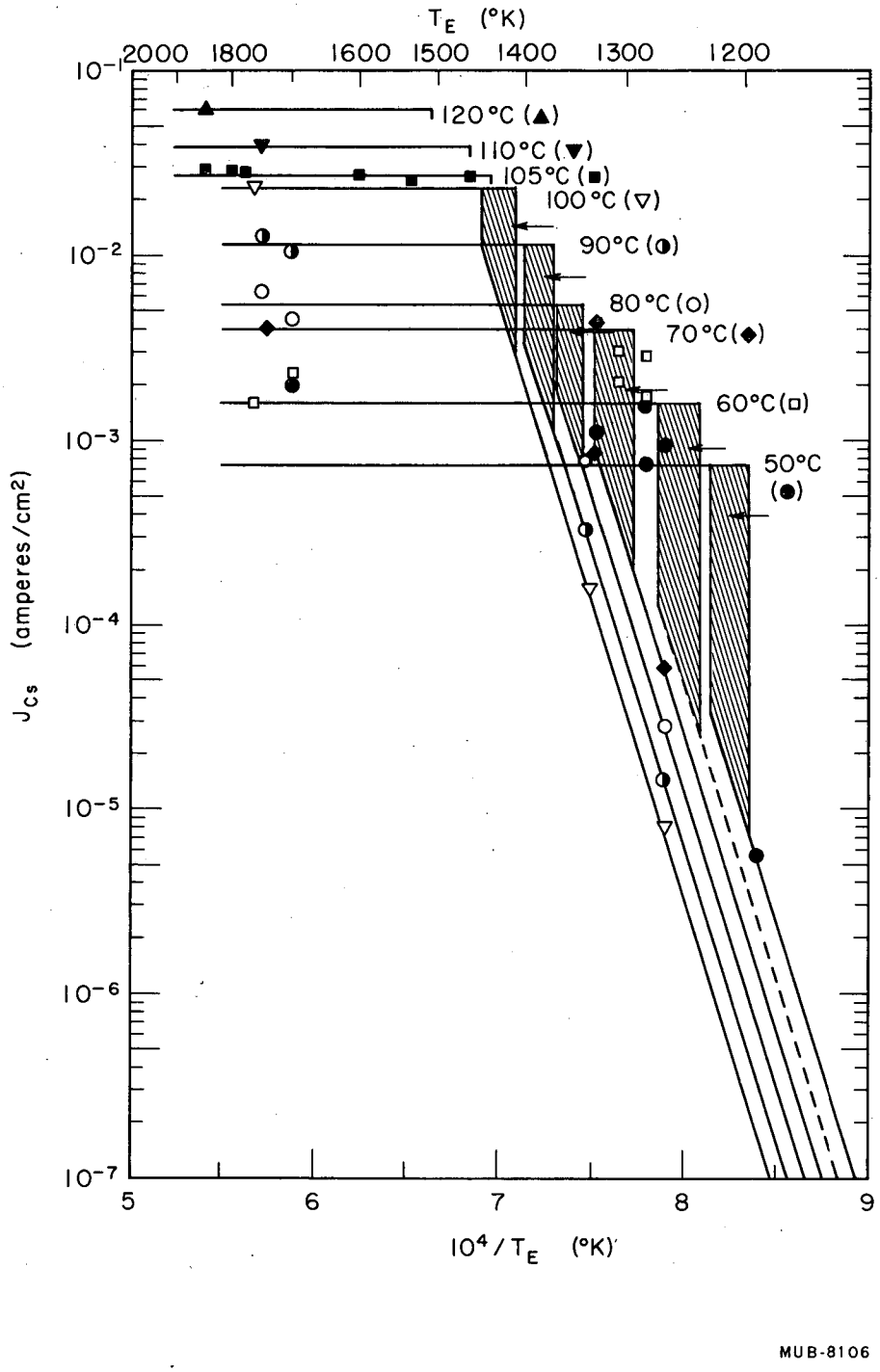
T_E (°K)
2000 1800 1600 1500 1400 1300 1200
10^{-1}
10^{-2}
10^{-3}
10^{-4}
10^{-5}
10^{-6}
10^{-7}
J_{cs} (amperes/cm²)
120°C (▲)
110°C (▼)
105°C (■)
100°C (▽)
90°C (◑)
80°C (○)
70°C (◆)
60°C (□)
50°C (●)
5 6 7 8 9
$10^4 / T_E$ (°K)
MUB-8106

Fig. V.6

function ϕ_o which was determined in Sec. III and the work function with adsorbed cesium ϕ, is plotted versus the ratio T_E/T_{Cs} for the (100) crystal, in Fig. V.7. The parameter T_E/T_{Cs} has been chosen to describe $\Delta\phi$ because, as is discussed in Sec. VI, the surface contentration of adsorbed cesium, which we could not measure directly, is practically a unique function of T_E/T_{Cs} within the range of our observations. The dashed line in Fig. V.7 represents the corresponding result as determined from electron emission data, shown in Fig. VI.6 of Sec. VI.B. The agreement between the two methods is excellent for values of T_E/T_{Cs} below 3.5. The two curves depart from each other at higher values of T_E/T_{Cs} because the corresponding effective emitter work function ϕ becomes greater than the cesium ionization potential V_i. In this region, the ratio of ion to atom emissions is no longer negligible, and therefore the surface coverage of cesium on the emitter is greatly influenced by the polarity of the applied electric field needed to observe either the electron or ion emission from which the work function is evaluated. Whereas, as mentioned earlier, the polarity of the applied field has little effect on the surface coverage when $\beta = n_i/n_o \ll 1$, i.e., $\phi < V_i$. One would expect, then, that the two methods would deviate when ϕ is somewhat less than V_i (which is equal to 3.89eV). From Fig. V.7 we see that the two curves depart when $\phi \approx 3.7$eV.

The work function of the (110) crystal with adsorbed cesium, as determined from the ion currents is plotted versus T_E/T_{Cs} in Fig. V.8, which also includes the (100) result, for comparison. Again the dashed line shows the corresponding result obtained from electron emission data, shown in Fig. VI.7 of Sec. VI.B. The agreement between the two methods is fairly good but not as good as it was for the (100) crystal. We have plotted ϕ (rather than $\Delta\phi$) versus T_E/T_{Cs}, because it is rather unlikely that the

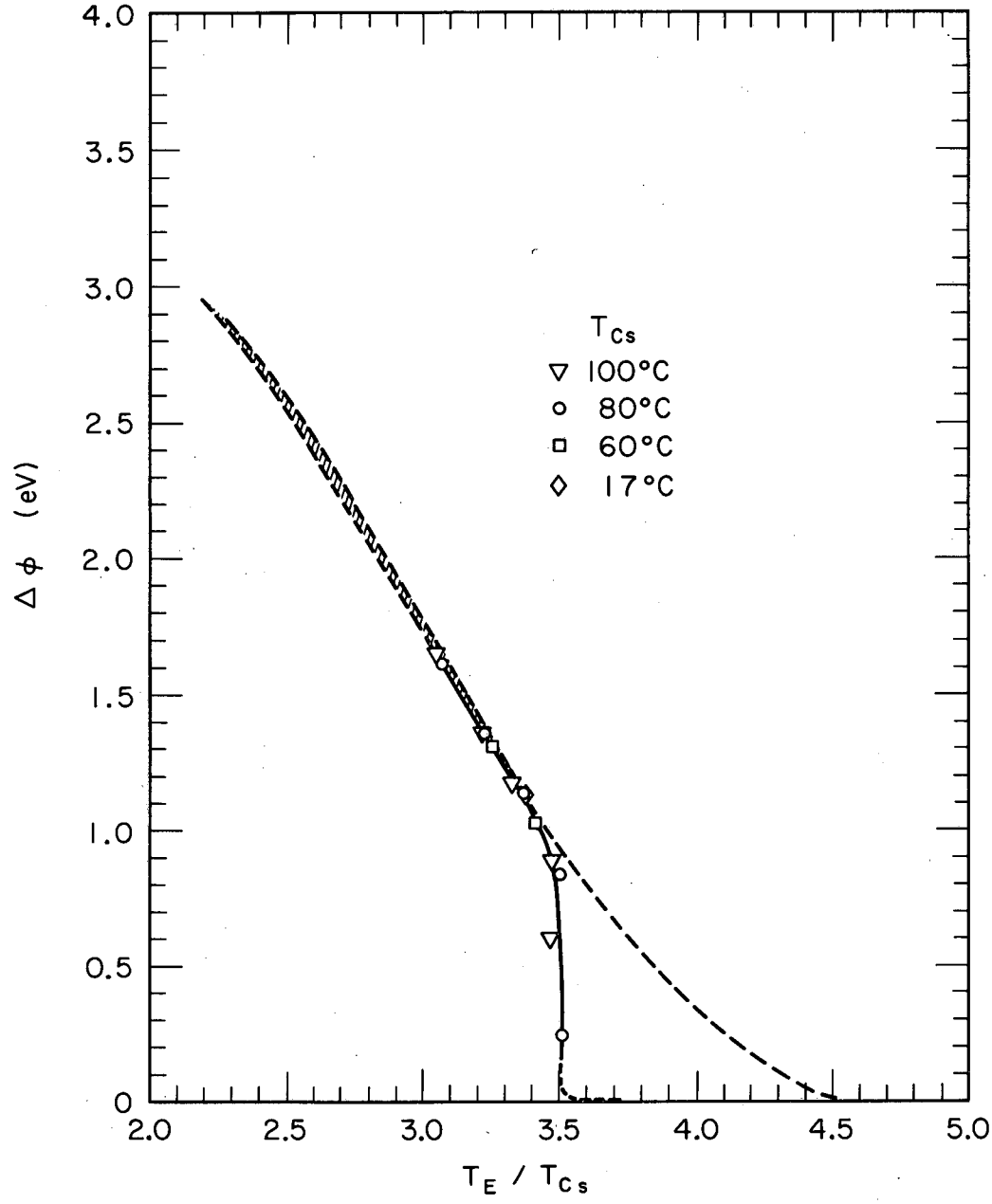
4.0
3.5
3.0
2.5
2.0
1.5
1.0
0.5
0
Δφ (eV)
2.0
2.5
3.0
3.5
4.0
4.5
5.0
T_E / T_Cs
T_Cs
100°C
80°C
60°C
17°C
MUB-8107

Fig. V.7

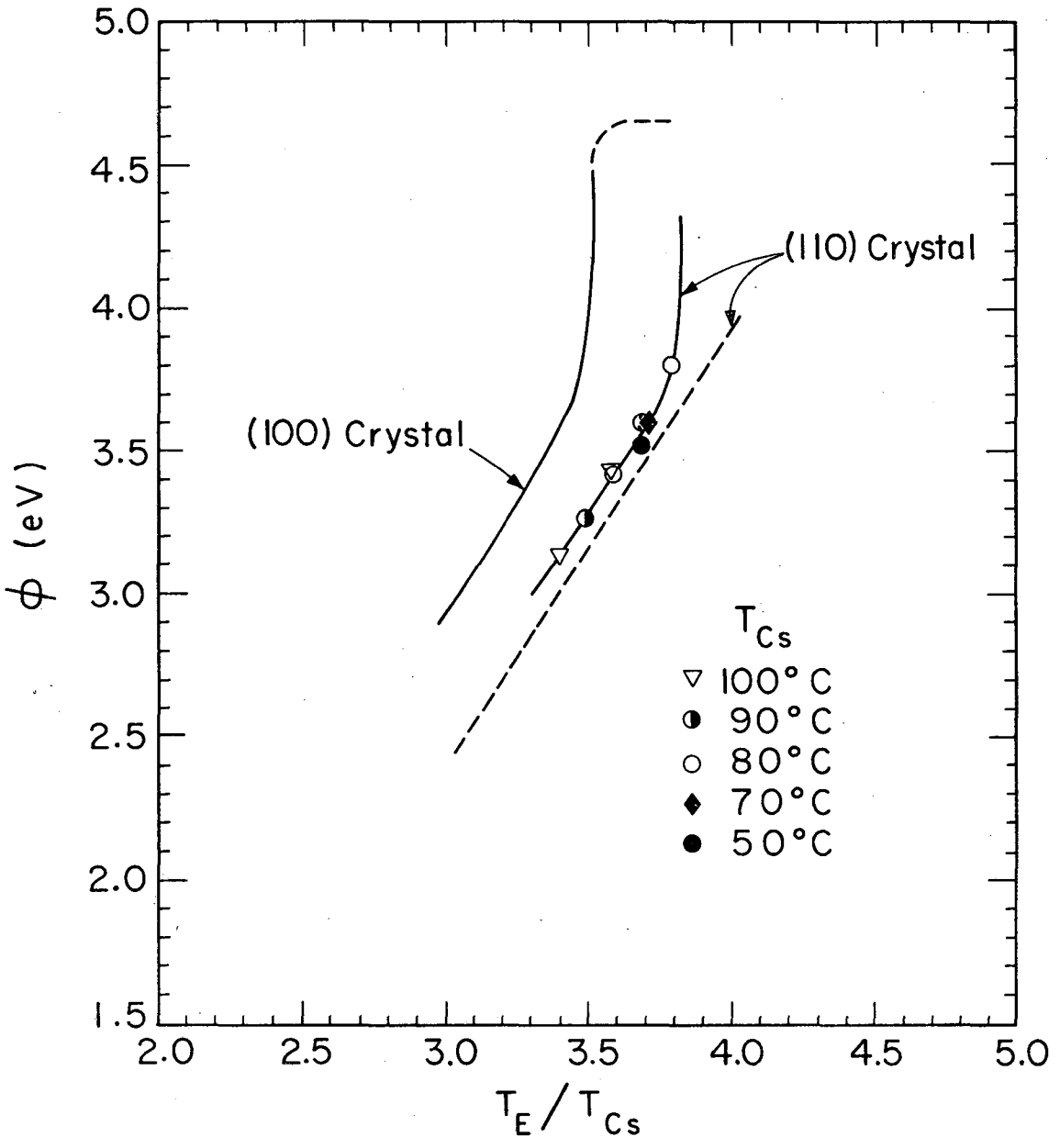
5.0
4.5
4.0
3.5
3.0
2.5
2.0
1.5
φ (eV)
2.0
2.5
3.0
3.5
4.0
4.5
5.0
T_E / T_{Cs}
(100) Crystal
(110) Crystal
T_{Cs}
100° C
90° C
80° C
70° C
50° C
MUB-9822

Fig. V.8

data for the (110) crystal presented in Fig. V.8 are characteristic of the bare-metal work function $\phi_o = 5.33$ determined in Sec. III.C. We recall from that section that as the temperature of the (110) emitter was lowered below a certain transition value (greater than the temperature at which any of the data presented in this section were obtained), the bare work function decreased, owing to some apparent surface contamination, to a value of about 5.1eV. To compound the uncertainties in the surface condition of this crystal, three events occurred in the interim period between the determination of the bare work function and desorption energies, and the measurement of the data of Fig. V.8. The emitter and collector accidentally made contact for a few seconds while the former was at 1500°K; at a later date the diode developed a small vacuum leak, and finally the diode windows became partially coated permanently. We attempted to remedy the first condition by heating the emitter to 2200°K for several minutes to drive off any adsorbed or alloyed copper. The vacuum leak developed while the diode was in air, but not operating. It was then operated for several hours in an oxygen-free helium atmosphere before a leak was determined to have developed. Subsequently we were able to operate the diode in spite of the leak by evacuating the chamber into which the diode was placed. Unfortunately the minimum pressure that we could achieve in the chamber was 0.015 mm Hg. The extent to which the (110) crystal surface was contaminated by all these factors cannot be evaluated, but undoubtedly it was not negligible.

In spite of the fogging of the (110) diode windows we were able to determine the emitter's temperature from a previously measured calibration curve of the power input to the electron gun versus emitter temperature. However, the precision of this temperature determination was about 2% as

compared with 0.2% when the optical pyrometer was used.

We are including the cesium data obtained from the (110) diode in spite of its questionable relation to the properties of a clean (110) tungsten crystal because it is still characteristic of a high substrate work function and thus provides a useful comparison for the (100) data.

C. Threshold Temperature for 100% Surface Ionization of Cesium on (100) and (110) Crystals

The threshold temperature T_{EO} is loosely defined as that emitter temperature at which, for a given incident flux of cesium, a transition occurs between the condition of 100% and that of small fractional surface ionization. From the careful study of ion current-voltage curves obtained at or near this transition, we were able to place rough limits on the threshold temperature, as indicated by the width of the shaded regions in Figs. V.5 and V.6.

The saturation ion current for a given T_E and T_{Cs} in a transition region was multivalued. That is, it could be made to increase from a minimum to a maximum value within the bounds set by the lower and upper limits of the transition region, by increasing the applied voltage across the electrodes. We observed a few ion current-voltage curves that displayed this behavior, as exemplified in Fig. V.9. Considering the curve for 80°C, for example, we see that the current starts to saturate at a collector voltage $V_c \approx 50V$ and a current $I_{Cs} \approx 6\times10^{-4}$ amperes; but as the collector voltage is made increasingly negative the current increases, until it finally saturates at a value around 2.5×10^{-3} amperes. The values of these two currents can be found in Fig. V.5 as the two round data points in the shaded region for the 80°C curve.

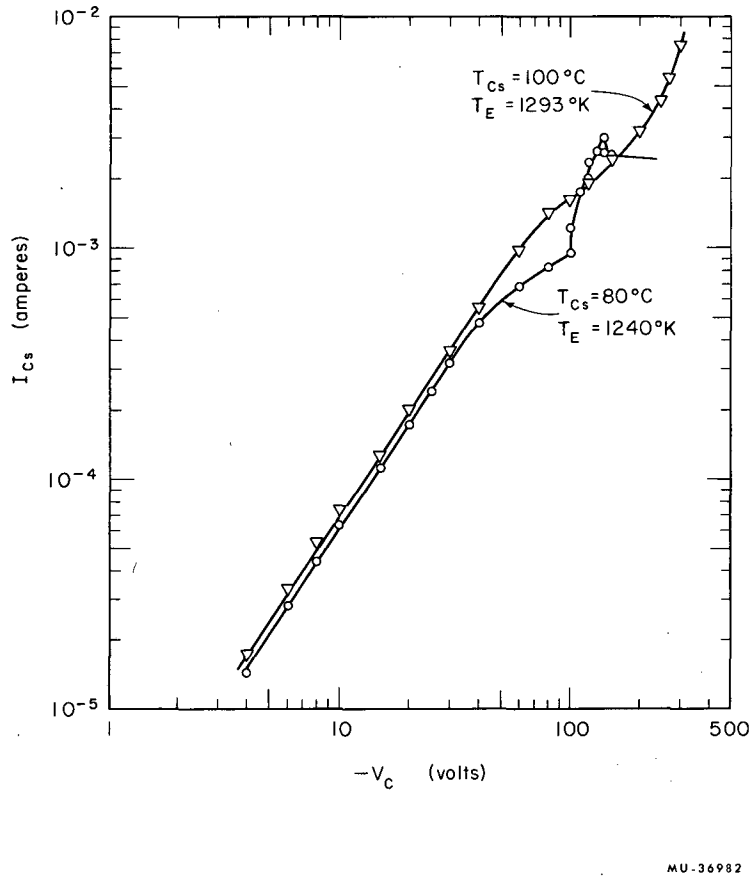
10^{-2}
10^{-3}
10^{-4}
10^{-5}
I_{Cs} (amperes)
T_{Cs} = 100 °C
T_E = 1293 °K
T_{Cs} = 80 °C
T_E = 1240 °K
1
10
100
500
$-V_C$ (volts)
MU-36982

Fig. V.9

These discontinuities were observed by Becker, Killian, and Langmuir and are attributed to the simultaneous existence of two distinct phases of adsorbed atoms on the surface, a dilute phase from which the evaporation of ions predominates over that of atoms, and a more concentrated phase for which the converse is true.[56,50,7] This dual phase condition occurs at low surface coverage (<20%) where the ion- and atom-evaporation rates are comparable. The current discontinuity is a consequence of the fact that the ion-evaporation probability decreases with increasing coverage of adsorbed atoms, whereas the atom-evaporation probability increases; because the evaporation of ions is influenced by electric fields, the application of an attractive field for ions can effectuate a transition from the concentrated to the dilute phase, resulting in a discontinuous increase in ion current.

Figures V.5 and V.6 show that the threshold temperature T_{EO} increases with increasing cesium temperature. We have plotted the Taylor-Langmuir values for the ion current densities at 100% surface ionization, shown by the arrows in Figs V.5 and V.6, versus $1/T_{EO}$, in Fig. V.10. The data can be fitted fairly well with straight lines. The dashed line is the result obtained by Taylor and Langmuir for cesium on polycrystalline tungsten.[88,89] Figure V.10 shows that for a given cesium flux, the threshold temperature of the (110) emitter is greater than that of the (100) crystal. This means that cesium is adsorbed more strongly on the (110) crystal than on the (100), because T_{EO} is essentially the temperature to which a surface must be heated, in order to prevent the adsorption of an appreciable surface coverage. This result is consistent with the fact that the work function and the cesium-atom desorption energy for the bare (110) emitter were greater than those of the (100) cyrstal. The data shown in Fig. V.10 are of practical value because

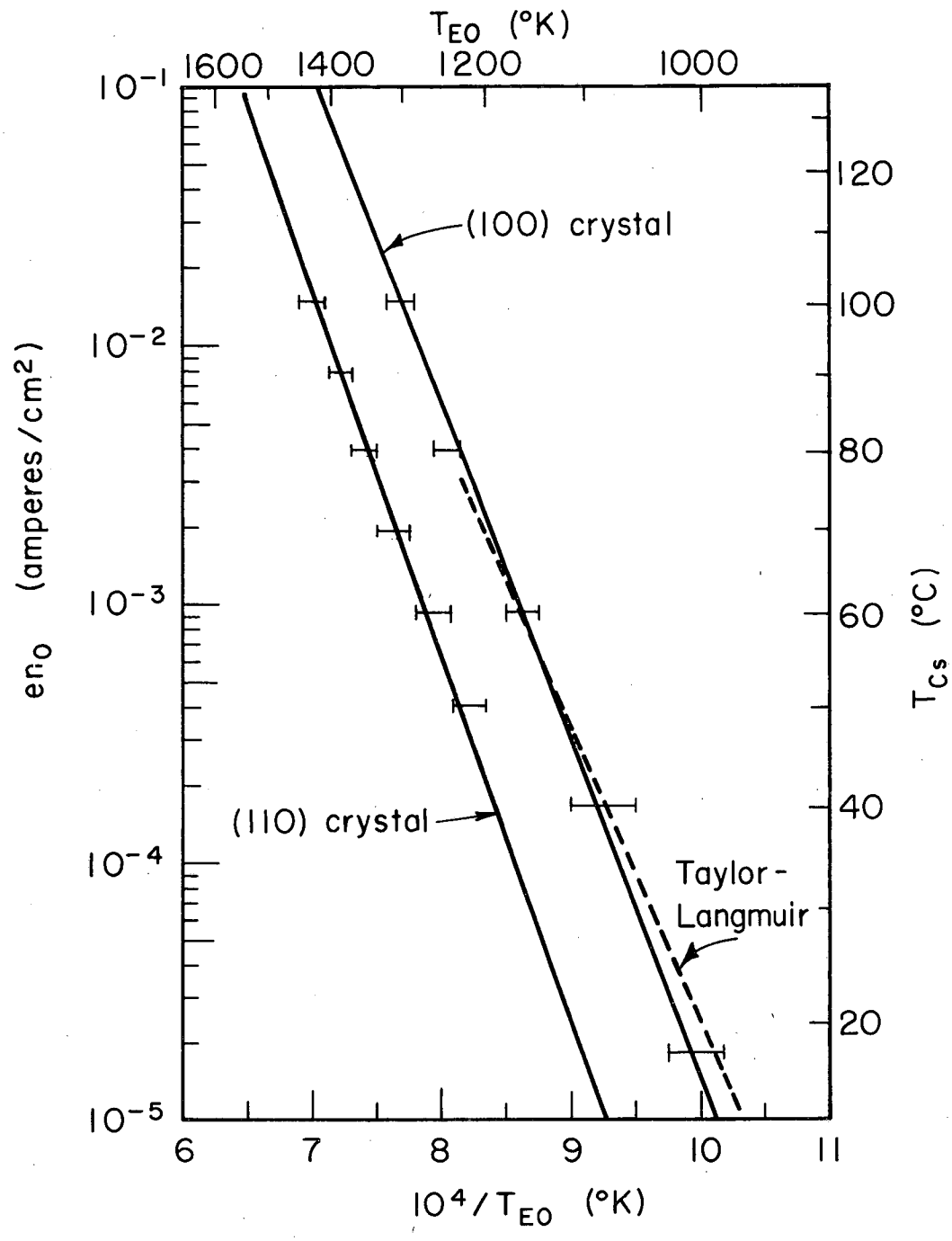
T_{EO} (°K)
1600
1400
1200
1000
10^{-1}
10^{-2}
10^{-3}
10^{-4}
10^{-5}
en_o (amperes/cm²)
120
100
80
60
40
20
T_{Cs} (°C)
(100) crystal
(110) crystal
Taylor-
Langmuir
6
7
8
9
10
11
$10^4/T_{EO}$ (°K)
MUB-8104

Fig. V.10

they enable one to determine the minimum temperatures to which these surfaces must be heated in order to yield essentially 100% surface ionization for any desired cesium flux.

The value of the ratio T_{EO}/T_{Cs} was evaluated at several points on the curves of Fig. V.10 and found to be a constant for each line, equal to 3.5 and 3.8 for the (100) and (110) crystal, respectively. Not surprisingly, these values of T_E/T_{Cs} are the same values above which the ion-current method of determining $\Delta\phi$ deviates from the electron current method, as shown in Figs. V.7 and V.8.

The fact that the threshold temperature for a given surface occurs for a constant value of T_E/T_{Cs} indicates that the surface coverage of cesium at the threshold temperature is also essentially constant and is independent of T_{EO}. This latter possibility was recognized by Zandberg et al., who suggested that if it were the case, the slope of the en_o versus $1/T_{EO}$ curve should be equal to the heat of evaporation of ions for the bare surface, i.e., ϕ_{io}.[101] Their argument was as follows: in the presence of a small attractive field for ions (sufficient to overcome space charge), the ion-evaporation rate n_i is given at low surface coverage by,

$$n_i = N P_{io} = N Q_{io} \exp\left(-\frac{\phi_{io}}{k T_E}\right) . \qquad (V\text{-}3)$$

The ionization coefficient β is, by definition,

$$\beta = \frac{n_i}{n_o} . \qquad (V\text{-}4)$$

When $T_E = T_{EO}$, we have $\beta \approx 1$. Therefore from Eqs. (V-3) and (V-4) we obtain

$$\log n_o \approx \log n_i = \log (NQ_{io}) - \frac{\phi_{io}}{kT_{EO}} . \qquad (V\text{-}5)$$

From the discussion of Sec. IV.A we know that Q_{io} is independent of temperature and of N for small N. Therefore if N is a weak function of T_{EO}, a plot of $\ell n\ n_o$ versus $1/T_{EO}$ should be a straight line with slope $-\phi_{io}/k$. The slopes of both (100) and (110) lines in Fig. V.10 correspond to 2.6 and 2.8eV, respectively, and the slope of the Taylor-Langmuir curve for polycrystalline tungsten in the same figure is 2.3eV. These values are high compared with the values of ϕ_{io} described in Sec. IV.E (essentially 2.05eV for all these surfaces). The lines in Fig. V.10 are described by the following Arrhenius relations:

$$\text{(100) crystal, } en_o(\text{ampere/cm}^2) = 1.8\times10^{8}\exp(-2.6/kT_{EO})$$

$$\text{(110) crystal, } en_o(\text{ampere/cm}^2) = 1.2\times10^{8}\exp(-2.8/kT_{EO}),$$

where the numerator in the exponent is in eV. We can estimate the value of N for each crystal by dividing the linear factors by the value for $Q_{io} = 6.6\times10^{12}\text{sec}^{-1}$, determined in Sec. IV.D. In this way we find,

$$N(100) = 1.7\times10^{14}\text{atom/cm}^2$$

$$N(110) = 1.1\times10^{14}\text{atom/cm}^2 .$$

These values are too high (a monolayer of cesium on (100) tungsten is $2.5\times10^{14}\text{atom/cm}^2$) to be realistic. Therefore our values for the desorption energy at the threshold temperature must be too high also. It may be useful to choose a point on each curve in Fig. V.10 and to solve for N, assuming the above value for Q_{io} and the value $\phi_{io} = 2.05$eV. Choosing the points on the (100) and (110) curves corresponding to $10^4/T_{EO} = 8$ and 7, respectively, we find

$$N(100) \simeq 1\times10^{12}\text{atom/cm}^2$$

$$N(110) \simeq 0.3\times10^{12}\text{atom/cm}^2.$$

These values for N correspond to fractional coverages in the range 0.1 to 0.5% of a monolayer, and may be fairly realistic. The data of Taylor and Langmuir indicate that the ion desorption energy increases rapidly for fractional coverages above 0.5%.[88]

Although our results here were not experimentally very accurate, they cannot easily be fitted with lines having slopes corresponding to 2.05eV. It would appear, therefore, from our admittedly meager data, that for our crystals the ion desorption energy at the threshold temperature is probably intermediate between 2.05eV and the slope of our Arrhenius plots. We do not have sufficient data to verify Zandberg's hypothesis that the surface coverage may be essentially independent of T_{EO}.

D. Summary

The flux of cesium vapor in thermodynamic equilibrium with a condensed phase has been measured in the cesium-temperature range of 0 to 120°C. Our observed ion-current densities for 100% surface ionization on the emitter are consistently about 1.5 times the corresponding current densities measured by Taylor and Langmuir.[89] We believe that our measured currents were high as a result of the geometry of our closely spaced planar electrodes, as compared with their cylindrical collector and wire emitter.

The changes in the work functions of the (100) and (110) crystals due to the adsorption of cesium were determined from field-free ion emission data by means of the Saha-Langmuir equation. A plot of $\Delta\phi$ for the (100) crystal versus the ratio T_E/T_{Cs} was found to agree within 0.03eV with the corresponding results obtained from electron emission for values of emitter work function below the cesium ionization potential.

A plot of ϕ versus T_E/T_{Cs} for the (110) crystal was found to agree fairly well also with the results obtained from electron emission. A plot of $\Delta\phi$ versus T_E/T_{Cs} for this crystal was not made because several uncertainties in the surface condition of the crystal prevented us from knowing with any degree of confidence the bare work function of the (110) emitter at the time the ion-current measurements were made. The uncertainties were discussed in detail.

The threshold temperatures for 100% surface ionization from the (100) and (110) crystals occurred at a constant value of the ratio T_E/T_{Cs} equal to 3.5 and 3.8 for the (100) and (110) crystals, respectively.

VI. WORK-FUNCTION DEPRESSION OF (100) AND (110) CRYSTALS DUE TO CESIUM ADSORPTION; EVALUATED FROM ELECTRON EMISSION

In this section we outline several recent theories describing the effect of cesium adsorption on the work function of metal surfaces. We then describe how the work functions of the (100) and (110) crystal surfaces with adsorbed cesium were determined from the observed electron emission of the diodes operating in cesium vapor. Finally, we compare our results with those obtained for polycrystalline tungsten in the light of the theories presented.

A. Theory of Thermionic Emission for Adsorbed Alkali Films

The manner in which an adsorbed film of cesium affects the emission of electrons from a metal surface was first described theoretically, as well as experimentally, by Langmuir and his coworkers.[56,57,88] Langmuir's analysis successfully predicted the observed work function of a dilute film of cesium on tungsten, but it failed for fractional cesium coverages θ greater than 0.5.

Since then, several investigators have tried to improve on Langmuir's model in various ways.[63,40,41,24,62,31,33]

Quite recently three analyses emerged which are good in several respects. They apply over a greater range of cesium coverage than Langmuir's analysis, they are numerically simple to evaluate, and they contain only those parameters having real physical significance. They are the work of Rasor and Warner,[75,76,94] Carabateas, Stickney, and Aponick,[16] and Gyftopoulos and Levine.[35,58-60] The first two treatments derive from Langmuir's model and are very similar to each other, whereas the last uses a considerably different approach. These three analytical methods,

tabulated in Table VI.1 for ease of comparison, will be used to analyze our experimental results and will now be described in turn.

As mentioned in Sec. IV.A, at low surface coverage, cesium is adsorbed on tungsten in the ionic state. Therefore we might expect that classically such a layer of positive ions on the surface would affect its work function in the same manner as a positively charged grid placed near the surface. The latter case is depicted in Fig. VI.1 in which, additionally, the field outside the grid has been made zero to provide the field-free condition in space required by the definition of the work function given in Sec. III.A. The action of the charged grid on the potential energy of an electron as it leaves the metal surface is simply that of the Schottky effect. The point of Fig. VI.1 is that if the grid giving rise to the potential gradient shown is placed at a distance $x' \leq x_1$, $\Delta\phi = eV_g(x') = 4\pi e^2\sigma x'$, where σ is the charge density on the grid and $V_g(x')$ is the potential on the grid at x' relative to the metal surface. This situation corresponds to that of an adsorbed layer of cesium ions on a tungsten surface.

1. Theory of Rasor and Warner.

Rasor and Warner considered the existence of two kinds of adsorbed particles: ions and atoms.[75,76] They argued that the change in work function per electron is equal to half the potential drop across the dipole layer created by the adsorbed particles and their image charges as given by classical electrostatics. That is,

$$\Delta\phi/e = \frac{1}{e}(\phi_o - \phi) = \frac{4\pi\sigma}{2}(M_i\theta_i + M_a\theta_a) = 2\pi\sigma M_i\theta_i\left(1 + \frac{M_a\theta_a}{M_i\theta_i}\right), \quad \text{(VI.1)}$$

where σ is the surface density of adsorbed particles for a complete monolayer, θ_i and θ_a are the fractions of that surface density occupied by

TABLE VI.I. Comparison of three theories for the work-function depression of metals due to cesium adsorption.[a]

Eq. No.	Rasor and Warner[b] (Refs. 75,76)	Carabateas, Stickney, and Aponick (Ref. 16)	Gyftopoulos and Levine (Refs. 35, 58, 59)
1	$\Delta\phi = \dfrac{A\theta}{1 + \dfrac{g_a}{g_i}\exp(-\dfrac{E}{kT_E}) + B(1-f)\theta}$	$\Delta\phi = \dfrac{\Delta\psi_i}{1 + k_2\theta_a}$	$\Delta\phi = (\phi_o - \phi_f)\left\{1 - G(\theta)\left[1 - \dfrac{k_1\theta}{1+k_2\theta^{3/2}}\right]\right\}$
	where	where	where
	$A = 4\pi e^2 \sigma r_i$	$\Delta\psi_i = A\theta_i \dfrac{1-k_1\theta_i}{1+k_1\theta_i}$	$G(\theta) = 1 - 3\theta^2 + 2\theta^3$
	$B = 2\pi \sigma a_i / r_i$	$A = 4\pi e^2 \sigma r_i$	$k_1 = \dfrac{k_3 \sigma \cos\beta}{1 + a_o/R^3}$
	$E = E_o - (1-f)\Delta\phi$	$k_1 = 2\pi a_i \sigma(1-f)/r_i$	$k_2 = 9 a_o \sigma^{3/2}$
		$k_2 = 4\pi a_a \sigma(1-f)/r_i$	$k_3 = 0.76 \times 10^{-14}\,\text{cm}^2$
		$\theta_a = \theta_i \dfrac{g_a}{g_i}\exp(-E/kT_E)$	$\cos\beta = (1 - 1/2\sigma_m R^2)^{1/2}$
		$E = E_o - (1-f)\Delta\psi_i$	
2	$\Delta\phi_a^* = (1-f)\Delta\phi$	$\Delta\phi_a^* = (1-f)\Delta\psi_i$	$\phi_a^* = F\phi(1+\delta) + k_4(1-F^2)^{1/2}$
	where	where	define
	$(1-f) = 0.188 + 0.178\theta$	$(1-f) = 0.27$	$(1-f) = \Delta\phi_a^*/\Delta\phi$
			where
			$F = \dfrac{k_5(\phi_o - \phi_f)\,G(\theta)}{R(1 + a_o/R^3)}$
			$\delta = F(e^2/R - V_i)/\phi$
			$k_4 = (\phi_f'\phi_m')^{1/2} S_{fm}$
			$k_5 = 0.422\text{Å/eV}$
3	<---------- $\dfrac{T_E}{T_{Cs}} = \dfrac{\phi_a^*}{n} - \dfrac{kT_E}{h}\left[\ln\left(\dfrac{g_a \omega\sigma}{g_a \omega_{Cs}\sigma_{Cs}}\right) + K(\theta)\right]$ ---------->		
4	$K(\theta) = \ln\left(\dfrac{\theta}{1-\theta}\right) + \dfrac{\theta}{1-\theta}$	$K(\theta) = \ln\left(\dfrac{\theta}{1-\theta}\right) + \dfrac{\theta}{1-\theta} + 3\theta$	$K(\theta) = \ln\left[\dfrac{\theta(1-\theta)^{-1/2}}{(1-\theta^{1/2})}\right] \dfrac{\theta}{2(1-\theta)} + \dfrac{\theta^{1/2}}{2(1-\theta^{1/2})}$

a. cgs Units are used throughout. The symbols are defined in the text and in the nomenclature list. Numerical values are given in Appendix R.

b. NOTE: Eq. (8) in Ref. 76 by Rasor and Warner is dimensionally incorrect compared with Eq. (1) here.

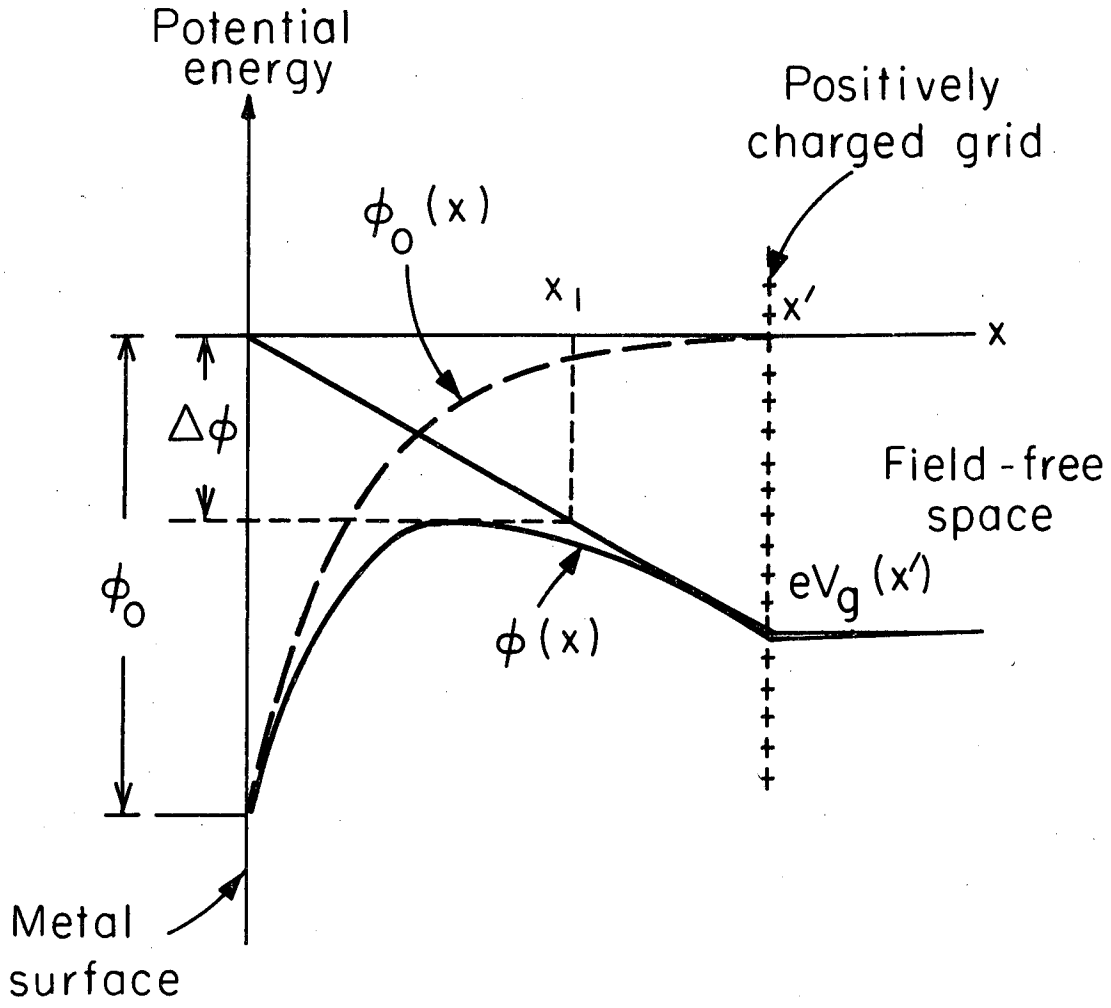
Potential energy
Positively charged grid
$\phi_0(x)$
x_1
x'
x
$\Delta\phi$
Field-free space
ϕ_0
$eV_g(x')$
$\phi(x)$
Metal surface
MUB-9818

Fig. VI. 1

ions and atoms, respectively, in such a manner that $\theta = \theta_i + \theta_a$, and M_i, M_a are the dipole moments per adsorbed ion and atom respectively. The dipole moments M_i, M_a are equal to the dipole moments at zero coverage M_{io}, M_{ao} reduced by the depolarizing electric field $\mathcal{E}$ due to all the other dipoles,

$$M_i = M_{io} - a_i\mathcal{E}, \quad M_a = M_{ao} - a_a\mathcal{E}, \tag{VI-2}$$

where a_i, a_a are the polarizabilities of the adsorbed ions and atoms, respectively. Now $M_{io} = 2\ e\ r_i$, where r_i is the distance of the cesium-ion nucleus from the image plane; r_i is approximately equal to the ionic radius (Sec. IV.E).

Rasor and Warner estimated the magnitude of the depolarizing electric field $\mathcal{E}$ as follows: because the adsorbed particles constituting the dipole layer occupy discrete positions on the surface, the effects of the dipoles extend beyond the plane defined by the cesium-ion nuclei. Therefore an ion at a distance r_i from the image plane penetrates a certain fraction f (called the penetration factor) of the potential energy difference $\Delta\phi$ due to the dipole layer. Or, in other words, the potential energy of an adsorbed ion in the field of all the other adsorbed ions and their image charges is $(1-f)\Delta\phi$. Hence, the electric field $\mathcal{E}$ in the vicinity of the nuclei of each adsorbed particle is approximately

$$\mathcal{E} \approx [(1-f)\Delta\phi]/er_i\ . \tag{VI-3}$$

Next, in order to express Eq. (VI-1) in terms of θ rather than θ_i, we need a relation between θ_i and θ_a. Referring to Sec. IV.A, we see that the desired expression is given by Eq. (IV-8)

$$\frac{\theta_i}{\theta_a} = \frac{g_i}{g_a} \exp\ (E/kT_E) \tag{VI-4}$$

or

$$\theta_i = \left[1 + \frac{g_a}{g_i} \exp(-E/kT_E)\right]^{-1} \theta \qquad \text{(VI.5)}$$

where E is the energy required to neutralize an ion on the surface. Combining Eqs. (VI.1) to (VI.5) Rasor and Warner arrived at the relation between work function and total surface coverage

$$\Delta\phi = \frac{4\pi e^2 \sigma r_i \theta \{1 - [a_i(1-f)/2e^2 r_i^2] \Delta\phi\}}{1 + \frac{g_a}{g_i} \exp(-E/kT_E)} \left(1 + \frac{M_a \theta_a}{M_i \theta_i}\right). \qquad \text{(VI.6)}$$

(Note, this is to be compared with Eq. (VI.8), Reference 76, which is not dimensionally correct.) From the definition of f given above, it follows that the adsorbed dipole layer has increased the ion desorption energy $\phi_i(\theta)$ by an amount $f\Delta\phi$ over its value ϕ_{io} for the bare surface. So, the change in the heat of desorption of ions is

$$\Delta\phi_i = \phi_i - \phi_{io} = f\Delta\phi \,. \qquad \text{(VI.7)}$$

Combining Eqs. (VI.7) and (IV.14) and (IV.15) and solving for E, one obtains

$$E = E_o - (1-f)\Delta\phi + \Delta\phi_a, \qquad \text{(VI.8)}$$

where

$$\Delta\phi_a = \phi_{ao} - \phi_a. \qquad \text{(VI.9)}$$

It also follows, from Eqs. (VI.8), (VI.9), and (IV.16), that

$$\frac{\Delta\phi_a^*}{\Delta\phi} = 1-f \qquad \text{(VI.10)}$$

where

$$\Delta\phi_a^* = \phi_{ao}^* - \phi_a^* = E_o - E + \Delta\phi_a \,. \qquad \text{(VI.11)}$$

Rasor and Warner assumed that $M_a\theta_a/M_i\theta_i << 1$ and $\Delta\phi_a << kT_E$; by combining Eqs. (VI.6) and (VI.8) and rearranging terms we obtain the result shown in Eq. (1) of Table VI.I.

2. Theory of Carabateas, Stickney, and Aponick

Carabateas et al. also considered the existence of ions and neutral atoms on the surface and started their analysis with Eq. (VI.1) above.[16] However, for M_i and M_a they used somewhat different expressions than those given by Eqs. (VI.2) and (VI.3). Using approximately their notation, we have

$$\Delta\phi = 4\pi e\sigma\,(M_i\theta_i/2 + M_a\theta_a) = \Delta\psi_i - \Delta\psi_a \qquad \text{(VI.12)}$$

where

$$\Delta\psi_i = 2\pi e\sigma\, M_i\theta_i \qquad \text{(VI.13)}$$

and

$$\Delta\psi_a = -4\pi e\sigma\, M_a\theta_a . \qquad \text{(VI.14)}$$

The quantities $\Delta\psi_i$ and $\Delta\psi_a$ are the changes in potential energy that an electron leaving the metal surface experiences in going through the dipole layers of the adsorbed ions and atoms, respectively.

At first glance it seems that Eqs. (VI.1) and (VI.12) are different by a factor of 2 in the atomic dipole moment term. However, it appears that the definitions of M_a used in the two studies differ by the factor of 2. The dipole moment M_a in Eq. (VI.1) is defined as the net dipole moment of the adsorbed polarized atom and its polarized image in the metal; whereas M_a in Eq. (VI.12) is defined by Carabateas et al. as being simply the dipole moment of the adsorbed polarized atom, without regard to its image. Clearly, the latter dipole moment M_a is half of that defined in

Eq. (VI.1); therefore, with these definitions Eqs. (VI.1) and (VI.12) are consistent.

In contrast to the previous theory, Carabateas et al. did not neglect the dipole moment of the adsorbed atoms. They evaluated it in the same manner, by means of Eqs. (VI.2) and (VI.3); however they neglected the dipole moment at zero coverage M_{ao}. In effect,

$$M_a \approx -a_a \mathcal{E} \approx -a_a(1-f)\Delta\phi/er_i. \qquad \text{(VI.15)}$$

For the dipole moment of the ions they used, without explanation, the expression

$$M_i = M_{io}\left(\frac{1 - 2\pi a_i \sigma\theta_i(1-f)/r_i}{1 + 2\pi a_i \sigma\theta_i(1-f)/r_i}\right), \qquad \text{(VI.16)}$$

where as before $M_{io} = 2er_i$. For clarification Eq. (VI.16) can be written as follows,

$$M_i = M_{io}\left(\frac{1 - 2a_i \mathcal{E}_i/M_{io}}{1 + 2a_i \mathcal{E}_i/M_{io}}\right), \qquad \text{(VI.17)}$$

where $\mathcal{E}_i$ would be the depolarizing electric field due to the ion dipole layer, without considering the depolarization action of the ions on the field; comparing Eqs. (VI.13), (VI.16), and (VI.17), the field $\mathcal{E}_i$ is defined by a relation similar to Eqs. (VI.3). That is,

$$\mathcal{E}_i = (1-f)\Delta\psi_{io}/er_i, \qquad \text{(VI.18)}$$

where

$$\Delta\psi_{io} = 2\pi e\sigma M_{io}\theta_i. \qquad \text{(VI.19)}$$

The term $\Delta\psi_{io}$ is the potential energy drop across the dipole layer of the adsorbed ions in the absence of depolarization effects.

Carabateas et al. related θ_i and θ_a by Eq. (VI.4); however they tacitly neglected the statistical weighting factor g_i/g_a, which equals 1/2 according to the simplest assumption. They used an expression for E, the energy required to neutralize an ion on the surface, which is slightly different from Eq. (VI.8). They argued that because the radius of adatoms (about 2.7Å) is considerably greater than that of adions (about 1.8Å), an ion escaping the surface travels through the entire dipole layer of the polarized adatoms but through only the fraction f of the adion dipole layer; therefore the effect of adsorbed cesium on the ion desorption energy is

$$\Delta\phi_i = \phi_i - \phi_{io} = f\Delta\psi_i - \Delta\psi_a \ . \qquad \text{(VI.20)}$$

Combining Eqs. (VI.20), (IV.14) and (IV.15) and solving for E yields

$$E = E_o - (1-f)\Delta\psi_i + \Delta\phi_a \ . \qquad \text{(VI.21)}$$

Like Rasor and Warner, Carabateas et al. neglected the term $\Delta\phi_a$ in Eq. (VI.21). In analogy with Eq. (VI.10) it follows that

$$\frac{\Delta\phi_a^*}{\Delta\psi_i} = 1-f \ . \qquad \text{(VI.22)}$$

Combining Eqs. (VI.12) to (VI.22) yields the result shown in Eq. (1) of Table VI.I.

3. Theory of Gyftopoulos and Levine.

The analysis of Gyftopoulos and Levine differs from the previous two in two main respects.[35,58-60] First, they do not make the distinction

that an adsorbed particle is an ion or an atom; and second they pointed out that the adsorbed particles will change the work function of a surface whether or not they are ionized, because as the surface becomes completely coated its work function must eventually be that of the adsorbate. In essence, besides any dipole layer effect, the adsorbate alters the height of the potential barrier (above the Fermi level) at the surface by changing the position of the Fermi level. Hence the expression used by Gyftopoulos and Levine for $\Delta\phi$ versus θ contains the usual dipole term plus another term to account for the latter effect, which they call the change in the electronegativity barrier,

$$\Delta\phi = (\phi_o - \phi_f)[1 - G(\theta)] + 4\pi e\sigma M\theta \,, \qquad \text{(VI.23)}$$

where ϕ_f is the bare work function of the adsorbate and

$$G(\theta) = 1 - 3\theta^2 + 2\theta^3 \,; \qquad \text{(VI.24)}$$

$G(\theta)$ is a polynominal arbitrarily chosen so that its derivative is zero when θ is 0 and 1, and the value of the electronegativity barrier is ϕ_o when θ is 0 and equal to ϕ_f when θ is 1. The expression for the dipole moment M chosen by Gyftopoulos and Levine is different still from that of the two studies described above.

$$M = M_2 - a_o \mathcal{E} \,, \qquad \text{(VI.25)}$$

where M_2 is the dipole moment in the absence of dipole-dipole interraction. Assuming that the dipoles are uniformly distributed in a square array, they estimated that the depolarizing field is

$$\mathcal{E} = 9\sigma^{3/2}\,\theta^{3/2}\,M \,. \qquad \text{(VI.26)}$$

They evaluated the dipole moment M_2 as follows:

$$M_2 = M_1/(1 + a_o R^3) = M_o G(\theta)/(1 + a_o/R^3) , \qquad (VI.27)$$

where M_o is the dipole moment of a single adsorbate-substrate dipole at zero coverage, M_1 which is equal to $M_o G(0)$ is the dipole moment of a single dipole when the surface is partially covered (M_1 reflects the change in the effective charge of the dipole with coverage), M_2 accounts for the reduction in the dipole moment due to self-depolarization, R is the sum of the adsorbate and substrate covalent radii. They calculated M_o in terms of the electronegativity, using a constant deduced from existing data on the relationship between molecular dipole moments and electronegativities.

$$M_o = 2.03 \times 10^{-18} (\phi_o - \phi_f) \cos\beta, \text{ in esu} \cdot \text{cm}, \qquad (VI.28)$$

where $\cos\beta = (1 - 1/2\ \sigma_m R^2)^{1/2}$, and σ_m is the surface density of substrate atoms. The term $\cos\beta$ arises because M_o was calculated to be the component, normal to the surface, of the vector sum of the dipole interactions between one adsorbate particle and four substrate atoms (i.e., it was assumed $\sigma_m = 4\sigma$) arranged on a square lattice. Combining Eqs. (VI.23) to (VI.28) and converting esu to eV yields the result shown in Eq. (1) of Table VI.I. It was postulated that an effective charge eF could be associated with the dipole moment M_2, so that by definition

$$F = \frac{M_2}{eR\cos\beta} = \frac{0.422\ (\phi - \phi_f)\ G(\theta)}{R\ (1 + a_o/R^3)} . \qquad (VI.29)$$

In Eq. (VI.29), F is dimensionless if $(\phi - \phi_f)$ is given in eV, R in angstroms, and a_o in cubic angstroms.

Levine and Gyftopoulos did not use the concept of the penetration factor f. Instead they evaluated the desorption energy of atoms ϕ_a^* as a function of surface coverage, assuming this energy consists of separable ionic and covalent parts H_{ii} and H_{cc}, respectively:

$$\phi_a^* = H_{ii} + H_{cc} = F\phi(1+\delta) + (\phi_f' \phi_m')^{1/2} S_{fm}(1-F^2/\nu^2)^{1/2} \quad \text{(VI.30)}$$

where

$$\delta = F(e^2/R - V_i)/\phi \ . \quad \text{(VI.31)}$$

In Eq. (VI.30), ϕ_m' and ϕ_f' are the heats of sublimation of substrate and adsorbate, respectively, ν is the number of valence electrons participating in the covalent bond (equal to 1 for the alkali metals), and $S_{fm} = 2(S_f/S_m + S_m/S_f)$ is a mean orbital angular-strength factor where S_m and S_f are the angular strength of the valence orbitals of the substrate and adsorbate atoms. The quantity V_i in Eq. (VI.31) is the ionization potential of the adsorbate. Numerical values of these quantities for cesium and tungsten are given in Appendix R.

The purpose of the quantity δ in Eq. (VI.30) is not clear. Levine and Gyftopoulos mentioned in Ref. 58 that the energy required to remove an adsorbed particle with a fractional charge eF to infinity is e^2F^2/R; a more correct value, based on the image charge theory is half of that. They stated that for F = 1, H_{ii} reduces to the energy required to remove an adsorbed ion from the surface; what they probably meant is that H_{ii}, in this case, is the energy required to convert an adsorbed ion into a free atom at infinity [Eq. (IV.17)] assuming that the ion desportion energy is given by e^2/R. However, at zero coverage there is poor agreement between $H_{ii}(F = 1)$ and experimentally measured values of ϕ_{ao}^* (Sec. IV.E), unless the ion desorption energy in this theory is about $e^2/2R$.

4. Equation of State for Adsorbed Cesium.

We have now presented three formulations expressing the variation of work function with the surface coverage of the adsorbate. Unfortunately, as with most similar experiments, we were not able to measure the surface coverage θ directly. Rather we measured the current-voltage characteristics of the diodes as a function of emitter and cesium reservoir temperatures. Rasor and Warner have shown that a relation between these two temperatures and the surface coverage can be obtained from a consideration of the evaporation rates of cesium from the reservoir and the emitter. When electron current is drawn, the electric field at the emitter surface prevents the emission of ions. Hence at steady state the evaporation rate of neutral atoms n_a from the emitter is equal to the incident flux of cesium n_o.

$$n_a = n_o \qquad \text{(VI.32)}$$

In thermodynamic equilibrium n_o is equal to the flux of cesium evaporating from the cesium reservoir

$$n_o = C \exp\left(\frac{-h}{kT_{Cs}}\right), \qquad \text{(VI.33)}$$

where h (= 0.75 eV) is the heat of evaporation of cesium from a liquid cesium surface, and

$$C = g_a' \omega_{Cs} \sigma_{Cs} = 1.3 \times 10^{27}/\text{cm}^2\text{sec}, \qquad \text{(VI.34)}$$

according to Langmuir's data (Sec. V.A). Now g_a' is the statistical weight of the cesium vapor, ω_{Cs} is the vibrational frequency and σ_{Cs} the surface density of atoms on the liquid cesium surface. As shown in Sec. IV.A, Eqs. (IV.18) and (IV.27), n_a is of the form

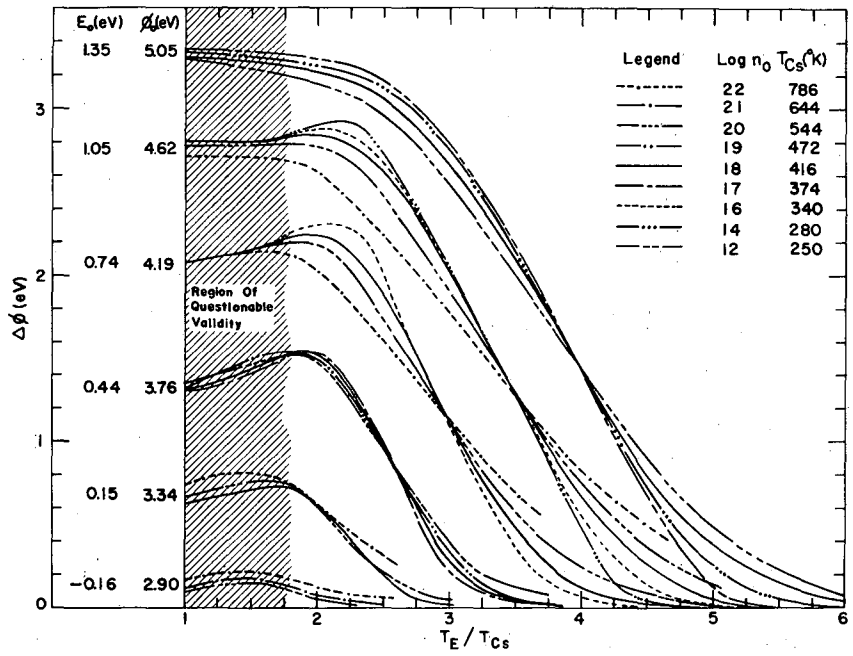

MU-36993

Fig. VI.3

In each of the studies described, a different expression was used for each of these three calculations. It should be immediately apparent therefore that in order to obtain a detailed comparison between the theories and experiments the experimenter should ideally measure ϕ, ϕ_a^* (or ϕ_i) and θ for a given T_E and T_{Cs}.

B. Discussion of Results

Our procedure to obtain the complete current-voltage characteristics of the diodes operating in cesium vapor was described in Sec. V.A. The temperature range of the emitter at which we obtained useful electron emission data was 850 to 1450°K and that of the cesium reservoir was 40 to 100°C. As mentioned earlier, the premature failure of both diodes prevented us from extending our measurements to higher cesium temperatures.

The current-voltage curves were measured point by point with the test circuit described in Sec. III.B. The maximum electron current-density drawn from either the (110) or (100) diode was about 10^{-2} amperes/cm^2; hence the corresponding electron cooling of the emitter (essentially the product of the emitter work function per electron in volts and the emitted electron current) was negligible.

A 60-cps ac sampling circuit was designed and built because we had expected to extend our measurements to include current densities on the order of 10 amperes/cm^2; in this region the electron cooling becomes an appreciable fraction of the heating power into the emitter. The idea behind the use of an ac circuit is that the heat capacity of the emitter prevents its temperature from varying appreciably although the electron emission, and therefore the electron cooling, changes with the applied voltage. The test circuit, described in detail in Appendix L, was not

completed in time to be used in this study. Through its use the diode voltage would have been varied sinusoidally 60 times a second; but by the use of a sampler the resulting current-voltage curve, or any part of it, would have been conveniently displayed on an X-Y plotter, in a time selectable from 3 to 60 seconds.

The electron current-voltage curves that we observed (point by point) were essentially free of peculiarities and were similar to the vacuum data described in Sec. III. This similarity was to be expected because the conditions for a collisionless plasma were satisfied in the range of cesium pressure and interelectrode spacing (0.010 to 0.020 in.) at which the diodes operated. The observed electron emission was therefore truly representative of the work function of the electrodes and was not influenced by plasma sheaths and transport phonomena which occur at higher cesium pressures when the mean free paths of the electrons and cesium ions are smaller than the interelectrode spacing.

The electron-current distribution (i.e., the Boltzmann line) in the retarding potential region of the I-V curves, was readily measurable whenever the emitter work function was low enough that the ion emission from the emitter was negligible compared to the saturation electron emission. The slope of the Boltzmann lines yielded electron temperatures 50 to 100°C greater than the measured emitter temperatures. Under these conditions and in the absence of space-charge limitations, the knee (contact potential) of the current-voltage curves was very sharply defined (within 50 mV), and the contact potential was measured with a precision of 0.01 eV. From these measurements and the calculated value of the emitter work function, the work function of the cesiated collector in each diode was determined; it was found to vary within the range 1.95±0.05 eV and 1.85±0.05 eV

for the (100) and (110) diodes, respectively, as the collector-to-cesium-reservoir temperature ratio ranged from 1.1 to 1.3.

The field-free electron emission J_{so} was determined from the intercept, at zero inter-electrode potential, of Schottky plots of the observed saturation electron currents. The saturation currents were measured in the range 0 to 100 V for the (100) diode and 0 to 20 V for the (110) diode. The emitter work function ϕ was evaluated at each observed combination of T_E and T_{Cs} by means of the Richardson equation,

$$\phi = kT_E \left[\ell nA - \ell n(J_{so}/T_E^2) \right], \qquad \text{(VI.44)}$$

where, to be consistent, the value of the Richardson constant A used in this calculation was 238 ampere/cm^2°K^2 and 207 ampere/cm^2°K^2 for the (100) and (110) crystals respectively, as determined from our vacuum data.

All of the field-free electron emission data that we obtained for both diodes are displayed in Figs. VI.4 and VI.5 (so-called Langmuir S-curves). In addition, the data have been tabulated in Tables Q.I and Q.II of Appendix Q. The lines of constant negative slope in Figs. VI.4 and VI.5 represent thermionic emission at the constant emitter work function indicated on the lines; these lines were calculated with Eq. (VI.44) and the above values of A. The points on the S-lines are the experimentally determined emissions at constant cesium-reservoir temperature (therefore constant flux of cesium incident on the emitter). The S-curves were extrapolated beyond the range of the data by means of the curves shown in Figs. VI.6 and VI.7. Figure VI.6 is a plot of the change in the (100) emitter work function, $\Delta\phi(100)$ versus T_E/T_{Cs}. Because of the uncertainties discussed in Sec. V.B, the data for the (110) crystal shown in Figs. VI.5 and VI.7 could not be related to the bare surface properties determined in

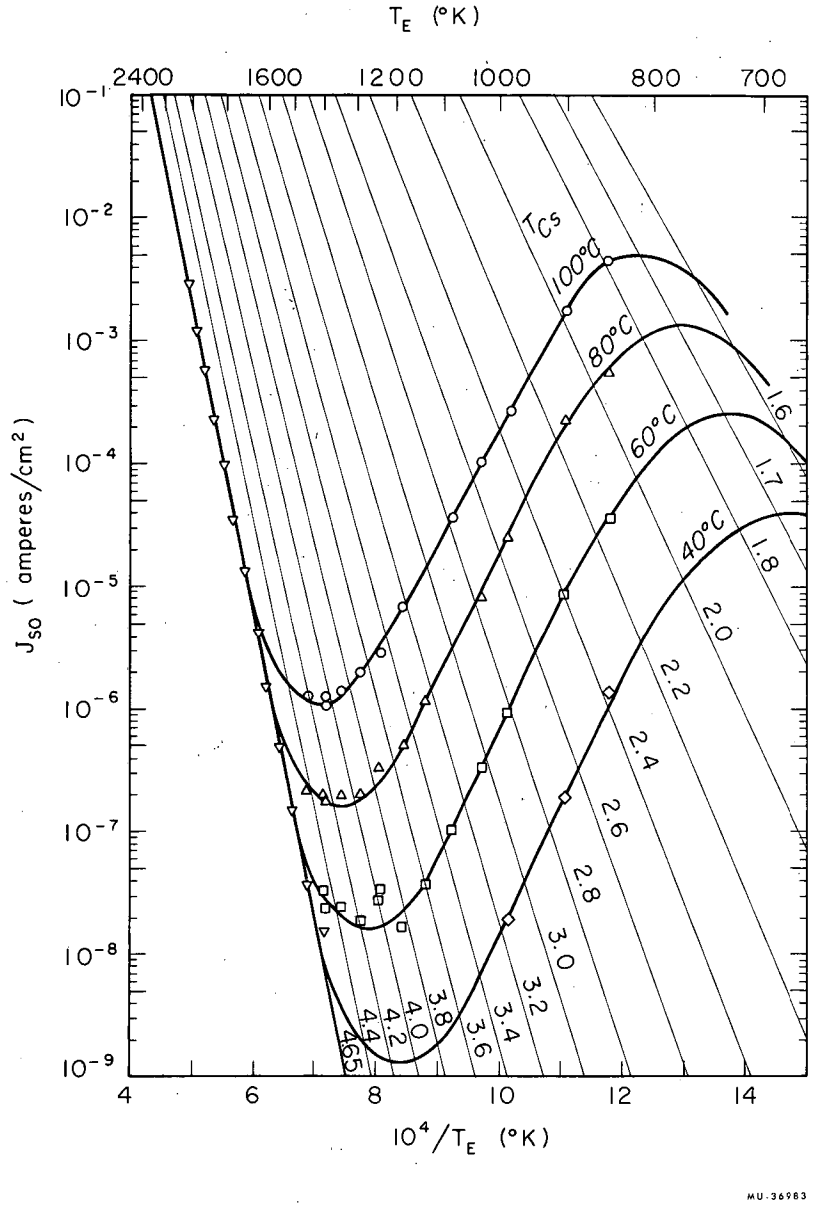
T_E (°K)
2400
1600
1200
1000
800
700
10^{-1}
10^{-2}
10^{-3}
10^{-4}
10^{-5}
10^{-6}
10^{-7}
10^{-8}
10^{-9}
J_{so} (amperes/cm^2)
T_{Cs}
100°C
80°C
60°C
40°C
1.6
1.7
1.8
2.0
2.2
2.4
2.6
2.8
3.0
3.2
3.4
3.6
3.8
4.0
4.2
4.4
4.65
4
6
8
10
12
14
$10^4/T_E$ (°K)
MU-36983

Fig. VI.4

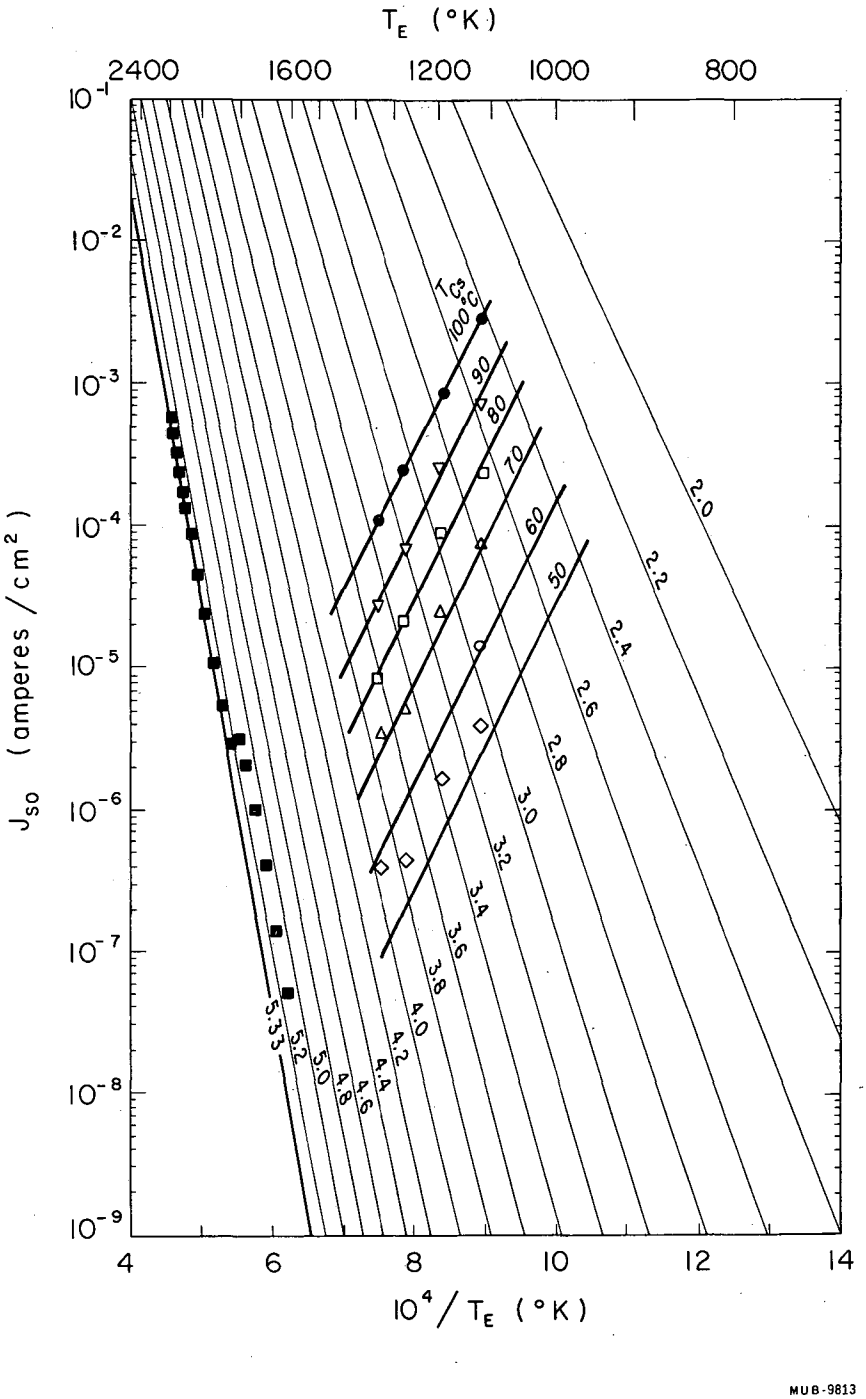
T_E (°K)
2400
1600
1200
1000
800
10^{-1}
10^{-2}
10^{-3}
10^{-4}
10^{-5}
10^{-6}
10^{-7}
10^{-8}
10^{-9}
J_{so} (amperes / cm^2)
T_c, °C
100
90
80
70
60
50
2.0
2.2
2.4
2.6
2.8
3.0
3.2
3.4
3.6
3.8
4.0
4.2
4.4
4.6
4.8
5.0
5.2
5.33
4
6
8
10
12
14
$10^4 / T_E$ (°K)
MUB-9813

Fig. VI.5

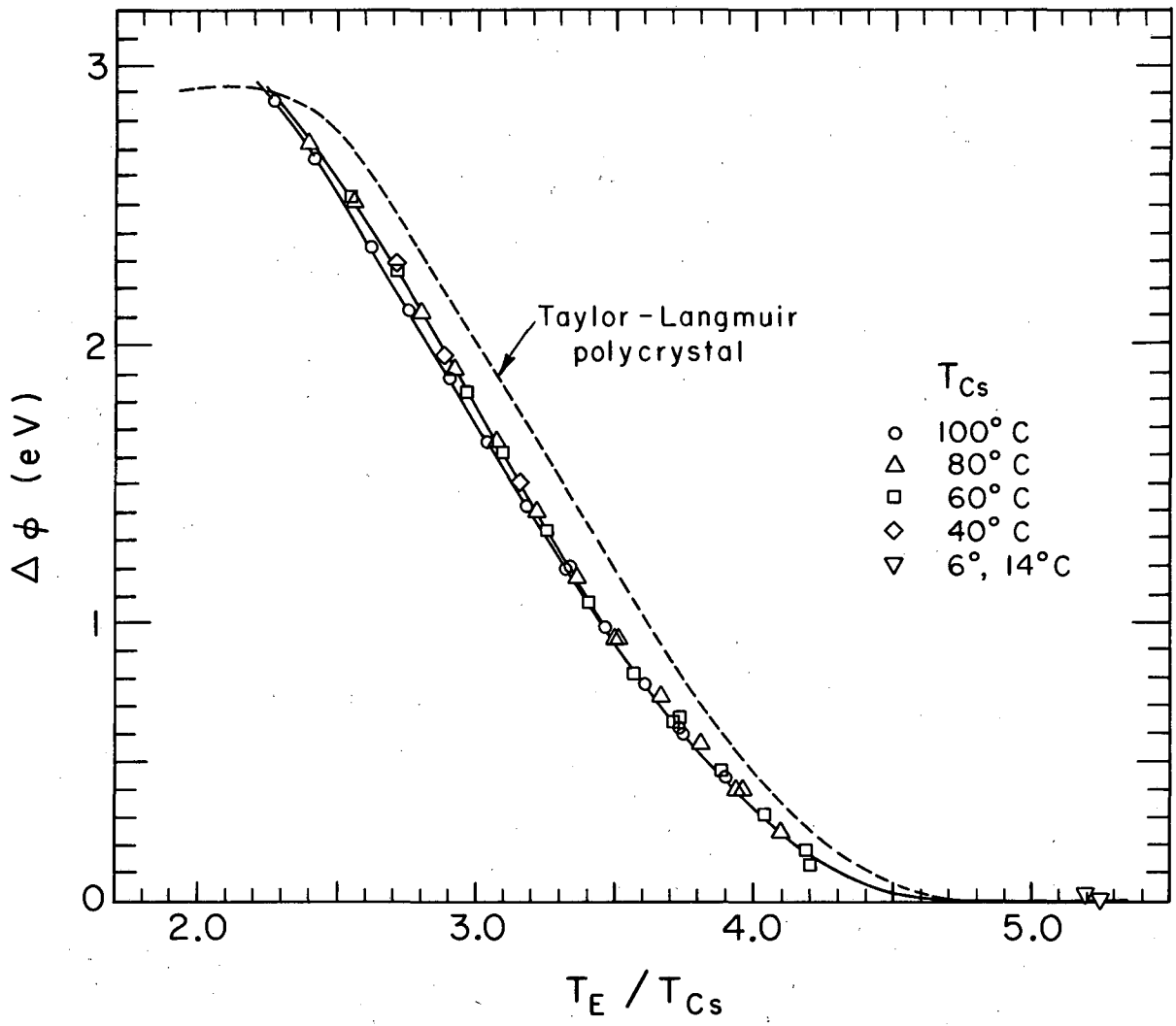
3
2
1
0
Δ φ (eV)
2.0
3.0
4.0
5.0
T_E / T_Cs
Taylor - Langmuir
polycrystal
T_Cs
100° C
80° C
60° C
40° C
6°, 14°C
MUB-9526

Fig. VI.6

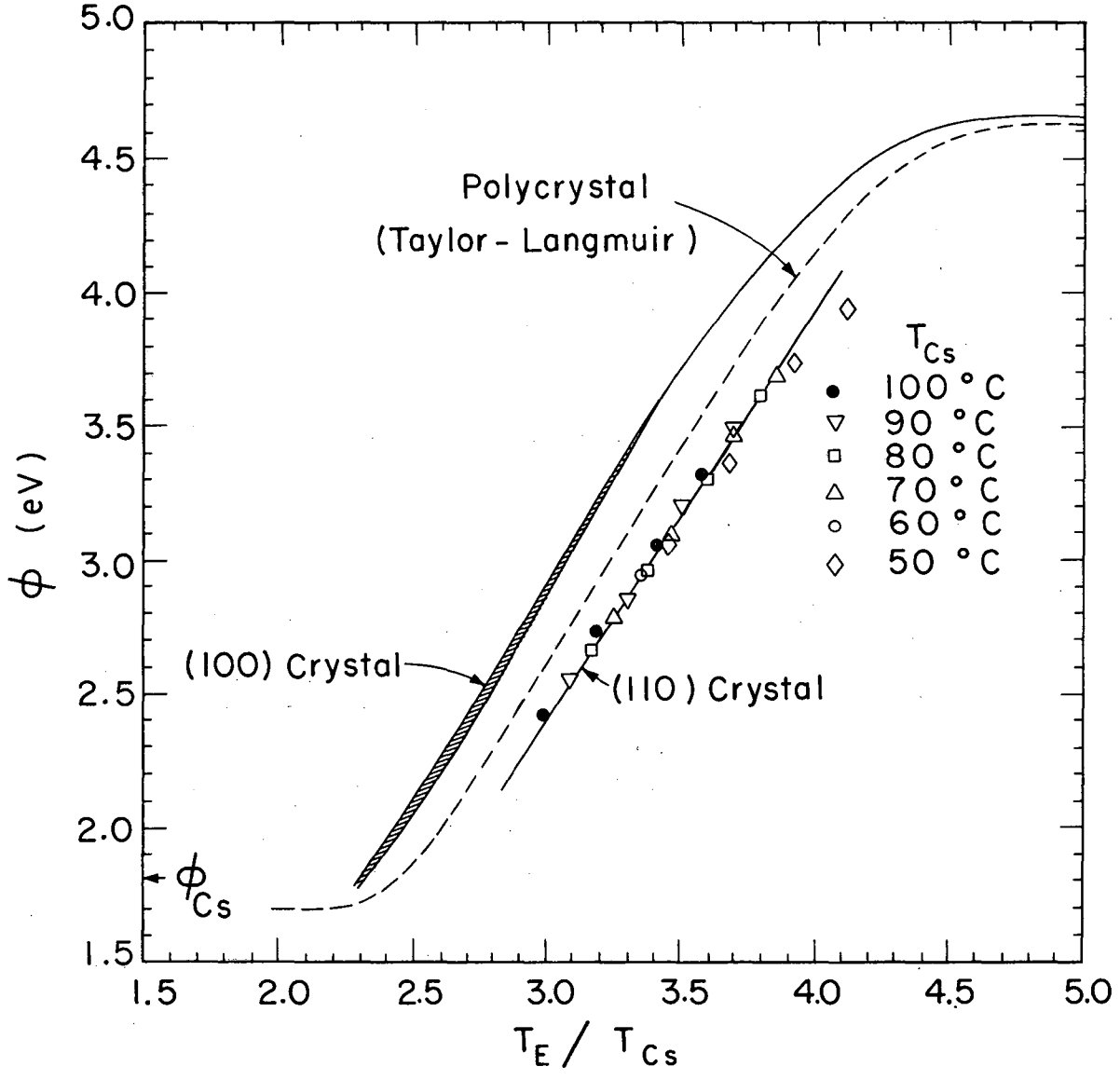
5.0
4.5
4.0
3.5
3.0
2.5
2.0
1.5
φ (eV)
Polycrystal
(Taylor - Langmuir)
(100) Crystal
(110) Crystal
ϕ_{Cs}
T_{Cs}
100 °C
90 °C
80 °C
70 °C
60 °C
50 °C
1.5
2.0
2.5
3.0
3.5
4.0
4.5
5.0
T_E / T_{Cs}
MUB-9814

Fig. VI.7

Secs. III and IV; consequently these data will not be discussed any further. The lower of the two distinct but narrowly separated lines in Fig. VI.6 has been drawn through the data points obtained at a cesium-reservoir temperature of 100°C, and the upper line has been drawn through the data points obtained at all the lower cesium-reservoir temperatures from 40 to 80°C. This behavior agrees qualitatively with the theoretical predictions of Rasor and Warner (Fig. VI.3), which indicate that the slopes of the $\Delta\phi$ versus T_E/T_{Cs} curves at constant cesium-reservoir temperature become shallower as that temperature increases. We wish to recall at this point the excellent agreement between the data shown in Fig. VI.6 and the similar results obtained from ion emission (Fig. V.7). This agreement is an indication of the uniformity of the work function over the (100) crystal surface.

C. Comparison with Data of Taylor and Langmuir

We now compare our results for the (100) crystal (Fig. VI.6) with those of Taylor and Langmuir[88] for polycrystalline tungsten, shown as the dashed line in the same figure. The Taylor-Langmuir data shown here are also tabulated in Table R.II of Appendix R. They were estimated from Fig. 15 of Ref. 88. The curves for (100) and polycrystalline tungsten shown in Fig. VI.6 are very nearly identical in shape but are displaced horizontally in such a way that at constant $\Delta\phi$

$$\frac{T_E}{T_{Cs}}(100) = \frac{T_E}{T_{Cs}}(\text{poly}) - 0.15 \ . \qquad \text{(VI.45)}$$

This constant lateral offset is demonstrated in Fig. VI.8. We have seen (Secs. III.D and IV.F) that our measurements of the bare work function ϕ_o

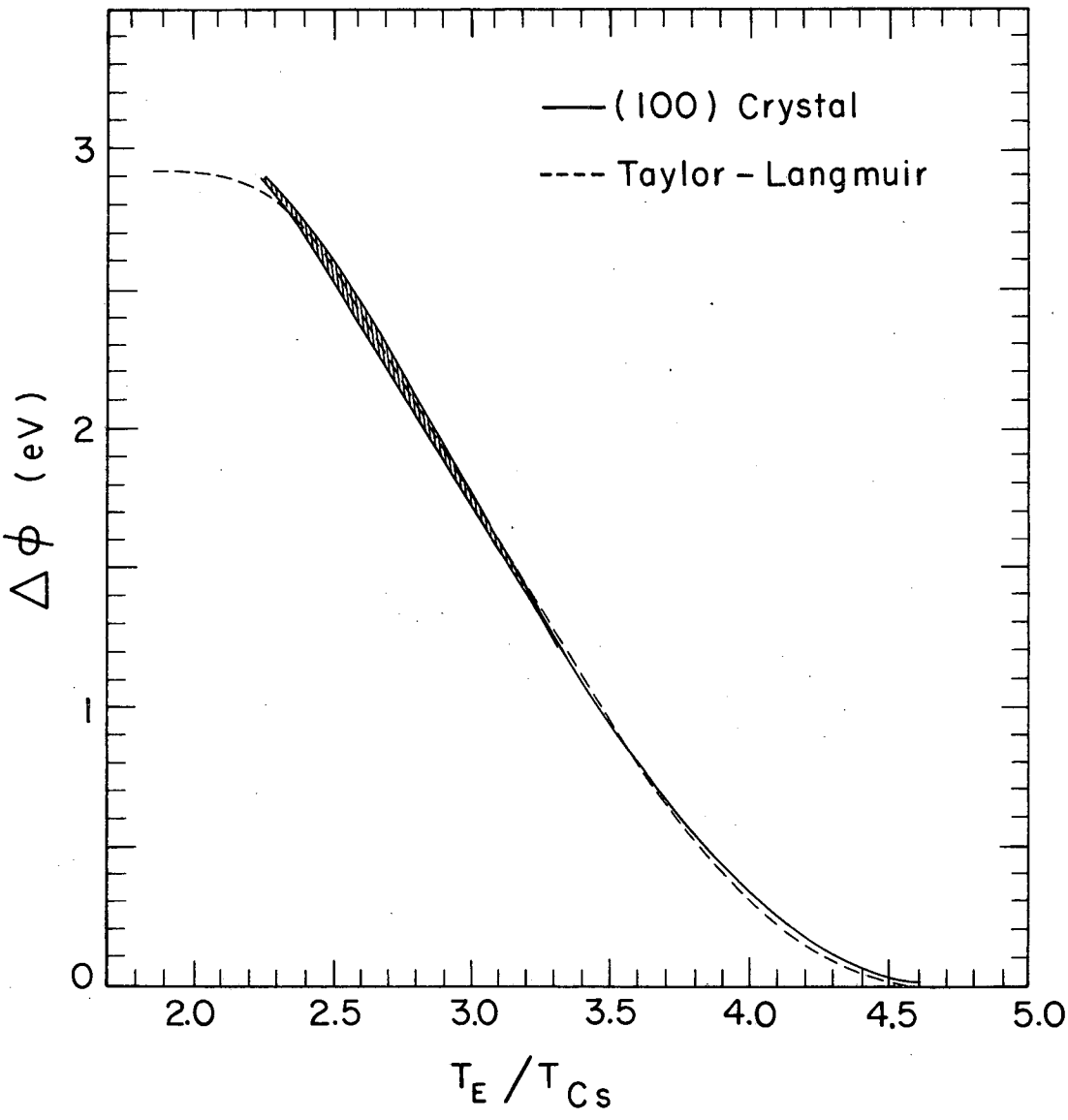
(100) Crystal
Taylor – Langmuir
Δφ (eV)
0
1
2
3
2.0
2.5
3.0
3.5
4.0
4.5
5.0
T_E / T_{Cs}
MUB-9819

Fig. VI.8

and the cesium ion and atom desorption energies ϕ_{io} and ϕ^{*}_{ao} for (100) tungsten are essentially identical with those of Taylor and Langmuir for polycrystalline tungsten [ϕ_o(poly) = 4.62 eV].

We might, for the moment, entertain the possibility that the difference between these two data sets, exemplified by Eq. (VI.45), is due to differences in the vibrational frequency ω of adsorbed cesium and/or to differences in the surface density σ of an adsorbed cesium monolayer. This possibility is suggested by Eqs. (VI.36) and (VI.42) which show that these properties affect the surface coverage and work function depression that occur for a given T_E and T_{Cs}. Let us assume first that the differences between the two curves in Fig. VI.6 are due only to a difference in ω (i.e., Q_a) between the surfaces. Because ϕ_{io} has the same value for (100) and polycrystalline tungsten, we expect that the half width of the dipole layer r_i is essentially the same for both surfaces (assuming ϕ_{io} is equal to the image-charge potential energy). Therefore, under these assumptions $f(\theta)$ should be similar for both surfaces [Eq. (VI.40)]. The frequency ω does not enter into the evaluation of $\Delta\phi(\theta)$ in any of the theories described in Sec. VI.A; hence for a constant θ and T_E and therefore constant $\Delta\phi$ and f we deduce from Eq. (VI.42) that

$$\frac{T_E}{T_{Cs}}(100) = \frac{T_E}{T_{Cs}}(\text{poly}) - \frac{kT_E}{h} \ln\left[\frac{\omega(100)}{\omega(\text{poly})}\right] . \qquad \text{(VI.46)}$$

Comparing Eqs. (VI.46) and (VI.45) and using a mean temperature of 1000°K and a value for h of 0.75 eV (Sec. VI.A.4), we obtain

$$\frac{\omega(100)}{\omega(\text{poly})} = 2.7 . \qquad \text{(VI.47)}$$

This result agrees qualitatively with the experimental findings (summarized in Table IV.I), which yield a ratio of 5.6; however the experimental uncertainty in this ratio is about ±50%.

Although this simple analysis correlates our results very well with those of Taylor and Langmuir, we cannot explain the magnitude of the ratio in Eq. (VI.47) from physical or theoretical considerations. In fact, it appears from our experimental results and the theoretical work of Levine and Gyftopoulos that ω is essentially independent of crystallographic orientation for cesium adsorbed on tungsten (Eq. (IV.51) in Sec. IV.D).

Let us now take the position that the difference in Fig. VI.6 is due only to a difference in adsorption-site density σ between the two surfaces. Taylor and Langmuir thought that the heat treatment to which they subjected their polycrystalline wire emitter resulted in exposing only (110) planes to the surface. From their results they deduced a σ value of 4.8×10^{14} cesium atoms/cm^2, compared to the theoretical value of 3.5×10^{14} atoms/cm^2 based on the lattice spacing of a (110) tungsten surface and assuming one adsorbed cesium atom for every four tungsten atoms. Rasor and Warner, and Carabateas et al. normalized their theoretical treatments to the data of Taylor and Langmuir by using $\sigma_{poly} = \sigma_{110} = 3.5\times10^{14}$ atoms/cm^2 whereas Levine and Gyftopoulos used $\sigma_{poly} = 4.8\times10^{14}$ atoms/cm^2. With these values of σ, the variation of $\Delta\phi$ with θ for the three analyses is compared with the data of Taylor and Langmuir in Fig. VI.9. All the numerical calculations from which the curves in Fig. VI.9 and in the next three figures, were obtained have been tabulated in Appendix R. The variation of $\Delta\phi$ with T_E/T_{Cs} was computed for each analysis with Eqs. (1) to (4) of Table VI.I. Each curve was shifted horizontally by adjusting the ratio $Q_a\sigma/C$, until the curve coincided with the data of Taylor and Langmuir at a value

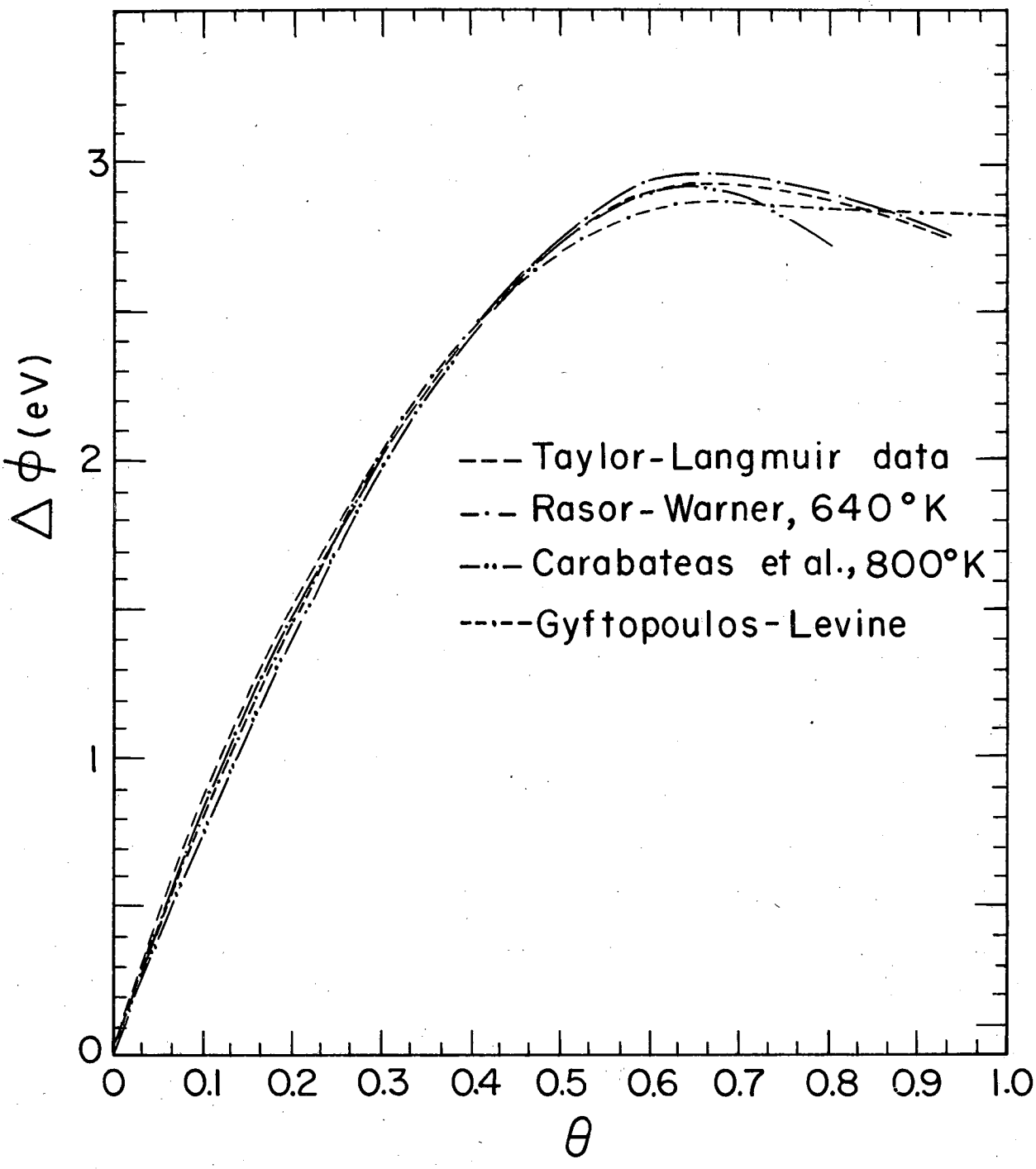
Δφ (eV)
θ
0
1
2
3
0
0.1
0.2
0.3
0.4
0.5
0.6
0.7
0.8
0.9
1.0
--- Taylor-Langmuir data
-·- Rasor-Warner, 640°K
-··- Carabateas et al., 800°K
--·-- Gyftopoulos-Levine
MUB-9815

Fig. VI.9

of $\Delta\phi$ = 2.0 eV, as shown in Fig. VI.10. This value of $\Delta\phi$ was chosen because for all three analyses it occured at a value of $\theta \approx 0.3$ at which $K(\theta) \approx 0$. The ratios $Q_a\sigma/C$ required to match the Taylor-Langmuir data were

Rasor and Warner	$(Q_a\sigma/C)$	= 3.9
Carabateas et al.	$(Q_a\sigma/C)$	= 2.4
Levine and Gyftopoulos	$(Q_a\sigma/C)$	= 0.65

whereas the value of this ratio, determined from the data of Taylor and Langmuir was 0.85. Note that in arriving at the results shown in Figs. VI.9 and VI.10, differing values for T_E, ϕ^*_{ao}, and r_i were used in each analysis as suggested by the authors, and these quantities were not always in agreement with the experimental data of Taylor and Langmuir. Hence Figs. VI.9 and 10 are not to be construed as demonstrating the fundamental differences between the three theories.

The above calculations were repeated for a (100) surface, the only basic difference being that we assumed that $\sigma_{100} = (\sigma_{110}/\sqrt{2}) = 2.5\times10^{14}$ atoms/cm^2. The results are shown in Figs. VI.11 and VI.12. Figure VI.12 shows that the agreement between all three analyses and our experimental data is qualitatively fairly good although not nearly as good as the result of Fig. VI.8. All three methods deviate significantly at large θ or small T_E/T_{Cs}. The methods of Rasor and Warner, and Carabateas et al. inherently predict a decrease in $\Delta\phi_{max}$ for a decrease in σ. This is basically incorrect because regardless of the value of σ the work function of any surface must eventually approach that of a pure cesium surface at large coverage. However the treatment of Levine and Gyftopoulos which takes this fact into account approaches $\Delta\phi_{max}$ too slowly to fit our data. The discrepancies in both $\Delta\phi_{max}$ and the slope of the $\Delta\phi$ vs T_E/T_{Cs} curves for

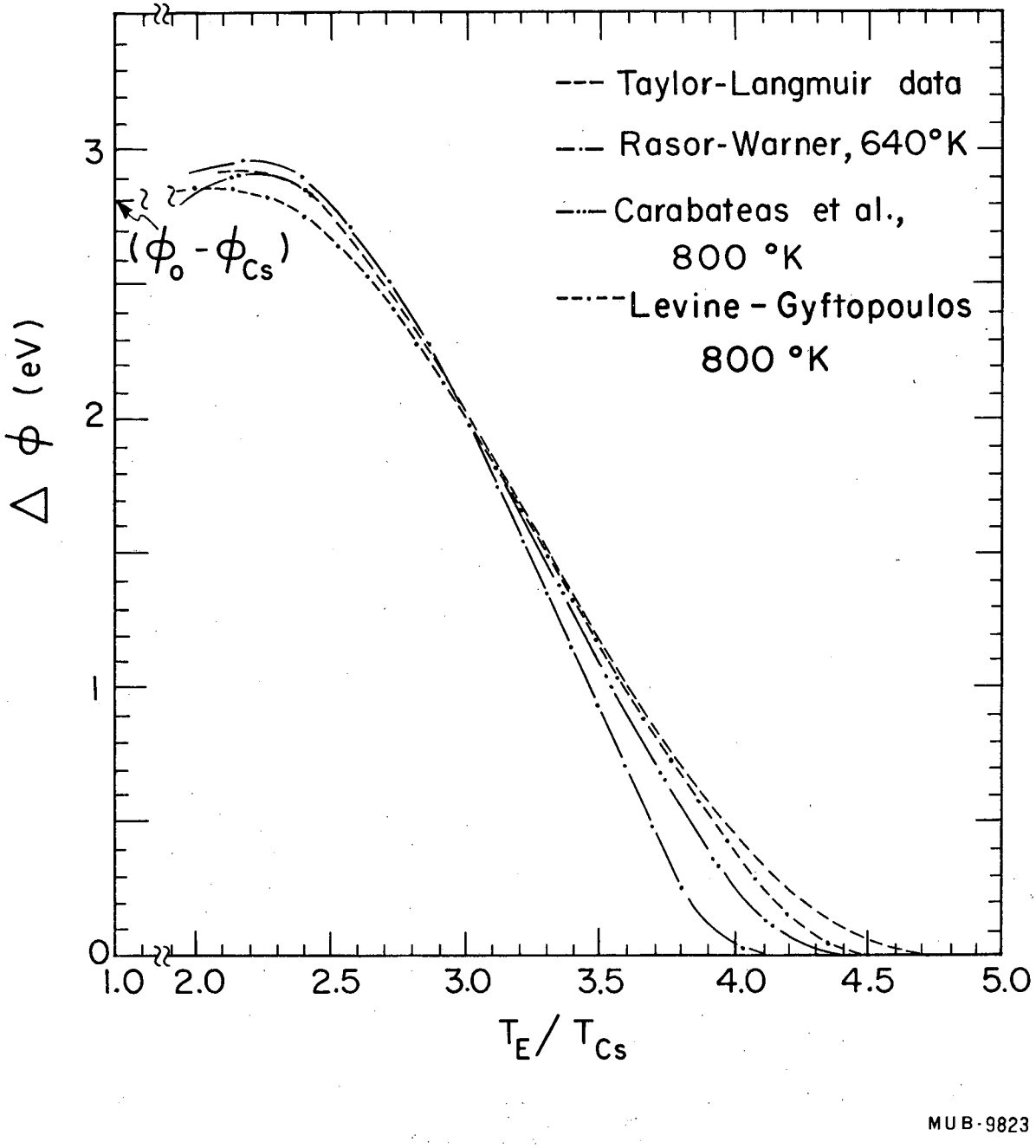
--- Taylor-Langmuir data
-·- Rasor-Warner, 640°K
-··- Carabateas et al., 800 °K
-···- Levine - Gyftopoulos 800 °K
$(\phi_o - \phi_{Cs})$
$\Delta\phi$ (eV)
0
1
2
3
1.0
2.0
2.5
3.0
3.5
4.0
4.5
5.0
T_E / T_{Cs}
MUB-9823

Fig. VI. 10

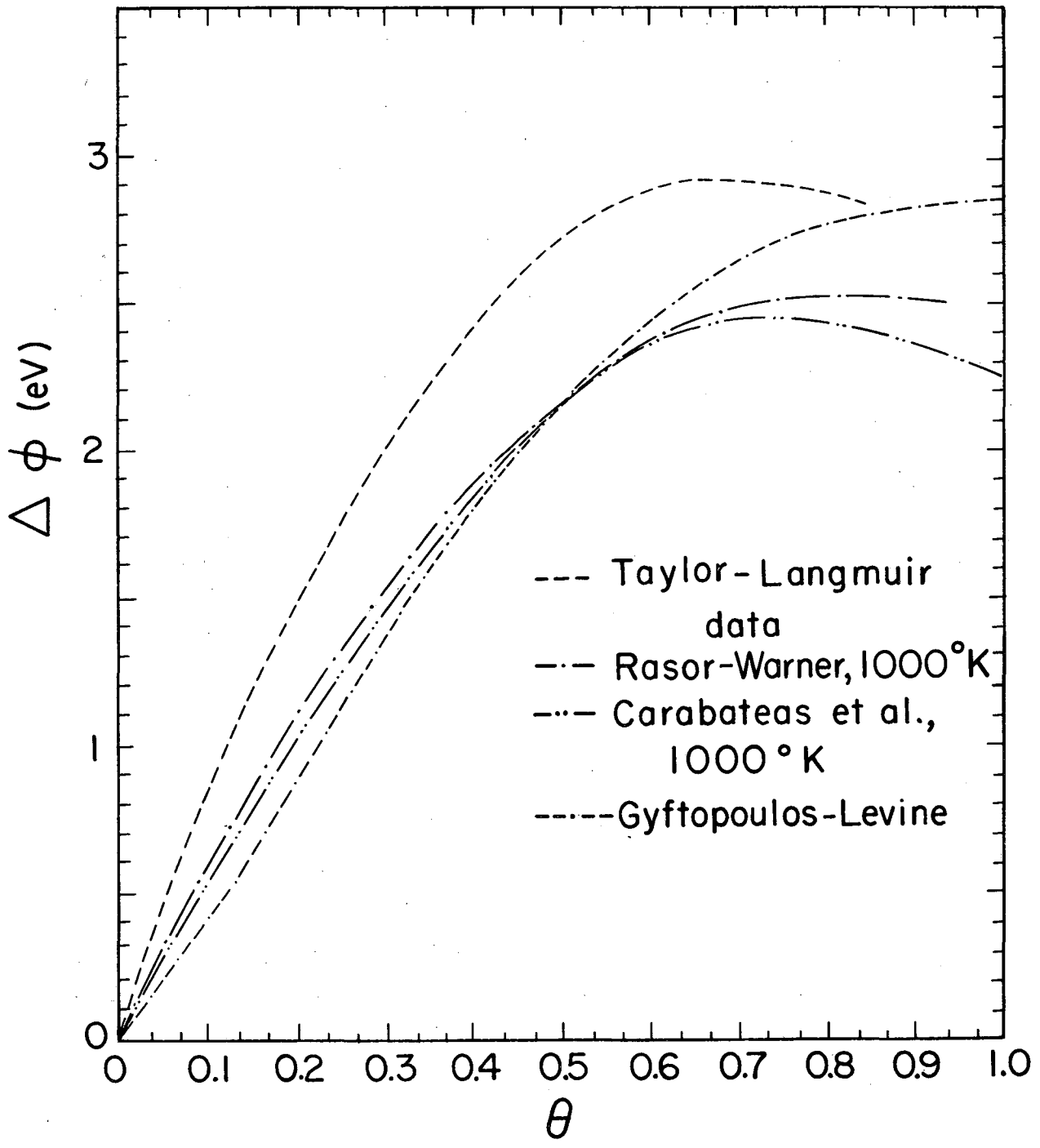
Δ φ (eV)
θ
0
1
2
3
0
0.1
0.2
0.3
0.4
0.5
0.6
0.7
0.8
0.9
1.0
--- Taylor-Langmuir data
-·- Rasor-Warner, 1000°K
-··- Carabateas et al., 1000°K
-·-·-Gyftopoulos-Levine
MUB-9821

Fig. VI. 11

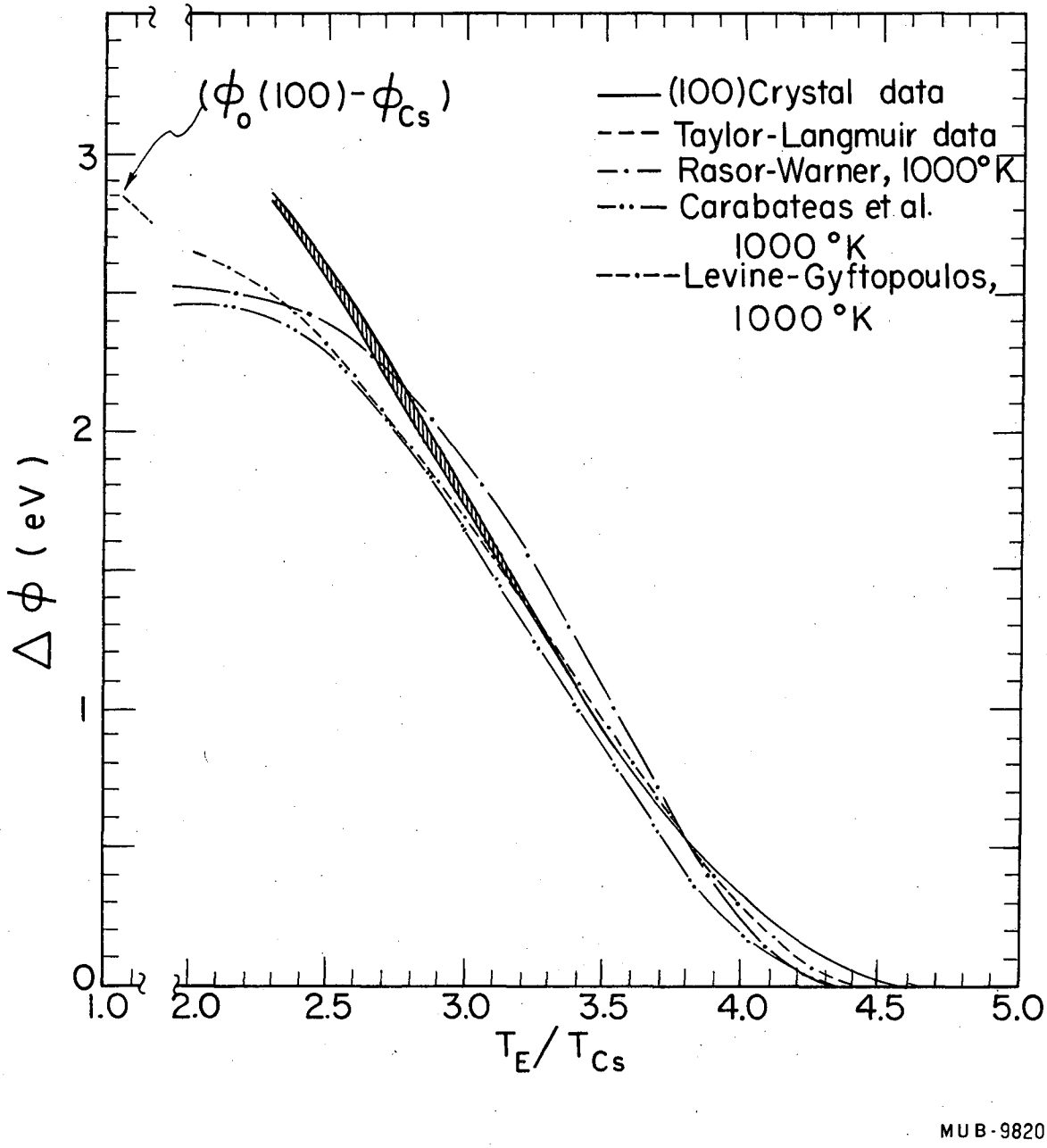
$(\phi_o(100)-\phi_{Cs})$
(100)Crystal data
Taylor-Langmuir data
Rasor-Warner, 1000°K
Carabateas et al. 1000 °K
Levine-Gyftopoulos, 1000 °K
$\Delta\phi$ (eV)
0
1
2
3
1.0
2.0
2.5
3.0
3.5
4.0
4.5
5.0
T_E/T_{Cs}
MUB-9820

Fig. VI. 12

$T_E/T_{Cs} < 3.0$ lead us to the conclusion that the difference between the density of cesium adsorption sites σ on our (100) crystal and on Taylor and Langmuir's polycrystalline wire cannot be nearly as large as $\sqrt{2}$; and that therefore the average surface of Taylor and Langmuir's wire was closer to being a (100) surface than a (110) surface. This view is in agreement with the general belief today that in view of the recent measurements, including our own, of the bare work function of (110) tungsten surfaces (see Table III.4), the data of Taylor and Langmuir were not characteristic of the (110) surface.

We have presented two simple analyses in an attempt to explain the differences between the work function depression of (100) and polycrystalline tungsten as a function of the ratio T_E/T_{Cs}. Neither of these analyses was really successful; and yet the theories described in Sec. VI.A contain no other physical parameters that we could vary, except for the ionic and atomic polarizabilities which we do not expect to depend very much on the metal substrate.

It is likely, therefore, that these differences are a result of the nonuniformity of the polycrystalline surface. The minimum bare work function on a polycrystalline surface cannot be much smaller than 4.62 eV, but we know from our results on the (110) crystal that the maximum bare work function can be greater by 0.7 eV. All three of the theories presented in Sec. VI.A predict that, for a value of T_E/T_{Cs} low enough to result in a significant surface coverage on patches having a bare work function equal to the average bare work function of the polycrystalline surface, the effective work function of the high, bare work-function patches will be lower than that of the patches having the average bare work function. These initially high work-function patches will therefore emit more

electrons per unit area than the patches initially having the average bare work function. We deduce from this discussion that for a given value of T_E/T_{Cs}, a polycrystalline tungsten surface will have a greater electron emission than a uniform tungsten surface with the same bare work function [i.e., (100) crystal]. Because the effective work function is evaluated from the Richardson equation [Eq. (VI.44)], we would expect the observed work function depression of polycrystalline tungsten to be greater than that of the (100) crystal, for the same value of T_E/T_{Cs}. The curves in Fig. VI.6 are in agreement with this expectation. The validity of all three theories becomes questionable as the fractional surface coverage θ approaches unity. However, eventually the work function of the cesiated surface must become that of bare cesium, or in other words the work function depression becomes equal to the difference in the bare work functions of the substrate and adsorbate. Therefore we would expect the maximum work function depression of (100) and polycrystalline tungsten to be about the same. The data shown in Fig. VI.6 tend in that direction (ϕ_{Cs} = 1.8 eV).

In conclusion, we have experimentally demonstrated that the work function depression of a polycrystalline tungsten surface is greater for a given T_E/T_{Cs} ratio than that of a tungsten single crystal having essentially the same bare work function, in qualitative agreement with theoretical predictions based on the nonuniformity of the polycrystalline surface.

It is also evident that the measurement of $\Delta\phi$ versus T_E/T_{Cs} is not sufficient to provide an adequate comparison of the three theoretical analyses that we have presented. It would be desirable to measure $\Delta\phi_a^*$ versus T_E/T_{Cs} in addition, but of course it would be still more desirable to measure θ, as did Taylor and Langmuir.

D. Summary

In Sec. VI we have described three recent analytical methods for predicting the work-function depression of metal surfaces due to the adsorption of alkali atoms (see Table VI.I). They are the work of Rasor and Warner,[75,76] Carabateas, Stickney, and Aponick,[16] and Gyftopoulos and Levine.[35,58-60] We have presented our experimental results for the measurement of the electron emission from the (100) and (110) tungsten crystal exposed to a cesium vapor. The range of emitter and cesium reservoir temperatures were 850 to 1450°K and 40 to 100°C, respectively. The data were presented in the form of Langmuir S-curves, and were also tabulated in Appendix Q. The work function of the emitters was calculated by substituting the observed saturation currents at zero field into the Richardson equation. These results were displayed in the form of $\Delta\phi$ and ϕ vs T_E/T_{Cs} curves and compared with similar curves derived from the data of Taylor and Langmuir on polycrystalline tungsten. We found that for the (100) crystal the slope of the $\Delta\phi$ versus T_E/T_{Cs} curve at constant T_{Cs} tended to decrease as T_{Cs} was increased, in qualitative agreement with the theoretical predictions of Rasor and Warner. For the (100) crystal the shape of the $\Delta\phi$ versus T_E/T_{Cs} curve was closely similar to that of polycrystalline tungsten but displaced towards lower values of T_E/T_{Cs} by an amount of this ratio equal to 0.15. This displacement was analyzed in terms of the theories mentioned above; it appears that the differences in the work function depression for these two surfaces, which have nearly identical bare work functions, is a result of the nonuniformity of the polycrystalline surface. The (110) crystal data were not analyzed in detail for the reasons discussed in Sec. V.B.

VII. WORK-FUNCTION DISTRIBUTION ON EMITTERS

A. Uniformity of Crystal Surfaces

No direct observation of the degree of crystallographic perfection of the surface of either crystal could be made, but qualitative indications of the work function uniformity over the surface of the crystals could be deduced from some of our experimental results. The x-ray Laue patterns that we obtained were very sharp; as mentioned in Sec. II, this sharpness does not insure that either (110) or (100) planes were ever exposed to the surface but it does mean that the crystals were free of gross imperfections near the surface. Deductions concerning the work function distribution were obtained by contrasting results derived from electron emission with corresponding observations obtained from cesium-ion emission. Such a contrast can give information about the work-function distribution because the electron and ion emissions per unit area are weighted differently with respect to the work function. For a given surface area and temperature, electron emission increases exponentially with decreasing work function; whereas ion emission, under conditions of low fractional ionization, increases exponentially with increasing work function. Under conditions of 100% surface ionization, ion emission is independent of work function. It should be evident then that the average work function of a nonuniform surface deduced from electron emission will be lower than that derived from observed ion emission; and strictly speaking, these two determinations will give the same result only when the work function of the surface is uniform (single valued).

Therefore, the excellent agreement (within 0.05eV) that we observed between our determinations of the work function depression of the (100) crystal from electron emission and from ion emission data is a good

indication of the uniformity of the work function over the crystal surface. These two methods agreed only within 0.1eV in the case of the (110) crystal which had by then become contaminated.

Additional estimates of the work-function nonuniformity of a surface can be evaluated by studying the shape of electron and ion current-voltage curves in the retarding potential region; these determinations, which are discussed in Sec. VII.B, require that the collector work function be uniform; hence we could not analyze our vacuum data in this respect because our collector was polycrystalline. However, in cesium vapor the work function of the collector in our experiments was essentially that of a cesium surface, and the shape of the current-voltage curves under these conditions should be representative of the emitter surface. We found for the (100) crystal, as mentioned in Sec. VI.B, that the transition from the saturation region to the retarding potential region of the electron current-voltage curves occurred within 0.05V (in the absence of space charge); we found also that the slope of these log I-V curves agreed with the measured emitter temperature within 50 to 100°C. These two observations are indicative of a fairly uniform emitter work function.

B. Work-Function Distribution from Cesium-Ion Emission

From the electron current-voltage characteristics of a diode, it is possible to determine the fraction of the emitter surface that is occupied by patches having a given work function.[14,74] It occurred to us that a similar and more sensitive determination can be obtained from the cesium-ion current-voltage characteristics of cesium diodes, so long as the minimum work function of the emitter is greater than 3.9V, the ionization potential of cesium.

If the diode is operated under conditions at which the ionization coefficient β of each patch of the emitter is 1, the ion-current density $j_{Cs}(\phi)$ emitted from a patch of work function ϕ (in the absence of space-charge effects), is given by

$$j_{Cs}(\phi) = en_o, \qquad V_E > \frac{1}{e}(\phi - \phi_c) \quad \text{(VII.1)}$$

and

$$j_{Cs}(\phi) = en_o \exp\left(-\frac{\phi - \phi_c - eV_E}{kT_E}\right), \quad V_E < \frac{1}{e}(\phi - \phi_c) \quad \text{(VII.2)}$$

where n_o is the neutral-cesium flux incident on the emitter (equal to the saturation ion-current density), ϕ_c is the collector work function (assumed uniform), V_E (equal to $-V_c$) is the applied emitter voltage relative to the collector, T_E is the emitter temperature, and e is the electronic charge. If it can be assumed that the observed total cesium-ion current J_{Cs} from an emitter of unit area is the sum of the contributions from each patch, then

$$J_{Cs} = \int_{\phi_{min}}^{\infty} j_{Cs}(\phi)\, f(\phi)\, d\phi, \quad \text{(VII.3)}$$

where this analysis is restricted to the case where the minumum work function ϕ_{min} is greater than the ionization potential V_i, and where $f(\phi)\, d\phi$ is the fraction of the emitter surface having a work function between ϕ and $(\phi + d\phi)$. Substituting Eqs. (VII.1) and (VII.2) into (VII.3) we obtain

$$\frac{J_{Cs}}{en_o} = \int_{\phi_{min}}^{(eV_E+\phi_c)} f(\phi)d\phi + \int_{(eV_E+\phi_c)}^{\infty} \exp\left(-\frac{\phi - \phi_c - eV_E}{kT_E}\right) f(\phi)\, d\phi. \quad \text{(VII.4)}$$

Leibnitz'formula for differentiating integrals is

$$\frac{d}{dy}\int_{u_0(y)}^{u_1(y)} f(x,y)dx = f(u_1,y)\frac{du_1}{dy} - f(u_0,y)\frac{du_0}{dy} + \int\frac{\partial f}{\partial y}\,dx; \qquad \text{(VII.5)}$$

Applying Eq. (VII.5) to differentiate Eq. (VII.4) with respect to eV_E, we obtain

$$\frac{d}{deV_E}\left(\frac{J_{Cs}}{en_o}\right) = \frac{1}{kT_E}\int_{(eV_E+\phi_c)}^{\infty} \exp\left(-\frac{\phi-\phi_c-eV_E}{kT_E}\right) f(\phi)\,d\phi; \qquad \text{(VII.6)}$$

and now differentiating Eq. (VII.6) yields

$$\frac{d^2}{d(eV_E)^2}\left(\frac{J_{Cs}}{en_o}\right) = -\frac{1}{kT_E}f(eV_E+\phi_c) + \frac{1}{(kT_E)^2}\int_{(eV_E+\phi_c)}^{\infty}\exp\left(-\frac{\phi-\phi_c-eV_E}{kT_E}\right)f(\phi)d\phi. \qquad \text{(VII.7)}$$

Combining Eqs. (VII.6) and (VII.7) and solving for $f(eV_E+\phi_c')$, we obtain the result

$$f(\phi) = f(eV_E + \phi_c) = Y' - kT_E Y'' \qquad \text{(VII.8)}$$

where

$$Y = J_{Cs}/en_o \qquad \text{(VII.9)}$$

and Y' and Y" are, respectively, the first and second derivatives with respect to eV_E and are determined directly from the observed ion current-voltage characteristics.

As mentioned earlier, a similar result has been derived from electron emission.[74] In this case Eqs. (VII.1) and (VII.2) are replaced by

$$j_e(\phi) = AT_E^2 \exp\left(-\frac{eV_E + \phi_c}{kT_E}\right) \qquad V_E > \frac{1}{e}(\phi - \phi_c) \qquad \text{(VII.10)}$$

and

$$j_e(\phi) = AT_E^2 \exp(-\phi/kT_E) \qquad V_E < \frac{1}{e}(\phi - \phi_c), \qquad \text{(VII.11)}$$

where j_e is the electron current density emitted from the patches with work function ϕ, and A is the Richardson constant. If the collector work function is uniform and J_e is the total electron current from the emitter, then

$$J_e = \int_0^\infty j_e(\phi) f(\phi) d(\phi), \qquad \text{(VII.12)}$$

and in the same manner as before the combination of Eqs. (VII.10) to (VII.12) yields

$$f(\phi) = f(eV_E + \phi_c) = \frac{1}{AT_E^2 \exp(-\frac{eV_E + \phi_c}{kT_E})}\left(\frac{dJ}{deV_E} - kT_E \frac{d^2J}{d(eV_E)^2}\right) = \epsilon' - kT_E\epsilon'', \qquad \text{(VII.13)}$$

where

$$\epsilon = J_e/J_B, \quad J_B = AT_E^2 \exp\left(-\frac{eV_E + \phi_c}{kT_E}\right), \qquad \text{(VII.14)}$$

and ϵ' and ϵ'' are derivatives with respect to eV_E. Note that ϵ' and ϵ'' are not obtained by simple differentiation of the observed electron current-voltage curve, because the factor J_B is a function of voltage.

Equation (VII.8) provides a more sensitive determination of $f(\phi)$ because the maximum ion-current density from any patch is weighted equally (Eq. (VII.1)), whereas the maximum electron-current density from a patch having work function ϕ is weighted according to Eq. (VII.11). This means that the precision with which $f(\phi)$ can be determined from Eq. (VII.8) is independent of ϕ, whereas it decreases as ϕ increases when Eq. (VII.13) is used.

The relative sensitivities of the two methods are demonstrated in Fig. VII.1, which shows the electron and ion currents versus voltage that

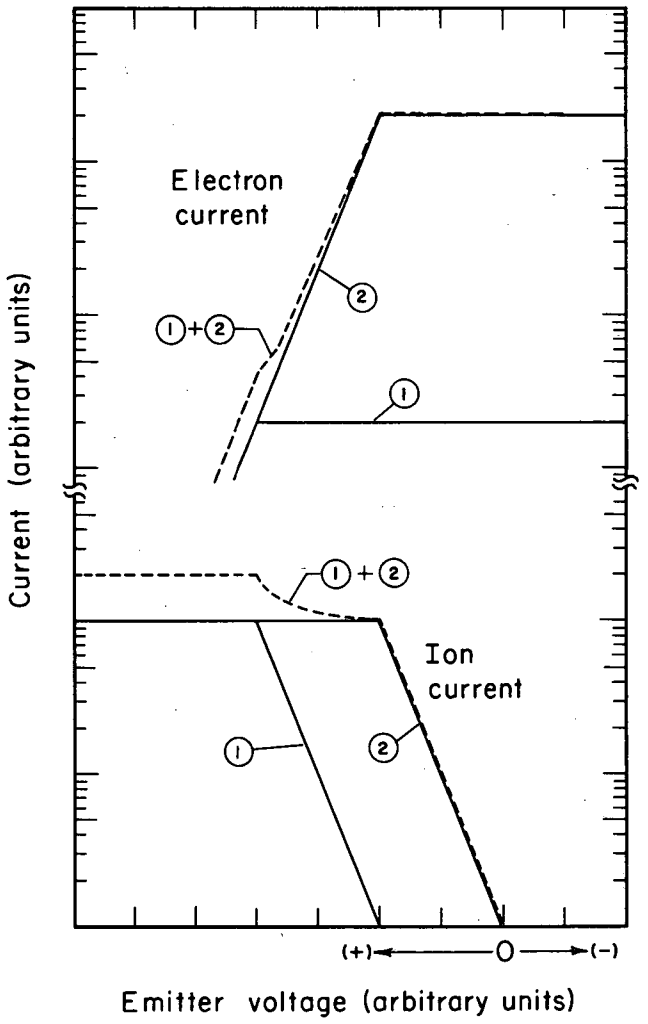
Electron
current
1+2
2
1
1+2
Ion
current
1
2
(+)
0
(-)
Current (arbitrary units)
Emitter voltage (arbitrary units)
MU-36667

Fig. VII. 1

would ideally be observed from a surface composed of two patches of identical area, one having work function ϕ_1 and the other, ϕ_2, with $\phi_1 > \phi_2$. It is evident that the change in the slope of the combined ion-current curve is greater than that of the electron-current curve. A little reflection on the derivations presented above will reveal that Eq. (VII.8) can be applied in the case where both emitter and collector are polycrystalline, yielding the relative work function distribution $f(\phi - \phi_c) = f(eV_E)$ of the two electrodes. On the other hand, the electron-current analysis cannot in this case yield a unique relative distribution $f(\phi - \phi_c)$, as discussed by Caulfield[19] although it can be applied with high sensitivity, to the case of a uniform emitter and a polycrystalline collector simply by integrating Eq. (VII.12) with respect to $f(\phi_c)\, d\phi_c$, with the result that

$$f(\phi_c) = f(\phi - eV_E) = \frac{-1}{AT_E^2 \exp(-\phi/kT_E)} \left(\frac{dJ_e}{deV_E} + kT_E \frac{d^2 J_e}{d(eV_E)^2} \right). \tag{VII.15}$$

C. Experimental Results

The vacuum electron I-V curves described in Sec. III do not deviate much from the ideal, even though the collector was polycrystalline. For comparison, in Figs. VII.2 and VII.3 we show ion I-V curves and corresponding electron I-V curves for the (110) and (100) diodes, respectively. The ion and electron currents were determined from the observed net current by assuming that the observed current was the algebraic sum of ideal ion and electron I-V curves. These data were obtained, under conditions of 100% surface ionization, after the conclusion of the vacuum thermionic-emission experiments and just prior to the heat-of-evaporation experiments; they were part of the fourth and sixth data set for the (100) and (110) diodes,

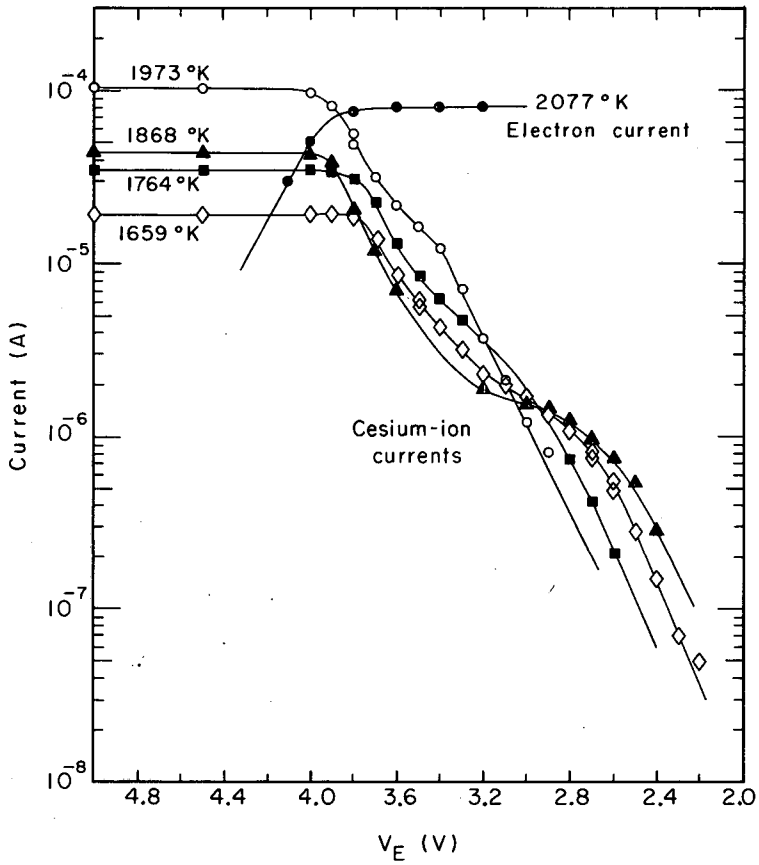
1973 °K
2077 °K
Electron current
1868 °K
1764 °K
1659 °K
Cesium-ion
currents
Current (A)
10^{-4}
10^{-5}
10^{-6}
10^{-7}
10^{-8}
4.8
4.4
4.0
3.6
3.2
2.8
2.4
2.0
V_E (V)
MU-36705

Fig. VII.2

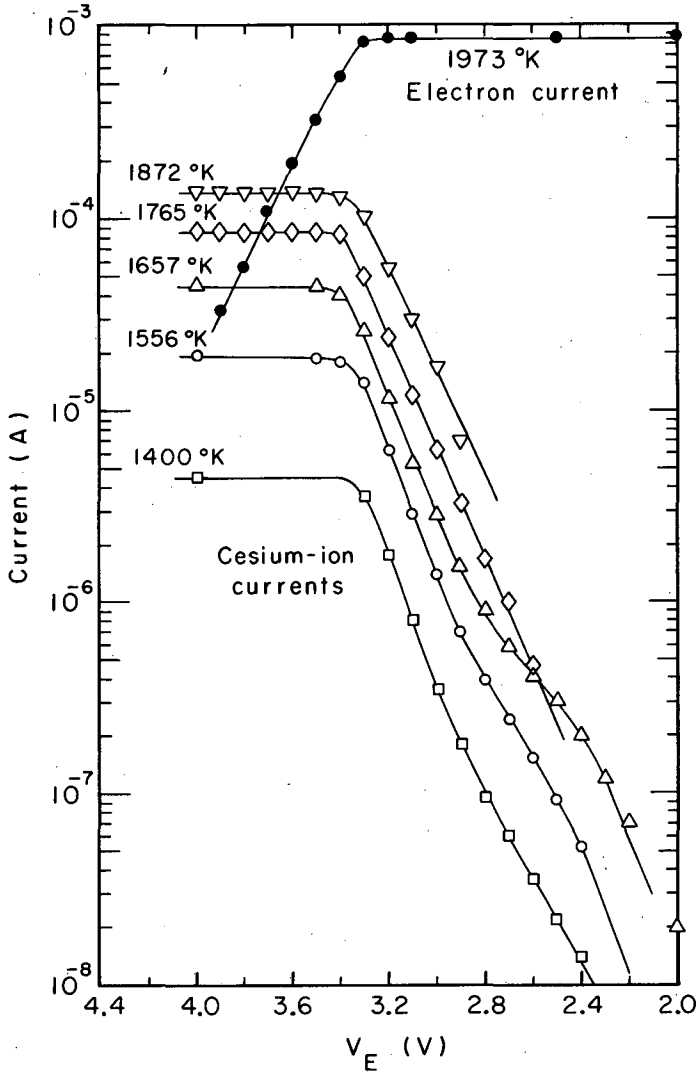
1973 °K
Electron current
1872 °K
1765 °K
1657 °K
1556 °K
1400 °K
Cesium-ion
currents
Current (A)
10^{-3}
10^{-4}
10^{-5}
10^{-6}
10^{-7}
10^{-8}
4.4
4.0
3.6
3.2
2.8
2.4
2.0
V_E (V)
MU-36706

Fig. VII. 3

respectively, described in Sec. III. In each case, the cesium reservoir was immersed in liquid nitrogen; however, as mentioned in Sec. IV.D, the cesium vapor in the diode was not in equilibrium with the cesium reservoir at low temperatures. Possibly a fraction of the apparent ion current was due to secondary-electron and photoelectron emission from the collector. In fact, it is likely that most of the apparent ion current for the (100) diode was photoelectron emission from the collector; what effect this emission would have on the determination of the work function distribution was not investigated. The apparent ion currents in Figs. VII.2 and VII.3 were normalized by dividing by their saturation value (en_o) and were then replotted in Figs. VII.4 and VII.5. The work function distributions corresponding to these currents were not calculated, partly because of the uncertainties already mentioned, and partly because we were not sure of the surface condition of the collectors. The knees of the electron- and ion-current curves in Fig. VII.2 occur between 3.8 and 4.0V. Since the (110) emitter work function determined in Sec. III varied from 5.1 to 5.3V over the whole temperature range, the collector work function must have been around 1.3 to 1.5V. Likewise the knees of both ion and electron I-V curves in Fig. VII.3 occur at about 3.4V, and since the (100) emitter work function was 4.65V, the collector work function was 1.3 to 1.4V, or essentially the same value as that of the (110) diode. These collector work functions, somewhat lower than those of most cesiated metal surfaces, could be the result of impurities adsorbed on the collectors.[20,78]

The surface of the collector in both diodes was evidently well coated with cesium; therefore the collector work function was probably fairly uniform. If that was the case, Figs. VII.4 and VII.5 are representative of the emitter work-function distribution. The slope of the bottom of the

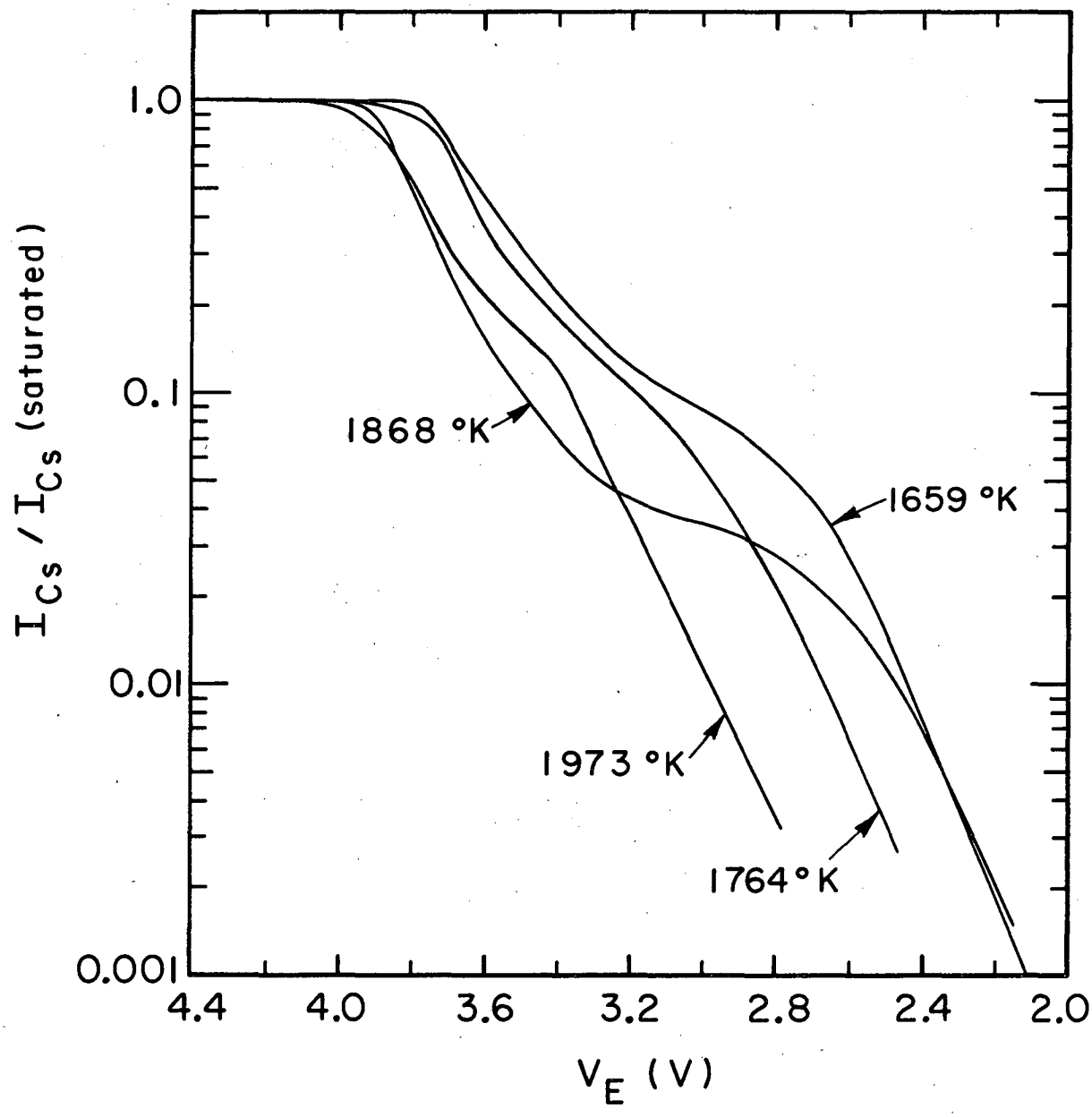
1.0
0.1
0.01
0.001
I_{Cs} / I_{Cs} (saturated)
1868 °K
1659 °K
1973 °K
1764 °K
4.4
4.0
3.6
3.2
2.8
2.4
2.0
V_E (V)
MU-36707

Fig. VII.4

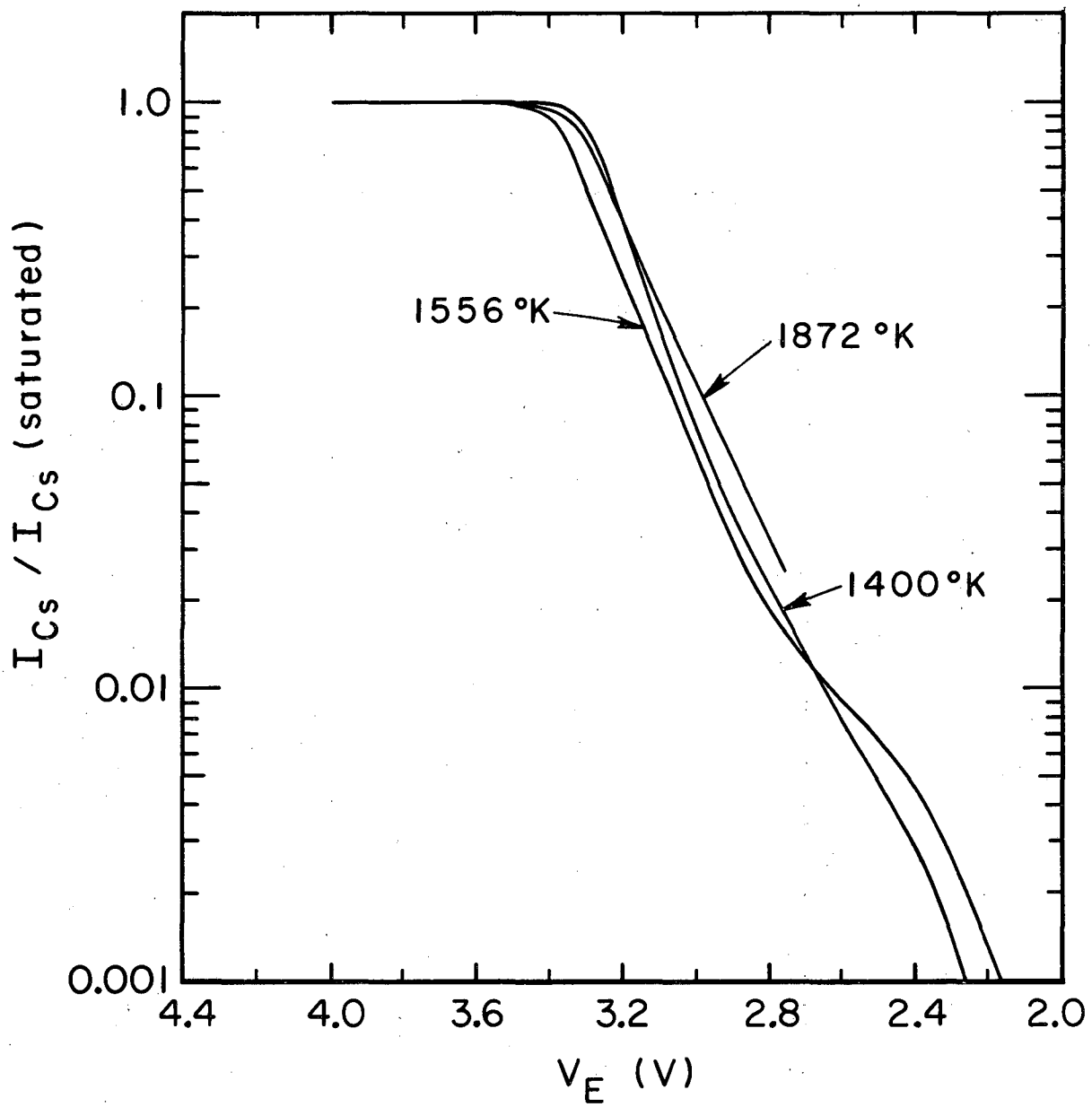
1.0
0.1
0.01
0.001
I_{Cs} / I_{Cs} (saturated)
1556 °K
1872 °K
1400 °K
4.4
4.0
3.6
3.2
2.8
2.4
2.0
V_E (V)
MU-36708

Fig. VII.5

curves in Fig. VII.4 corresponds to the measured emitter temperature. Figure VII.4 indicates that below the transition temperature (1800°- 2000°K), the spread in the work function of the (110) crystal was around 0.5V. It also shows the hardening (shift toward higher values) of about 0.2V and narrowing of the work-function distribution as the temperature is increased through the transition region discussed in Sec. III.C. Unfortunately we could not obtain good ion-current data at temperatures well above the transition because they were masked by the thermionic electron current.

In Figs. VII.3 and VII.5, the slopes of the ion-current curves for nearly two decades below the knees correspond exactly to the measured emitter temperatures. This correspondence indicates that the work function of the (100) crystal was practically uniform. For clarity, only three of the five ion curves shown in Fig. VII.3 were included in Fig. VII.5 because the other two lay within the bounds of the ones shown. At low currents deviations from ideality may be real or may be due to errors in subtracting the estimated ideal thermionic electron current from the net observed current. The slight shift in the contact potential was due to a change in collector work function, because it was not reflected by a corresponding change in electron emission.

D. Conclusions

We have attempted to estimate the uniformity of the work function over the surface of our crystal emitters from some of the results obtained throughout this study. From all indications the work function of the (100) crystal was essentially single valued. That of the (110) crystal appeared to be fairly uniform above the transition temperature but seemed to have a spread at lower temperatures.

We have presented a method for determining the work-function distribution on the electrode surfaces of planar cesium-plasma diodes from the observed ion-current-voltage characteristics. The method parallels one already developed for determining the work-function distribution from the electron-current-voltage characteristics. The applicability of the cesium-ion-current method is as follows: because we depend on 100% surface ionization, the minimum work function of the surface has to be above 3.9V. This restriction essentially limits the technique to the study of bare (free of cesium) surfaces, having rather high average work functions. The method, which is applicable when one or both electrodes of the diode have patchy surfaces, can be applied at a temperature much below that required for the appearance of thermionic emission from the bare metal surface, but it is limited at high temperatures by the interference of the thermionic electron current.

The ion and electron retarding-potential techniques described in this section are not as sophisticated nor as promising as some of the electron-beam scanning and electron microscope techniques, which have recently been developed to study patch effects.[84,51,25,36] However, they can be used in a simple thermionic plasma diode and they should complement each other nicely.

VIII. SUMMARY AND CONCLUSIONS

This dissertation describes an experimental study of the surface ionization of cesium and the thermionic emission from two large (≈ 1.5 cm^2), flat, monocrystalline, tungsten surfaces oriented in the [100] and [110] crystallographic directions.

All experimental results were obtained by measuring the current-voltage-time characteristics of two diodes, each having one of the tungsten single crystals for the cathode (emitter). A guard ring in the plane of the collector ensured accuracy of the current measurements.

The bare-surface properties that we determined were measured first and are summarized in Table VIII.1 below.

The bare work function ϕ_o of each crystal surface was determined from measurements of the field-free thermionic emission J_{so} (amperes/cm^2) in vacuum (about 10^{-8} torr) in the temperature range 1400 to 2200°K. The constants in the Richardson equation, $J_{so} = AT_E^2 \exp(-\phi_o/kT_E)$, were determined from the slope and intercept of Richardson plots. Our results agree with recent measurements of the work function for these tungsten crystal surfaces.

The desorption energies ϕ_{io} and ϕ^*_{ao} of cesium ions and atoms, respectively, evaporating from very dilute films of cesium adsorbed on the crystal surfaces, were determined by measuring transient ion currents resulting from the sudden polarity reversal of an applied electric field at the crystal surface. The technique results in the measurement of the evaporation probability per unit time (reciprocal of the mean adsorption lifetime) P_{io} and P_{ao} for cesium ions and atoms, respectively, where P_{io} is given by the Arrhenius expression, $P_{io} = Q_{io} \exp(-\phi_{io}/kT_E)$, and similarly for P_{ao}.

Table VIII.I. Properties of (100) and (110) Surfaces of Tungsten Single Crystals.

Properties	(100)	(110)[a]
Work-function ϕ_o(eV)	4.65±0.02	5.33±0.04
Richardson constant A (amperes/cm^2°K^2)	238±75	207±50
Cs-ion desorption energy ϕ_{io}(eV)	2.05±0.05	2.06
Cs-ion vibration-frequency term Q_{io} (sec^{-1})	6.6 ±2x10^{12}	
Cs-atom desorption energy ϕ^*_{ao}(eV)	2.77±0.05	3.28±0.03
Cs-atom vibration-frequency term Q_{ao} (sec^{-1})	1.3± 0.4x10^{13}	1.3x10^{13}
T_{EO}/T_{Cs}[ab]	3.5	3.8

a. The results of the cesium desorption experiment shown here for the (110) crystal are for a slightly contaminated surface having a work function of 5.11 eV. The value of T_{EO} is for a contaminated surface of still high (but probably less than 5.0 eV) work function.

b. T_{EO} is the threshold temperature of the crystal surface for 100% surface ionization of the incident flux of cesium vapor in thermodynamic equilibrium with a reservoir of condensed cesium at temperature T_{Cs}.

This method is ideally suited for the study of emitter materials of interest to thermionic energy conversion. Our results, obtained in the temperature range 1000 to 1500°K, are consistent with the work function measurements and with the theoretical predictions of Levine and Gyftopoulos.[58] Our data together with published results for polycrystalline tungsten[88,79] indicate that the ion desorption energy ϕ_{io} is essentially independent of the crystallographic orientation of the tungsten surface.

The detailed analysis of the results of the heat of evaporation of cesium atoms and ions experiment led to the suggestion of a technique for studying the sputtering yield of alkali-metal surfaces under bombardment by ions of their own kind.

The threshold temperature T_{EO} for 100% surface ionization of cesium is defined as that surface temperature below which complete surface ionization of the incident cesium-atom flux no longer occurs because the adsorption of cesium on the surface becomes sufficient to depress its work function below the ionization potential of cesium. This temperature T_{EO} was determined by studying the emission of cesium ions from the crystal surfaces, and was found to occur at a constant value (different for each crystal) of the ratio T_E/T_{Cs}, as listed in Table VIII.I.

The current-voltage characteristics of the diodes operating in cesium vapor were studied as a function of the cesium-reservoir temperature T_{Cs} (0 to 100°C) and of the emitter temperature T_E (850 to 1450°K). The work function depression $\Delta\phi$ due to the adsorption of cesium on the emitter was evaluated from the field-free electron emission by means of the Richardson equation, and also from the field-free cesium-ion emission by means of the Saha-Langmuir equation. Excellent agreement was found between these two independent determinations for values of the work function smaller than the

ionization potential of cesium. The results are displayed in the form of ϕ and $\Delta\phi$ versus T_E/T_{Cs} curves and Langmuir S-curves of the field-free electron emission.

The work-function depression data for the (110) crystal were not analyzed in detail because of insufficient data and because we suspect that the surface of the crystal had become contaminated.

For the (100) crystal, the slope of the $\Delta\phi$ versus T_E/T_{Cs} curves at constant T_{Cs} decreases slightly with increasing T_{Cs}, in qualitative agreement with the theoretical analysis of Rasor and Warner.[76]

The work-function depression of the (100) crystal was found to be close to but significantly different from that determined by Taylor and Langmuir[88] for polycrystalline tungsten. This difference is interesting in that the bare-surface properties (work function, cesium atom and ion desorption energies) of these two surfaces are practically identical. An attempt was made to analyze these differences with the help of the theory mentioned above[76] plus the treatments of Carabateas, Stickney, and Aponick,[16] and Gyftopoulos and Levine.[35,58-60] Our data were insufficient to resolve the differences between these theories. It appears from this effort, however, that the difference between our data and those of Taylor and Langmuir is a result of the work-function nonuniformity over the polycrystalline tungsten surface. It is also apparent from our results that factors in addition to variations in the bare work functions must be considered when extrapolating the data of Taylor and Langmuir to other metal surfaces.

We attempted to determine the uniformity of the work function over the surface of our crystals from some of our experimental results and by studying the energy distribution of ions thermally emitted from dilute films of adsorbed cesium on the emitters. Our data qualitatively indicate that the bare work function of the (100) crystal surface was very uniform.

As part of this overall study, we measured the flux of cesium vapor as a function of the temperature T_{Cs} of its condensed phase (liquid) and compared our results with those of Taylor and Langmuir.[89] We obtained the same heat of evaporation, h = 0.75 eV, as did these investigators, but our measured flux was greater than theirs by a factor of about 1.5. This discrepancy which we observed with both diodes is probably a result of the difference in geometry between our closely spaced planar diode and the cylindrical diode with wire emitter used by Taylor and Langmuir. It is likely that our higher saturation ion-currents were due to the effect of the applied electric field on the angular distribution of cesium leaving the emitter, and to possible sputtering of cesium atoms from the collector surface.

In conclusion, we suggest extensions of the work performed in this study. First, the (110) tungsten surface should be reinvestigated because we could not relate our cesium data at large coverage for this crystal to its bare surface properties. To complete the picture on tungsten we suggest that a similar study be done with a (111) crystal surface whose bare work function should be lower than that of the (100) crystal. Such a complete study would, among other things, provide upper and lower limits on the work function distribution of a polycrystalline tungsten surface, and provide a better understanding of the latter's behavior with adsorbed cesium.

In order to obtain decisive tests of the theories mentioned above, careful measurements of the work-function depression $\Delta\phi$ of these crystal surfaces versus the ratio T_E/T_{Cs} at constant T_E (or T_{Cs}) need to be made in regions of both low and high values of T_E/T_{Cs}; in addition, it would be desirable to measure the desorption energies ϕ_a^* or ϕ_i as a function of

the cesiated work function ϕ, or preferable of course to measure all these properties as a function of the surface coverage of adsorbed cesium.

From a fundamental point of view, at least, it would be worthwhile to perform all these experiments with potassium or rubidium in addition to cesium.

In view of the differences between our measurements of the cesium-vapor flux and those of Taylor and Langmuir, we feel that such measurements should be undertaken in more detail in the parallel-plane geometry to determine the phenomonology of these differences; also, the range of data should be extended to higher temperatures.

ACKNOWLEDGMENTS

I wish to express my deep gratitude to: Professor T. H. Pigford who introduced me to the field of thermionic energy conversion for his guidance and support during the course of the work and for his critical review of this report, and Professors H. P. Smith and A. C. English for the time and effort each spent reviewing this dissertation.

I am greatly indebted to Mr. B. E. Thinger for his enthusiastic participation in many phases of this work, from building equipment to analyzing data, and to Mr. Ronald Wichner, who in many ways shared this project with me since its inception, for his general assistance and thought-provoking discussions. In this latter respect the contributions of Mr. H. C. Carney, Dr. L. D. Posey, and Professor H. M. Mark are gratefully acknowledged.

I wish to extend my appreciation to Mr. Alfredo Diaz for his assistance in analyzing some of the results and to my brother Thierry who donated much of his time helping me to process data.

The contributions of the following individuals are also greatly appreciated: Mr. C. E. Litton of Litton Engineering Laboratories who built the diodes and contributed many design suggestions, Mr. F. L. Reynolds who kindly furnished the bulk single crystal, Mr. Daniel O'Connell who introduced me to the technique of electron beam brazing, Mr. A. J. Shand who assisted with acquiring the diodes and various laboratory equipment, and Messrs. Joe Fashin and Don Sikkema who designed and built several electronic components.

Finally, I owe a great debt of gratitude to my wife Nadine for her infinite patience, understanding, and generous encouragements, and

for her innumerable contributions to this work.

This work was performed under the auspices of the Atomic Energy Commission and was supported by the Inorganic Materials Research Division of the Lawrence Radiation Laboratory, and by the Space Sciences Laboratory of the University of California.

NOMENCLATURE

A	Richardson constant
a_a	polarizability of adsorbed atom
a_i	polarizability of adsorbed ion
a_o	polarizability of adsorbed particle
C	$g'_a \omega_{Cs} \sigma_{Cs}$, evaporation rate of cesium at $T_{Cs} = \infty$ ($\approx 1.3 \times 10^{27}/cm^2 sec$)
$\mathcal{E}$	electric field
$\mathcal{E}_i$	depolarization electric field for adsorbed ions
$\mathcal{E}_a$	depolarization electric field for adsorbed atoms
e	magnitude of the electronic charge
E	energy needed to neutralize adsorbed ion on cesiated surface
E_o	energy needed to neutralize adsorbed ion on bare surface
f	penetration coefficient for adsorbed ions (usually $\Delta\phi_i/\Delta\phi$)
F	fraction of the electronic charge of an adsorbed particle
g'_a	statistical weight of cesium vapor
g_a	statistical weight of adsorbed atom
g_i	statistical weight of adsorbed ion
G	coefficient of the electronegativity barrier ($1-3\theta^2+2\theta^3$)
h	cesium heat of evaporation (=0.75 eV)
H_{cc}	covalent part of cesium-atom desorption energy
H_{ii}	ionic part of cesium-atom desorption energy
I	current (usually electrons)
I_{Cs}	cesium-ion current

J	electron current-density, ampere/cm^2
J_{Cs}	cesium-ion current-density
J_{max}	space-charge limited current-density
J_s	saturation electron current-density
J_{so}	saturation electron current-density at zero electric field (field-free)
k	Boltzmann constant
K	$\ell n\, K^*$
K^*	thermodynamic function of coverage for the equation of state of adsorbed cesium.
K'	K^*/θ
m	mass of an electron
m_f	mass of adsorbate particle
m_m	mass of substrate atom
M	dipole moment of adsorbed particle $(M_2 - a_o \mathcal{E})$
M_a	dipole moment of adsorbed atom $(M_{ao} - a_a \mathcal{E})$
M_{ao}	dipole moment of adsorbed atom at zero coverage
M_i	dipole moment of adsorbed ion $(M_{io} - a_i \mathcal{E})$
M_{io}	dipole moment of adsorbed ion at zero coverage
M_o	dipole moment of adsorbed particle at zero coverage
M_1	$M_o\, G(\theta)$
M_2	$M_1/(1 + a/R^3)$
n_a	evaporation flux of atoms, atom/cm^2 sec
n_i	evaporation flux of ions
n_o	flux of atoms incident on emitter surface
N	surface concentration of adsorbed particles, particles/cm^2

P_a	probability per unit time that an adsorbed particle evaporates as an atom
P_a'	probability per unit time that an adsorbed atom evaporates as an atom
P_a^*	$n_a/N = K'(\theta)\ P_a$
P_{ao}	probability per unit time at zero coverage that an adsorbed particle evaporates as an atom
P_i	probability per unit time that an adsorbed particle evaporates as an ion
P_{io}	probability per unit time at zero coverage that an adsorbed particle evaporates as an ion
P_i'	probability per unit time that an adsorbed ion evaporates as an ion
Q_a	$g_a\omega$, atom frequency-term
Q_{ao}	$g_a\omega_o$, atom frequency-term at zero coverage
Q_i	$g_i\omega$, ion frequency term
Q_{io}	$g_i\omega_o$, ion frequency-term at zero coverage
r_i	radius of adsorbed ion
R	interaction distance between adsorbed particle and substrate metal (equal to sum of adsorbate and substrate covalent radii)
R_c	current-measuring resistor in series with collector
R_g	current-measuring resistor in series with guard ring
S_f	angular strength of valence orbital of adsorbate
S_m	angular strength of valence orbital of substrate
S_{fm}	$= 2/(S_f/S_m + S_m/S_f)$
t	time
T_{Cs}	cesium-reservoir temperature
T_e	electron temperature
T_E	emitter temperature

T_{EO}	threshold temperature for 100% surface ionization
V	volt
V_c	applied collector voltage relative to the emitter
V_d	interelectrode potential ($= V_c - V_o$)
V_E	applied emitter voltage relative to collector
V_i	ionization potential of cesium (3.89 eV, Ref. 21)
V_o	$(\phi_c - \phi)/e$, contact potential
W_a	probability that an adsorbed particle is an atom
W_i	probability that an adsorbed particle is an ion
α	degree of ionization, n_i/n_a
β	ionization coefficient, n_i/n_o
γ	number of sputtered atoms per ion incident on the collector (sputtering yield)
δ	$F(e^2/R - V_i)/\phi$
θ	fractional surface coverage ($= N/\sigma$)
θ_a	fractional surface coverage of atoms
θ_i	fractional surface coverage of ions
σ	surface concentration of a monolayer of adsorbed cesium
σ_m	surface concentration of substrate atoms
ϕ	emitter work function (usually with adsorbed cesium)
ϕ_a	energy required to remove an adsorbed atom (adatom) to infinity as an atom
ϕ_a^*	$(\phi_a + E)$ energy to desorb an adion as an atom (observed C_s atom desorption energy)
ϕ_i	energy required to remove an adsorbed ion (adion) to infinity as an ion
ϕ_o	emitter work function at zero coverage (bare surface)

ϕ_c	collector work function
ϕ_{ao}, ϕ^*_{ao}, ϕ_{io}	same meaning as without subscript o but for zero coverage
$\Delta\phi$	$(\phi_o - \phi)$, emitter work-function depression
$\Delta\phi_a$	$(\phi_{ao} - \phi_o)$
$\Delta\phi^*_a$	$(\phi^*_{ao} - \phi^*_a)$
$\Delta\phi_i$	$(\phi_i - \phi_{io})$
$\Delta\psi_i$	potential energy drop across adsorbed ion dipole-layer
$\Delta\psi_a$	potential energy rise across adsorbed atom dipole-layer
ω	frequency of vibration (normal to the surface) of an adsorbed particle
ω_o	vibrational frequency of adsorbed particle at zero coverage

APPENDICES

A. Cesium-Plasma Diode

The diode shown in Figs. II.1 through II.3 was that used to study the (110) crystal emitter. The diode was built so that either the electron gun or the whole emitter assembly could be replaced several times by filing off the brazed flanges on which they were mounted. The windows could be replaced by filing off their welded flanges. It was also possible but more difficult to replace the collector-guard-ring assembly. All of these replacements were done when the (100) crystal emitter was substituted into the diode. The replacement of the collector guard-ring assembly was necessitated by the need for making certain minor design changes which are described in Appendix B.

The emitter was heated by electron bombardment from a spirally wound filament [(F) in Fig. II.3] located 0.10 in. from the end of the tantalum support tube. The filament evolved from an axial stem and spiraled out to a heat shield that provided the return path for the filament current. The electron-gun chamber, confined by the tantalum support tube, was operated in a static vacuum.

The molybdenum heat shield surrounding the emitter assembly was electrically insulated from both the emitter and the guard ring (most of the diode body was at guard-ring potential) so that the heat shield could be operated as a guarding electrode if desired. To minimize radial heat losses from the emitter, the heat shield was extended above the emitter face. The interelectrode spacing and the emitter holhraum would have been completely hidden from view were it not that several narrow slots were cut along the heat-shield periphery.

The interelectrode spacing was adjusted with four screws that could be linked together or actuated individually to adjust the parallelism of the electrodes (Fig. II.2).

The diode body was air (or inert gas) cooled by forced or natural convection, and it was heated by several independent windings of Kanthal wire sheathed in Fiberglass insulation. By a combination of cooling and heating, it was possible to achieve a fairly uniform temperature distribution of the diode body.

As mentioned in Sec. II, the cesium reservoir was inserted tightly into a heavy copper jacket (visible in Fig. II.7) which could be both water cooled and electrically heated. For the (110) diode the copper jacket was electrically insulated from the cesium reservoir by a mica sheet 0.002 in. thick, to prevent current leakage from the guard ring to ground. The need for the mica foil was eliminated in the (100) diode by providing a ceramic insulator between the cesium reservoir and the diode body (Fig. B.1).

B. (100) Diode Alterations

Several significant changes in the description given in Sec. II were incorporated in the diode after the (110) crystal study was terminated. Then the (100) crystal was substituted into the rebuilt diode.

These design alterations are demonstrated in Fig. B.1 and were as follows:

a. The width of the gap (1) between the collector and the guard ring was increased to 0.010 in. to prevent these two electrodes from shorting out, as occasionally happened in the original diode assembly. The effective collector area was kept unchanged at 0.71 cm^2.

b. The collector and guard below the insulator joining them were made equal in length (2) so that the faces of both would remain in the same plane regardless of thermal expansion. (Both collector and guard were maintained at approximately the same temperature.)

c. Placement of a ceramic insulator (3) in the connecting tube between the cesium reservoir and the diode body eliminated the need for mica foil between the cesium reservoir and the copper jacket controlling its temperature, and thereby improved the heat transfer between the reservoir and the jacket.

d. The inside diameter of the tube (4) connecting the cesium reservoir to the diode body was increased from 0.125 to 0.5 in. to increase the rate of transfer of cesium vapor between the reservoir and the diode chamber.

e. A copper slug (5) was brazed onto the bottom of the cesium reservoir. A thermocouple imbedded in the slug accurately measured the temperature of the bottom of the cesium reservoir.

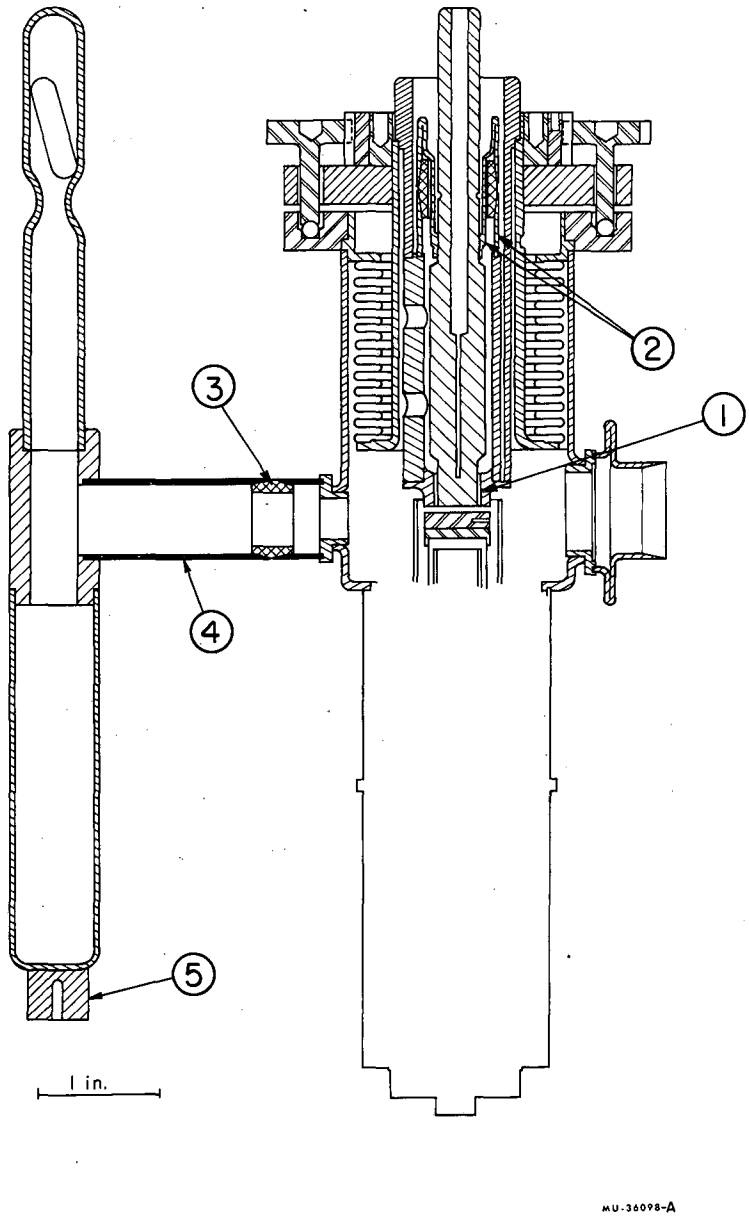

Fig. B.1

C. Diode Processing

Before assembly, each part of the diode was baked under vacuum. The assembled diode was then evacuated with a multistage oil-diffusion pump. A charcoal trap cooled with liquid nitrogen was placed between the diode and the pump. Both the gun and diode chambers were evacuated simultaneously. During evacuation the entire diode (except for the part of the appendage containing the sealed Pyrex-glass cesium capsule) was placed in an oven and baked out in air for 24 hours at a maximum diode-body temperature of 600°C. The temperature of the Cs ampoule was maintained below 300°C. Then with the diode still in the oven the emitter was heated to 1750°C for 4 to 18 hours. During this baking-out process the diode was periodically isolated from the diffusion pump and a static pressure reading taken with an ionization guage; when the static pressure dropped into the 10^{-8}-torr range, the diode was cooled to room temperature. The pressure just prior to the sealing off of the electron gun and diode chambers was about 2×10^{-9} torr. The chambers were sealed off by severing with a pinch-off tool the copper lines connecting them to the pump. Total evacuation time for each diode varied from 30 to 60 hours.

D. Environmental Chamber of Diode

The diode was suspended from a large metal flange that was part of a metal water-cooled vacuum chamber, as shown in Figs. II.7 and D.1. The diode could be operated either outside (in air) or inside the chamber in vacuum or inert gas). The chamber could be evacuated to about 1.5×10^{-2} torr or filled with argon or helium; the primary object in either case being prevention or reduction of the oxidation of the diode body and lengthening of the life of the diode. The chamber also contained a hot zirconium filament to getter any oxygen that might be present. The top flange contained all the necessary electrical and thermocouple feed-throughs plus two coolant feed-throughs and four O-ring feed-throughs into which four connecting rods were inserted to actuate the spacing-adjusting screws of the diode.

The chamber also served as a shield against stray electromagnetic fields.

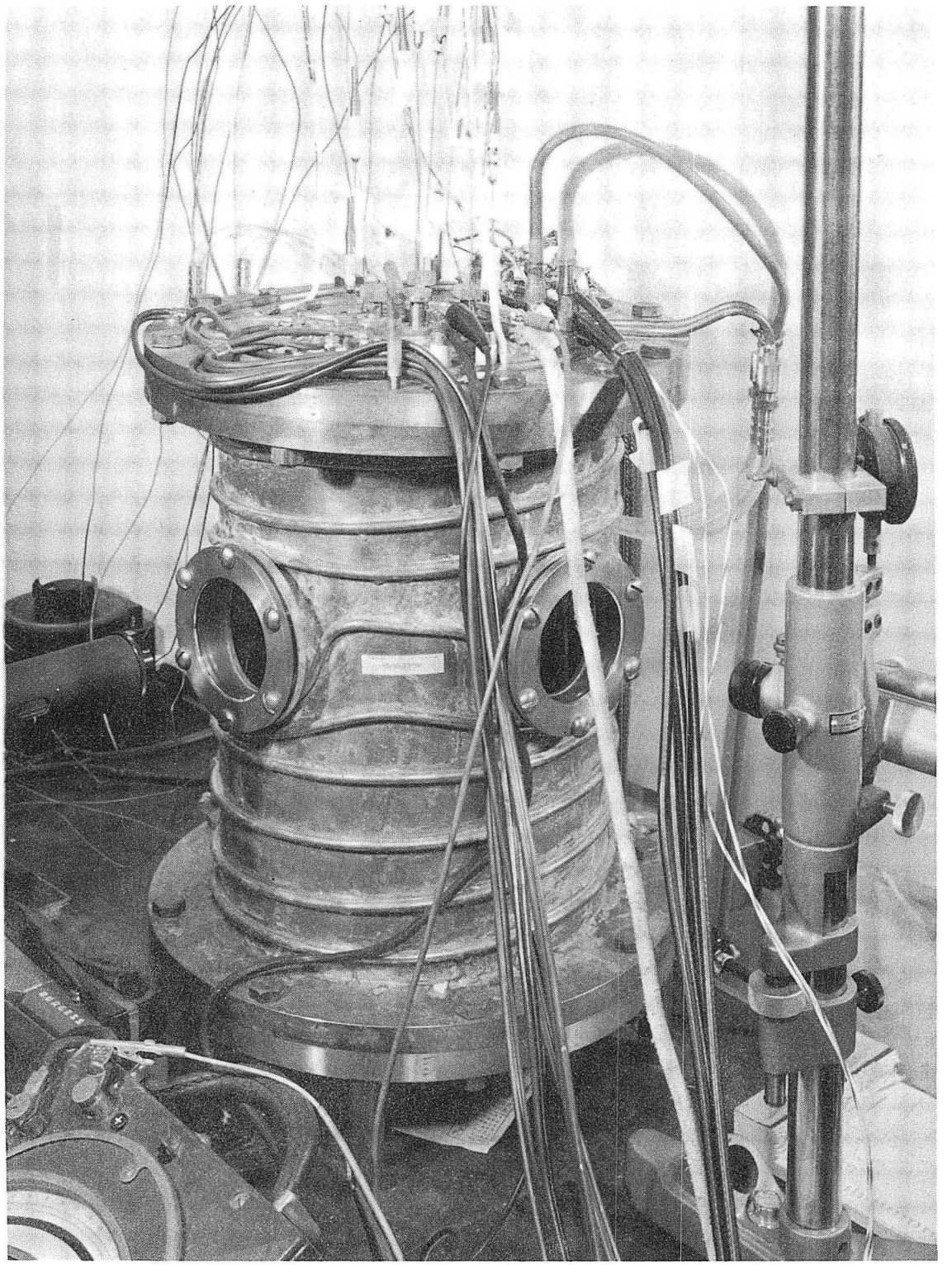

ZN-5596

Fig. D. 1

E. Cesium Distillation

A Pyrex-glass ampoule containing 10 g of high-purity triple-distilled cesium metal was placed in the Pyrex-glass distilling apparatus shown in Fig. E.1. A typical chemical analysis of the cesium is shown in Table E.1. The cesium was encapsulated by the supplier at a pressure of about 10^{-4} torr. The apparatus was evacuated for 36 hours with a VacIon pump in series with a charcoal trap cooled with liquid nitrogen, with the glass thoroughly torched several times during the evacuation. Before the cesium transfer began, the final pressure in the system was 8×10^{-9} torr at the VacIon pump and 1×10^{-7} torr at the ionization gage. The cesium capsule was first broken by dropping the steel balls onto it, and the cesium was then melted and transferred into several small ampoules containing 1/2 to 1 g each. After being heated for some time to expel trapped gases, the small ampoules of cesium were sealed off, nearly full, one at a time. The pressure, recorded by the ion gage at the time of each seal-off, always remained below 1.6×10^{-6} torr and that of the ion pump below 1×10^{-8} torr. One of these small ampoules was then inserted in the appendage of the diode.

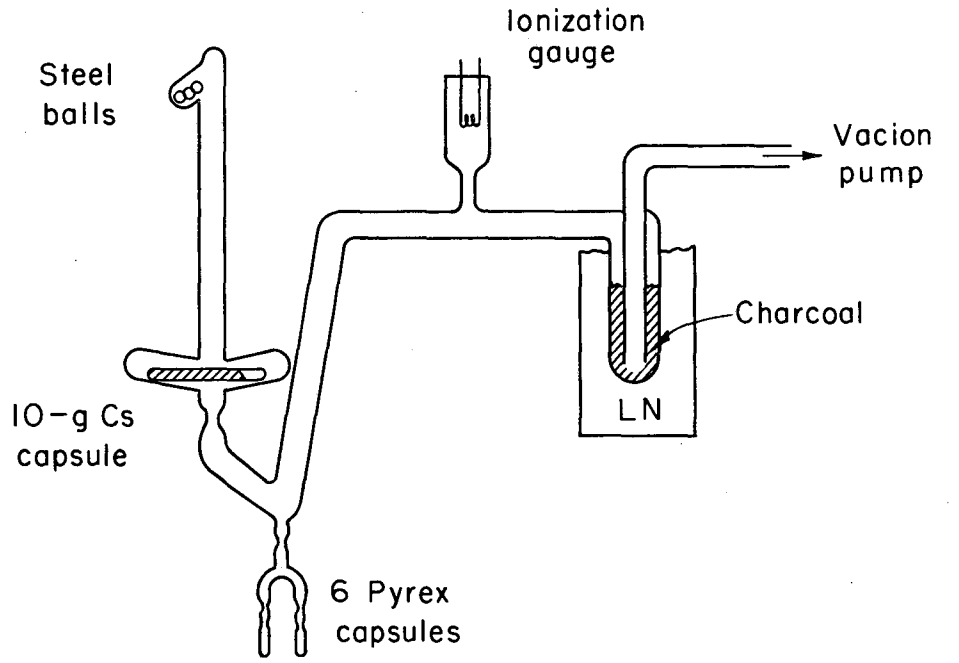
Ionization
gauge
Steel
balls
Vacion
pump
Charcoal
LN
10-g Cs
capsule
6 Pyrex
capsules
MU-36605

Fig. E.1

Table E.I Typical impurity analysis of cesium[a]

Element	%
Al	<0.0002
Ba	<0.0008
B	<0.0016
Ca	0.0027
Cu	0.0003
Cr	<0.0002
Fe	0.0011
Mg	<0.0002
Mn	<0.0002
Ni	<0.0002
Pb	<0.0002
Si	0.0002
Sr	<0.0002
Li	<0.0016
Ti	<0.0002
Tl	<0.0002
Na	0.0043
K	0.0019
Rb	0.0595
Sn	<0.0008

[a] Chemical analyses by Dow Chemical Co., supplier.

F. Preparation of Single-Crystal Tungsten Emitters

Both the (110) and (100) crystals were cut from roughtly cylindrical single-crystal stock (manufactured by Linde Co., Crystal Products Div., Los angeles, Calif.) 5/8 to 3/4 in. in diameter and several inches in length, oriented with the [110] direction within 3° of the rod axis.

The stock crystal was first ground on a lathe to a maximum smooth diameter of about 5/8 in., after which a 1-in. section was ground to a final diameter of 0.524 in. To minimize surface deformation, all subsequent cutting of the crystal, including drilling of the blackbody hole, was done under kerosene with a spark cutter. Several wafers of each orientation were cut and then ground optically flat on a precision ceramic lapping wheel with a suspension of Al_2O_3 powder in oil. The faces of each wafer were made parallel to within 0.0001 in. One face of each wafer was electropolished with a solution of 2 wt.% NaOH for 20-30 minutes, which was a sufficient time for the removal of several mils of metal. The negative electrode was of stainless steel. Best results were obtained with an applied voltage of 5 volts at a current of about 0.3 ampere/cm^2. Great care was exercised to maintain the flatness of the crystal face being electropolished. To this end, a polycrystalline tungsten annulus acting as a guard ring was cemented around the wafer, and the crystal face was placed in a near-vertical direction and rotated slowly about its axis as shown in Fig. F.1.

This procedure produces a very well-polished flat surface, although not optically flat. The surface has an orange-peel type of finish characteristic of the electropolishing process. The final thickness of the crystal wafers was about 0.18 in.

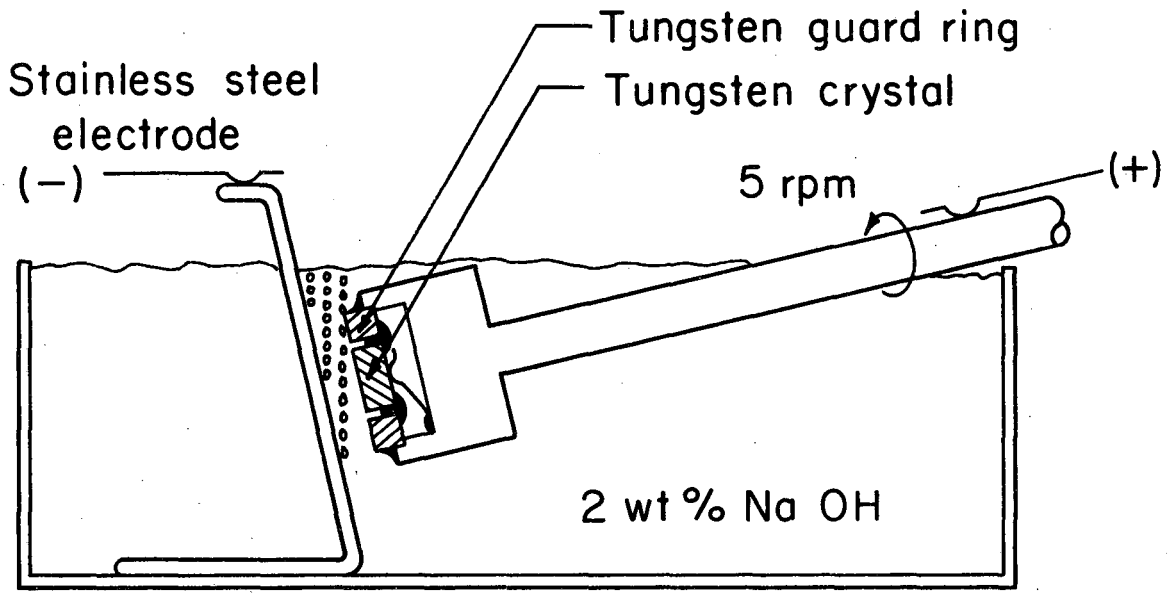

MU-36606

Fig. F.1

At this point the crystals were brazed to their tantalum support and electropolished again to eliminate the slight surface deformations that sometimes occurred during brazing. To insure a clean surface the crystals were then reheated in the brazing furnace to 2000°C, and finally they were installed in the diode.

At various stages of the process described above, the crystal orientation was measured and adjusted. The orientation of the crystal lattice relative to the surface normal was measured by means of x-ray Laue patterns.[22] Figures II.4 and II.5 show the Laue patterns of the (110) and (100) emitters, respectively, taken normal to the crystal surface just prior to their insertion in the diode. For both emitters the surface normals lie within 1° of the desired lattice orientation. This does not necessarily mean that either the (110) and (100) planes were ever exposed to the surface. X-ray diffraction cannot guarantee the surface orientation because the rays penetrate too deeply into the crystal. Nor is it implied from Figs. II.4 and II.5 that the emitters were perfect single crystals throughout, although the clarity of these Laue patterns suggests that the crystals were relatively free of deformation. Microscopic observations of the crystal surfaces revealed a structure of grains approximately 1 mm square. Laue patterns taken at different points on the surface sometimes showed close-grouped double-spot patterns (Fig. II.6), indicating that the crystals actually consisted of many small crystals all oriented with each other to within a fraction of a degree.

G. Brazing of Crystal Emitters

As mentioned in Sec. II, the emitter crystal was brazed to a tantalum supporting cup, which was a tube of 0.524-in. outer diameter, 0.020-in. wall thickness, and 3-in. length, and closed on the end supporting the crystal. The wall thickness near the closed end was reduced to 0.007 in. over a 0.75-in. length to reduce heat-conduction losses. The tube, made from a flat sheet of tantalum, drawn through a series of dies to its final shape. This difficult manufacturing technique was necessitated so that the grain structure of the tantalum cup would be everywhere parallel to its surface, thereby minimizing the possibility of a vacuum leak between the diode chamber and the electron-gun chamber. The other alternative was to braze the crystals onto an open-ended tube, but it was not known whether the brazed joing could be made vacuum-tight and maintained so at the high temperatures of the emitter.

The crystal was brazed to the tantalum by first inserting a 2-to-4-mil molybdenum foil between the two and then heating the crystal in vacuum to 2750°C by electron bombardment from a hot surrounding tantalum filament, as shown in Figs. G.1 and G.2. The electron-bombarding power needed was about 700V at 1A, whereas the filament required 100A. In order to minimize thermal stresses and to facilitate reproducibility, the crystal was heated at the rate of 100°C/minute. Although the foil melted between 2600 and 2700°C, the temperature was further raised to 2750°C and held for one to two minutes, after which the crystal was again cooled at the rate of 100°C per minute.

As mentioned in Appendix F, after brazing the crystal surfaces generally showed some defects having about the same symmetry as the heat-

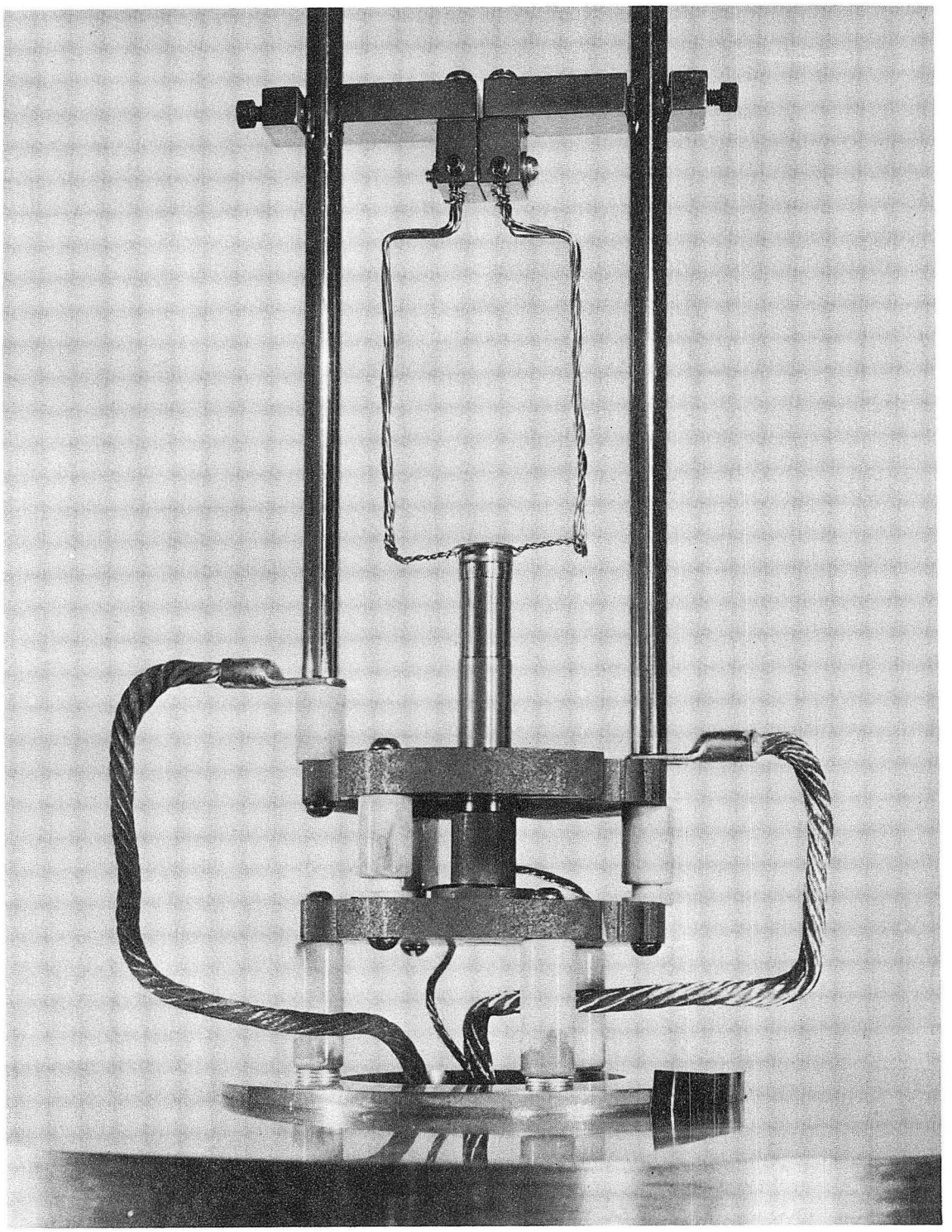

ZN-5593

Fig. G. 1

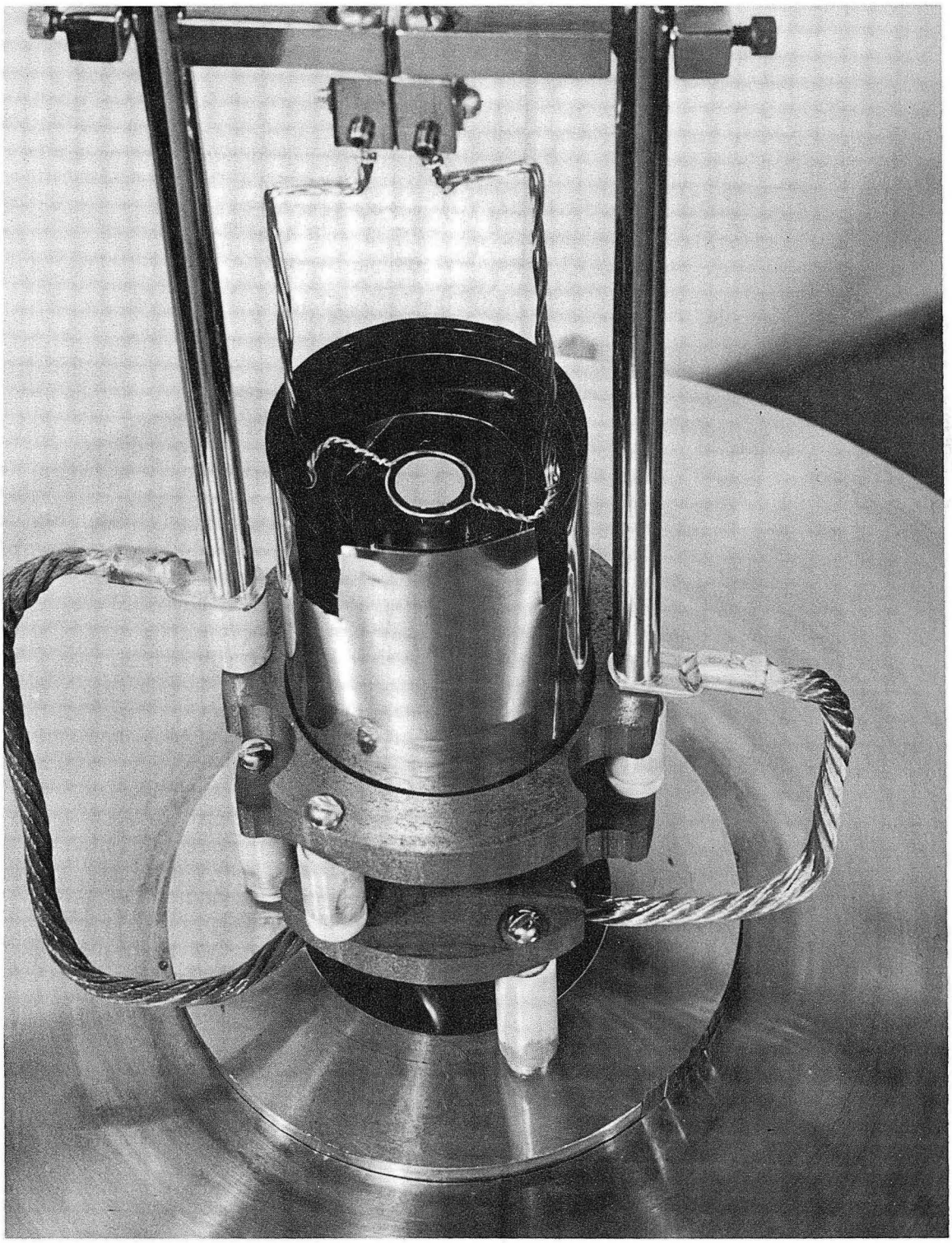

ZN-5594

Fig. G.2

ing filament. The origin of these defects was undetermined. It was unclear whether they were due to electron erosion, etching by evaporation, or thermal stresses due to uneven heating that caused dislocations or slight uneven crystal growth, or a combination of all of these. Microscopically the defects had the geometry of the particular crystallographic orientation of the surface. In all but a couple of instances which required additional lapping, these surface defects were eliminated by further electropolishing.

Although molybdenum was selected to braze the crystals, two other metals--nickel and copper-- were also tried. The same brazing procedure described above was used for all three materials. Figure G.3 shows the metallographic analysis of the resulting bond for each case. Polycrystalline tungsten buttons were used in these tests to economize on the single crystals. Nickel was rejected on the basis of the large voids which formed in the bond (Fig. G.3); the voids were probably due to either dissolved gases in the nickel or large density changes brought on by alloying. The other two brazes were each subjected to 50 severe thermal cycles, according to the following scheme: The tungsten buttons brazed to the tantalum cups were heated with an electron gun (identical to the one used in the diode) from 900°C to 2100°C in four minutes. The bombarding power was then abruptly cut off for 2 minutes, the time necessary to cool the button to 900°C. The total cycling period was therefore 6 minutes. Although the copper and molybdenum brazes successfully weathered this treatment, there was evidence of extensive crystal growth in the tantalum. The copper braze was finally rejected on the basis that the bond is extremely thin, as can be seen from Fig. G.3; therefore a good bond would be obtained only if the two surfaces to be brazed were absolutely smooth and

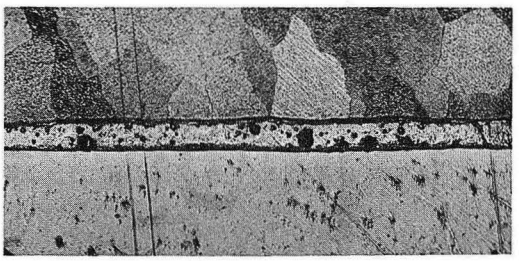

(a)

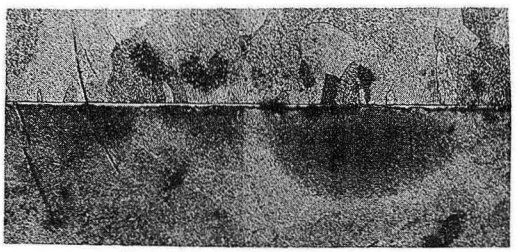

(b)

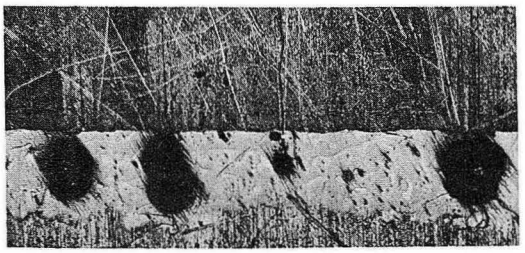

0.2 mm

(c)

ZN-5114

Fig. G.3

flat. This left molybdenum, which goes into solution with both tantalum and tungsten without forming a low-melting eutectic and which has a low vapor pressure up to 2000°C. As seen in Fig. G.3, the molybdenum bond is fairly wide and free of large voids.

However, the molybdenum bond may possible be brittle, because one did fail after it was accidentally dropped to the floor.

H. Radial Temperature Distribution on Emitter Surface-Experimental

Considerable attention was given to the radial temperature distribution on the surface of the emitter. A theoretical analysis described in Appendix I was carried out to determine how the surface-temperature profile varied with the thickness of the emitter button. The theoretical model assumes either a uniform temperature or a uniform heat flux into the button from the electron gun, and heat losses linearly proportional to the surface temperature along both the periphery and the face of the emitter, but with different heat-transfer coefficients for each of these two surfaces. However, due to uncertainties in the heat-transfer coefficients, the physical properties of tungsten, and the radial uniformity of the heat source, we decided to actually measure the temperature distribution on the face of the emitter under conditions closely approximating those of the diode.

A dummy diode shown in Figs. H.1 through H.5 was built for that purpose. The device is actually a holder for the very emitter and electron gun subsequently incorporated in the diode. The spacing between the electron-gun filament and the end of the tantalum cup could be adjusted so that the resulting effects on the temperature profile could be observed.

A copper collector with four radial rows of 0.016-in. diameter holes drilled into its face was placed opposite the emitter. The emitter temperature distribution was measured by sighting an optical pyrometer through each hole. The position of the holes can be seen in the mirror on top of the dummy diode chamber in Fig. H.5.

The absolute temperature of the emitter at each hole position could not be accurately measured because the effective emissivity of the emitter-collector arrangement was not known, but the relative temperature could be

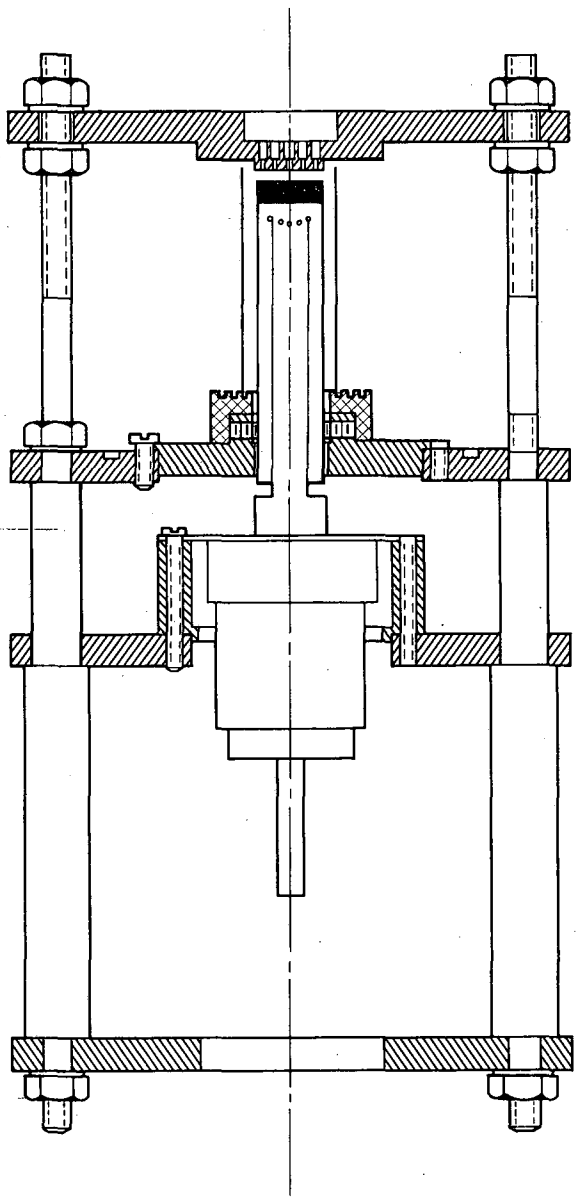

MU-36609

Fig. H.1

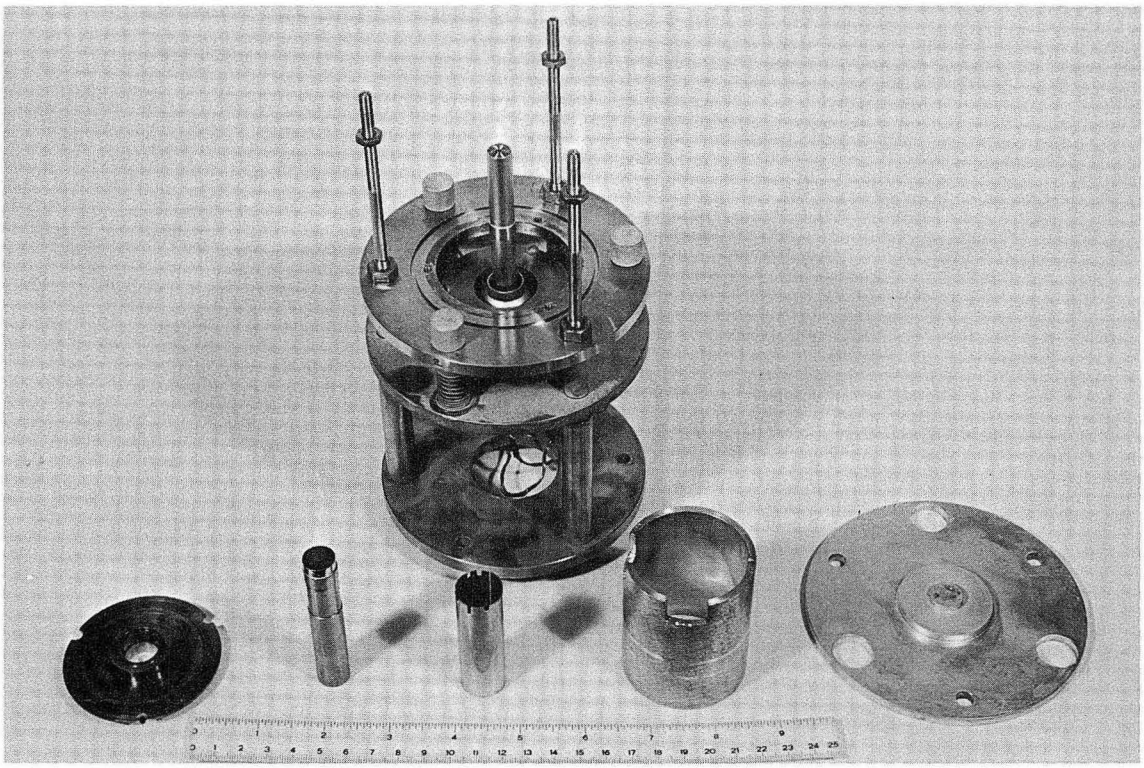

ZN-5588

Fig. H.2

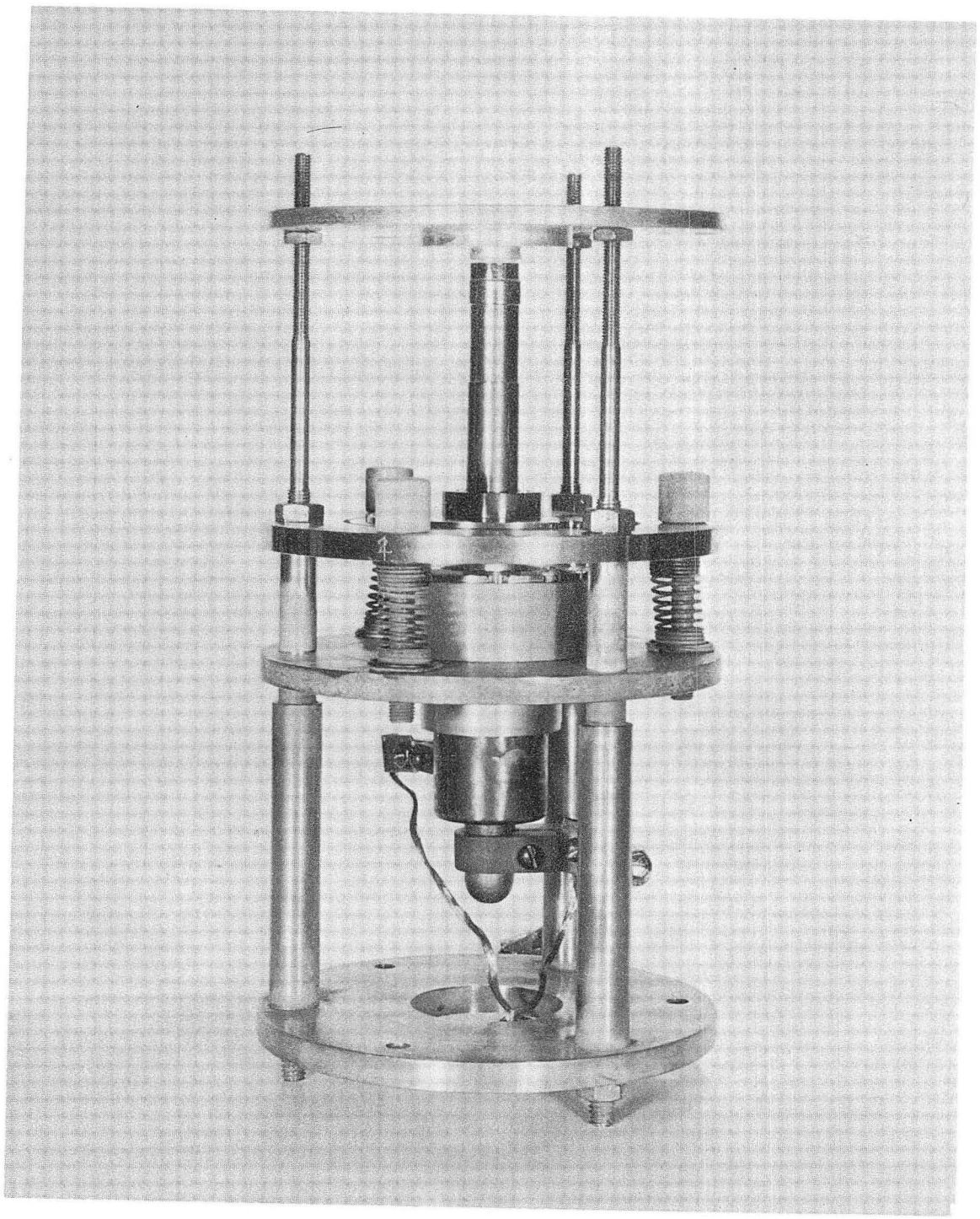

ZN-5587

Fig. H.3

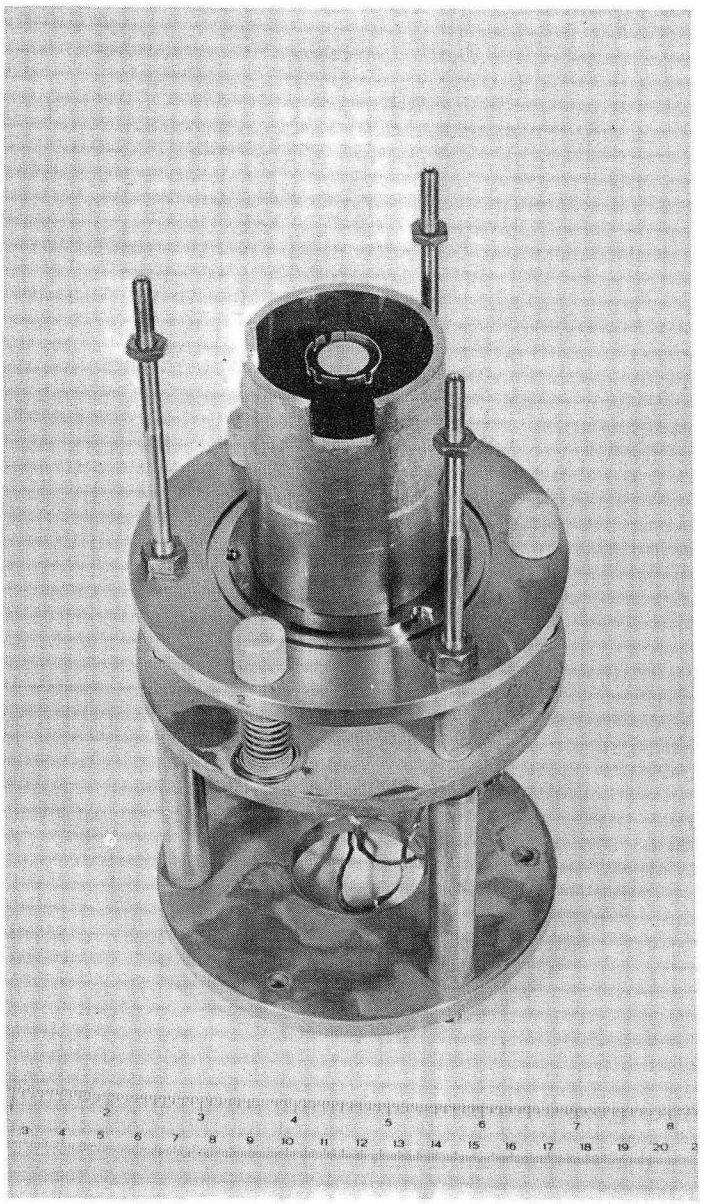

ZN-5589

Fig. H.4

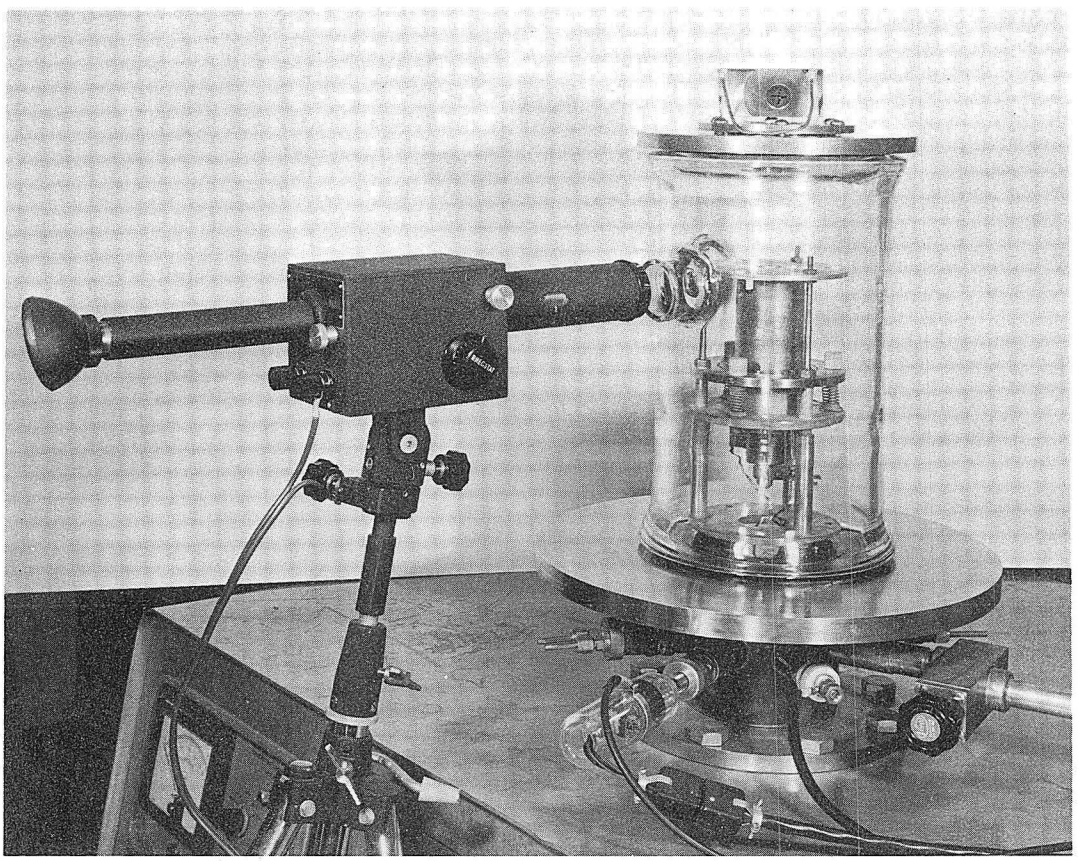

ZN-5590

Fig. H.5

measured to the precision of the pyrometer, namely about 0.2% of the temperature. It is important, however, that both collector and emitter surfaces be uniformly polished to ensure a constant radial emissivity, otherwise the relative temperature will not be accurately measured. The absolute temperature of the emitter was obtained by measuring the temperature of the blackbody hole on its side.

Figure H.6 shows the radial temperature distribution on the surface of a (110) crystal 0.18-in. thick, and Fig. H.7 shows the same plot for a polycrystalline button 0.165-in. thick. As can be seen, for all practical purposes the emitter surface temperature is uniform at all temperatures. The temperature of the heat shield in these two tests was only about 3% higher than the heat-shield temperature measured in the cesium diode.

It was observed also that the temperature profile was very insensitive to the spacing between the electron-gun filament and the emitter. The cold spacing in Fig. H.6 was 0.100-in. and that of Fig. H.7 was 0.020-in. A cold spacing of 0.100-in. was selected for the cesium diode because its use resulted in a somewhat better electron-gun current-voltage characteristic.

The dummy diode described here was also used in thermal cycling of the various brazes discussed in Appendix G.

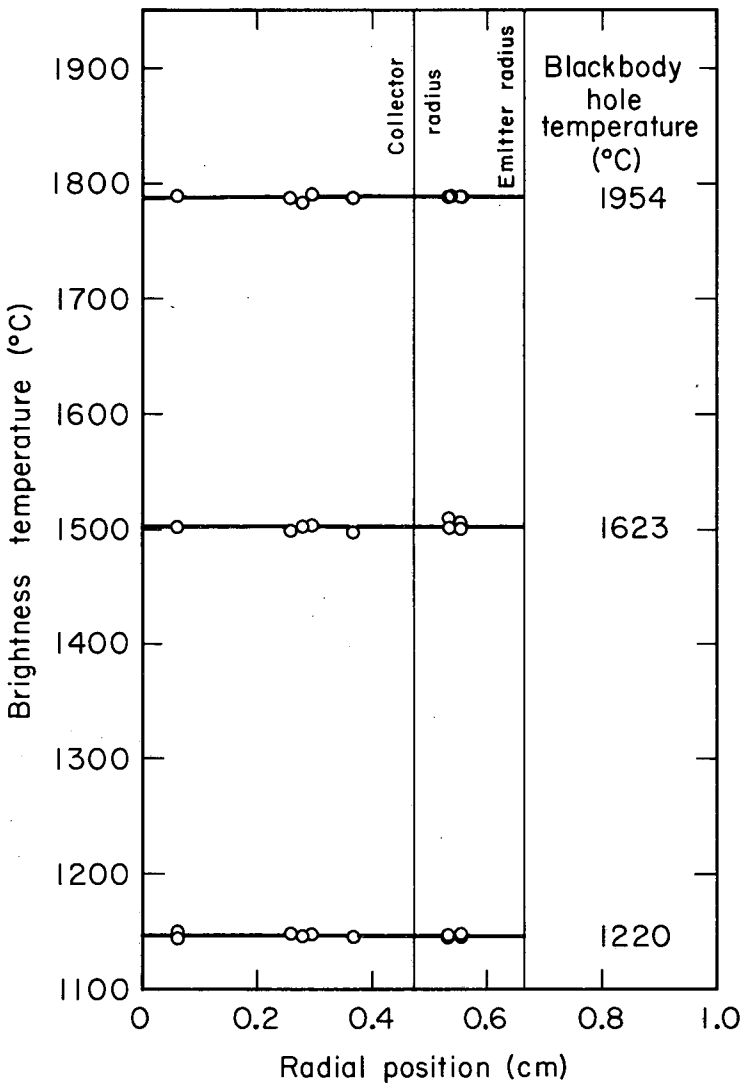
Collector radius
Emitter radius
Blackbody hole temperature (°C)
1954
1623
1220
Brightness temperature (°C)
1900
1800
1700
1600
1500
1400
1300
1200
1100
0
0.2
0.4
0.6
0.8
1.0
Radial position (cm)
MU-36193

Fig. H.6

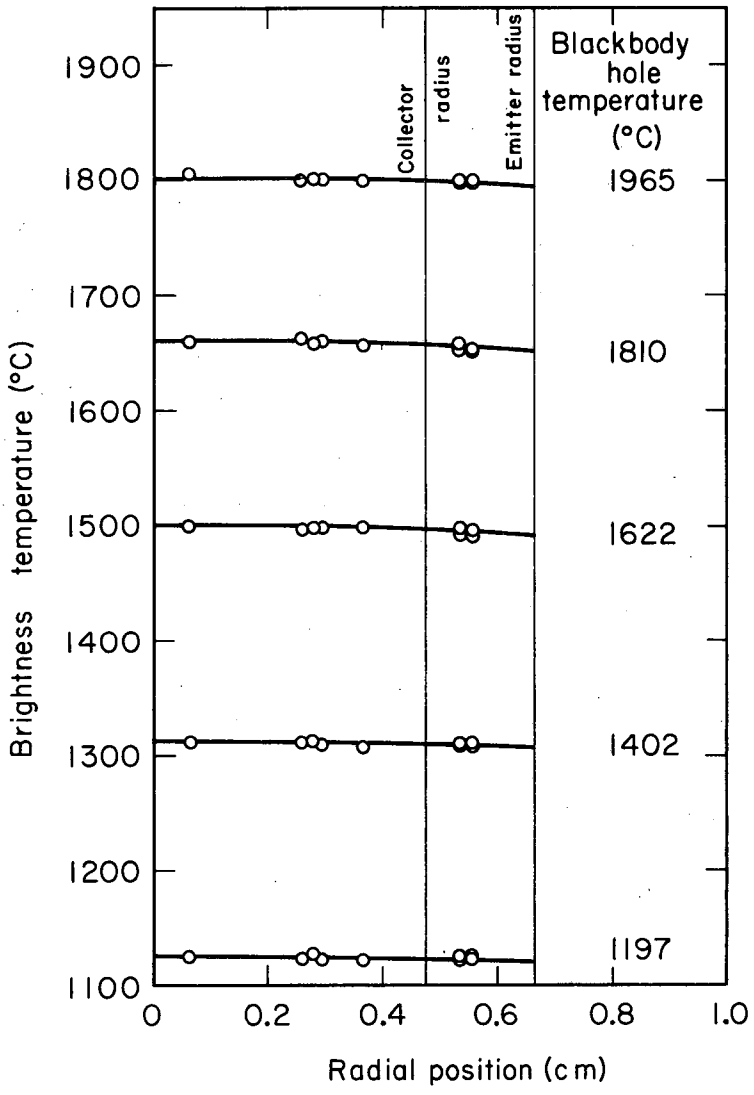
Brightness temperature (°C)
1900
1800
1700
1600
1500
1400
1300
1200
1100
0
0.2
0.4
0.6
0.8
1.0
Radial position (cm)
Collector radius
Emitter radius
Blackbody hole temperature (°C)
1965
1810
1622
1402
1197
MU-36194

Fig. H.7

I. Radial Temperature Distribution on Emitter Surface-Theoretical

Consider a finite solid cylinder of radius R and thickness ℓ as shown in Fig. I.1. Heat $q(r,0)$ is being added through the plane $z = 0$, and removed from the plane $z = \ell$ at a rate $q_1 \propto h_1 T(r,\ell)$ and from the circumferential surface $r = R$ at a different rate $q_2 \propto h_2 T(R,z)$, where h_1, h_2 are the heat-transfer coefficients of the surfaces and T is the temperature. Extending the treatment of Carslaw and Jaeger,[18] we shall solve this heat-transfer problem for the following two cases:

a. The plane $z = 0$ is kept at a prescribed temperature $T(r,0) = T_o$.

b. A prescribed heat flux $q(r,0) = q_o$ is incident on the plane $z = 0$.

Case a.

The heat-conduction equation is

$$\frac{1}{r}\frac{\partial}{\partial r}\left(r\frac{\partial T}{\partial r}\right) + \frac{\partial^2 T}{\partial z^2} = 0; \quad 0 \le r \le R, \; 0 < z \le \ell, \tag{I.1}$$

The boundary conditions are as follows:

$$z = 0 \qquad T(r,0) = T_o \tag{I.2}$$

$$z = \ell \qquad \left.\frac{dT(r,z)}{dz}\right|_{\ell} + H_1 T(r,\ell) = 0 \tag{I.3}$$

$$r = 0 \qquad T(0,z) < \infty \tag{I.4}$$

$$r = R \qquad \left.\frac{dT(r,z)}{dr}\right|_{R} + H_2 T(R,z) = 0 \tag{I.5}$$

where $H = h/k$

k = heat conductivity of cylinder

h = heat-transfer coefficient at surface.

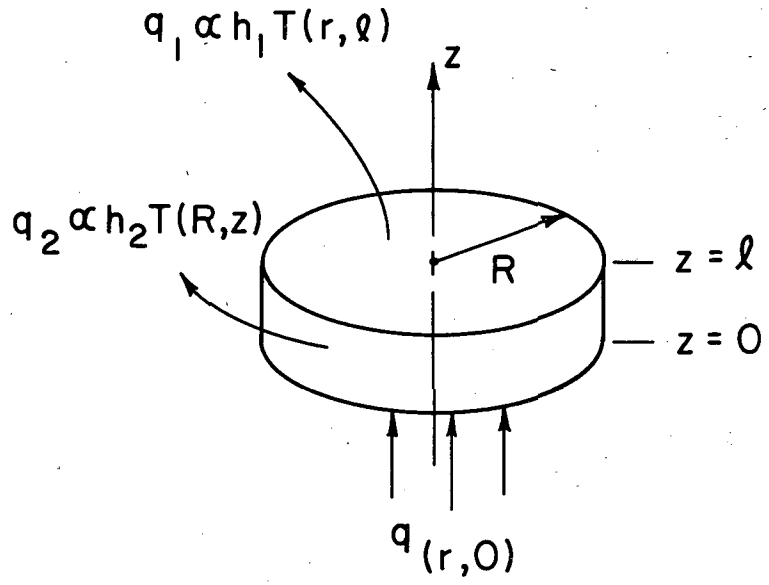

MU-36665

Fig. I.1

The function $J_0(\alpha r)[C \sinh \alpha(\ell-z) + D \cosh \alpha(\ell-z)]$ is a solution to Eq. (I.1) with the boundary contition of Eq. (I.4). The complete solution has the form

$$T(r,z) = \sum_{n=1}^{\infty} J_0(\alpha_n r)[C_n \sinh \alpha_n(\ell-z) + D_n \cosh \alpha_n(\ell-z)] . \qquad (I.6)$$

From Eq. (I.3) we find

$$\frac{C_n}{D_n} = \frac{H_1}{\alpha_n} .$$

Therefore

$$T(r,z) = \sum_{n=1}^{\infty} B_n J_0(\alpha_n r) [H_1 \sinh \alpha_n(\ell-z) + \alpha_n \cosh \alpha_n(\ell-z)] \qquad (I.7)$$

where $B_n = \frac{D_n}{\alpha_n}$.

The coefficient B_n is found by applying Eq. (I.2).

$$T(r,0) = T_o = \sum_{n=1}^{\infty} B_n J_0(\alpha_n r) [H_1 \sinh \alpha_n \ell + \alpha_n \cosh \alpha_n \ell] \qquad (I.8)$$

$$T_o = \sum_{n=1}^{\infty} A_n J_0(\alpha_n r), \qquad (I.9)$$

where

$$A_n = B_n[H_1 \sinh \alpha_n \ell + \alpha_n \cosh \alpha_n \ell].$$

Substituting Eq. (I.9) into Eq. (I.7), we obtain

$$T(r,z) = \sum_{n=1}^{\infty} A_n J_0(\alpha_n r) \frac{H_1 \sinh \alpha_n(\ell-z) + \alpha_n \cosh \alpha_n(\ell-z)}{H_1 \sinh \alpha_n \ell + \alpha_n \cosh \alpha_n \ell} . \qquad (I.10)$$

The term α_n is found from Eq. (I.5).

$$\alpha_n J_1(\alpha_n R) = H_2 J_0(\alpha_n R) \tag{I.11}$$

or

$$\chi_n \frac{J_1(\chi_n)}{J_0(\chi_n)} = H_2 R = P, \tag{I.12}$$

where $\chi_n = \alpha_n R$.

Tables and curves for the determination of the roots of this equation are given in Refs. 67 and 95. Table 2 of Ref. 67 is reporduced here as Table I.1. A_n is obtained by applying the orthogonality relation to Eq. (I.9).

$$A_n = \frac{2}{R^2 [J_1^2(\alpha_n R) + J_0^2(\alpha_n R)]} \int_0^R r\, T(r,0)\, J_0(\alpha_n r)\, dr, \tag{I.13}$$

or from Eq. (I.12) this becomes

$$A_n = \frac{2 \alpha_n^2}{(P^2 + \chi_n^2) J_0^2(\chi_n)} \int_0^R r\, T_o\, J_0(\alpha_n r)\, dr \tag{I.14}$$

$$= \frac{2 T_o P}{(P^2 + \chi_n^2)} \frac{1}{J_0(\chi_n)}. \tag{I.15}$$

The general solution of Case a in its final form is

$$T(r,z) = 2 T_o P \sum_{n=1}^{\infty} \frac{J_0(\alpha_n r)}{J_0(\chi_n)} \frac{1}{(P^2 + \chi_n^2)} \frac{H_1 \sinh \alpha_n(\ell - z) + \alpha_n \cosh \alpha_n(\ell - z)}{H_1 \sinh \alpha_n \ell + \alpha_n \cosh \alpha_n \ell} \tag{I.16}$$

and the radial temperature distribution on surface $z = \ell$ is

$$T(r,\ell) = 2 T_o P \sum_{n=1}^{\infty} \frac{J_0(\alpha_n r)}{J_0(\chi_n)} \frac{1}{(P^2 + \chi_n^2)} \frac{\alpha_n}{H_1 \sinh \alpha_n \ell + \alpha_n \cosh \alpha_n \ell} \tag{I.17}$$

x	$\frac{xJ_1(x)}{J_0(x)}$	x	$\frac{xJ_1(x)}{J_0(x)}$	x	$\frac{xJ_1(x)}{J_0(x)}$
0·00	0·00	2·20	11·083	8·00	10·936
·01	·00005	2·4048	∞	8·20	17·310
·02	·00020	2·50	− 25·64	8·40	32·890
·03	·00045	2·75	− 7·137	8·6537	∞
·04	·00080	3·00	− 3·911	9·00	− 24·442
·05	·00125	3·25	− 2·355	9·25	− 13·125
·06	·00180	3·50	− 1·268	9·50	− 7·795
·07	·00245	3·75	− 0·310	9·75	− 4·393
·08	·00320	3·8317	0·000	10·00	− 1·769
·09	·00405	3·85	0·0703	10·1735	0·000
·10	·00501	3·90	0·2644	10·20	0·2705
·15	·0113	3·95	0·4624	10·25	0·7830
·20	·0201	4·00	0·6651	10·30	1·3053
·25	·0315	4·05	0·8738	10·35	1·8305
·30	·0455	4·10	1·0894	10·40	2·3704
·35	·0622	4·15	1·3132	10·60	4·7138
·40	·0816	4·20	1·5464	10·80	7·5563
·45	·1039	4·40	2·6069	11·00	11·360
·50	·1291	4·60	3·9850	11·20	17·167
·55	·1573	4·80	5·9592	11·40	28·111
·60	·1886	5·00	9·2222	11·60	60·314
·65	·2243	5·10	11·967	11·7915	∞
·70	·2614	5·20	16·182	12·00	− 56·21
·75	·3031	5·40	45·252	12·25	− 24·32
·80	·3487	5·5201	∞	12·50	− 14·08
·85	·3984	5·75	− 24·06	12·75	− 8·448
·90	·4524	5·85	− 16·58	13·00	− 4·418
·95	·5112	6·00	− 11·03	13·25	− 0·981
1·00	·5751	6·25	− 6·474	13·3237	0·000
1·05	·6444	6·50	− 3·843	13·35	0·3511
1·10	·7197	6·75	− 1·873	13·40	1·0216
1·15	·8018	7·00	− 0·109	13·45	1·7000
1·20	·8909	7·0156	0·000	13·50	2·3892
1·25	·9882	7·05	0·2421	13·55	3·0937
1·30	1·0944	7·10	0·5971	13·60	3·8160
1·35	1·2117	7·15	0·9577	13·80	6·9886
1·40	1·3385	7·20	1·3257	14·00	10·916
1·45	1·4792	7·25	1·7028	14·20	16·333
1·50	1·6351	7·30	2·0913	14·40	25·022
1·60	1·9976	7·35	2·4935	14·60	42·998
1·80	3·0789	7·40	2·9116	14·80	112·92
2·00	5·2719	7·60	4·8092	14·9309	∞
2·10	7·1627	7·80	7·2910		

Permission, Institute of Physics and Physical Society of London.

Table I.1 Tabulation of $x\frac{J_1(x)}{J_0(x)}$ versus x.

$$T(r,\ell) = \sum_{n=1}^{\infty} A_n^{T_o} \quad J_0(\alpha_n r) \tag{I.18}$$

where

$$A_n^{T_o} = \frac{2\, T_o\, P\, \alpha_n}{J_0(\chi_n)\,(P^2 + \chi_n^2)(H_1 \sinh \alpha_n \ell + \alpha_n \cosh \alpha_n \ell)}. \tag{I.19}$$

Case b.

The boundary conditions are the same as above except for Eq. (I.2), which is now

$$z = 0, \quad q(r,0) = q_o = -\,k \left.\frac{dT(r,z)}{dz}\right|_0 . \tag{I.20}$$

The general solution is still given by Eq. (I.7) and α_n is still determined by Eq. (I.12). Applying Eq. (I.20) to Eq. (I.7), we obtain

$$q(r,0) = -k \left.\frac{dT(r,z)}{dz}\right|_0 = k \sum_{n=1}^{\infty} B_n' J_0(\alpha_n r)\, \alpha_n [H_1 \cosh \alpha_n \ell_n + \alpha_n \sinh \alpha_n \ell] \tag{I.21}$$

or

$$q(r,0) = \sum_{n=1}^{\infty} A_n' J_0(\alpha_n r), \tag{I.22}$$

where $A_n' = B_n' k \alpha_n [H_1 \cosh \alpha_n \ell + \alpha_n \sinh \alpha_n \ell]$.

The term $T(r,z)$ then becomes

$$T(r,z) = \sum_{n=1}^{\infty} A_n' \frac{J_0(\alpha_n r)}{k\alpha_n} \frac{H_1 \sinh \alpha_n(\ell - z) + \alpha_n \cosh \alpha_n(\ell - z)}{H_1 \cosh \alpha_n \ell + \alpha_n \sinh \alpha_n(\ell - z)} \tag{I.23}$$

Applying the orthogonality relation to Eq. (I.22), we obtain

$$A_n' = \frac{2}{R^2[J_1^2(\alpha_n R) + J_0^2(\alpha_n R)]} \int_0^R r q(r,0) J_0(\alpha_n r)\, dr \tag{I.24}$$

$$A_n' = \frac{2q_o P}{(P^2+\chi_n 2)} \quad \frac{1}{0(\chi_n)}, \tag{I.25}$$

and the general solution of Case b is

$$T(r,z) = 2\frac{q_o}{k} P \sum_{n=1}^{\infty} \frac{J_0(\alpha_n r)}{J_0(\chi_n)\alpha_n} \frac{1}{(P^2+\chi_n^2)} \frac{H_1 \sinh \alpha_n(\ell-z) + \alpha_n \cosh \alpha_n(\ell-z)}{H_1 \cosh \alpha_n \ell + \alpha_n \sinh \alpha_n \ell}. \tag{I.26}$$

The radial temperature distribution on the surface $z = \ell$ is

$$T(r,\ell) = \frac{2q_o}{k} P \sum_{n=1}^{\infty} \frac{J_0(\alpha_n r)}{J_0(\chi_n)} \frac{1}{(P^2+\chi_n^2)} \frac{1}{(H_1 \cosh \alpha_n \ell + \alpha_n \sinh \alpha_n \ell)} \tag{I.27}$$

$$T(r,\ell) = \sum_{n=1}^{\infty} A_n^{q_o} J_0(\alpha_n r) \tag{I.28}$$

where

$$A_n^{q_o} = \frac{2q_o P/k}{J_0(\chi_n)(P^2+\chi_n^2)(H_1 \cosh \alpha_n \ell + \alpha_n \sinh \alpha_n \ell)}. \tag{I.29}$$

Comparing Eqs. (I.29) and (I.19), we obtain

$$A_n^{q_o} = A_n^{T_o} \frac{q_o}{T_o k H_1} \frac{1+(H_1/\alpha_n)\tanh \alpha_n \ell}{1+(\alpha_n/H_1)\tanh \alpha_n \ell}. \tag{I.30}$$

We are interested in calculating the difference, or the fractional difference, between the surface temperature at the center and at the edge of the emitter. The latter is given by

$$\frac{T(0,\ell) - T(R,\ell)}{T(0,\ell)} = \frac{\sum_{n=1}^{\infty} A_n^{q_o} [1-J_0(\chi_n)]}{\sum_{n=1}^{\infty} A_n^{q_o}}. \tag{I.31}$$

A similar result is obtained for Case a. If the experimental conditions allow terminating the series expansion after the first term, as they did in our experiment, Eq. (I.31) becomes for both Case a and Case b,

$$\frac{T(0,\ell) - T(R,\ell)}{T(0,\ell)} \approx 1 - J_0(\chi_1), \tag{I.32}$$

where χ_1 is the first root of Eq. (I.12). The heat-transfer coefficients h_1 and h_2 were calculated in the following way. If the radial change in temperature is small, then

$$q_1(r,\ell) \approx \epsilon_1 \sigma T^3(0,\ell) T(r,\ell) = h_1 T(r,\ell) \tag{I.33}$$

and

$$q_2(R,z) \approx \epsilon_2 \sigma T^3_{(0,\ell)} T(R,z) = h_2 T(R,z), \tag{I.34}$$

where ϵ_1, ϵ_2 are the effective thermal emissivities, and σ is the Stefan-Boltzmann constant equal to 5.67 watt/cm^2(1000°K)^4. Let us calculate h_2 at 1960°C, which is near the top of the temperature range in Figs. H.6 and H.7. Assuming that the side, circumferential surface of the emitter is radiating out to space, we choose $\epsilon_2 = 0.3$. Then from Eq. (I.34), $h_2 = 0.19$ watt/cm^2°K. The heat conductivity of tungsten in the temperature range 1500 to 2300°K is about 1 watt/cm°K. The radius of the emitter was 0.67 cm. Therefore $P = H_2R = h_2R/k = 0.013$. Substituting this value of P in Eq. (I.12) and solving for χ_1, we get $\chi_1 = 0.16$ or $J(\chi_1) = 0.994$. Hence,

$$\frac{T(0,\ell) - T(R,\ell)}{T(0,\ell)} \approx 1 - 0.994 = 0.006,$$

or $T(0,\ell) - T(R,\ell) \approx 0.006\, T(0,\ell) \approx 13$°K. This temperature change is about twice that observed in Fig. H.7.

J. Temperature Calibration of Windows and Pyrometer

The dummy diode described in Appendix H was also used in the temperature calibration of the diode sapphire window and the environmental chamber window. We determined the absorptivity of the windows by observing the change in the measured temperature of the emitter hohlraum when a sapphire window, similar to that installed in the diode, and the environmental chamber window were placed in the line of sight of the pyrometer.

The window-temperature calibration curve thus obtained is shown in Fig. J.1. Whenever the diode was operated in air outside the chamber, the chamber window was placed in the line of sight of the pyrometer so this same calibration curve was used throughout this whole study.

The calibration of the optical pyrometer was checked, before and after the series of experiments performed in this study, with a tungsten-lamp standard. In both cases the pyrometer gave the correct temperature reading, within the precision of the instrument (±0.2%), in the range of brightness temperatures 950 to 1750°C.

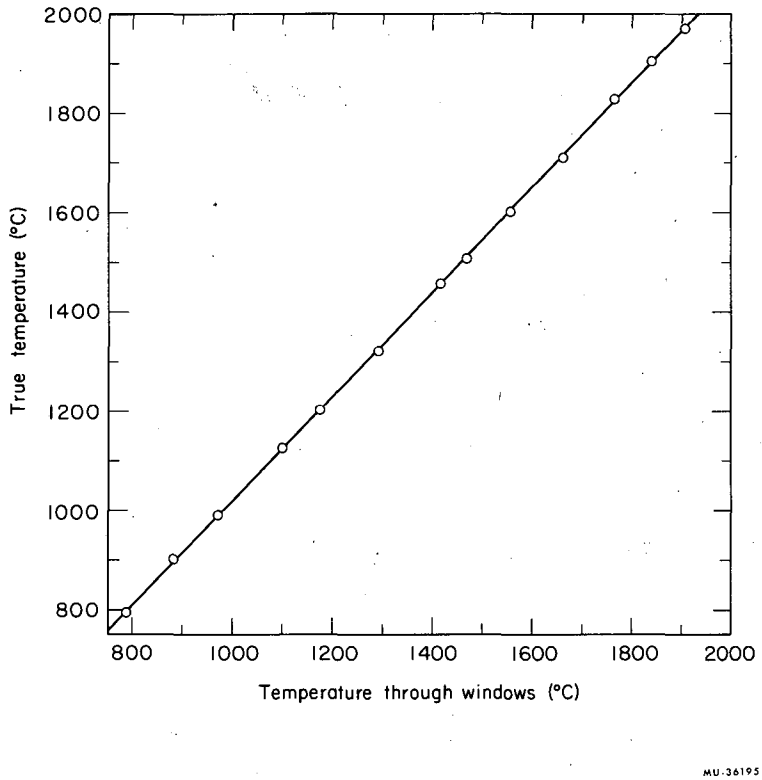
2000
1800
1600
1400
1200
1000
800
True temperature (°C)
800
1000
1200
1400
1600
1800
2000
Temperature through windows (°C)
MU-36195

Fig. J. 1

K. Laboratory Layout

Figure K.1 shows the laboratory layout in which this study was performed. Starting on the left side of the photograph and going clockwise around both benches, we see first the helium and argon tanks for the diode environmental chamber. On the bench are the potentiometer used to measure the thermocouple outputs, followed by a 6-channel Brush recorder, then the diode in its chamber. On the rack behind the bench is the cesium-reservoir temperature controller and recorder, and under it is a 12-point recorder for thermocouples. Under the bench is a mechanical pump to evacuate the diode chamber and water in a thermally insulated water tank serving as the temperature sink for the cesium reservoir. At the far end of the bench is a rack containing power supplies for the diode electron gun and for the various heaters wrapped around the diode. Then there is an X-Y oscilloscope with a mounted Polaroid camera and next to it a low rack containing the various electronic circuits used in diode operation. At the far end of the front bench is a tall rack containing the various dc and ac power supplies used in the diode circuit. On the bench are several voltmeters used to measure the diode current-voltage characteristics, and an X-Y plotter, and in the front there is the dummy diode used to measure the emitter temperature distribution and to test the endurance to thermal cycling of the emitter brazes. The bottom of the picture shows a dc power supply used for electropolishing. Not shown in the picture and off to the right are an all-purpose high-vacuum pump station, mainly used for vacuum brazing, a 3kVA dc power supply with a 100-A 10-V ac power supply attached (also used for vacuum brazing) and finally a large wall rack for mounting glassware and doing glass blowing such as building the cesium-transfer apparatus.

ZN-5595

Fig. K.1

L. Circuit Diagrams and Performance Characteristics

The circuit diagram for the operational power amplifier [Fig. III.3(b)] used to maintain the voltage difference between the collector and guard ring within 1 mv is shown in Fig. L.1. The amplifier, which had a current rating exceeding 10 amperes, was designed for use in the ac-sweep method of obtaining the current-voltage characteristics of the plasma diodes. This technique is a convenient way of acquiring data, especially, as discussed in section VI, when the current output of the diode is large (> 1 ampere). A 60 cps ac test-circuit (Fig. L.2) with a sampling capability was designed and built for this purpose. The circuit diagrams associated with the sampling units are shown in Figs. L.3 to L.6. The test circuit in Fig. L.2 was not used to gather any of our data because the sampler was not completed in time. However, the operational amplifier was used with great effectiveness to measure, point by point, the current-voltage characteristics of the (100) diode operating in vacuum and in cesium vapor. The general characteristics of the amplifier are as follows: (a) The range of input signal is 0 to ±4 V; (b) the voltage gain is 1 with a linearity of about 0.3%; (c) the dc input impedance is > 200 MΩ; (d) the ac input impedance decreases with increasing frequency due to phase shift in the feedback loop; with a low-impedance source the gain is unity from dc to about 4 kc, and with a 1-MΩ impedance source the gain is unity from dc to about 800 cps; above these frequencies the phase shift causes distortion in the wave form; (e) the B^+ and B^- voltages in Fig. L.1 should be about 10 V.

The characteristics of the sampler amplifiers are similar to those above except, of course, for the current rating. The current gain is about 10^{14} and the voltage gain is unity. The output impedance is about 100Ω.

The output of the samplers is linear within 1% but has a constant dc offset which can be corrected by placing a voltage suppressor between each sampler and the X-Y plotter.

The sampler has a sampling width of 15 μsec and a sweep time continuously selectable from 3 to 60 sec. Because both the starting and ending points of the sample are continuously adjustable, the capability is provided of examining any desired portion of the diode current-voltage curve.

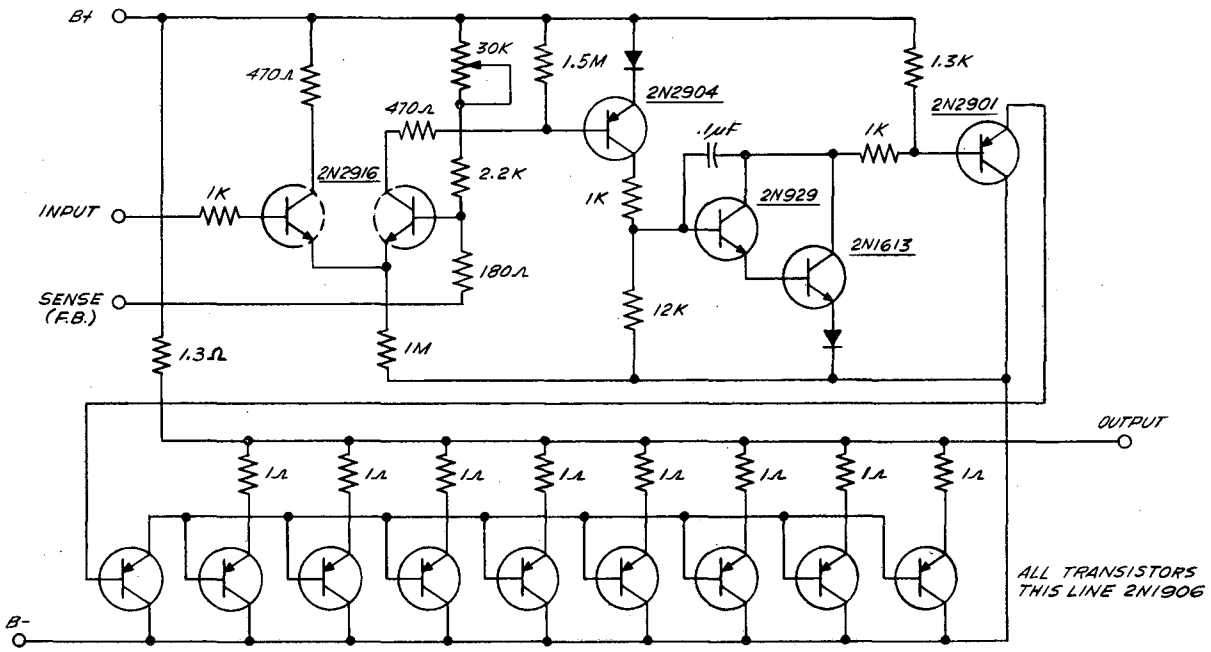
B+
470Ω
30K
1.5M
2N2904
1.3K
2N2901
470Ω
.1μF
1K
2N2916
2.2K
INPUT
1K
1K
2N929
2N1613
180Ω
SENSE
(F.B.)
12K
1.3Ω
1M
OUTPUT
1Ω
1Ω
1Ω
1Ω
1Ω
1Ω
1Ω
1Ω
1Ω
ALL TRANSISTORS
THIS LINE 2N1906
B-
MU-36175

Fig. L. 1

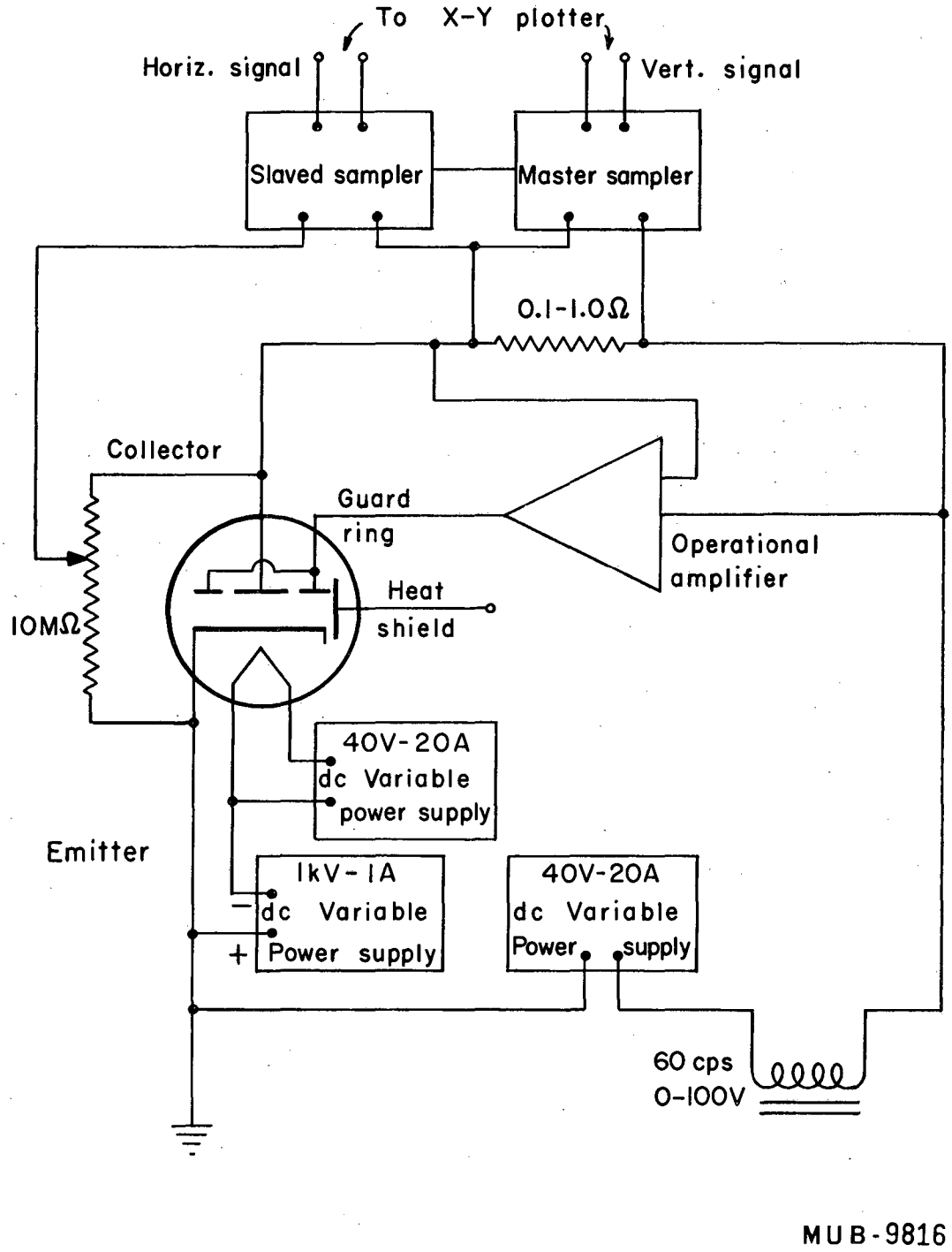
To X-Y plotter
Horiz. signal
Vert. signal
Slaved sampler
Master sampler
0.1-1.0Ω
Collector
Guard ring
Operational amplifier
Heat shield
10MΩ
40V-20A dc Variable power supply
Emitter
1kV-1A dc Variable Power supply
40V-20A dc Variable Power supply
60 cps 0-100V
MUB-9816

Fig. L.2

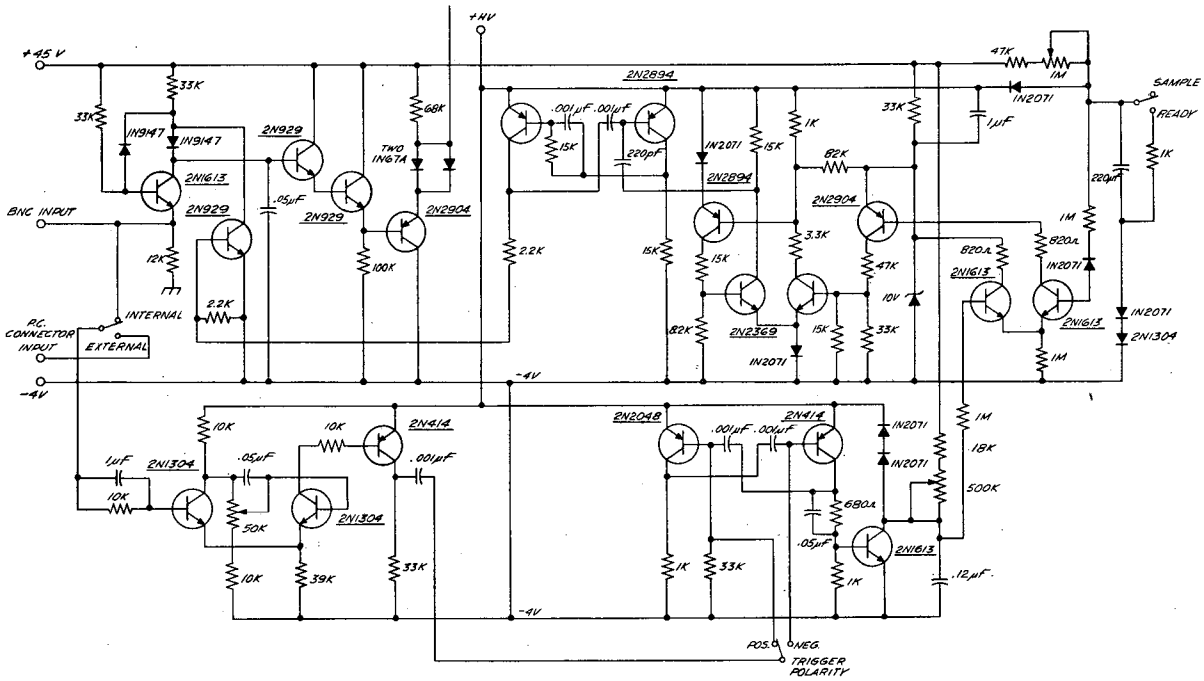
+45 V
+HV
33K
33K
1N9147
1N9147
2N1613
2N929
BNC INPUT
12K
2.2K
INTERNAL
P.C. CONNECTOR INPUT
EXTERNAL
-4V
2N929
.05μF
2N929
68K
TWO IN67A
2N2904
100K
2.2K
2N2894
.001μF
.001μF
15K
220pF
IN2071
15K
1K
82K
2N2894
2N2904
3.3K
15K
15K
47K
10V
82K
2N2369
15K
33K
IN2071
-4V
33K
1μF
47K
1M
IN2071
SAMPLE
READY
1K
220pF
1M
820Ω
820Ω
2N1613
IN2071
2N1613
IN2071
2N1304
1M
10K
10K
2N414
.001μF
1μF
2N1304
.05μF
10K
50K
2N1304
10K
39K
33K
-4V
2N2048
.001μF
.001μF
2N414
IN2071
IN2071
1M
18K
500K
680Ω
.05μF
2N1613
1K
33K
1K
.12μF
POS.
NEG.
TRIGGER POLARITY
MU-36173

Fig. L. 3

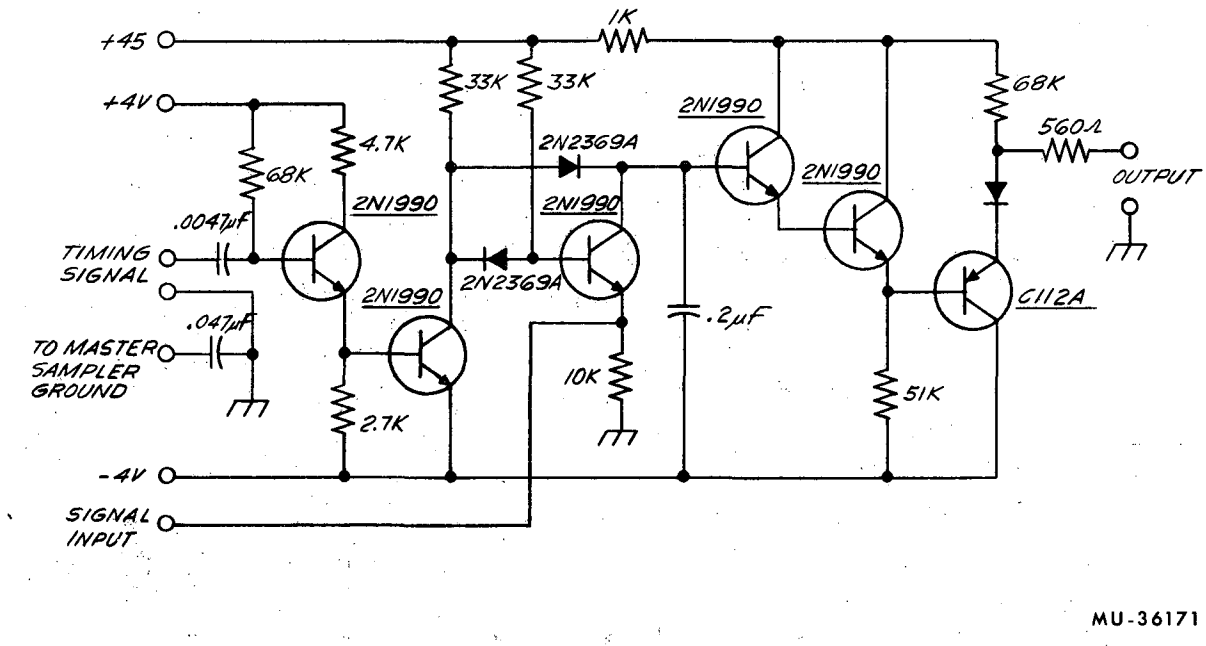
+45
+4V
TIMING SIGNAL
TO MASTER SAMPLER GROUND
-4V
SIGNAL INPUT
1K
33K
33K
68K
4.7K
.0047μF
.047μF
2N1990
2N1990
2N1990
2N1990
2N1990
2N2369A
2N2369A
.2μF
10K
2.7K
51K
68K
560Ω
OUTPUT
C112A
MU-36171

Fig. L.4

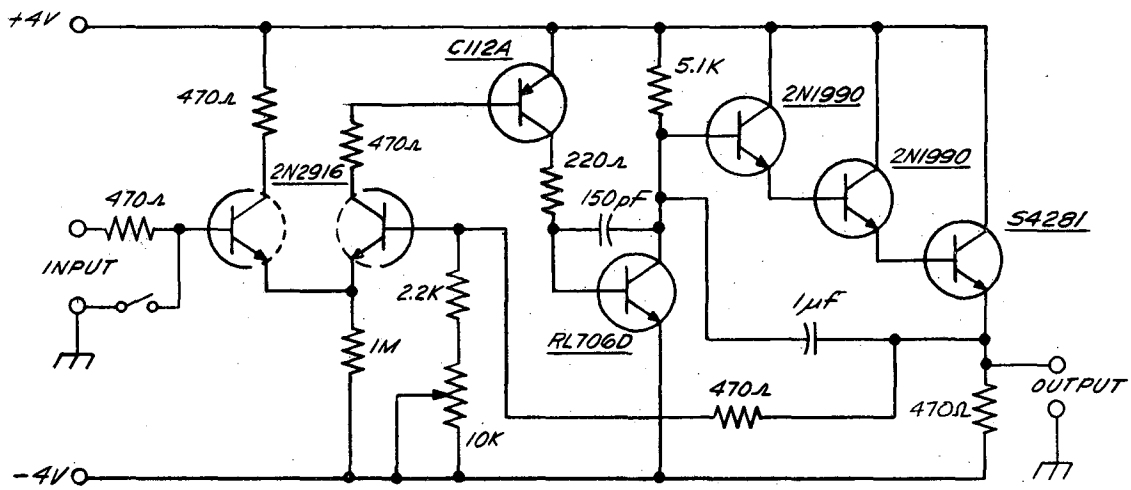
+4V
C112A
5.1K
2N1990
470Ω
470Ω
2N2916
220Ω
2N1990
470Ω
150pF
INPUT
2N4281
2.2K
1μF
1M
RL706D
OUTPUT
470Ω
470Ω
10K
-4V
MU-36172

Fig. L.5

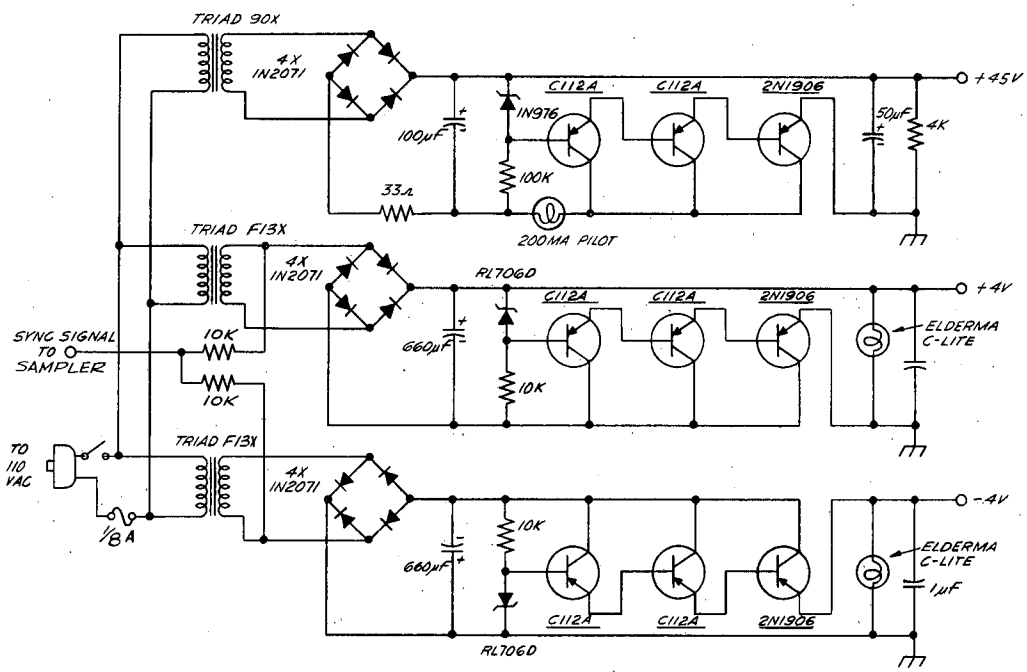
TRIAD 90X
4X IN2071
C112A
C112A
2N1906
+45V
IN976
100μF
100K
33Ω
50μF
4K
200MA PILOT
TRIAD F13X
4X IN2071
RL706D
C112A
C112A
2N1906
+4V
ELDERMA C-LITE
SYNC SIGNAL TO SAMPLER
10K
10K
660μF
10K
TO 110 VAC
TRIAD F13X
4X IN2071
-4V
1/8A
10K
ELDERMA C-LITE
660μF
1μF
C112A
C112A
2N1906
RL706D
MU-36174

Fig. L.6

M. Theoretical Effectiveness of Guard Ring at Zero Field

In calculating current densities, we assumed that the effective area of the emitter is equal to the area of the collector plus half of the area of the annular gap between collector and guard ring.

There can be little doubt that this is a good approximation in the presence of an applied electric field, since the electron or ion trajectories will be essentially perpendicular to the electrode surfaces. One may question the accuracy of the assumption, however, near the region of zero interelectrode potential, where the angular distribution of emitted charges could become important. What has been assumed in effect is (a) that the collector is surrounded by a guard ring of infinite extent, and (b) that the emitting plane is also infinite, so that any charge that is emitted from the region of the emitter directly facing the collector but that misses the collector is made up by contributions from the infinite remainder of the emitter. But in fact both guard ring and emitter areas are finite and the collector current will be reduced to the extent that it is not collecting charges emitted from the emitter region bounded by the diameter of the emitter and infinity. In the following analysis we evaluate this effect.

We assume for simplification that the angular distribution of emitted charges is the familiar cosine ditribution (Lambert's law), so that the results already available in the literature for thermal radiation from surfaces can be applied. Obviously if the angular distribution is more peaked toward the surface normal, then the effect under consideration is even more negligible.

The following analysis is from Jacob.[44] The emission from two disks

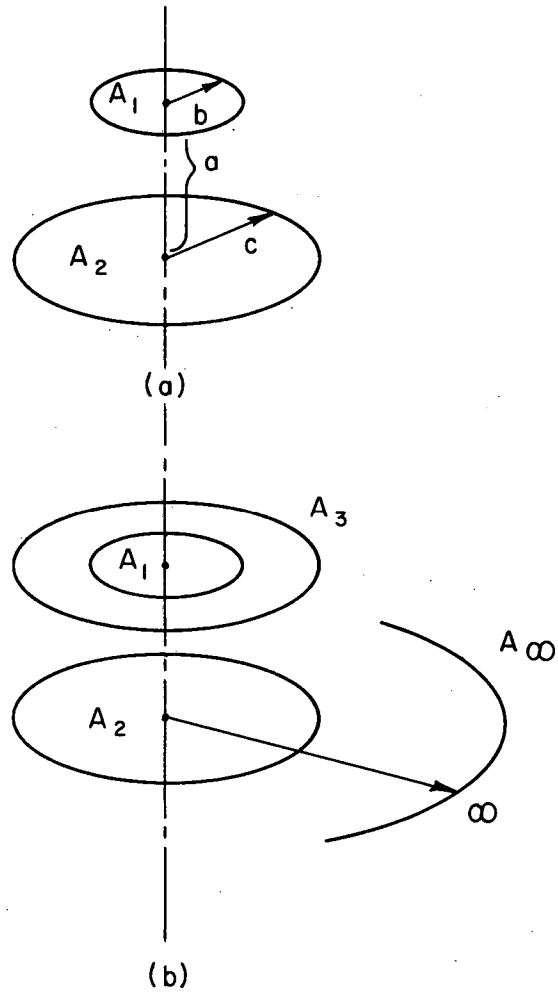

MU-36666

Fig. M. 1

having the same axis is shown in Fig. M.1(a). If J_{12} is the area A_1 emission which falls on A_2, then

$$J_{12} = F_{12} W_1 A_1, \tag{M-1}$$

where W_1 = total emission per unit area from area A_1,

F_{12} = fraction of emission from A_1 which falls on A_2

$$F_{12} = \frac{1}{A_1} \int_{A_1} \int_{A_2} \frac{\cos\phi_1 \cos\phi_2}{\pi r^2} \, dA_1 \, dA_2 \tag{M-2}$$

where r is the length of the vector $\vec{r}$ joining elementary areas dA_1 and dA_2 and ϕ_1 and ϕ_2 are the angles between $\vec{r}$ and the surface normals of dA_1 and dA_2 respectively. In general,

$$\frac{J_{ke}}{W_k} = \frac{J_{ek}}{W_e} \tag{M-3}$$

$$\text{or} \qquad A_k F_{ke} = A_e F_{ek}. \tag{M-4}$$

For two disks on the same axis,

$$F_{12} = \frac{1 + B^2 + C^2 - [(1 + B^2 + C^2)^2 - 4 B^2 C^2]^{1/2}}{2B^2}, \tag{M-5}$$

where B = b/a, and C = c/a; the dimensions a, b, and c are shown in Fig. M.1(a).

The geometry of the electrodes is represented in Fig. M.1(b), where

A_1 = collector

A_2 = emitter $\approx 2A_1$

A_3 = collector plus guard ring = A_2

A_∞ = emitter of infinite radius.

The emission that comes from the emitter and that falls on the collector is

$$J_{21} = W_2 \, A_2 \, F_{21} \, . \qquad \text{(M-6)}$$

However, we have assumed that

$$J_{21} = J_{\infty 1} \qquad \text{(M-7)}$$

where

$$J_{\infty 1} = W_2 \, A_\infty \, F_{\infty 1} = W_2 \, A_1 \, . \qquad \text{(M-8)}$$

Therefore the fractional error in our assumption is

$$\frac{\Delta(J_{21})}{J_{\infty 1}} = \frac{J_{\infty 1} - J_{21}}{J_{\infty 1}} = \frac{A_1 - A_2 \, F_{21}}{A_1} = 1 - F_{12} \, . \qquad \text{(M-9)}$$

The diameter of the emitter was 0.52 in., so for interelectrode spacing a = 0.030 in., we find that

$$1 - F_{12} = 0.7\% \, .$$

Since practically all the data were obtained at spacings smaller than 0.030 in., the error in the assumption that the effective emitter area is equal to the collector area is negligible.

For the conditions just considered $F_{23} = 0.95$, which means that at least 95% of the emission or radiation from the whole emitter surface was collected by the collector-guard assembly.

N. Determination of P_{ao} in the Space-charge Limited Case

Let P_{ao} = probability per unit time of evaporation of a neutral atom, in sec^{-1}

P_{io} = probability per unit time of evaporation of an ion, in sec^{-1}

$P = P_{io} + P_{ao}$ = total evaporation probability per unit time, in sec^{-1}

n_o = incident flux of cesium, in $atom/cm^2$ sec

N = surface concentration of adsorbed particles, in $particles/cm^2$

I = cesium-ion current leaving emitter surface of unit area, in $ions/cm^2$ (the subscript Cs has been omitted here for convenience).

Initially at $t \leq 0$ we prevent the evaporation of ions by applying a retarding electric field for ions at the emitter surface. Therefore, the initial surface concentration N_o is

$$N_o = N(0) = \frac{n_o}{P_{ao}} \quad . \tag{N-1}$$

At time $t = 0$ we reverse the polarity of the electric field and allow the ions to evaporate. The rate of change of the surface concentration is then

$$\frac{dN}{dt} = n_o - I(t) - P_{ao}N(t), \tag{N-2}$$

where $I(t)$ is the ion current leaving the emitter. We assume that n_o, P_{ao}, and P_{io} are constant in time and independent of N; thus the general solution of Eq. (N-2) is

$$N(t) = \exp(-P_{ao}t)\left\{\int_0^t [n_o - I(t')] \exp(P_{ao}t')\, dt' + N(0)\right\}, \quad \text{(N-3)}$$

or solving for $N(0) = N_o$, we obtain

$$N_o = N(t) \exp(P_{ao}t) + \int_0^t [I(t') - n_o] \exp(P_{ao}t')\, dt' . \quad \text{(N-4)}$$

Let us assume that the ion current $I(t)$ varies in the manner shown in Fig. N.1. That is,

$$I(t) = I_o, \; 0 < t < t_o \quad \text{(N-5)}$$

$$= I_\infty + (I_o - I_\infty) \exp[-P(t-t_o)], \; t_o < t < \infty . \quad \text{(N-6)}$$

The final surface concentration and ion current will be

$$N(\infty) = \frac{n_o}{P} \; ; \; I(\infty) = I_\infty = P_{io} N(\infty) = \frac{P_{io} n_o}{P} . \quad \text{(N-7)}$$

We now solve Eq. (N-4) for $t = t_1$, $t_o < t_1 < \infty$

$$N_o = N(t_1) \exp(P_{ao}t_1) + \int_0^{t_1} [I(t) - n_o] \exp(P_{ao}t)\, dt \quad \text{(N-8)}$$

$$= N(t_1) \exp(P_{ao}t_1) + \int_0^{t_1} (I_\infty - n_o) \exp(P_{ao}t)\, dt + \int_0^{t_1} [I(t) - I_\infty] \exp(P_{ao}t)\, dt \quad \text{(N-9)}$$

$$= N(t_1) \exp(P_{ao}t_1) + \frac{I_\infty - n_o}{P_{ao}} [\exp(P_{ao}t_1) - 1] + \int_0^{t_1} [I(t) - I_\infty] \exp(P_{ao}t)\, dt. \quad \text{(N-10)}$$

If we let t_1 go to infinity and make use of Eq. (N-7), then

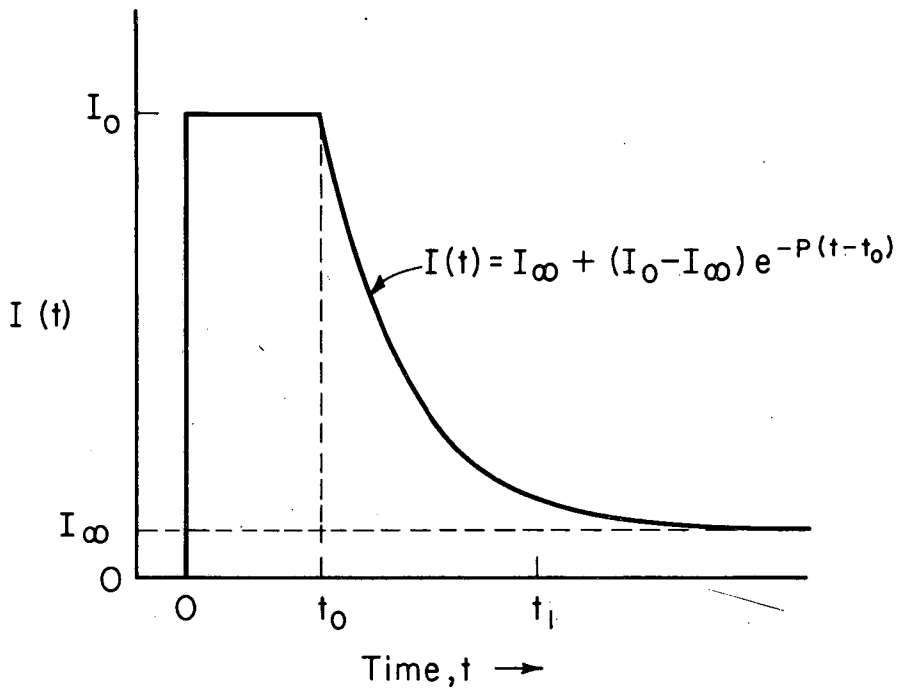

MU-36610

Fig. N. 1

$$\lim_{t_1 \to \infty} \left\{ N(t_1) \exp(P_{ao} t_1) + \frac{I_\infty - n_o}{P_{ao}} [\exp(P_{ao} t_1) - 1] \right\} = \frac{n_o}{P} \exp(P_{ao} t_1)$$

$$- \frac{n_o}{P} [\exp(P_{ao} t_1) - 1] = \frac{I_\infty}{P_{io}} \quad . \tag{N-11}$$

and Eq. (N-10) becomes

$$N_o = \frac{I_\infty}{P_{io}} + \int_0^\infty [I(t) - I_\infty] \exp(P_{ao} t) \, dt \quad . \tag{N-12}$$

If we expand $\exp(P_{ao} t) = 1 + P_{ao} t + \frac{P_{ao}^2 t^2}{2} + \ldots$, we obtain

$$N_o \approx \frac{I_\infty}{P_{io}} + \int_0^\infty [I(t) - I_\infty] \, dt + P_{ao} \int_0^\infty [I(t) - I_\infty] t \, dt$$

$$+ \frac{P_{ao}^2}{2} \int_0^\infty [I(t) - I_\infty] \, t^2 \, dt. \tag{N-13}$$

We will keep the first integral in Eq. (N-13) in integral form, as is, and solve the last two integrals, which are first- and second-order terms, by using Eqs. (N-5) and (N-6), as follows,

$$P_{ao} \int_0^\infty [I(t) - I_\infty] t \, dt = P_{ao} \int_0^{t_o} (I_o - I_\infty) \, t \, dt$$

$$+ P_{ao} \int_{t_o}^\infty (I_o - I_\infty) \exp[-P(t - t_o)] t \, dt \tag{N-14}$$

$$= \frac{(I_o - I_\infty)}{2} P_{ao} t_o^2 + (I_o - I_\infty) \frac{P_{ao}}{P^2} (P t_o + 1) \tag{N-15}$$

$$\frac{P_{ao}^2}{2} \int_0^\infty [I(t) - I_\infty] t^2 dt = \frac{P_{ao}^2}{2} \int_0^{t_o} (I_o - I_\infty) t^2 dt$$

$$+ \frac{P_{ao}^2}{2} \int_{t_o}^\infty (I_o - I_\infty) \exp[-P(t - t_o)] t^2 dt \tag{N-16}$$

$$= \frac{(I_o - I_\infty)}{2} \frac{P_{ao}^2 t_o^3}{3} + \frac{(I_o - I_\infty)}{2} \frac{P_{ao}^2}{P^3} (P^2 t_o^2 + 2Pt_o + 2) . \qquad \text{(N-17)}$$

We will neglect the second term in Eqs. (N-15) and (N-17). It can be shown that for $t_o < 1/P_{ao}$, each neglected term is not greater than the factor P_{ao}/P times the first integral term in Eq. (N-13)[the analytical evaluation of this integral is $(I_o - I_\infty)(1 + Pt_o)/P$]. Because the conditions $P_{ao}/P < 1\%$ and $t_o < 1/P_{ao}$ prevailed in the complete range of our experimental observations, we are justified in making this approximation.

So, incorporating Eqs. (N-15) and (N-17) into Eq. (N-13) and rearranging terms, we obtain, to a second-order approximation,

$$N_o = \frac{n_o}{P_{ao}} = \frac{I_\infty}{P_{io}} + \int_0^\infty [I(t) - I_\infty] \, dt + t_o \frac{(I_o - I_\infty)}{2} \left[P_{ao} t_o + \frac{(P_{ao} t_o)^2}{3} \right] . \qquad \text{(N-18)}$$

The first term on the right side of the equation represents the final equilibrium surface concentration after the field reversal and is essentially negligible. The integral is the net number of ions removed from the surface, and the last term represents the net number of atoms that leave the surface during time t_o. The terms that we neglected in Eqs. (N-15) and (N-17) represent the net number of atoms that leave the surface after time t_o.

We did not use the analytic evaluation of the integral in Eq. (N-18) because the oscilloscope traces did not exactly follow our model, (Fig. N.1) and we felt that it would be more accurate to integrate the actual enlarged traces with a planimeter. The last term in Eq. (N-18) was usually a few percent of the integral and was never more than 15%, so that P_{ao} could be evaluated in one or two iterations.

O. Heat-of-Evaporation Data for the (110) and (100) Crystals

Tables O.I through IV comprise all of the significant data obtained for both (110) and (100) crystals. The definitions of the symbols used in the tables are as follows:

T_E - true emitter temperature

V_E - voltage applied to the emitter at time zero. The instantaneous applied voltage between the electrodes is equal to V_E less the voltage across the current measuring resistor. This resistor was 10 kΩ for the (110) crystal (Table O.I.) and the low-Cs-temperature (Tables O.II and III) experiments on the (100) crystal, and 1 kΩ for the high Cs-temperature experiment on the (100) crystal (Table O.IV). The interelectrode potential is obtained by subtracting, in addition, the contact potential [about 3.5V for the (110) crystal and 3V for the (100) crystal experiments].

t_o - elapsed time noted at the knee of the oscilloscope traces

$(I_o - I_\infty)^a$ - difference between initial and final ion currents to the collector after field reversal.

$n_o{}^a$ - observed current of cesium atoms incident on the emitter, assuming no secondary electron emission. It is equal to $I_\infty P_{io}/(P_{io} + P_{ao}) \approx I_\infty$.

---

a - To obtain current (or atom) densities (i.e., per unit area), divide these quantities by the collector area (0.71 cm^2); also, 1 ampere = 6.281×10^{18} charge/sec.

N_o^a - initial surface concentration of cesium on the emitter

N'^a - surface concentration of cesium on the emitter at the beginning of the exponentially decaying part of the oscilloscope trace

P_{io} - reciprocal of the mean adsorption lifetime for ions

P_{ao} - reciprocal of the mean adsorption lifetime for atoms

---

a - To obtain current (or atom) densities (i.e., per unit area), divide these quantities by the collector area (0.71 cm^2; also, 1 ampere = 6.281×10^{18} charge/sec.

TABLE O.I. Heat-of-evaporation data analysis for the (110) crystal, T_{C_s} = -196°C.

Photo no.[a]	T_E (°K)	n_o (μA)	V_E (V)	t_o (msec)	$I_o - I_\infty$ (μA)	N_o (10^{12} atoms)	N' (10^{10} atoms)	P_{io} (sec^{-1})	P_{ao} (sec^{-1})
A5	1193	7.8	18	14.2	244	26.5	53	987	1.85
			15	18.0	179	25.2	100	508	1.94
			12.5	23.5	129	23.8	77	352	2.06
			10	32.8	82	21.5			2.28
			7.5	60.3	41	20.6			2.38
A9	1242	19.0	18	11.3	262	24.8	73	814	4.80
			15	15.2	195	24.0	80	540	4.96
			12.5	20.1	138	23.5	91	381	5.07
			10	29.2	88	23.1			5.17
			7.5	52.8	39	21.5			5.55
A13	1295	24.0	18	7.4	299	18.7	41	1140	8.05
			15	9.8	222	18.7	67	706	8.07
			12.5	13.2	156	18.1	68	557	8.33
			10	19.3	101	18.0			8.39
			7.5	34.8	48	17.0			8.88

TABLE 0.I (Continued)

Photo no.[a]	T_E (°K)	n_o (μA)	V_E (V)	t_o (msec)	$I_o - I_\infty$ (μA)	N_o (10^{12} atoms)	N' (10^{10} atoms)	P_{io} (sec^{-1})	P_{ao} (sec^{-1})
A16	1348	34.0	18	4.9	349	15.1	39	1340	14.1
			15	6.3	258	15.0	53	984	14.2
			12.5	8.5	185	14.6	83	637	14.7
			10	12.6	117	14.5			14.7
			7.5	21.8	56	13.3			16.0
A19	1399	54.0	18	2.25	424	8.47	24	3270	40.1
			15	2.85	315	8.15	34	2340	41.6
			12.5	3.65	232	8.03	50	1570	42.3
			10	5.25	152	8.00			42.4
			7.5	9.05	75	7.60			44.6
A22[b]	1503	156	18	1.17	477	6.43	65	3240	152
			15	1.50	347	6.06	63	2370	162
			12.5	2.00	237	5.67	58	1960	173
			10	2.95	128	5.19			189
			7.5	5.26	33	3.40			288

a. Pictures A5 to A22 correspond to Fig. IV.5(a) to (f) respectively.

b. Measured interelectrode spacing = 0.26mm.

Table O.II. Heat-of-evaporation data analysis for the (100) crystal, with emitter temperature increasing and T_{Cs} = -196°C.

Photo no.	T_E (°K)	n_o (μA)	V_E (V)	t_o (msec)	$I_o - I_\infty$ (μA)	N_o (10^{10} atoms)	N' (10^{10} atoms)	P_{io} (sec^{-1})
B2	1078[a]	0.04	30	0	12.7		9.05	8.82×10^2
B3	1078[a]	0.04	8	0.23	9.50	5.46		
B3	1078[a]	0.04	6	0.91	5.10	5.38		
B3	1078[a]	0.04	5	1.60	3.18	4.86		
B3	1078[a]	0.04	4	3.64	1.60	5.20		
B4	1078[a]	0.04	15	0	13.1		6.96	1.18×10^3
B5	1141	0.08	15	0	7.3		0.974	4.70×10^3
B6	1141	0.08	15	0	7.0		0.934	4.70×10^3
B8	1194	0.19	10	0	3.92		0.195	1.26×10^4
B9	1194	0.19	10	0	3.08			1.27×10^4
B11	1241	0.38	10	0	4.2		0.0908	2.90×10^4

Table O.II. (continued)

Photo no.	T_E (°K)	n_o (μA)	V_E (V)	t_o (msec)	$I_o - I_\infty$ (μA)	N_o (10^{10} atoms)	N' (10^{10} atoms)	P_{io} (sec^{-1})
B17	1295[b]	0.83	10	0	6.1		0.0679	5.64×10^{4}
B21	1346[c]	1.60	25	0	20.4		0.121	1.06×10^{5}
B22	1346[c]	1.60	10	0	11.4			1.13×10^{5}
B23	1346[c]	1.60	40	0	8.6			4.82×10^{4}
B24	1398[d]	3.15	40	0	6.4		0.0416	9.67×10^{4}
B24	1398[d]	3.15	10					2.28×10^{5} [e]

(a) to (d): interelectrode spacing was: (a) 0.76 mm, (b) 0.66 mm, (c) 0.43 mm, (d) 0.41 mm.

(e) Estimated from B24 using the ratio of $P_{io}(40V)/P_{io}(10V)$ obtained from B22 and B23.

Table O.III Heat-of-evaporation data analysis for the (100) crystal, with emitter temperature decreasing and T_{Cs} = -196°C.

Photo no.	T_E (°K)	n_o (μA)	V_E (V)	t_o (msec)	$I_o - I_\infty$ (μA)	N_o (10^{10} atoms)	N' (10^{10} atoms)	P_{io} (sec^{-1})
C1	1372	2.39	30	0	9.8		0.0586	1.05×10^5
C4	1372	2.39	15	0	7.5		0.0386	1.22×10^5
C7	1316	1.19	10	0	4.5		0.0332	8.50×10^4
C8	1271	0.61	25	0	5.5		0.109	3.18×10^4
C9	1271	0.61	15	0	5.5			3.57×10^4
C10	1271	0.61	5	0	4.7			4.37×10^4
C11	1271	0.61	4	0	4.7			4.26×10^4
C13	1216	0.26	10	0	5.6		0.183	1.92×10^4
C14	1158	0.10	10	0	9.5		0.832	7.17×10^3
C17	1110	0.06	20	0	69		20.1	2.16×10^3
C18	1110	0.06	10	0.41	28.9	15.6	3.7	2.54×10^3
C18	1110	0.06	8	0.71	19.6	14.4		
C18	1110	0.06	7	1.00	14.6	14.3		
C18	1110	0.06	5.4	1.76	8.6	14.1		
C18	1110	0.06	4.3	3.13	4.5	12.8		

Table 0.III (Continued)

Photo no.	T_E (°K)	n_o (μA)	V_E (V)	t_o (msec)	$I_o - I_\infty$ (μA)	N_o (10^{10} atoms)	N' (10^{10} atoms)	P_{io} (sec^{-1})
C19	1110	0.06	6	1.46	10.53	14.4		
C19	1110	0.06	5.3	1.89	8.09	14.6		
C19	1110	0.06	4.7	2.66	6.38	15.8		
C19	1110	0.06	4.0	4.38	3.50	14.2		
C21	1053	0.06	25	0	78		93.7	5.23×10^{2}
C23	1053	0.06	15	0.58	55.8	73.6		
C23	1053	0.06	12	1.43	38.6	70.3	27	7.02×10^{2}
C23	1053	0.06	10	2.04	28.3	61.6	17	7.48×10^{2}
C23	1053	0.06	8.5	3.18	19.5	56.5	8.1	7.78×10^{2}
C23	1053	0.06	6	6.55	10.3	52.7		
C24	1053	0.06	6	5.6	11.37	55.9		
C24	1053	0.06	5	9.0	7.06	52.2		
C24	1053	0.06	4	17.8	3.26	48.4		
C27	1021	0.07	25	0	110		304	2.27×10^{2}
C28	1021	0.07	15	1.7	56.8	207		
C28	1021	0.07	10	6.7	26.9	171	8.0	3.95×10^{2}
C28	1021	0.07	8	11.1	17.6	155		
C28	1021	0.07	6	19.9	10.1	139		
C29	1021	0.07	6	18.8	10.63	151		
C29	1021	0.07	4	61.5	3.43	142		

TABLE O.IV Heat-of-evaporation data analysis for the (100) crystal, T_{Cs} = 0°C.

Photo no.	T_E (°K)	n_o (μA)	V_E (V)	t_o (μsec)	$I_o - I_\infty$ (μA)	N_o (10^{10} atoms)	N' (10^{10} atoms)	P_{io} (sec^{-1})	P_{ao} (sec^{-1})
D1	1503	15.4	40	4.50	569	3.08			3140
D3	1503	15.4	40				1.0	2.39×10^5	
D4	1503	15.4	15	22.3	104	1.75			5460
D4	1503	15.4	12	29.1	68	1.59			6040
D4	1503	15.4	10	36.9	49.3	1.45			6590
D4	1503	15.4	8	51.5	30.2	1.31			7300
D4	1503	15.4	7	66.6	20.8	1.23			7790
D5	1503	15.4	15				0.09	4.79×10^5	
D8	1479[a]	11.8	40				1.1	2.25×10^5	
D9	1479	11.8	15	23.5	94.0	1.72			4310
D9	1479	11.8	12	30.3	67.2	1.60			4620
D9	1479	11.8	10	38.8	49.3	1.53			4840
D9	1479	11.8	8	54.3	30.3	1.37			5390
D9	1479	11.8	6	90.1	15.0	1.22			6100
D10	1479[a]	11.8	15				0.05	4.62×10^5	
D11	1453	9.4	40	4.85	520	3.34	1.8	1.80×10^5	1770
D12	1453	9.4	40				1.8	1.80×10^5	

TABLE O.IV (Continued)

Photo no.	T_E (°K)	n_o° (μA)	V_E (V)	t_o (μsec)	$I_o - I_\infty$ (μA)	N_o (10^{10} atoms)	N' (10^{10} atoms)	P_{io} (sec^{-1})	P_{ao} (sec^{-1})
D13	1453	9.4	15	24.7	101.0	1.96			3010
D13	1453	9.4	12	33.6	66.0	1.80			3290
D13	1453	9.4	10	42.9	49.1	1.75			3360
D13	1453	9.4	8	61.8	30.3	1.55			3800
D13	1453	9.4	6	102.3	15.3	1.43			4120
D14	1453	9.4	15				0.09	3.38×10^5	
D15	1424	7.7	40				3.0	1.42×10^5	
D16	1424	7.7	15	33.1	97.0	2.54			1910
D16	1424	7.7	12	44.1	66.6	2.35			2060
D16	1424	7.7	10	59.8	46.0	2.15			2250
D16	1424	7.7	8	84.2	29.4	1.93			2500
D16	1424	7.7	6	136.1	15.0	1.84			2620
D17	1424	7.7	15				0.11	2.58×10^5	
D18	1398[b]	6.4	40	8.7	408	4.98			807
D19	1398	6.4	40				2.3	1.07×10^5	
D20	1398	6.4	15	46.3	92.6	3.28	0.12	1.93×10^5	1220
D20	1398	6.4	12	63.0	61.5	2.94			1370
D20	1398	6.4	10	81.7	43.5	2.73			1480

TABLE O.IV (Continued)

Photo no.	T_E (°K)	n_o (μA)	V_E (V)	t_o (μsec)	$I_o - I_\infty$ (μA)	N_o (10^{10} atoms)	N' (10^{10} atoms)	P_{io_1} (sec^{-1})	P_{ac} (sec^{-1})
D20	1398	6.4	8	115.8	28.1	2.58			1560
D21	1398[b]	6.4	15				0.12	1.84×10^5	
D22	1398[c]	6.4	40	3.60	783	6.38			631
D23	1398	6.4	40				2.2	1.16×10^5	
D24	1398	6.4	30	8.3	514	4.91			819
D24	1398	6.4	25	9.7	385	4.43			908
D24	1398	6.4	20	15.0	269	3.76			1068
D24	1398	6.4	15	23.2	167	3.33	0.15	2.33×10^5	1208
D24	1398[c]	6.4	10	43.8	81	2.91			1373
D25	1347	6.5	40	14.6	707	14.7			277
D26	1347	6.5	40				5.2	6.02×10^4	
D27	1347	6.5	35	25.5	584	16.3			250
D27	1347	6.5	30	30.0	454	13.2			309
D27	1347	6.5	25	38.6	328	11.0			371
D27	1347	6.5	20	50.3	232	9.65	0.43	1.12×10^5	423
D27	1347	6.5	15	73.1	141	8.14			502
D27	1347	6.5	12	100.0	93	7.42			550

TABLE O.IV (Continued)

Photo no.	T_E (°K)	n_o (μA)	V_E (V)	t_o (μsec)	$I_o - I_\infty$ (μA)	N_o (10^{10} atoms)	N' (10^{10} atoms)	P_{io} (sec^{-1})	P_{ao} (sec^{-1})
D28	1347	6.5	30				1.9	8.37×10^4	
D29	1347	6.5	12	94	102.9	7.57			539
D29	1347	6.5	10	120	79.5	7.47			546
D29	1347	6.5	8	191	49.0	7.37			554
D29	1347	6.5	7	244	37.0	7.16			570
D29	1347	6.5	6	340	25.4	7.13			572
D31	1296	6.0	40	51.5	596	34.9			108
D32	1296	6.0	40				4.5	2.82×10^4	
D33	1296	6.0	35	55	498	29.0			130
D33	1296	6.0	30	69	399	24.8			152
D33	1296	6.0	25	87	292	21.5			175
D33	1296	6.0	20	117	200	19.1	0.94	5.07×10^4	198
D33	1296	6.0	15	176	123	17.0			222
D33	1296	6.0	12	250	80	15.9			235
D33A	1296	6.0	12	255	90.7	17.8			212
D33A	1296	6.0	10	338	66.4	17.3			218
D33A	1296	6.0	8	503	42.8	16.9			223
D33A	1296	6.0	7	644	32.1	16.7			227
D33A	1296	6.0	6	894	22.8	16.9			224

TABLE O.IV (Continued)

Photo no.	T_E (°K)	n_o (μA)	V_E (V)	t_o (μsec)	$I_o - I_\infty$ (μA)	N_o (10^{10} atoms)	N' (10^{10} atoms)	P_{io} (sec^{-1})	P_{ao} (sec^{-1})
D34	1243	6.1	40	155	555	110			34.8
D35	1243	6.1	40				12	1.09×10^4	
D36	1243	6.1	35	180	457	85.1			45.0
D36	1243	6.1	30	204	360	71.0			54.0
D36	1243	6.1	25	306	251	59.2			64.8
D36	1243	6.1	20	388	176	51.9	1.7	2.40×10^4	73.8
D36	1243	6.1	15	553	111	45.9			83.6
D36	1243	6.1	12	775	73	42.1			91.0
D37	1243	6.1	9	1170	51.1	44.3			86.4
D37	1243	6.1	8	1500	39.2	44.3			86.4
D37	1243	6.1	7	1880	30.9	44.3			86.4
D37	1243	6.1	6	2580	21.7	43.7			87.6
D37	1243	6.1	5	3900	13.2	43.0			89.1
D38	1189	6.1	40	528	546	404			9.49
D39	1189	6.1	40				18	3.64×10^3	
D40	1189	6.1	40	510	551	380			10.1
D40	1189	6.1	30	710	341	237			16.1
D40	1189	6.1	25	910	248	198			19.4

TABLE O.IV (Continued)

Photo no.	T_E (°K)	n_o (μA)	V_E (V)	t_o (μsec)	$I_o - I_\infty$ (μA)	N_o (10^{10} atoms)	N' (10^{10} atoms)	P_{io} (sec^{-1})	P_{ao} (sec^{-1})
D40	1189	6.1	20	1300	165	168			22.8
D40	1189	6.1	15	1910	99	148			25.8
D41	1189	6.1	35	620	450	307			12.5
D41	1189	6.1	30	785	341	244			15.7
D41	1189	6.1	25	1065	250	204			18.8
D41	1189	6.1	20	1370	174	173	5.0	9.64×10^3	22.2
D41	1189	6.1	15	1945	109	147			26.1
D42	1189	6.1	15	1900	113.1	158			24.3
D42	1189	6.1	12	2560	78.7	150			25.5
D42	1189	6.1	10	3480	55.5	144			26.5
D42	1189	6.1	8	5060	35.7	138			27.9
D42	1189	6.1	7	6450	26.7	135			28.4
D43	1136[d]	6.2	40	1490	474	991			3.93
D44	1136	6.2	40				36	1.33×10^3	
D45	1136	6.2	40	1340	472	901			4.32
D45	1136	6.2	30	1980	304	576			6.76
D45	1136	6.2	25	2420	225	477			8.16
D45	1136	6.2	20	3220	154	406	4.6	4.07×10^3	9.59
D45	1136	6.2	15	5130	91	360			10.8

TABLE O.IV (Continued)

Photo no.	T_E (°K)	n_o (μA)	V_E (V)	t_o (μsec)	$I_o - I_\infty$ (μA)	N_o (10^{10} atoms)	N' (10^{10} atoms)	P_{io} (sec^{-1})	P_{ao} (sec^{-1})
D46	1136	6.2	15	4950	102	366			10.6
D46	1136	6.2	12	6350	71.5	346			11.2
D46	1136	6.2	10	8750	51.1	328			11.9
D46	1136	6.2	8	13,050	32.5	317			12.3
D46	1136	6.2	6	23,350	17.5	316			12.3
D47	1136	6.2	35	1600	389	704			5.53
D47	1136	6.2	30	2020	299	559			6.97
D47	1136	6.2	25	2620	219	468			8.33
D47	1136	6.2	20	3280	153	399			9.77
D47	1136[d]	6.2	15	5110	91	347			11.2

a. Interelectrode spacing = 0.46mm.

b. Interelectrode spacing = 0.47mm.

c. Interelectrode spacing = 0.35mm.

d. Interelectrode spacing = 0.45mm.

P. Cesium-ion Emission Data for the (100) and (110) Crystals

The effective work function ϕ was evaluated from the Saha-Langmuir equation

$$\phi = V_i - k\, T_E\, [\ell n\ 1/2\ (en_o/J_{Cs}-1)], \qquad (P.1)$$

where V_i = 3.89 eV = first ionization potential of cesium

en_o = flux of cesium vapor incident on the emitter

J_{Cs} = field-free cesium-ion emission from the emitter

T_E = emitter temperature.

The value of en_o for each observed cesium-reservoir temperature T_{Cs} was obtained from the data of Taylor and Langmuir (Fig. V.2). The field-free ion current-density J_{Cs} was determined from the extrapolation to zero electric field of Schottky plots. Schottky plots were obtained for all data except those within 10°K of the threshold temperature T_{Eo} for 100% surface ionization. The value of T_{Eo} for each corresponding T_{Cs} was obtained from Fig. V.10. The results for the (100) and (110) crystals are shown in Tables P.I and P.II, respectively.

Table P.1. Summary of results for surface ionization of cesium on (100) tungsten.

T_{Cs} (°C)	T_E (°K)	T_E/T_{Cs} (°K/°K)	en_o (ampere/cm^2)	J_{Cs} (ampere/cm^2)	ϕ (eV)	$\Delta\phi$[a] (eV)
100	1300[b]	3.48	1.48×10^{-2}			
	1293	3.47		1.00×10^{-2}	4.05	0.60
	1293	3.47		2.25×10^{-3}	3.77	0.88
	1240	3.32		1.67×10^{-4}	3.48	1.17
	1188	3.21		1.48×10^{-5}	3.30	1.35
	1135	3.04		9.30×10^{-7}	3.01	1.64
80	1230[b]	3.48	3.90×10^{-3}			
	1240	3.51		3.86×10^{-3}	4.43	0.22
	1240	3.51		8.00×10^{-4}	3.81	0.84
	1188	3.37		5.27×10^{-5}	3.52	1.13
	1135	3.22		4.80×10^{-6}	3.30	1.35
	1083	3.07		2.35×10^{-7}	3.04	1.61
60	1160[b]	3.48	9.20×10^{-4}			
	1135	3.41		3.52×10^{-5}	3.63	1.02
	1083	3.25		1.69×10^{-6}	3.36	1.29
40	1090[b]	3.48	1.65×10^{-4}			
17	1010[b]	3.48	1.80×10^{-5}			
	977	3.37		1.41×10^{-7}	3.53	1.12

[a] $\Delta\phi = \phi_o - \phi = 4.65 - \phi$.

[b] Emitter threshold temperature for 100% surface ionization at corresponding T_{Cs}.

Table P.2. Summary of results for surface ionization of cesium on (110) tungsten

T_{Cs} (°C)	T_E (°K)	T_E/T_{Cs} (°K/°K)	en_o (ampere/cm^2)	J_{Cs} (ampere/cm^2)	ϕ (eV)
100	1418[a]	3.80	1.48×10^{-2}		
	1335	3.58		1.54×10^{-4}	3.44
	1267	3.40		7.89×10^{-6}	3.14
90	1380[a]	3.80	7.80×10^{-3}		
	1340	3.69		3.27×10^{-4}	3.60
	1267	3.49		1.42×10^{-5}	3.27
80	1342[a]	3.80	3.90×10^{-3}		
	1339	3.79		7.61×10^{-4}	3.80
	1268	3.59		2.77×10^{-5}	3.42
70	1303[a]	3.80	1.90×10^{-3}		
	1267	3.69		5.77×10^{-5}	3.59
50	1228[a]	3.80	4.40×10^{-4}		
	1192	3.69		5.45×10^{-6}	3.52

[a] Emitter threshold temperature for 100% surface ionization at corresponding T_{Cs}.

Q. Thermionic Emission Data for (100) and (110) Crystals Exposed to Cesium Vapor

The effective work function ϕ was evaluated from the Richardson equation

$$\phi = k\, T_E\, [\ell n\, A - \ell n\, J_{so}/T_E^2],$$

where A = Richardson constant determined from the vacuum data ($A = 238$ ampere/cm^2 °K^2 for the (100) crystal and 207 ampere/cm^2 K^2 for the (110) crystal).

J_{so} = field-free electron emission from the emitter

T_E = emitter temperature.

The field-free electron current-density J_{so} was determined from the extrapolation to zero electric field of Schottky plots. The results for the (100) and (110) crystals are shown in Tables Q.I and Q.II, respectively.

Table Q.I. Summary of results for thermionic emission from (100) tungsten exposed to cesium vapor.

T_E (°K)	T_{Cs} (°C)	T_E/T_{Cs} (°K/°K)	I_{so}[a] (amperes)	ϕ (eV)	$\Delta\phi$[b] (eV)
1505	14	5.25	8.40×10^{-8}	4.64	0.01
1453	6	5.20	2.40×10^{-8}	4.62	0.03
1453	100	3.90	8.00×10^{-7}	4.22	0.43
1445	80	4.09	1.53×10^{-7}	4.41	0.24
1396	100	3.74	7.70×10^{-7}	4.05	0.60
1396	80	3.96	1.46×10^{-7}	4.25	0.40
1396	60	4.19	2.40×10^{-8}	4.47	0.18
1392	100	3.73	8.00×10^{-7}	4.04	0.61
1392	80	3.94	1.30×10^{-7}	4.25	0.40
1398	60	4.20	1.70×10^{-8}	4.52	0.13
1345	100	3.61	1.00×10^{-6}	3.87	0.78
1345	80	3.81	1.42×10^{-7}	4.09	0.56
1345	60	4.04	1.70×10^{-8}	4.34	0.31
1293	100	3.47	1.42×10^{-6}	3.67	0.98
1293	80	3.66	1.50×10^{-7}	3.92	0.73
1293	60	3.88	1.30×10^{-8}	4.19	0.46
1242	100	3.33	2.30×10^{-6}	3.46	1.19
1242	80	3.52	2.30×10^{-7}	3.71	0.94
1242	60	3.73	1.50×10^{-8}	4.00	0.65
1240	100	3.32	2.28×10^{-6}	3.46	1.19
1240	80	3.51	2.20×10^{-7}	3.71	0.94
1240	60	3.72	1.30×10^{-8}	4.01	0.64

Table Q.I. (continued)

T_E (°K)	T_{Cs} (°C)	T_E/T_{Cs} (°K/°K)	I_{so} [a] (amperes)	ϕ (eV)	$\Delta\phi$ [b] (eV)
1188	100	3.19	4.84×10^{-6}	3.23	1.42
1188	80	3.37	3.90×10^{-7}	3.49	1.16
1188	60	3.57	1.20×10^{-8}	3.84	0.81
1135	100	3.04	1.06×10^{-5}	3.00	1.65
1135	80	3.22	8.40×10^{-7}	3.25	1.40
1135	60	3.41	2.70×10^{-8}	3.58	1.07
1083	100	2.90	2.53×10^{-5}	2.77	1.88
1083	80	3.07	2.08×10^{-6}	3.00	1.65
1083	60	3.25	7.30×10^{-8}	3.32	1.33
1030	100	2.76	7.30×10^{-5}	2.53	2.12
1030	80	2.92	6.00×10^{-6}	2.75	1.90
1030	60	3.09	2.35×10^{-7}	3.04	1.61
977	100	2.62	2.02×10^{-4}	2.30	2.35
988	80	2.80	1.80×10^{-5}	2.54	2.11
988	60	2.97	6.80×10^{-7}	2.82	1.83
988	40	3.16	1.40×10^{-8}	3.15	1.50
903 [c]	100	2.42	1.23×10^{-3}	1.98	2.67
903	80	2.56	1.58×10^{-4}	2.14	2.51
903	60	2.71	6.10×10^{-6}	2.39	2.26
903	40	2.89	1.35×10^{-7}	2.69	1.96
848 [c]	100	2.27	3.25×10^{-3}	1.78	2.87
848	80	2.40	3.94×10^{-4}	1.93	2.72
848	60	2.55	2.56×10^{-5}	2.13	2.52
848	40	2.71	9.80×10^{-7}	2.37	2.28

Table Q.II. (continued)

a. To convert I_{so} to current density J_{so}, ampere/cm^2, divide by 0.71 cm^2 (effective collector area).

b. $\Delta\phi = \phi_o - \phi = 4.65 - \phi$.

c. Emitter temperatures 903 and 848°K were estimated within 2% from extrapolation of a heating power versus T_E curve. All other emitter temperatures were measured with an optical pyrometer having a precision of 0.2%.

Table Q.II. Summary of results for thermionic emission from (110) tungsten exposed to cesium vapor

T_E (°K)	T_{Cs} (°C)	T_E/T_{Cs} (°K/°K)	J_{so} (ampere/cm^2)	ϕ (eV)
1335	100	3.58	1.11×10^{-4}	3.32
1340	90	3.69	2.76×10^{-5}	3.49
1339	80	3.79	8.60×10^{-6}	3.62
1330	71	3.87	3.60×10^{-6}	3.70
1330	50	4.12	4.06×10^{-7}	3.95
1268	99	3.41	2.40×10^{-4}	3.05
1268	89	3.50	7.05×10^{-5}	3.19
1268	80	3.59	2.18×10^{-5}	3.31
1268	70	3.70	5.30×10^{-6}	3.47
1268	51	3.93	4.51×10^{-7}	3.74
1192	101	3.19	8.74×10^{-4}	2.73
1192	88	3.30	2.60×10^{-4}	2.85
1192	80	3.38	8.87×10^{-5}	2.96
1192	70	3.48	2.48×10^{-5}	3.09
1192	50	3.69	1.69×10^{-6}	3.37
1117	101	2.99	2.90×10^{-3}	2.43
1117	89	3.09	7.32×10^{-4}	2.56
1117	80	3.16	2.44×10^{-4}	2.67
1117	70	3.26	6.90×10^{-5}	2.79
1117	60	3.35	1.42×10^{-5}	2.94
1117	50	3.46	3.94×10^{-6}	3.06

R. Theoretical Evaluations of the Work-Function Depression of Polycrystalline and (100) Tungsten Due to Cesium Adsorption

This appendix contains the numerical computations (Tables R.I through R.V) from which Figs. VI.2 and VI.9 to VI.12 were drawn. It also includes a tabulation of the experimental results of Taylor and Langmuir[88] (Table R.II). The physical properties of polycrystalline tungsten that we used in each analysis were those suggested by the authors of the theory. These properties did not always agree with the data of Taylor and Langmuir. In particular, Carabateas et al.[16] and Levine and Gyftopoulos[58] used a value for the cesium-atom desorption energy ϕ^*_{ao} of 2.9 eV instead of the measured value 2.8 eV. We wish to point out that $\Delta\phi_{max}$ and the horizontal position of the $\Delta\phi$ versus T_E/T_{Cs} curve are both strongly influenced by the choice of ϕ^*_{ao}. In evaluating the work function depression of the (100) crystal, we used $\sigma = 2.5\times10^{14}$ atom/cm^2, $\phi_o = 4.65$ eV, $\phi^*_{ao} = \phi_o + \phi_{io} - V_i = 2.81$ eV (see Sec. IV.D) and $T_E = 1000°K$. Although this temperature was not exactly in the midrange of our data, it was chosen arbitrarily to facilitate the computations.

Table R.I. Tabulation of $K(\theta)$ versus θ.

θ	$K(\theta)^a$	$K(\theta)^b$	$K(\theta)^c$
0.01	-4.58	-4.55	-4.45
0.02	-3.87	-3.81	-3.64
0.04	-3.14	-3.02	-2.83
0.05	-2.89	-2.74	-2.55
0.06	-2.69	-2.51	-2.31
0.08	-2.35	-2.11	-1.91
0.10	-2.09	-1.79	-1.58
0.20	-1.14	-0.54	-0.38
0.30	-0.42	+0.48	+0.59
0.40	+0.26	+1.46	+1.53
0.50	+1.00	+2.50	+2.59
0.60	+1.91	+3.71	+3.91
0.70	+3.18	+5.28	+5.80
0.80	+5.39	+7.79	+9.05
0.90	+11.20	+13.90	+17.92

[a] Rasor and Warner, (Ref. 76), $K(\theta) = \ln\left(\frac{\theta}{1-\theta}\right) + \frac{\theta}{1-\theta}$.

[b] Carabateas et al., (Ref. 16), $K(\theta) = \ln\left(\frac{\theta}{1-\theta}\right) + \frac{\theta}{1-\theta} + 3\theta$.

[c] Levine and Gyftopoulos, (Ref. 59), $K(\theta) = \ln\left[\frac{\theta(1-\theta)^{-1/2}}{(1-\theta^{1/2})}\right] + \frac{\theta}{2(1-\theta)} + \frac{\theta^{1/2}}{2(1-\theta^{1/2})}$.

Table R.II. Data of Taylor and Langmuir for cesium adsorption on polycrystalline tungsten.

θ	ϕ_i (eV)	ϕ_a^* (eV)	$\Delta\phi$ (eV)	T_E/T_{Cs} (°K/°K)
0	2.04	2.79	0	
0.01	2.13	2.77	0.11	4.40
0.05	2.43	2.70	0.48	3.98
0.10	2.73	2.61	0.87	3.69
0.20	3.19	2.44	1.50	3.32
0.30	3.55	2.30	2.00	3.00
0.40	3.84	2.17	2.42	2.75
0.50	4.04	2.06	2.73	2.52
0.55	4.09	2.00	2.83	2.42
0.60	4.10	1.96	2.89	
0.65	4.08	1.91	2.92	2.16
0.70	4.04	1.87	2.92	
0.75	3.99	1.84	2.90	
0.80	3.93	1.81	2.87	

[a] These data were obtained from Ref. 88. Values for ϕ_i, ϕ_a^*, and $\Delta\phi(=\Delta\phi_i + \Delta\phi_a^*)$ were obtained from Table I and values for T_E/T_{Cs} were obtained for $T_{Cs} = 290°$ from Fig. 15 in that reference.

Table R.III. Theoretical evaluation of $\Delta\phi$ versus T_E/T_{Cs} by means of the theory of Rasor and Warner (Refs. 75 and 76).

	(poly) tungsten, T_E = 640°K				(100) tungsten, T_E = 1000°K			
θ	$\Delta\phi$[a] (eV)	1-f	ϕ_a^{*}[b] (eV)	T_E/T_{Cs}[c]	$\Delta\phi$[d] (eV)	E (eV)	ϕ_a^{*}[e] (eV)	T_E/T_{Cs}[f]
0.00	0	0.188	2.79		0.00	1.054	2.81	
0.01	0.09	0.190	2.77	4.03	0.06	1.042	2.80	4.21
0.05	0.42	0.197	2.71	3.82	0.31	0.994	2.75	3.94
0.10	0.80	0.206	2.63	3.67	0.59	0.932	2.69	3.78
0.20	1.47	0.224	2.46	3.36	1.11	0.806	2.56	3.48
0.30	2.01	0.241	2.31	3.11	1.54	0.684	2.44	3.24
0.40	2.44	0.259	2.16	2.86	1.89	0.564	2.32	3.00
0.50	2.73	0.277	2.03	2.64	2.17	0.453	2.21	2.77
0.60	2.93	0.295	1.93	2.43	2.37	0.358	2.11	2.55
0.70	2.95	0.313	1.87	2.25	2.48	0.278	2.03	2.28
0.80	2.88	0.330	1.84	2.05	2.52	0.222	1.98	1.96
0.90	2.79	0.348	1.82	1.61	2.51	0.177	1.94	1.24

[a] $\Delta\phi$ was determined from Fig. 4 of Ref. 75. It was evaluated by Rasor and Warner with the values $A = 4\pi e^2 \sigma r_i = 8.92$ eV, $B = 2\pi\sigma a_i r_i = 4.51$ and $E_o = 1.054$ eV.

[b] $\phi_{ao}^{*} = 2.79$ eV is the measured value of Taylor-Langmuir (Table IV.II).

[c] T_E/T_{Cs} calculated from Eq. (3) in Table VI.I with h = 0.75 eV, K(θ) given in Table R.I., and $(Q_a\sigma/C) = 1$. To fit the Taylor-Langmuir data at $\Delta\phi$ = 2.0 eV, we must use $Q_a\sigma/C = 3.9$.

[d] $\Delta\phi(100)$ and E evaluated by iteration with $A = 8.92/\sqrt{2} = 6.30$ eV, and $B = 4.51/\sqrt{2} = 3.19$.

[e] ϕ_a^{*} evaluated from Eq. (2) in Table VI.I with $\phi_{ao}^{*}(100) = \phi_o + \phi_{io} - V_i = 2.81$ eV.

[f] T_E/T_{Cs} evaluated from Eq. (3) in Table VI.I with $Q_a\sigma/C = 3.9/\sqrt{2} = 2.8$.

NOTE: The factor $\sqrt{2}$ is the ratio of surface densities for a monolayer adsorption used by Rasor and Warner for polycrystalline tungsten (3.56×10^{14} atom/cm^2) and that for (100) tungsten (2.5×10^{14} atom/cm^2).

Table R.IV. Theoretical evaluation of $\Delta\phi$ versus T_E/T_{Cs} by means of the theory of Carabateas et al. (Ref. 16).

	(poly) tungsten, T_E = 800°K					(100) tungsten, T_E = 1000°K				
θ_i	θ [a]	$\Delta\psi_i$ [b] (eV)	$\Delta\phi$ [c] (eV)	ϕ_a^* [d] (eV)	T_E/T_{Cs} [e]	θ [f]	$\Delta\psi_i$	$\Delta\phi$ [g] (eV)	ϕ_a^* [h] (ev)	T_E/T_{Cs} [i]
0.00	0.00	0.00	0.00	2.90		0.00	0.00	0.00	2.81	
0.01	0.01	0.08	0.08	2.88	4.26	0.01	0.06	0.06	2.80	4.21
0.05	0.05	0.39	0.39	2.80	3.99	0.05	0.28	0.28	2.73	3.91
0.10	0.10	0.75	0.75	2.70	3.77	0.10	0.54	0.54	2.66	3.72
0.20	0.20	1.39	1.39	2.53	3.42	0.20	1.03	1.03	2.52	3.38
0.30	0.30	1.94	1.94	2.38	3.12	0.30	1.46	1.46	2.41	3.11
0.40	0.40	2.41	2.41	2.25	2.87	0.40	1.86	1.85	2.30	2.86
0.50	0.51	2.80	2.74	2.14	2.61	0.51	2.21	2.17	2.21	2.60
0.60	0.63	3.13	2.91	2.05	2.35	0.63	2.52	2.40	2.12	2.32
0.70	0.80	3.40	2.71	1.98	1.92	0.78	2.79	2.44	2.05	1.87

[a] $\theta = (\theta_i + \theta_a)$, with $\theta_a = 2\theta_i \exp(-E/kT_E)$, E_o = 1.1 eV, and f = 0.73.

[b] $\Delta\psi_i$ evaluated with $A = 4\pi e^2\sigma r_i$ = 8.0 eV, $k_1 = 2\pi a_i\sigma(1-f)/r_i$ = 0.35.

[c] $\Delta\phi$ evaluated from Eq. (1) in Table VI.I, with $k_2 = 4\pi\sigma(1-f)/r_i$ = 2.5.

[d] ϕ_{ao}^* = 2.9 eV is the value suggested in Ref. 16.

[e] T_E/T_{Cs} calculated with h = 0.75 eV and $Q_a\sigma/C$ = 1 and $K(\theta)$ given in Table R.I. To fit the Taylor-Langmuir data at $\Delta\phi$ = 2.0 eV, we must use $Q_a\sigma/C$ = 2.4.

[f] θ evaluated with $\theta_a = 2\theta_i \exp(-E/kT_E)$, with E_o = 1.01 eV, f = 0.73.

[g] $\Delta\phi$ calculated with $A = 8.0/\sqrt{2} = 5.66$ eV, $k_1 = 0.35/\sqrt{2} = 0.247$, $k_2 = 2.5/\sqrt{2} = 1.77$.

[h] ϕ_a^* evaluated with ϕ_{ao}^* (100) = $\phi_o + \phi_{io} - V_i$ = 2.81 eV.

[i] T_E/T_{Cs} evaluated with $Q_a\sigma/C = 2.4/\sqrt{2} = 1.7$.

NOTE: The factor $\sqrt{2}$ is the ratio of surface densities for a monolayer adsorption used by Carabateas et al. for polycrystalline tungsten (3.56×10^{14} atom/cm^2) and that for (100) tungsten (2.5×10^{14} atom/cm^2).

Table R.V. Theoretical evaluation of $\Delta\phi$ versus T_E/T_{Cs} by means of the theory of Gyftopoulos and Levine (Refs. 35 and 58).

	(poly) tungsten, T_E = 800°K				(100) tungsten, T_E = 1000°K		
θ	$G(\theta)$	$\Delta\phi$[a] (eV)	ϕ_a^*[b] (eV)	T_E/T_{Cs}[c]	$\Delta\phi$[d] (eV)	ϕ_a^*[e] (eV)	T_E/T_{Cs}[f]
0.00	1.000	0.00	2.88		0.00	2.81	
0.02	0.999	0.14	2.88	4.17	0.07	2.80	4.25
0.05	0.992	0.38	2.78	3.97	0.19	2.76	4.11
0.10	0.972	0.77	2.66	3.70	0.41	2.69	3.89
0.20	0.896	1.47	2.43	3.28	0.88	2.55	3.56
0.30	0.784	2.04	2.24	2.95	1.37	2.37	3.21
0.40	0.638	2.44	2.09	2.66	1.81	2.22	2.91
0.50	0.500	2.69	1.99	2.43	2.16	2.10	2.63
0.60	0.352	2.83	1.90	2.19	2.44	2.01	2.36
0.70	0.216	2.85	1.85	1.95	2.64	1.93	2.03
0.80	0.104	2.82	1.80	1.61	2.77	1.88	1.63

[a] $\Delta\phi$ evaluated with $(\phi_m - \phi_f) = 2.81$ eV, $k_1 = 2.6$, $k_2 = 1.22$.

[b] ϕ_a^* calculated with $F = 0.256\ G(\theta)$, $e^2/R = 4.02$ eV, $V_i = 3.87$ eV, $k_4 = 1.75$ eV.

[c] Calculated with $h = 0.75$ eV, $Q_a\sigma/C = 1$ and $K(\theta)$ given in Table R.I. To fit the Taylor-Langmuir data at $\Delta\phi = 2.0$ eV, we must use $Q_a\sigma/C = 0.65$.

[d] $\Delta\phi$ evaluated with $(\phi_m - \phi_f) = 2.85$ eV, $k_1 = 1.2$, $k_2 = 0.47$.

[e] ϕ_a^* evaluated with $F = 0.218\ G(\theta)$, $\delta = 0$, $k_4 = 1.84$ eV.

[f] T_E/T_{Cs} evaluated with $Q_a\sigma/C = 0.34$.

NOTE: The parameters that we used for ϕ_a^* were chosen to yield $\phi_{ao}^*(100) = \phi_o + \phi_{io} - V_i = 2.81$ eV, and $H_{cc}(\theta = 0) = 1.80$ eV, the latter value conforming with estimates of ϕ_{ao} used in the two other studies. Gyftopoulos and Levine used $\sigma(\text{poly}) = 4.8\times10^{14}$ atoms/cm^2; they also listed values for properties of Cs and W as follows: $R = 3.65$Å, $\phi_m' = 8.68$ eV, $\phi_f' = 0.80$ eV, $S_m = 2.62$, $S_f = 1.0$, $\phi_f = 1.81$ eV, $a_o = 13$Å^3.

REFERENCES

1. R. L. Aamodt, L. J. Brown, and B. D. Nichols, Thermionic Emission from Molybdenum in Vapors of Cesium and Cesium Fluoride, J. Appl. Phys., 33 (6), 2080 (1962).

2. U. A. Arifov and A. Kh. Ayukhanov, Investigation of Secondary Emission from Metals Under Bombardment by Positive Ions of Alkali Elements, Akad. Nauk. (SSSR), Bull. Phys. Ser., 20, 1057 (1956).

3. U. A. Arifov, and Kh. Kh. Khadzhimukhamedov, Concerning Neutralization of Fast Positive Ions on Metal Surfaces, Bull. Acad. Sci., USSR - Phys. Ser. (Engl. Trans.) 24, 711 (1960).

4. U. A. Arifov, A. Kh. Ayukhanov, and D. D. Gruich, On Scattering of Slow Alkali Metal Ions from Metal Surfaces, Bull. Acad. Sci. USSR - Phys. Ser. (Engl. Trans.) 24, 716 (1960).

5. U. A. Arifov, N. N. Flyants, and A. Kh. Ayukhanov, Some Properties of Secondary Ion-Neutral Emission, Soviet Phys., Doklady (Engl. Trans.) 7 (2), 131 (1962).

6. John Bardeen, Theory of the Work Function. II. The Surface Double Layer, Phys. Rev., 49 (9), 653 (1936).

7. Joseph A. Becker, Thermionic and Adsorption Characteristics of Cesium on Tungsten and Oxidized Tungsten, Phys. Rev., 28, 341 (1926).

8. J. A. Becker, Thermionic Electron Emission and Adsorption, Rev. Mod. Phys., 7 (2), 95 (1935).

9. M. Benjamin and R. O. Jenkins, The Distribution of Autelectronic Emission from Single Crystal Metal Points. I. Tungsten, Molybdenum, Nickel in the Clean State, Proc. Roy. Soc., (London) A176, 262 (1940).

10. Samuel H. Bosch and Gunkis Kuskevics, Kinetic Secondary Electron Ejection from Tungsten by Cesium Ions, Phys. Rev., 134 (5A), A1356 (1964).

11. Richard C. Bradley, Sputtering of Alkali Atoms by Inert Gas Ions of Low Energy, Phys. Rev., 93 (4), 719 (1954).

12. Roland Breitweiser, On the Relation of Ion and Electron Emission to Diode Diagnostics, in Report on the Thermionic Conversion Specialist Conference, Gatlinburg, Tenn., sponsored by IEEE and AIAA, issued by General Electric Research Laboratory, P. O. Box 1088, Schenectady, N. Y., Oct. 7-9, 1963, p. 17.

13. A. A. Brown, L. J. Neeland, and H. E. Farnsworth, Thermionic Work Function of the (100) Face of a Tungsten Single Crystal, J. Appl. Phys., 21 (1), 1 (1950).

14. D. G. Bulyginsky and L. N. Dobretsov, Investigation of the Surface Work-Function Distribution for Oxide Cathodes, Soviet Phys., Tech. Phys., 1, 1115 (1956).

15. E. N. Carabateas, Thermodynamics of Surface Films, J. Appl. Phys., 33 (9), 2698 (1962).

16. E. N. Carabateas, R. Stickney and T. Aponick, Basic Studies of Cesium Thermionic Converters, Report to the National Science Foundation, Project No. DSR 8955, Dept. Mech. Engr., MIT, Cambridge, Mass. (1964).

17. Homer Charles Carney, Space Charge Neutralization by Cesium, Rubidium and Potassium in Plasma Diodes (M.S.Thesis), University of California, Berkeley, July 1964 (unpublished).

18. H. S. Carslaw and J. C. Jaeger, Conduction of Heat in Solids, 2nd Ed., (Oxford University Press, N. Y., 1959) p. 219.

19. H. J. Caulfield, Estimation of Contact Potential Differences in Thermionic Energy Converters, J. Appl. Phys. 35 (10), 2862 (1964).

20. R. A. Chapman, Thermionic Work Function of Thin-Oxide-Coated Aluminum Electrodes in Vacuum and in Cesium Vapor, J. Appl. Phys., 35 (10), 2832 (1964).

21. E. U. Condon and Hugh Odishaw, Handbook of Physics (McGraw-Hill Book Co., N. Y., 1958) pp. 7-21.

22. B. D. Cullity, Elements of X-Ray Diffraction (Addison-Wesley Publishing Co., Inc., Reading, Mass., 1956).

23. P. H. Cutler and J. J. Gibbons, Model for the Surface Potential Barrier and the Periodic Deviations in the Schottky Effect, Phys. Rev., 111 (2),394 (1958).

24. J. H. DeBoer, Adsorption Phenomena, in Advances in Catalysis, Vol. VIII, (Academic Press, N. Y., 1956).

25. B. Devin, G. Gayte, L. Koch and L. Sondaar, Study of Thermoemissive Properties of Uranium Carbides by an Emission Electron Microscope, Advanced Energy Conversion 3, 287 (1963).

26. Bernard Devin, et Nguyen Xuan Phuc, Les Effets des Taches (ou Grains) et le Travail de Sortie Moyen d'un Emetteur Polycristallin (Patch Effects and Average Work Functions of Polycrystalline Thermionic Emitters), Centre d'Études Nucléaires de Scalay, Commissariat à l'Energie Atomique Rapport CEA-R-2519 (1964).

27. L. N. Dobretsov, Electron and Ion Emission (State Publishing House for Technical and Theoretical Literature, Moscow-Leningrad) NASA Technical Translation (English) (Nov. 1963) NASA-TT-F-73 (1952).

28. W. P. Dyke, J. K. Trolan, W. W. Dolan and F. J. Grundhauser, Field Emission Current-Density Distribution, J. Appl. Phys., 25 (1), 106 (1954).

29. R. C. Evans, The Positive Ion Work Function of Tungsten for the Alkali Metals, Proc. Roy. Soc., (London) A139, 604 (1933).

30. R. C. Evans, The Equilibrium of Atoms and Ions Adsorbed on a Metal Surface, Proc. Cambridge Phil. Soc., 29, 161 (1933).

31. Raymond Fox and William Gust, Ion Adsorption on Metals for Low Fractional Surface Coverage, UCRL-6389 (1961).

32. J. W. Gadzuk and E. N. Carabateas, Penetration of an Ion Through a Monolayer of Similar Ions Adsorbed on a Metal, J. Appl. Phys., 36 (2), 357 (1965).

33. Robert Gomer and Lynn W. Swanson, Theory of Field Desorption, J. Chem. Phys., 38 (7), 1613 (1963).

34. R. W. Gurney, Theory of Electrical Double Layers in Adsorbed Films, Phys. Rev., 47, 479 (1935).

35. Elias P. Gyftopoulos and Jules D. Levine, Work Function Variation of Metals Coated by Metallic Films, J. Appl. Phys., 33 (1), 67 (1962).

36. George A. Haas and Richard E. Thomas, Investigation of the Patch Effect in Uranium Carbide, J. Appl. Phys., 34 (12), 3457 (1963).

37. Homer D. Hagstrum, Auger Ejection of Electrons from Tungsten by Noble Gas Ions, Phys. Rev., 96 (2), 325 (1954).

38. Homer D. Hagstrum, Theory of Auger Ejection of Electrons from Metals by Ions, Phys. Rev., 96 (2), 336 (1954).

39. Conyers Herring and M. H. Nichols, Thermionic Emission, Rev. Mod. Phys., 21 (2), 185 (1949).

40. Izumi Higuchi, Taikyue Ree, and Henry Eyring, Adsorption Kinetics. I. The System of Alkali Atoms on Tungsten, J. Am. Chem. Soc., 77, 4969 (1955).

41. Izumi Higuchi, Taikyue Ree, and Henry Eyring, Adsorption Kinetics. II. Nature of the Adsorption Bond, J. Am. Chem. Soc., 79, 1330 (1957).

42. F. L. Hughes, H. Levinstein, and R. Kaplan, Surface Properties of Etched Tungsten Single Crystals, Phys. Rev., 113 (4), 1023 (1959).

43. Andrew R. Hutson, Velocity Analysis of Thermionic Emission from Single-Crystal Tungsten, Phys. Rev., 98 (4), 889 (1955).

44. Max Jacob, Heat Transfer, Vol. II (John Wiley and Sons, Inc., N. Y., 1957)p. 14.

45. R. P. Johnson and W. Shockley, An Electron Microscope for Filaments: Emission and Adsorption by Tungsten Single Crystals, Phys. Rev., 49, 436 (1936).

46. D. W. Juenker, G. S. Colladay, and E. A. Coomes, Surface Barrier Analysis for the Highly Refractory Metals by Means of Schottky Deviations, Phys. Rev., 90 (5),772 (1953).

47. D. W. Juenker, Surface Barrier Analysis for Metals by Means of Schottky Deviations, Phys. Rev., 99 (4),1155 (1955).

48. Manfred Kaminsky, A Pulsed-Molecular-Beam Mass Spectrometer for Studies of Atomic and Ionic Impact Phenomena on Metal Surfaces, Advanced Energy Conversion, 3, 255 (1963).

49. Manfred Kaminsky, Atomic and Ionic Impact Phenomena on Metal Surfaces, Argonne National Laboratory Report (1964); or Struktur und Eigenschaften der Materie, Prof. S. Flugge, (Springer-Verlag, Heidelberg, Germany) (to be published).

50. J. T. Killian, Thermionic Phenomena Caused by Vapors of Rubidium and Potassium, Phys. Rev., 27, 578 (1926).

51. Sitiri Kitrilakis, D. Lieb, and L. van Someren, Emitter Crystal Structure Study, Thermo Electron Engineering Corp., Second Quarterly Progress Report No. 27-63, April 1963.

52. S. Kitrilakis, N. Rasor, and L. van Someren, Third Quarterly Report for Emitter Crystal Structure Study, Thermo Electron Engineering Corp., Report TE 18-64, Nov. 1963.

53. S. S. Kitrilakis and J. H. Weinstein, Additive Converter Studies, Air Force Aero Propulsion Laboratory Report AFL-TDR-64-2 (Jan. 1964).

54. Friedrich Knauer, Die Verweilzeit adsorbierter Alkaline an erhitztem Wolfram, Z. Physik, 125, 278 (1948-49).

55. Irving Langmuir, The Effect of Space Charge and Residual Gases on Thermionic Currents in High Vacuum, Phys. Rev., 2, 450 (1913).

56. Irving Langmuir and K. H. Kingdon, Thermionic Effects Caused by Vapours of Alkali Metals, Proc. Roy. Soc (London) A107, 61 (1925).

57. Irving Langmuir, Vapor Pressures, Evaporation, Condensation and Adsorption, J. Am. Chem. Soc., 54, 2798 (1932).

58. Jules D. Levine and Elias P. Gyftopoulos, Adsorption Physics of Metallic Surfaces Partially Covered by Metallic Particles. I. Atom and Ion Desorption Energies, Surface Science, 1, 171 (1964).

59. Jules D. Levine and Elias P. Gyftopoulos, Adsorption Physics of Metals Partially Covered by Metallic Particles. II. Desorption Rates of Atoms and Ions, Surface Science, 1, 225 (1964).

60. Jules D. Levine and Elias P. Gyftopoulos, Adsorption Physics of Metals Partially Covered by Metallic Particles. III. Equations of State and Electron Emission S-Curves, Surface Science, 1, 349 (1964).

61. S. T. Martin, On the Thermionic and Adsorptive Properties of the Surfaces of a Tungsten Single Crystal, Phys. Rev., 56, 947 (1939).

62. G. C. Mikhailov, L. A. Kutovaia and L. A. Pospelov, On the Dependence of Work Function of Film Cathodes on the Ionization Potential of Adsorbed Atoms, Radiotekhnika i elektronika, 5 (10), 1658 (1960).

63. A. R. Miller, The Variation of the Dipole Moment of Adsorbed Particles with the Fraction of the Surface Covered, Proc. Cambridge Phil. Soc., 42, 292 (1946).

64. R. A. Missman and B. L. Gehman, Experimental Studies of Low-Work-Function Collectors, Advan. Energy Conversion, 3, 229 (1963).

65. P. B. Moon and M. L. E. Oliphant, The Surface Ionization of Potassium by Tungsten, Proc. Roy. Soc. (London) A137, 463 (1932).

66. Erwin W. Müller, Work Function of Tungsten Single Crystal Planes Measured by the Field Emission Microscope, J. Appl. Phys., 26 (6), 732 (1955).

67. H. A. Nancarrow, Tables of Facilitate the Calculation of the Temperature-Distribution in a Cylinder, Proc. Phys. Soc. (London) 45, 462 (1933).

68. M. H. Nichols, The Thermionic Constants of Tungsten as a Function of Crystallographic Direction, Phys. Rev., 57, 297 (1940).

69. William Tobias Norris, Thermionic Emission from a Single Crystal of Tantalum Exposed to Cesium Vapor (Ph.D. Thesis) M.I.T., Aug. 1962, p.106.

70. William Tobias Norris, Work Function of the (110) Face of Tantalum in a Cesium Vapor, J. Appl. Phys., 35 (3), 467 (1964).

71. Wayne B. Nottingham, Thermionic Emission, in Handbuch der Physik, Ed., S. Flugge, (Springer-Verlag, Berlin, Vol. 21, 1956) p.1.

72. Julius Perel, Richard H. Vernon, and Howard L. Daley, Desorption Time Measurements using ac Modulation Techniques, J. Appl. Phys., 36 (7), 2157 (1965).

73. Ioannis Psarovthakis, The Design, Construction, and Testing of A Cesium Thermionic Energy Converter with Single Crystal Molybdenum Emitter (M.S. Thesis) M.I.T., May 1962.

74. N. S. Rasor, G. N. Hatsopoulos, and S. Kitrilakis, The Cesium Vapor Thermionic Converter: II. Patch and Transport Effects, Advan. Energy Conversion, 2, 569 (1961).

75. Ned S. Rasor and Charles Warner, III, Correlation of Electron, Ion, and Atom Emission Energies, Atomic International Report AI-6799, (Nov. 1961) p. 45. Also AD-267930.

76. Ned. S. Rasor and Charles Warner, Correlation of Emission Processes for Adsorbed Alkali Films on Metal Surfaces, J. Appl. Phys., 35 (9), 2589 (1964).

77. Fred L. Ryenolds, Ionization on Tungsten Single-Crystal Surfaces, J. Chem. Phys., 39 (4), 1107 (1963).

78. B. S. Rump and B. L. Gehman, Work Function Measurements of Nickel, Molybdenum, and Tungsten in a Cesium-Hydrogen Atmosphere, J. Appl. Phys., 36 (8), 2347 (1965).

79. Milton D. Scheer and Joseph Fine, Kinetics of Cs^+ Desorption from Tungsten, J. Chem.Phys., 37 (1),107 (1962).

80. Haywood Shelton, Thermionic Emission from a Planar Tantalum Crystal, Phys. Rev., 107 (6), 1553 (1957).

81. G. N. Shuppe, E. P. Sytaia, and R. M. Kadyrov, Work Function of the (110) Face of a Tungsten Single Crystal and Positive Surface Ionization of Sodium on this Face, Akad. Nauk. (SSSR) (Engl. Trans.) Bull. Phys. Ser., 20, 1035 (1956).

82. George F. Smith, Thermionic and Surface Properties of Tungsten Crystals, Phys. Rev., 94 (2),295 (1954).

83. R. Smoluchowski, Anisotropy of the Electronic Work Function of Metals, Phys. Rev., 60, 661 (1941).

84. G. V. Spivak, I. A. Pryamkova and N. N. Sedov, Electron-Optical Contrast in Observation of Patch Fields on Emitters, Bull. Acad. Sci., USSR-Phys. Ser., 24, 648 (1960).

85. Robert E. Stickney, Thermionic Emission from an Exponential Patch Distribution, J. Appl. Phys., 34 (10), 3145 (1963).

86. L. W. Swanson, R. W. Strayer, F. M. Charbonnier, and E. C. Cooper, Field Emission Investigation of Thermal Desorption and Surface Diffusion of Cesium on Tungsten, NASA Report - CR-22 (1964).

87. E. P. Sytaya, M. I. Smorodinova, and N. I. Imangulova, Electron and Ion Emission from the (110) and (100) Faces of a Large Tungsten Monocrystal, Soviet Physics - Solid State (Engl. Transl.) 4, (4), 750 (1962).

88. John Bradshaw Taylor and Irving Langmuir, The Evaporation of Atoms, Ions and Electrons from Caesium Films on Tungsten, Phys. Rev., 44 (6), 423 (1933).

89. John Bradshaw Taylor and Irving Langmuir, Vapor Pressure of Caesium by the Positive Ion Method, Phys. Rev., 51, 753 (1937).

90. Albert van der Ziel, Solid State Physical Electronics, (Prentice-Hall, Inc., Englewood Cliffs, N. J., 1957).

91. L. J. Varnerin, Jr., Neutralization of Ions and Ionization of Atoms Near Metal Surfaces, Phys. Rev., 91 (4), 859 (1953).

92. V. I. Veksler, Interaction of Slow Positive Rubidium and Cesium Ions with the Surface of Molybdenum, Soviet Physics JETP, 15 (2), 222 (1962).

93. R. Vernon, Potential of an Ion in a Discrete Dipole Layer, Atomics International Report AI-6799 (1961) p. 81. Also AD-267930.

94. Charles Warner, III, Statistical Mechanical Treatment of Surface Ionization, Atomics International Report AI-6799 (1961) p. 85. Also AD-267930.

95. G. N. Watson, Theory of Bessel Functions, 2d Ed., (Cambridge University Press, N. Y., 1944) p. 666.

96. H. F. Webster, Thermionic Emission from a Tantalum Crystal in Cesium or Rubidium Vapor, J. Appl. Phys., 32 (9), 1802 (1961).

97. E. Wigner and J. Bardeen, Theory of the Work Functions of Monovalent Metals, Phys. Rev., 48, 84 (1935).

98. M. K. Wilkinson, Crystallographic Variations of Field Emission from Tungsten, J. Appl. Phys., 24 (9), 1203 (1953).

99. Russel D. Young and Erwin W. Müller, Progress in Field-Emission Work-Function Measurements of Atomically Perfect Crystal Planes, J. Appl. Phys., 33 (1), 91 (1962).

100. E. Ya. Zandberg and N. I. Ionov, Surface Ionization, Soviet Physics USPEHKI 67 (2), 255 (1959).

101. E. Ya. Zandberg, V. I. Paleev, and A. Ya. Tontegode, Threshold Temperature for Surface Ionization on Tungsten as a Function of the Cesium Vapor Pressure, Soviet Physics - Technical Physics 7 (2), 147 (1962).

FIGURE CAPTIONS

Fig. II.1 Cesium plasma diode, front view.

Fig. II.2 Cesium plasma diode, top view.

Fig. II.3 Schematic of (110) diode. (A) Pyrex-glass ampoule of cesium, (B) bellows, (C) copper collector, (D) sapphire window, (E) single-crystal tungsten emitter, (F) tungsten filament, (G) copper guard ring, (H) molybdenum heat shield, (I) ceramic insulator, (J) tantalum cup, (K) cesium reservoir. The diode body was mainly monel.

Fig. II.4 X-ray Laue pattern (actual size) of the tungsten emitter with the [110] direction normal to the surface. White radiation from a tungsten tube was employed, and the spacing between the film and the crystal was the usual 3 cm.

Fig. II.5 X-ray Laue pattern of the tungsten emitter with the [100] direction normal to the surface. This photograph was obtained in the same way as Fig. II.4.

Fig. II.6 X-ray Laue pattern of the (100) tungsten emitter showing the close-grouped double spots. This photograph was obtained in the same way as Fig. II.4.

Fig. II.7 Diode operating in air.

Fig. III.1 (a) Ideal curve of electron emission J vs applied collector voltage V_c for a vacuum diode having an emitter with work function ϕ and a collector with work function ϕ_c such that $\phi > \phi_c$. (b) Diagrams of potential energy (relative to the emitter Fermi level represented by dotted line) of electrons traversing the diode; each diagram corresponds to a region of the curve in (a).

Fig.III.2 Effects of individual variations in ϕ_c, ϕ, and T_E on ideal log J versus V_c curve (1) drawn for $\phi > \phi_c$; (2) ϕ_c increased; (3) ϕ decreased; (4) T_E increased.

Fig.III.3 (a) Circuit diagram for (110) diode; voltage difference V_{CG} is nulled by manually adjusting the voltage divider in series with R_G. (b) Circuit diagram for (100) diode; the amplifier in series with R_G maintains $|V_{CG}| < 1$ mV.

Fig.III.4 Current versus applied collector voltage for the (110) diode operating in vacuum, with the heat shield at the same applied potential as that of both collector and guard ring.

Fig.III.5 Current versus applied collector voltage for the fourth vacuum-data set (increasing temperature) of the (110) diode.

Fig.III.6 Current versus applied collector voltage for the fifth vacuum-data set (increasing temperature) of the (110) diode.

Fig.III.7 Current versus applied collector voltage for the fifth vacuum-data set (decreasing temperature) of the (110) diode.

Fig.III.8 Schottky plot for the fifth vacuum-data set (increasing temperature) of the (110) diode. V_c is the applied collector voltage and V_o is the contact potential.

Fig.III.9 Richardson plots for the (110) crystal emitter. The arrows along the lines point to the direction in which the data were taken. The bottom line (□) is a plot of $J(V_c = -2.04V)/T_E^2$ vs $1/T_E$ for the data of set 4 (Fig. III.5).

Fig.III.10 Current versus applied collector voltage for the third vacuum-data set (increasing temperature) of the (100) diode.

Fig.III.11 Current versus applied collector voltage for the third vacuum-data set (decreasing temperature) of the (100) diode.

Fig.III.12 Schottky plot for the third vacuum-data set (decreasing temperature) of the (100) diode. V_c is the applied collector voltage and V_o is the contact potential.

Fig.III.13 Richardson plots for the (100) crystal emitter. The three lowest lines have been drawn only through the descending-temperature points (black) of each vacuum-data set (1 to 3). The top line was drawn through all the points of the fourth data set which was measured with cesium in the reservoir at -196°C.

Fig.III.14 Schematic Richardson plot for the (100) crystal emitter, showing the chronological, grossly exaggerated behavior of the data shown in Fig. III.13.

Fig.III.15 Saturation current at 2025°K versus accumulated time in vacuum at or above 2025°K (but less than 2078°K) for (100) crystal emitter.

Fig. IV.1 Schematic potential-energy diagram for the adsorption of an electron, and an alkali atom and ion on a metal surface.

Fig. IV.2 Hypothetical cycle for evaporation and re-adsoprtion of an alkali atom on a metal surface.

Fig. IV.3 Ion current I(t) versus time t resulting from the step change in emitter voltage $V_E(t)$, relative to the collector voltage.

Fig. IV.4 Test circuit for measurement of the desorption energies of cesium ions and atoms evaporating from the emitter surface.

Fig. IV.5 Cesium ion current versus time after reversal of applied electric field for (110) crystal. (a) T_E = 1193°K, en = 7.8 μA; (b) T_E = 1242°K, en_o = 19.0 μA; (c) T_E = 1295°K, en_o = 24 μA; (d) T_E = 1348°K, en_o = 34 μA; (e) T_E = 1399°K,

en_o = 54 μA; (f) T_E = 1503°K, en_o = 156 μA. The applied voltage V_E between the emitter and collector after field reversal in the traces a through e was, in consecutive order, 18, 15, 12.5, 10 and 7.5 V.

Fig. IV.6 Cesium ion current versus time after reversal of applied electric field for (100) crystal. T_E = 1243°K. (a) en_o ≈ 0.05 μA, V_E = 10 V; (b) en_o = 6.0 μA, V_E = 40V; (c) same as (b) but with oscilloscope trigger delayed about 300 μsec.

Fig. IV.7 Cesium ion current versus time after reversal of applied electric field for (100) crystal. T_E = 1243°K, en_o = 6.0 μA. The applied voltage V_E between emitter and collector after field reversal for each trace was, in order of descending current maximum, (a) 35, 30, 25, 20, and 15V, (b) 9, 8, 7, 6, and 5V.

Fig. IV.8 Cesium ion current versus time after reversal of applied electric field for (100) crystal. T_E = 1398°K, en_o = 6.4 μA, V_E = 40V. The interelectrode spacing was (a) 0.47 mm, (b) 0.35 mm.

Fig. IV.9 Apparent cesium-ion current I_{Cs} versus emitter voltage V_E, for (100) diode, with the cesium reservoir at -196°C.

Fig. IV.10 Observed cesium-ion current, I_{Cs}, versus emitter voltage V_E, for (100) diode with the cesium reservoir at 0°C.

Fig. IV.11 Cesium-atom evaporation probability per unit time P_{ao} versus applied emitter voltage V_E, for the (100) crystal.

Fig. IV.12 Cesium-ion evaporation probability per unit time P_{io} versus applied emitter voltage V_E, for the (100) crystal.

Fig. IV.13 Cesium-ion evaporation probability per unit time P_{io} versus $1/T_E$ for (100) crystal. Cesium reservoir at -196°C.

Fig. IV.14 Cesium-ion evaporation probability per unit time P_{io} versus $1/T_E$ for (100) crystal. Cesium reservoir at 0°C.

Fig. IV.15 Cesium-atom evaporation probability per unit time P_{ao} versus $1/T_E$ for (100) crystal. Cesium reservoir at 0°C.

Fig. IV.16 Sputtered cesium-atom yield, γ, versus interelectrode potential (applied voltage less contact potential), evaulated from the data for P_{io} and P_{ao}.

Fig. IV.17 Cesium-atom evaporation probability per unit time P_{ao} versus $1/T_E$ for (100) crystal. The straight line through the data is not characteristic of the bare surface because the surface coverage for each data point was not negligible.

Fig. V.1 Cesium-ion current I_{Cs} at 100% surface ionization versus applied collector voltage V_c measured with the (100) diode at an emitter temperature of 1293°K and interelectrode spacing of 0.44 mm.

Fig. V.2 Cesium-ion current density J_{Cs} at 100% surface ionization versus reciprocal cesium-reservoir temperature $1/T_{Cs}$.

Fig. V.3 Cesium-ion current I_{Cs} versus collector voltage V_c, emitted from the (100) crystal emitter at 1135°K under conditions of low fractional ionization.

Fig. V.4 Typical Schottky plots of cesium-ion currents I_{Cs} emitted from the (100) crystal emitter under conditions of low fractional ionization. V_c is the applied collector voltage and V_o is the contact potential.

Fig. V.5 Saturation cesium-ion emission J_{Cs} from the (100) crystal emitter versus reciprocal emitter temperature $1/T_E$, for various cesium-reservoir temperatures. The arrows indicate the cesium-ion current densities at 100% surface ionization measured by Taylor and Langmuir.

Fig. V.6 Saturation cesium-ion emission J_{Cs} from the (110) crystal emitter versus reciprocal emitter temperature $1/T_E$, for various cesium-reservoir temperatures. The arrows indicate the cesium-ion current densities at 100% surface ionization measured by Taylor and Langmuir.

Fig. V.7 Work-function depression $\Delta\phi$ of the (100) crystal emitter versus the emitter-to-cesium-reservoir temperature ratio T_E/T_{Cs}, determined from cesium-ion emission. The dashed lines show the corresponding result obtained from electron emission. $\Delta\phi = 4.65 - \phi$.

Fig. V.8 Work function ϕ of the (110) and (100) crystal emitters versus the emitter-to-cesium-reservoir temperature ratio T_E/T_{Cs}, determined from cesium-ion emission. The dashed line shows the corresponding result obtained from electron emission.

Fig. V.9 Cesium-ion current I_{Cs} versus collector voltage V_c emitted from the (100) crystal emitter at two threshold emitter temperatures for 100% surface ionization.

Fig. V.10 Cesium-vapor flux en_o versus reciprocal emitter threshold temperature $1/T_{EO}$ (T_{EO} is the emitter temperature below which 100% surface ionization of the flux en_o no longer occurs). The right ordinate is the cesium-reservoir temperature which gives rise to the cesium-vapor flux en_o, as measured by Taylor-Langmuir.

Fig. VI.1 Potential energy $\phi(x)$ of an electron at a distance x from a metal surface when a positively charged, transparent grid is placed at x'. The electric field has been made zero for $x > x'$.

Fig. VI.2 Comparison of $K(\theta)$ versus θ. The analytical expressions for $K(\theta)$ are given by Eq. (4) of Table VI.I.

Fig. VI.3 Change in work function, $\Delta\phi$, versus the ratio of emitter to cesium-reservoir temperature, T_E/T_{Cs}, computed by Rasor and Warner. Here n_o is the incident flux of cesium (atoms/sec.cm^2) corresponding to the reservoir temperature T_{Cs}. (Reporduced from Fig. 5 of Ref. 76.

Fig. VI.4 Field-free electron emission, J_{so}, from the (100) emitter versus reciprocal emitter temperature $1/T_E$ for various cesium reservoir temperatures T_{Cs}. The straight lines of constant negative slope give the corresponding values of the emitter work function ϕ.

Fig. VI.5 Field-free electron emission, J_{so}, from the (110) emitter versus recirpocal emitter temperature $1/T_E$ for various cesium reservoir temperatures T_{Cs}. The straight lines of constant negative slope give the corresponding values of the emitter work function ϕ.

Fig. VI.6 Work-function depression $\Delta\phi$ of the (100) emitter versus the emitter-to-cesium-reservoir temperature ratio T_E/T_{Cs}, determined from electron emission. The lower line was drawn through the data obtained at $T_{Cs} = 100°C$. The upper line is the best fit for the data obtained at all lower cesium temperatures. The dashed line shows the result obtained by Taylor and Langmuir for polycrystalline tungsten.

Fig. VI.7 Work-function ϕ of the (110) emitter versus T_E/T_{Cs}, determined from electron emission. Also included are our results for the (100) emitter and the data of Taylor and Langmuir for polycrystalline tungsten.

Fig. VI.8 Comparison of the (100) crystal and Taylor-Langmuir $\Delta\phi$ versus T_E/T_{Cs} curves. The latter has been displaced to the left by $\Delta(T_E/T_{Cs}) = 0.15$.

Fig. VI.9 Theoretical curves of $\Delta\phi$ versus θ for polycrystalline tungsten.

Fig. VI.10 Theoretical curves of $\Delta\phi$ versus T_E/T_{Cs} for polycrystalline tungsten. The curves have been displaced horizontally to match the data of Taylor-Langmuir at $\Delta\phi = 2.0$ eV.

Fig. VI.11 Theoretical curves of $\Delta\phi$ versus θ calculated with our measured parameters for bare (100) tungsten and for $\sigma(100) = 2.5\times10^{14}$ atoms/cm^2.

Fig. VI.12 Theoretical curves of $\Delta\phi$ versus T_E/T_{Cs} calculated using our measured parameters for bare (100) tungsten and for $\sigma = 2.5\times10^{14}$ atoms/cm^2.

Fig. VII.1 Ideal Current-voltage curves for a diode having a uniform collector and an emitter consisting of two patches of equal area with $\phi_1 > \phi_2$.

Fig. VII.2 Electron and apparent ion currents versus applied emitter voltage for the (110) diode. $T_{Cs} = -196°C$.

Fig. VII.3 Electron and apparent ion currents versus applied emitter voltage for the (100) diode. $T_{Cs} = -196°C$.

Fig. VII.4 Normalized ion current versus applied emitter voltage for the (110) diode.

Fig. VII.5 Normalized ion current versus applied emitter voltage for the (100) diode.

Fig. B.1 Schematic of (100) crystal diode. This is a revision of Fig. II.3. The alterations indicated by the numbers are described in this appendix.